UNIVERSITY OF BIRMINGHAM

A STUDY OF MIXED-ANION HYDRIDE LITHIUM-ION CONDUCTORS FOR APPLICATION IN ALL-SOLID-STATE BATTERIES

by

BETHAN LINDSAY HUGHES

A thesis submitted to the University of Birmingham for the degree of

DOCTOR OF PHILOSOPHY

School of Chemistry

College of Engineering and Physical Sciences

The University of Birmingham

September 2019

Abstract

Solid state lithium ion conductors are important in the development of electrolytes for all-solid-state lithium ion batteries. Complex hydrides are one such area of interest due to their thermal and chemical stability as well as their light weight and in this thesis the Li-BH_4-NH-NH_2 phase space was investigated. The structures of two lithium borohydride-imides: one orthorhombic with the formula $Li_5(BH_4)_3NH$, and another cubic with the formula Li_3BH_4NH have been determined through powder diffraction methods.

The reaction of lithium imide and lithium borohydride was studied through both *in-situ* and *ex-situ* powder diffraction methods and highlighted the formation of a melt upon heating. The studies also showed $Li_5(BH_4)_3NH$ formed rapidly upon heating whilst Li_3BH_4NH did not form until late in the cooling process. Further investigation into the reaction of lithium amide-imide and lithium borohydride also identified another phase, a new hexagonal lithium amide-borohydride-imide, $Li_4BH_4NHNH_2$. It was subsequently revealed that $Li_4BH_4NHBH_2$ was apparently the most thermodynamically stable of the three structures, forming upon slow cooling of the Li_2NH + $LiBH_4$ reaction mixture.

Investigations into the lithium ion conductivities of the materials produced promising results, with high conductivities at room temperature. All three materials displayed higher conductivities than lithium borohydride and their mechanical properties made them much more robust when manufacturing half cells as compared to lithium imide.

Acknowledgements

Firstly I would like to thank my supervisors Dr Paul Anderson and Dr Phil Chater for all their help and support over the last four years. Thank you for giving me the opportunity to work with you and continue my studies both at the University and at Diamond Light Source.

I would like to thank everyone of the 5th floor for any help you gave me over the course of my PhD and for making my experience as a postgraduate a great one, I've made some great memories here. Thank you to Dr Bo Dong for your help collecting conductivity data and to Dr Jackie Deans and Dr Louise Male for your help with the analytical equipment throughout.

I would also like to thank the staff on I15 and I15-1 for making my time working in Oxford enjoyable and for any support you provided during my year with you. Thank you as well to the staff on I11 for facilitating the collection of all our high resolution data which has contributed massively to this thesis.

I would like to thank the University of Birmingham and Diamond Light Source for funding my project and for making my PhD possible.

I would also like to thank my family for their support throughout my entire time at university. Thank you to all members of the second family circle of trust. I've finally made it to the end! Finally, I would like to thank Dean for being there for me during this process, for listening to my many thesis rambles and for reassuring me that I can do it.

Table of Contents

List of Figures

List of Tables

List of Abbreviations

A.C.	Alternating Current
a.u.	Arbitrary Units
DEC	Diethyl Carbonate
DFT	Density Functional Theory
DMC	Dimethyl Carbonate
DSC	Differential Scanning Calorimetry
DTA	Differential Thermal Analysis
EC	Ethylene Carbonate
EMC	Ethyl Methyl Carbonate
FTIR	Fourier Transform Infrared
HOMO	Highest Occupied Molecular Orbital
LCO	Lithium Cobalt Oxide
LFP	Lithium Iron Phosphate
LFSF	Lithium Iron Fluorosulfate
LISICONs	Li Super Ionic Conductors
LLTO	Lithium Lanthanum Titanates
LMO	Lithium Manganese Oxide
LNO	Lithium Nickel Oxide
LTO	Lithium Titanium Oxide
LUMO	Lowest Unoccupied Molecular Orbital
MAC	Multi Analyser Crystal

NASICONs	Na Super Ionic Conductors
NCA	Lithium Nickel Cobalt Aluminium Oxide
NMC	Lithium Nickel Manganese Cobalt Oxide
NMR	Nuclear Magnetic Resonance
PC	Principle Component
PCA	Principle Component Analysis
PDF	Pair Distribution Function
PSD	Position Sensitive detector
QPA	Quantitative Phase Analysis
SEI	Solid Electrolyte Interface
XPDF	X-ray Pair Distribution Function
XRD	X-ray Diffraction

Chapter 1 – Introduction

An ever-increasing demand for energy is putting an ever increasing strain on the world's energy sources. Fossil fuels are the main source of this energy, with the combined contribution of coal, oil and natural gas making up 85% of the world's primary energy consumption.[1] There are advantages to using these types of fuel: they are highly calorific, easy to mine, transport and store; and the infrastructure and technology is already in place. However, the production of greenhouse gases and the declining availability of these resources are major issues which need to be addressed. As the availability of fossil fuels continues to decline it is becoming increasingly important to find alternative power sources.

Renewable energy could be the solution to these problems. One of the major advantages is sustainability; energy from renewable sources will not run out. It is also much cleaner than fossil fuels with little or no production of greenhouse gases. Despite these advantages, renewable energy sources currently produce just 11% of the world's primary energy.[1] A major drawback in renewable technologies is continuity of supply; they often rely on weather conditions therefore when these conditions are not suitable there is no longer a supply of energy. One way in which researchers are looking to combat this issue is through improving energy storage technologies. Improved energy storage would enable continuity of supply even during periods of low production with unsuitable conditions. Fuel cells, used alongside electrolysers, are one possible option. Electrolysers use the energy produced to split water into hydrogen and oxygen, where the energy is stored. In order to harness the stored energy, fuel cells then perform the reverse process, combining oxygen and hydrogen to form water and supply energy. There is, however, a long way to go to make fuel cells

commercially viable and the high cost of production is a major drawback.[2] Lithium ion batteries are an alternative energy storage solution.

Lithium batteries are already widely used in modern society powering many different electrical devices. Over recent years there has been a drive to improve upon the current setup of the batteries used in these devices. There is a constant demand for better recharging abilities, higher voltages, longer lifetimes and the utilisation of more lightweight materials. Improvements in lithium battery technology will not only provide better energy storage solutions within power generation but also allow for major advancements in a huge array of electrical devices. Lithium is useful for battery applications as it has the lowest reduction potential of any element,[3] meaning Li-ion batteries have the highest cell potential. As well as this, lithium is very light and small so batteries based on lithium may have good volumetric and gravimetric capacities and power densities[3].

1.1 Battery Operation

The three key chemical components in a battery are: the anode, the cathode and the electrolyte. When a battery discharges, lithium ions travel from the anode through the electrolyte and into the cathode. In order to maintain an overall neutral charge, electrons in the anode travel though an external circuit into the cathode. In order to recharge a battery the reverse process is observed. Both processes are depicted in Figure 1.1. The discharge potential of the cathode is directly proportional to the reduction in Gibbs free energy of the system as ions are inserted into the cathode which is the driving force behind the process[4].

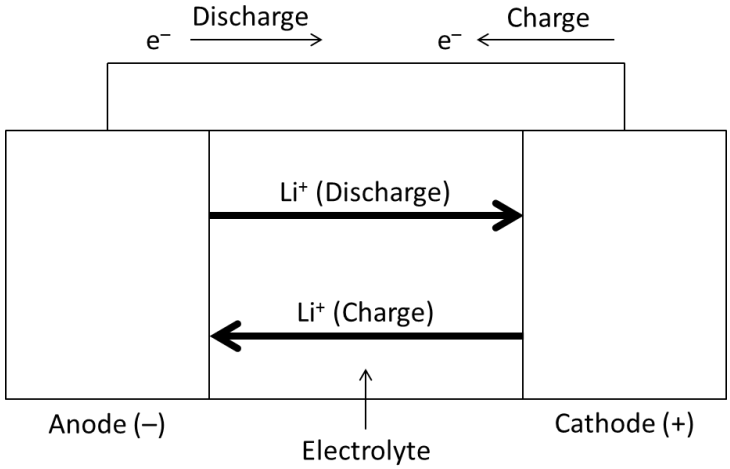

Figure 1.1 – Diagram demonstrating basic operation of a battery

When selecting materials for the construction of a battery, there are certain factors that need to be considered. Thermodynamic stability of the electrolyte is one key factor. It is the different energy levels within the anode, cathode and electrolyte which determine this stability. In order to have a stable system the Fermi energy of the anode needs to be lower in energy than the LUMO (lowest unoccupied molecular orbital) of the electrolyte; this prevents the transfer of electrons into the electrolyte. The same principle is implemented at the electrolyte–cathode interface. The HOMO (highest occupied molecular orbital) of the electrolyte needs to be lower in energy than the Fermi energy of the cathode, in order to prevent electrons being transferred into the cathode (Figure 1.2)[5].

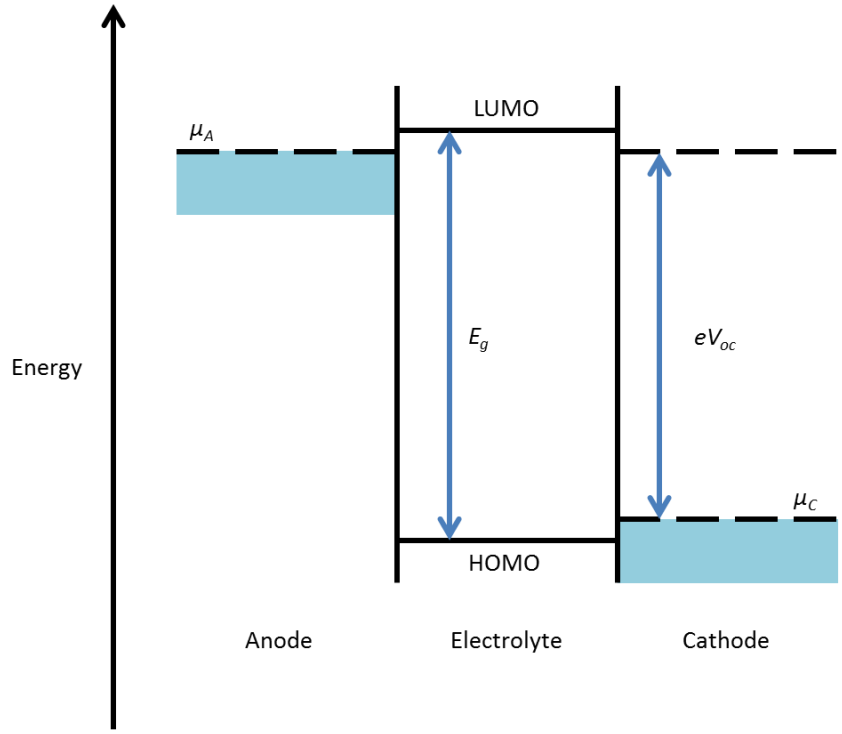

Figure 1.2 – Diagram showing the required energy levels for a thermodynamically stable electrolyte (Adapted from Goodenough *et al.*[5])

The difference in electrochemical potential (also referred to as Fermi energy) of the anode and the cathode (μ_A and μ_C) is what gives the working voltage for a system (V_{oc}), where e is the magnitude of the electronic charge[4]:

$$V_{oc} = \frac{\mu_A - \mu_C}{e} \tag{1.1}$$

The working voltage of the cell must always be smaller than the energy gap between the HOMO and LUMO of the electrolyte in order to be thermodynamically stable. If this is not the case the electrolyte will be either oxidised at the cathode or reduced at the anode, depending on the relative energy levels, and in some cases form a passivating solid electrolyte interface (SEI) film.[4] The SEI can act as a protective barrier allowing lithium ions

to pass through while maintaining a uniform composition at the electrodes. However, formation of an SEI can also result in both power and capacity loss as it consumes some of the lithium ions and increases the internal resistance of the cell.[4]

Theoretical capacity is also an important consideration; it defines how much charge could be stored in an electrode if conditions were optimal. Theoretical capacity is calculated using Faraday's law as in the equation below:

$$\text{Theoretical Capacity} = \left(\left(\frac{\text{nF}}{\text{M}_\text{r}}\right)\left(\frac{1000}{3600}\right)\right) \text{ mAh g}^{-1} \qquad (1.2)$$

n = number of electrons transferred, F is Faraday's constant, M_r is the molecular mass of the electrode and 1000/3600 is the factor used to convert from C g^{-1} into mAh g^{-1}. Theoretically a greater capacity can be achieved by using a lighter material or alternatively incorporating ions which can alter their charge by a value greater than 1.

Finally charge rate needs to be considered when designing a battery. The C-rate, as it is referred to, is the rate at which a battery can discharge from maximum capacity. A C-rate of 1C would completely discharge a battery in 1 hour; a C-rate of C/3 would fully discharge the same battery over the course of 3 hours. The charge rate is important because the ions travelling through the electrolyte need to be able to intercalate into the cathode at the same rate that the electrons are moving through the external circuit. If these are not balanced correctly then the capacity of the battery will decrease.

1.2 Anode Materials

Lithium metal, though a logical choice for a lithium ion battery anode material has never been made commercially viable. Lithium has a very high theoretical capacity of 3860 mA h g^{-1} and the lowest negative electrochemical potential of –3.040 V vs SHE (standard hydrogen electrode)[6]. It is also very light, with a density of 0.59 g cm^{-3}.[6] However, despite these advantages there are issues which consequently to date have prevented lithium from becoming a viable anode material. One of the issues is the growth of dendrites upon charge and discharge. The growth of these dendrites can lead to short circuiting. This leads to safety hazards and can result in the battery catching fire due to thermal runaway at the cathode.[3] The other problem is the low Coulombic efficiency observed during charge/discharge of the battery, resulting in a shorter lifetime. This inefficiency is as a result of the poor thermal stability of lithium metal with the electrolytes, in particular with organic solvents,[6] which can react with the entire lithium anode making the battery useless.[7] As lithium was determined not to be suitable, alternative materials had to be used.

Graphite is one alternative which is widely used as an anode material in commercially available lithium batteries. It has a low intercalation/deintercalation potential of less than 0.2 V (vs Li/Li^+) and its theoretical capacity is 372 mA h g^{-1}.[8] It is also able to intercalate up to one lithium ion for every six carbons, between the graphite layers[3]. Graphite is abundant and low cost; although the higher grades which are required for better efficiency do mean higher costs.[9] Graphite anodes also have moderate energy and power density and a good cycle life[3]. Despite these properties there are some drawbacks to its use. Graphite anodes can have deteriorating capacity due to: cointercalation of solvent molecules and lithium

ions, and graphite particles being isolated due to formation of a surface film.[7] Hard carbons have similar properties to graphite anodes, although their structure is disordered. This makes exfoliation less prevalent but also allows for increased SEI formation and thus a rapidly decreasing capacity as the battery is cycled.[3]

Lithium titanium oxide ($Li_4Ti_5O_{12}$/LTO) is another option which has also been successfully used commercially. Its main advantage is the minimal volume change exhibited upon intercalation. The volume change between the charged and discharged state is just 0.2% resulting in a "zero strain" anode[3]. LTO has a potential of ~1.5 V vs Li/Li^+ and therefore can be operated in a potential window which avoids the formation of SEIs, and even when an SEI is formed the minimal volume change helps it to remain stable. However both ionic and electrical conductivity are poor in LTO making it unsuitable for use in high power applications.[3]

Finally alloy materials are good alternatives to lithium due to their safety and high capacity[8]. They work using an alloying/dealloying mechanism:

$$xLi^+ + xe^- + M \leftrightarrow Li_xM \qquad (1.3)$$

They have very high volumetric and gravimetric capacity; however, a major drawback of these materials is the huge volume changes which can be displayed upon cycling. These volume changes place a significant amount of mechanical stress on the battery. They can also result in the SEI layer being destroyed and therefore a continual decomposition of the anode, loss of Li^+ and thus a short cycle life.[3]

1.3 Cathode Materials

In terms of cathode materials, intercalation materials are the main focus of both commercial success and current research. These intercalation compounds can be broken down into four different structure types: layered, spinel, olivine and tavorite.

The very first intercalation cathode material, $LiTiS_2$, was reported by Whittingham in 1976.[10] TiS_2 belongs to a group of materials called chalcogenides, known to be highly conductive and able to intercalate molecules/ ions into the layers within the structure.[10] At the time the material showed promise as a cathode material, however, later studies demonstrated that excess of Ti can sit within the layers of the structure hindering Li intercalation.[11]

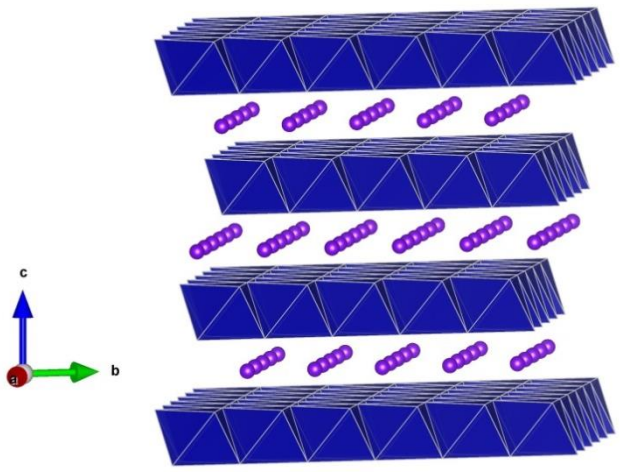

Figure 1.3 – Structure of $LiCoO_2$ where Li = purple sphere and CoO_2 polyhedra = blue polyhedra

In 1980 Goodenough *et al*. then introduced $LiCoO_2$ (LCO) (Figure 1.3).[12] It was the first transition metal layered oxide, the earliest commercial intercalation cathode material, and is still the most popular cathode choice to date. There are many advantages of LCO,

hence its commercial popularity. It has a high theoretical capacity of 274 mA h g^{-1}, high charge voltage, low self-discharge and good cycling performance.[13] However, the high cost of cobalt, declining capacity through deep cycling and use of high currents; and the safety issues associated with its low thermal stability[3] mean that there are still areas of improvement to be made.

Other layered oxides that have been considered are $LiNiO_2$ (LNO) and $LiMnO_2$ (LMO). LNO is very similar to LCO in that it has the same structure and similar theoretical capacity.[3] Although it has a higher energy density and is cheaper to produce than LCO, its thermal stability is less than that of LCO[14] and the nickel ions have a tendency to block the lithium diffusion pathways.[15] LMO is the most thermodynamically stable of the three undoped phases;[14] manganese is also less toxic and much cheaper than both cobalt and nickel. However, cycling is a major issue with $LiMnO_2$ due to both structure changes and leaching of Mn.[3] Research into doping has shown both thermal stability and electrochemical performance of $LiMO_2$ layered phases can be improved, resulting in the use of $LiNi_{0.8}Co_{0.15}Al_{0.05}O_2$ (NCA) and $LiNi_{1/3}Mn_{1/3}Co_{1/3}O_2$ (NMC) in many commercial batteries.[3] LMO can also exist as a spinel oxide with the chemical formula $LiMn_2O_4$. Although cycling is still a problem associated with the system, the use of nanoparticles and consequent reduction of the lithium diffusion pathways has improved the material[16] and as a result these materials became commercially viable.

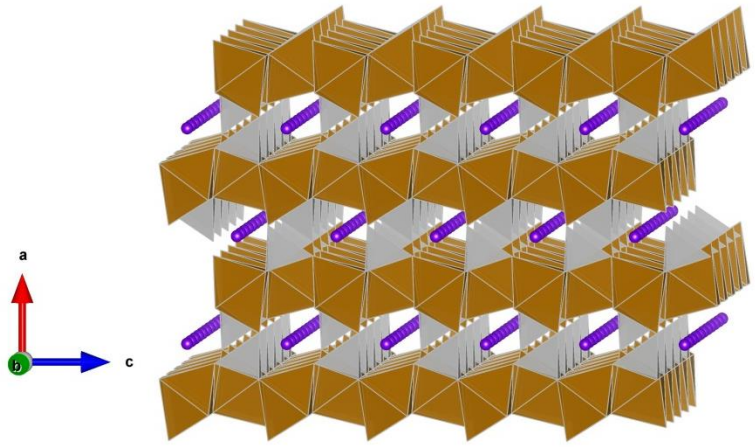

Figure 1.4 – Structure of $LiFePO_4$ where Li = purple spheres, Fe = brown polyhedra and PO_4 = grey polyhedra

More recently research has led to polyanion compounds being considered for cathode use. The large polyanions used in these compounds have the formula $(XO_4)^{n-}$ where X = S, P, Si, As, Mo or W. These large polyanions help to stabilise the framework, important for cycling and safety issues.[17] Their incorporation also increases the redox potential of the cathode.[18] These compounds exist in two different structure types, olivine and tavorite. An example olivine compound is $LiFePO_4$ (LFP)(Figure 1.4), which has been produced and used commercially.[3] One of its major issues is it has both low ionic and electronic conductivity, however, use of a carbon coating can drastically improve electrical conductivity.[17] Nevertheless the low potential of LFP of 3.4 V vs Li does limit the energy density of its batteries.[3,19] $LiFeSO_4F$ (LFSF) is an example of a material with a tavorite structure (Figure 1.5). LFSF has high cell voltage and lithium ion diffusion can occur at high rates in the tavorite structure.[17]

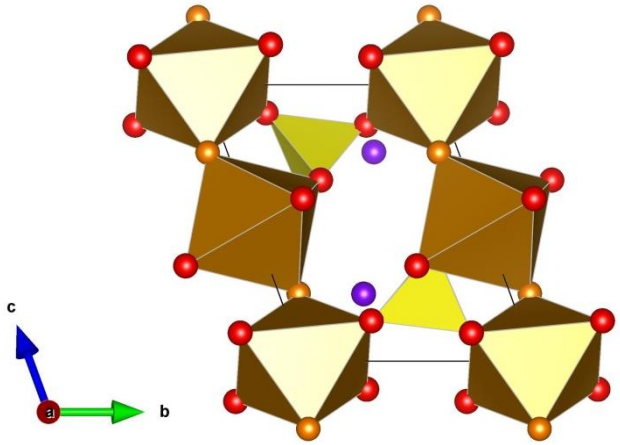

Figure 1.5 – Structure of $LiFeSO_4F$ where Li = purple spheres, Fe = brown polyhedra, S = yellow polyhedra, O = red spheres and F = orange spheres

Conversion cathode materials are an alternative to the intercalation materials described above. Delithiation/lithation occurs as a result of a redox reaction and change in structure of the cathode. There are two types of conversion cathode material, type A and type B, which undergo different chemical reactions:[3]

$$\text{Type A} \qquad MX_z + yLi \leftrightarrow M + zLi_{(y/z)}X \tag{1.4}$$

$$\text{Type B} \qquad yLi + X \leftrightarrow Li_yX \tag{1.5}$$

Type A materials are typically metal halides, such as MF_2 and MCl_2, where M is a metal with a valance of two or more. Their high theoretical capacities and reasonable operating voltages have made them materials of interest.[20,21] Yet there are major drawbacks to these materials including poor conductivity, unwanted side reactions, dissolution of active material and large volume changes.[3] Examples of type B conversion cathode materials include: S, Se, Te and I. However, there are similar issues associated with these materials. Sulfur for example, although it has a very high theoretical capacity and is both abundant and cheap,

has low conductivity, a low potential vs Li/Li^+, and a huge volume change of approximately 80%.[22] On the other hand, research has shown that using Li_2S based nanocomposites can help with volume expansion issues.[23] Moreover, changes to the electrolytes used can help prevent the dissolution of polysulfides, intermediate reaction products, which are another drawback of these materials.[24]

1.4 Electrolytes

A large proportion of current lithium ion batteries use an electrolyte which is made up of a lithium salt, commonly $LiPF_6$,[25] dissolved in an organic solvent. Nonaqueous solvents are used, typically a mixture of carbonates including: ethylene carbonate (EC), dimethyl carbonate (DMC), diethyl carbonate (DEC) and ethyl methyl carbonate (EMC). EC is particularly important as it is used to passivate the anode.[25] However, there are issues with the current setup, most critically safety concerns. There is always the possibility of the flammable solvents used causing corrosion and leaking.[26] There is also the added issue of the limits these systems place on miniaturisation;[27] just to include all the different electrolyte components the battery needs to remain a certain size. Solid state lithium ion conductors are a way of combatting these issues, provided a similarly high lithium ion conductivity can be achieved. These electrolytes could also enable lithium metal anodes to be used too, which could see a huge increase in power density. Lithium metal is not thermodynamically stable towards current organic solvents used and so cannot currently be used safely.[26]

There are many requirements that need to be met in order to provide a suitable alternative. The most important of these are: a high lithium ion conductivity at operating temperature and negligible electronic conductivity at that same temperature. Other factors

which need to be considered include: thermal expansion coefficients to match those of the electrodes, they must not undergo a chemical reaction with the electrodes and there must be a small grain-boundary resistance;[27] this contributes to a better lithium ion conductivity.

1.4.1 Solid State Lithium Ion Conductors

It is the inherent disorder in the structures of solid state lithium ion conductors which is thought to contribute to the lithium ion conduction seen.[28] In an ideal crystalline material the structure is free of any defects; however, without the presence of defects there would be no ionic movement within the structure.[29] There are 2 different types of stoichiometric defects, also known as intrinsic defects: Schottky and Frenkel (Figure 1.6).[29] Schottky defects result from an anion and cation being removed from the structure to leave vacancies. The removal of the ion pair allows a charge balance to be maintained. Frenkel defects on the other hand are the movement of an ion into an interstitial site, leaving behind a vacancy.

Figure 1.6 – Stoichiometric defects in 'MA' (A) Schottky defects (B) Frenkel defects

Extrinsic defects are another way of introducing disorder into a system. These occur as a result of doping the structure with ions of a different valency to those already in the structure. The resulting charge imbalance is corrected through the formation of a vacancy. The presence of defects is necessary to enable the lithium ions to be transported through

the structure. Therefore the greater the understanding of the disorder in these systems, the more can be known about the conductivity mechanism. In order for ions to move into vacancies created by defects, they must have sufficient energy to do so; this is known as the activation energy. This energy barrier is important in determining the likelihood of ions moving through the structure and therefore the material's suitability as an electrolyte material. The activation energy (E_a) is determined using the Arrhenius equation:

$$\sigma = \left(\frac{\mathrm{A}}{\mathrm{T}}\right) \exp\left(\frac{-E_a}{K_B \mathrm{T}}\right) \tag{1.6}$$

where σ is conductivity, T is temperature in Kelvin, A is the pre-exponential factor and K_B is the Boltzmann constant. There is a range of different lithium ion conductors which are part of current research; these will be discussed in the following sections.

1.4.2 Oxides

1.4.2.1 Perovskite Structure

A perovskite is any material with the $CaTiO_3$ structure.[8] The general formula for this family of materials is ABX_3, where A is usually an alkaline or rare earth metal and B is a transition metal. X is commonly oxygen meaning the formula ABO_3 is often used when describing perovskites. The ideal perovskite structure is cubic, with the space group *Pm*-3*m*.[8] Within the structure the A cations are coordinated to twelve oxygens and the B cations are coordinated to six oxygens; this is shown below in Figure 1.7.

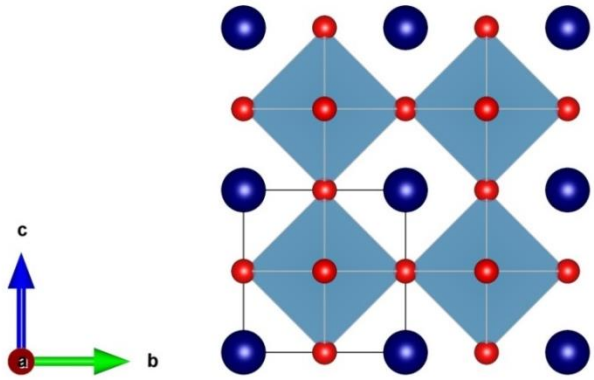

Figure 1.7 – Ideal cubic perovskite structure, ABO_3 where A = dark blue spheres, B = light blue polyhedra and O = red spheres, solid black line shows a single unit cell

Lithium based perovskite materials are formed by the introduction of lithium onto the A site via aliovalent doping, forming structures such as $Li_{3x}La_{2/3-x}\square_{1/3-2x}TiO_3$.[28] Brous *et al.* synthesised the first lithium lanthanum titanate, $Li_{0.5}La_{0.5}TiO_3$ in 1953[30] and since then there has been a lot more research into the properties of these materials. Varying the amount of lithium in the structure varies the amount of defects; and changing the number of defects in the structure changes the number of sites for the lithium ions to move between. Consequently tuning the lithium content can have a significant impact on the conductivity of a material. Researchers have seen bulk conductivities up to 1×10^{-3} S cm^{-1} at room temperature for $Li_{0.34}La_{0.56}TiO_3$ ($Li_{3x}La_{2/3-x}TiO_3$ where x = 0.113).[31] However, despite demonstrating relatively high bulk conductivities, the total conductivities are closer to 10^{-5} S cm^{-1} due to high grain boundary resistances.[31,32] Lithium lanthanum titanates (LLTO) also have issues with reactivity towards anode materials. Any electrode with a potential greater than 2.8 V will result in the titanium reducing at the interface from Ti^{4+} to Ti^{3+} and the lithium intercalating into the lattice;[33] this makes the choice of electrode very limited.

1.4.2.2 NASICON Structure

Materials with the structural formula $NaM_2(PO_4)_3$, where M = Ge, Ti, Zr, were first studied in the 1960s.[34] In 1976 Goodenough *et al*. modified the structure and synthesised $Na_{1+x}Zr_2Si_xP_{3-x}O_{12}$ (where $0 \leq x \leq 3$) which displayed high sodium ionic conductivity.[35] These structures, with the more general formula $AM_2(PO_4)_3$, are referred to as NASICON materials (Na Super Ionic Conductors). In this formula the A cation is an alkali metal (Li^+, Na^+, K^+) and the M cation is tetravalent (Ge^{4+}, Ti^{4+}, Zr^{4+}). The structure is generally rhombodehral, with the space group *R*-3*c*, and has a structure made up of corner sharing PO_4 tetrahedra and MO_6 octahedra. The A ions are then able to diffuse through the interconnected channels created by the polyhedra.[8] There are two different A positions, one 6-fold coordinated sitting directly between two MO_6 octahedra and the other 8-fold coordinated sitting between two MO_6 columns (Figure 1.8). A cation migration occurs by ions hopping between these two sites,[28] the ease of which depends on the nature of the skeleton polyhedra.[36]

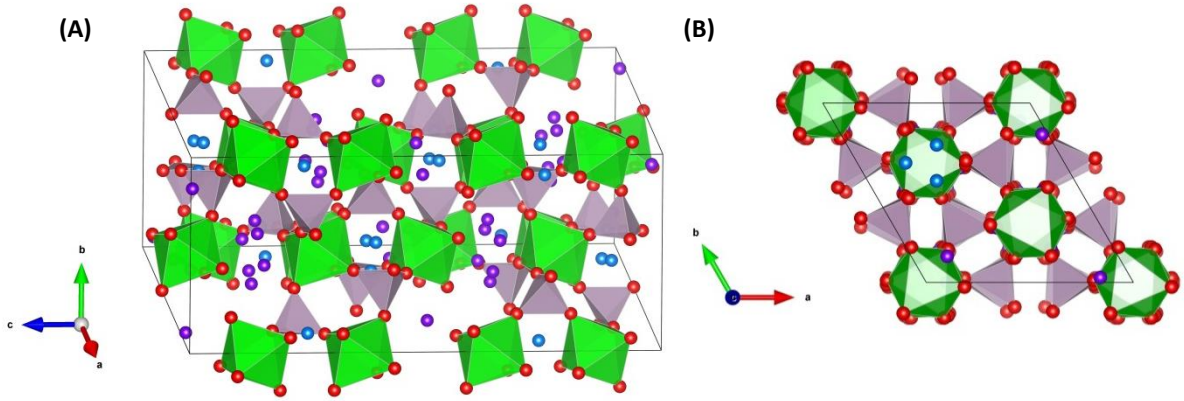

Figure 1.8 – (A) NASICON Structure, $AM_2(PO_4)_3$, where A1 = purple spheres (partial occupancy), A2 = blue spheres (partial occupancy), M = green polyhedra, P = pale purple polyhedra and O = red spheres (B) View along c axis displaying channels in NASICON structure

Lithium analogues (LISICONs) are synthesised by occupying the A site with Li^+. Lithium ion conductivity for these systems is determined by the size of the channel; for the highest conductivity the size of the channel and size of the ion need to match.[37] $LiZr_2(PO_4)_3$ has reportedly low conductivity but substitution of (Hf, Ti, Sn) for Zr can result in a drastic improvement,[38–40] with the best conductivity for $LiTi_2(PO_4)_3$, demonstrating the importance of size match.[37] The conductivity of $LiTi_2(PO_4)_3$ can be improved further by partially replacing Ti^{4+} with M^{3+} to form $Li_{1+x}Ti_{2-x}M_x(PO_4)_3$ (where M = Al, Cr, Ga, Fe, Sc, In, Lu, Y, La), achieving conductivities up to 7×10^{-4} S cm^{-1} at room temperature with Al substitution.[41] Although these materials display relatively fast ionic conductivity at room temperature and have a wide electrochemical window, there are still areas which require improvement, for example grain boundaries and charge density of the structure.[8]

1.4.2.3 Garnet Structure

The ideal garnet structure has the formula $A_3B_2(XO_4)_3$ where A = Ca, Mg, Y, La or a rare earth metal; B = Al, Fe, Ga, Ge, Mn, Ni or V; and X = Si, Ge, Al. The structure has the space group *Ia*-3*d* where A is 8-fold coordinated and B is 6-fold coordinated to oxygen.[42] The first lithium garnet, $Li_3M_2Ln_3O_{12}$ (M = W, Te) was synthesised by Kasper *et al*. in 1969[43] (Figure 1.9); however, later syntheses of garnets containing a lithium excess (Li-stuffed garnets) show promise as solid state lithium ion conductors. In these structures there is too much lithium for all the tetrahedral sites and so the excess is accommodated in usually empty interstitial octahedral sites.[44] In 1988 Mazza synthesised the first of the Li-stuffed garnets, $Li_5La_3M_2O_{12}$ (M = Nb, Ta),[45] which demonstrate conductivities of 10^{-6} S cm^{-1} at room temperature, activation energies of 0.43 eV for Nb and 0.56 eV for Ta, and wide electrochemical windows.[46]

Improvements can be made to the conductivity by substituting La with Ca, Sr or Ba to form $Li_6ALa_2Ta_2O_{12}$, where A = Ca, Sr, Ba. $Li_6BaLa_2Ta_2O_{12}$ gives both the highest conductivity and lowest activation energy with values of 4×10^{-5} S cm^{-1} and 0.40 eV, respectively at room temperature.[47,48] Further improvements still can be made by substitution of M (M = Nb, Ta) with In or Zr. Cubic $Li_7La_3Zr_2O_{12}$ has both a high conductivity, 3×10^{-4} S cm^{-1}, and low activation energy, 0.3 eV.[49] The equivalent tetragonal structure by comparison has low conductivity, with a bulk conductivity of 1.63×10^{-6} S cm^{-1} at 300 K and a high activation energy of 0.54 eV.[50] This difference between the two structures arises as a result of different levels of order and disorder, with lithium content and sintering temperature determining which one forms.[51] In the tetrahedral structure the tetrahedral and octahedral sites are ordered with regards to lithum ions and vacancies, while the cubic structure has disordering on both of these sites.[50] Unfortunately it is the tetrahedral structure which is stable at room temperature; the cubic structure forms when the garnet is heated above 100–150 °C. However, it has been found that doping with aluminium stabilises the high temperature cubic structure, enabling high conductivity to be observed at room temperature;[52,53] the same effect is also observed with Ga doping.[54] Doping is successful in stabilising the cubic structures and increasing room temperature conductivities. It causes vacancies to be introduced on the Li^+ sites as the structure accommodates greater charges, and consequently increases disorder.[54] Further studies into substitution of both Zr and La have given higher conductivities still with $Li_{6.5}La_3Zr_{1.75}Te_{0.25}O_{12}$ displaying a conductivity of 1.02×10^{-3} S cm^{-1} at room temperature.[55]

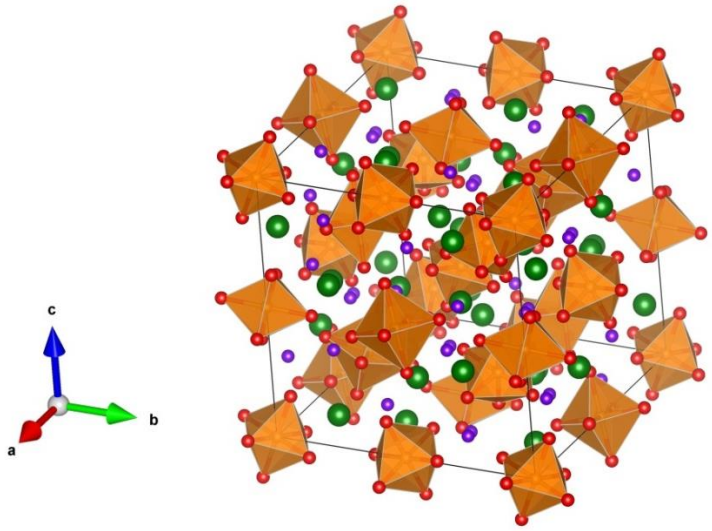

Figure 1.9 – Cubic garnet structure, $Li_5La_3M_2O_{12}$ where Li = purple spheres, La = green spheres, M = orange polyhedra, O = red spheres

1.4.3 Sulfides

1.4.3.1 Li_2S–SiS_2 System

The first Li_2S–SiS_2 solid electrolyte was synthesised using a melting–quench method and displayed conductivity between 10^{-6} and 10^{-3} S cm^{-1}. Mixing anhydrous Li_2S and SiS_2 and doping with LiI to form $0.6(0.4SiS_2–0.6Li_2S)–0.4LiI$ gave the best conductivity with a value of 1.8×10^{-3} S cm^{-1} at room temperature, and an activation energy of 0.28 eV.[56,57] Research since then has focused on improving both conductivity and electrochemical stability.[58,59]

1.4.3.2 *Thio*-LISICONs

Thio-LISICONs are adapted from originally oxide-containing LISICON materials. Sulfides have a larger ionic radius and are more polarisable and therefore it was hoped their use would result in a greater mobility of conducting ions, than their oxide counterparts.[60] A key study into the $Li_{4-x}Ge_{1-x}P_xS_4$ structure, and first introduction of this family, demonstrated

a high ionic conductivity of 2.2 × 10^{-3} S cm^{-1} at room temperature, along with negligible electronic conductivity and high electrochemical stability.[60] Materials found in the *thio*-LISICON family have the general formula $Li_xM_{1-y}M'_yS_4$, where M = Si, Ge and M' = P, Al, Zn, Ga, Sb,[61] with one of their key characteristics being the solid solution range available due to aliovalent doping.[27] One of the more recently discovered *thio*-LISICONs is $Li_{10}GeP_2S_{12}$, which has shown an ionic conductivity of 1.2 × 10^{-2} S cm^{-1}.[62] However, despite the high conductivity achieved, a major drawback is the cost of germanium which significantly reduces its commercial practicalities. A tin alternative has also been synthesised, a possible solution to the high cost, and displays a room temperature conductivity of 4 × 10^{-3} S cm^{-1}.[63] Although the conductivity achieved is not as high the as germanium counterpart, the huge reduction in material cost makes it an important alternative structure.

1.5 Complex Hydrides

Another group of materials that are an important part of research into the development of lithium ion conductors, and have produced promising results are often referred to as lithium complex hydrides. Complex hydrides can include $[BH_4]^-$, $[NH_2]^-$ and $[AlH_4]^-$ among others.[64] Although an important point to note is that the hydrogen is protic, δ^+, rather than hydridic, δ^-, in $[NH_2]^-$. There are several advantages to using complex hydrides over other lithium-conducting electrolytes. Firstly they are lightweight, usually more so than oxide and sulfide electrolytes.[64] In addition, a stable and reversible interface between the electrolyte and Li electrode is formed meaning complex hydrides are highly compatible with lithium electrodes.[65,66] These interfaces are relatively easy to form due to the deformable nature of complex hydride materials.[64] In oxide systems high grain boundary

resistance can be a major issue due to their high rigidity;[67] the softness of complex hydrides helps to reduce these issues at the grain boundaries. Complex hydrides also have high chemical stability in both reducing and oxidising environments,[64] with large potential windows over which they are stable. This is an issue in sulfur-based materials due to their reactivity with conventional cathode materials.[67] Finally, due to the strength of the covalent bonds in the anion, complex hydrides have good thermal stability in the temperature range of interest for solid state batteries.[64,68]

1.5.1 Li–N–H System

The Li–N–H system is a reversible system containing three different structures: the fully hydrogenated lithium amide, partially hydrogenated lithium imide, through to the fully dehydrogenated lithium nitride.[69] It cycles between them through the following reactions:

$$\mathrm{Li_3N} + 2\mathrm{H_2} \leftrightarrow \mathrm{Li_2NH} + \mathrm{LiH} + \mathrm{H_2} \leftrightarrow \mathrm{LiNH_2} + 2\mathrm{LiH} \qquad (1.7)$$

These materials, although largely studied for their hydrogen storage capabilities also display promising lithium ion conductivities. At room temperature lithium imide displays a lithium ion conductivity of 3×10^{-4} S cm^{-1}, and lithium nitride a conductivity of 6.6×10^{-4} S cm^{-1} (1.2×10^{-3} S cm^{-1} for single crystals).[70–72] Researchers have looked at the incorporation of halide anions into the Li–N–H system to form lithium amide halides and imide halides, as a way of increasing disorder and consequently improving these properties.[73–75] In doing so they have shown that improving ionic conductivity also results in improved hydrogen adsorption/desorption properties.[73] As well as being good lithium ion conductors in their own right, they are also important precursors for other potential lithium ion conductors, particularly for those structures studied in this thesis.

The structures of lithium imide and lithium amide are very closely related. Lithium amide has a tetragonal structure which is an ordered $a \times a \times 2a$ superstructure of disordered cubic antifluorite lithium imide (Figure 1.10). A layered structure is formed due to the conformation of the amide anions and the ordering of the lithium ions around those anions. Lithium cations sit on edges of the unit cell and the nitrogen atoms form tetrahedral clusters.[76] In the cubic antifluorite-like structure of lithium imide nitrogen atoms form a face-centred cubic lattice (Figure 1.10). Despite the overall cubic structure, the local structure can be tetragonal and small amounts of non-stoichiometry result in microstructural defects.[76]

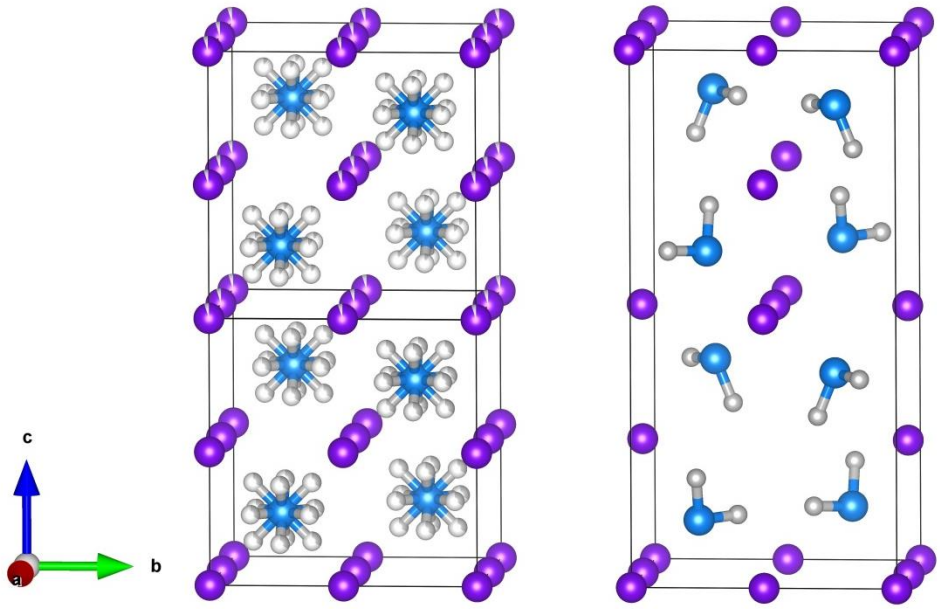

Figure 1.10 – (A) *a* × *a* × 2*a* super cell of Li_2NH with the origin shifted by (¼, ¼, ¼) and (B) $LiNH_2$ structures where Li = purple spheres, N = blue spheres and H = grey spheres (Adapted from Makepeace *et al.*[77])

Chen et *al*. proposed that the amide to imide reaction proceeds due to the charge difference between the hydrogen ions.[78] The hydrogen from the amide is positively charged,

i.e. protic not hydridic, and the hydrogen from the hydride is negatively charged. This charge difference causes a strong affinity between two hydrogen atoms.[78] This proposed mechanism would require very small crystallites in close proximity and does not proceed via an ammonia intermediate, differing from the commonly accepted mechanism.[76] The endothermic amide-imide reaction is widely accepted to proceed *via* two different stages:

$$2\mathrm{LiNH_2} \rightarrow \mathrm{Li_2NH} + \mathrm{NH_3} \quad (1.8)$$

$$\mathrm{LiH} + \mathrm{NH_3} \rightarrow \mathrm{LiNH_2} + \mathrm{H_2} \quad (1.9)$$

Initially $LiNH_2$ decomposes to Li_2NH and NH_3 (Equation 1.8).[79] The ammonia then reacts with the hydride, reforming amide and giving off hydrogen (Equation 1.9).[80] The initial amide decomposition controls the rate of reaction, which is found to be first order.[79] The second stage, in which the amide is reformed, is rapid. These two reaction stages repeat until all the amide and hydride have reacted.[79] In order to proceed at lower temperature, the proximity of the lithium hydride to the amide surface is important.[79] It enables any ammonia released to react quickly with the hydride, preventing ammonia release as a final product. In order to form the pure imide, as the intermediate between amide and nitride,[81] the reaction has to be stopped prior to nitride formation, which typically occurs at higher temperatures.

The decomposition of the amide to form imide proceeds in a non-stoichiometric manner:[76]

$$\mathrm{LiNH_2} \rightarrow (1-\varepsilon)\mathrm{Li_{1+x}NH_{2-x}} + \varepsilon\mathrm{NH_3} \quad [\,(1+\mathrm{x}) = 1/(1-\varepsilon)] \quad (1.10)$$

$$\mathrm{Li_{1+x}NH_{2-x}} \rightarrow (1-\varepsilon)\mathrm{Li_{(1+y)}NH_{(2-y)}} + \varepsilon\mathrm{NH_3} \quad [(1+\mathrm{y}) = (1+\mathrm{x})/(1-\varepsilon)] \quad (1.11)$$

The consequence of this is a range of amide-imides are formed with different stoichiometries as the reaction progresses until a pure imide phase is formed.[76] The intermediates in this solid solution range are, however, less stable than the pure imide and pure amide at either end.[77] Any ammonia that is given off reacts with the hydride forming amide and hydrogen gas, and leaving remnant LiH.

$$\mathrm{LiH} + \varepsilon\mathrm{NH_3} \rightarrow (1-\varepsilon)\mathrm{LiH} + \varepsilon\mathrm{LiNH_2} + \varepsilon\mathrm{H_2} \tag{1.12}$$

These products then go on to form lithium imide through Equations 1.10 and 1.11.[76]

It is believed to be the lithium and hydrogen ion mobility in cubic lithium imide that is driving the adsorption and desorption processes and causing non-stoichiometry.[76] The model used to describe the movement of ions in the Li−N−H system is the Frenkel defect pair model,[76] a model supported by in-situ synchrotron data.[77] Lithium ions move through the structure into vacant tetrahedral and octahedral sites creating two unstable charged species, which need their charge balance to be restored.

$$\mathrm{LiNH_2} + \mathrm{LiNH_2} \leftrightarrow [\mathrm{LiLiNH_2}]^+ + [\square\mathrm{NH_2}]^- \quad (\square = \text{ formerly occupied Li site}) \tag{1.13}$$

The charge balance can be restored in multiple ways: through the lithium rediffusing back into its original tetrahedral site (recombination of the Frenkel defect pair) or lithium hopping between sites without recombining the defect pair (Equation 1.14). Alternatively when the $[\mathrm{LiLiNH_2}]^+$ ion is formed, a proton can be expelled due to its attraction to the

nearby, unoccupied, tetrahedral site of $[\square NH_2]^-$ forming an NH_3 adduct alongside lithium imide (Equation 1.15).[76]

$$[LiLiNH_2]^+ \rightarrow LiNH_2 + Li^+ \quad (1.14)$$

$$[LiLiNH_2]^+ \rightarrow Li_2NH + H^+ \quad (1.15)$$

As well as the formation of lithium imide through the decomposition of lithium amide and through the reaction of $LiNH_2$ and LiH, lithium imide formation has also been reported to proceed via a Li_3N and $LiNH_2$ reaction (Equation 1.16). [82,83] This reaction can be performed at a much lower temperature than direct $LiNH_2$ decomposition, with temperatures reported as low as 210°C under vacuum.[82]

$$Li_3N + LiNH_2 \rightarrow 2Li_2NH \quad (1.16)$$

This reaction proceeds via two different pathways: formation of gas intermediates and direct ion exchange.[82] Hu *et al.* predicted the formation of gas intermediates is likely to be more dominant for a fast reaction as the interfaces between the particles limit direct ion exchange. Where the reaction proceeds via gas intermediates Equation 1.17 and Equation 1.18 show how the decomposition of $LiNH_2$ drives the formation of Li_2NH.[82]

$$2LiNH_2 \rightarrow Li_2NH + NH_3 \quad (1.17)$$

$$2Li_3N + NH_3 \rightarrow 3Li_2NH \quad (1.18)$$

Non-stoichiometry can also be incorporated for the nitride amide reaction, altering the ratio of Li_3N and $LiNH_2$ can result in a mixed amide-imide phase (Equation 1.19).[83]

$$(x)Li_3N + (2-x)LiNH_2 \rightarrow 2Li_{1+x}NH_{2-x} \quad (1.19)$$

Despite the stability of the intermediates, these reactions open up the possibility of forming mixed anion precursors which could then be used to form more complex lithium ion conductors.

1.5.2 Lithium Borohydride

Lithium borohydride is a commonly used reducing agent and has also been investigated as a potential hydrogen storage material.[84] However, more recently researchers have looked at its ability to act as a lithium ion conductor.[65] At room temperature, lithium borohydride demonstrates relatively low ionic conductivity, however, as the temperature is increased and the structure transitions into the high temperature form, a vast improvement in ionic conductivity is observed.[85]

The low temperature structure of lithium borohydride (LT) is orthorhombic with the space group *Pnma*. Within this structure the BH_4^- tetrahedra are quite distorted, sat on mirror planes, with both uneven bond lengths and angles.[86] The structure then transitions at around 108 °C to the high temperature structure.[87] This structure is hexagonal with space group $P6_3mc$, and is a layered system. In the HT structure the BH_4^- tetrahedra are aligned along c and are much more symmetrical, with a significantly reduced difference in both bond angles and lengths (Figure 1.11).[86]

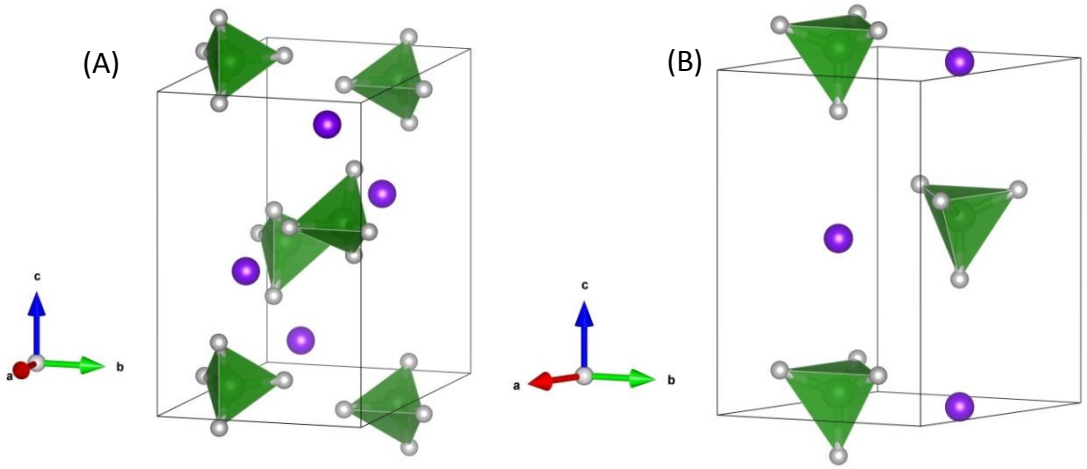

Figure 1.11 – $LiBH_4$ structures, where Li = purple spheres, B = green polyhedra and H = grey spheres (A) Low temperature orthorhombic $LiBH_4$ structure (B) High temperature hexagonal $LiBH_4$ structure

The lithium ion conductivity of the HT structure has been recorded to be of the order of 10^{-3} S cm^{-1}, just above the structural transition temperature.[65] It has been suggested that the disorder present in the high temperature phase is induced by the increased delocalisation and mobility of lithium ions in the low temperature phase as it approaches the transition temperature.[87–89] The structure transforms from one with very slow lithium ion movement to one of the fastest lithium ion conductors.[90] Coupled with this high conductivity, it is the high electrochemical reaction rates at the lithium borohydride–lithium metal electrode which makes it such a promising material.[67]

Unfortunately in order to be useful in lithium ion batteries, this high conductivity needs to be possible at room temperature. Research has shown that replacing some of the borohydride anions with halide anions, through combining $LiBH_4$ with Li*X* (where *X* is Cl, Br or I), can substantially decrease the temperature at which the transition to the HT phase occurs. The introduction of iodide ions has been found to be the best of the halides at

stabilising the HT phase, with some phases remaining in the HT structure even at room temperature.[67] As a result the observed room temperature conductivity increased up to 2 × 10^{-4} S cm^{-1},[26] a significant improvement on the original undoped LT phase. Nevertheless, despite the success of this research, further improvements still need to be made to continue to increase conductivity at room temperature. One way in which researchers have looked at doing this is by ball-milling the samples, in the hope of improving grain boundaries and introducing defects into the structure.[26,91,92]

1.5.3 Lithium Amide-Borohydride

Anion doping, as discussed in the previous section, can improve conductivity for a whole host of different structures, as it can enable more disorder to be accommodated. Due to this, there is a lot of research into both anion doping and the formation of mixed anion compounds.

The Li–BH_4–NH_2 phase space is an example of forming mixed anion compounds in order to try and improve upon the existing properties of both the lithium amide and lithium borohydride starting materials. Both $LiBH_4$ and $LiNH_2$ show promise in terms of their conductivity and, depending on the reaction ratios, different structures can be formed, with a wide variation in stoichiometry.

Reacting lithium amide and lithium borohydride at low temperatures or ball-milling the two in a 2:1 ratio results in the formation of a body–centred cubic phase, first reported as $Li_3BN_2H_8$.[93–95] Subsequent work demonstrated that the main phase actually exists at the 3:1 ratio; $Li_4BH_4(NH_2)_3$ is formed at temperatures below 180 °C.[96,97]

A number of studies have looked into the structure of lithium amide-borohydrides.[96,98] Initial investigations of the main phase, $Li_4BH_4(NH_2)_3$, narrowed it down to two possible space groups *I*23 and $I2_13$, a structure closely related to the lithium amide structure.[97] Further data analysis indicated that the system was composed of a body-centred cubic compound, with space group $I2_13$,[99] and a unit cell of approximately 10.66 Å (Figure 1.12).[96] Through refinement against both XRD and neutron data, the B–H bond lengths were found to be similar to lithium borohydride itself.[97]

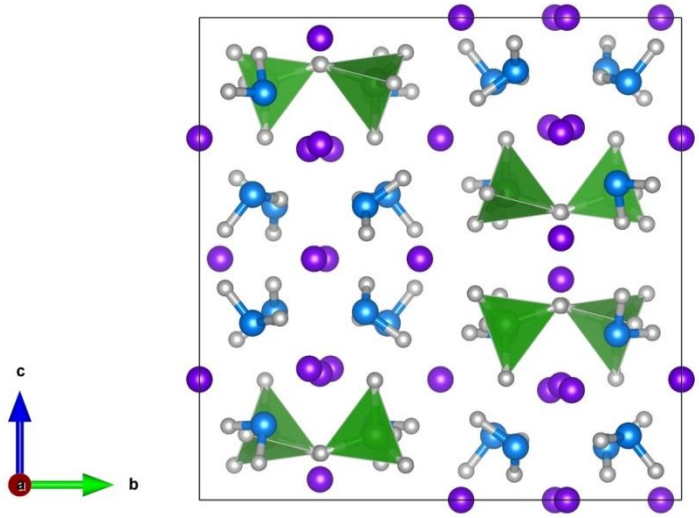

Figure 1.12 – Structure of $Li_4BH_4(NH_2)_3$, where Li = purple spheres, B = green polyhedra, N = blue spheres and H = grey spheres

Despite reports of both a $Li_3BN_2H_8$ and a $Li_4BH_4(NH_2)_3$ phase, further research found that only the $Li_4BH_4(NH_2)_3$ phase is stable.[97] $Li_3BH_4(NH_2)_2$ was determined to be a metastable non-stoichiometric composition of $Li_4BH_4(NH_2)_3$. This metastable phases is formed through substitution of amide anions within the $Li_4BH_4(NH_2)_3$ structure with larger borohydride

anions. This disordered substitution is equivalent to 2.6 amide anions out of the 24 in the unit cell being substituted.[100]

Another structure found within the Li–BH_4–NH_2 phase space is $Li_2BH_4NH_2$.[98] Although Meisner *et al.*[101] reportedly formed a body-centred cubic structure from ball-milling a 1:1 reaction mixture of $LiNH_2$ and $LiBH_4$, others reported a metastable phase formed under the same conditions[102] or alternatively by quenching a melt from 190 °C.[98] The structure of this material was found to be made up of a hexagonal arrangement of $Li(NH_2)_6$ clusters within a $LiBH_4$ matrix.[98]

Conductivity data of these structures has shown promise with both $Li_2BH_4NH_2$ and $Li_4BH_4(NH_2)_3$ displaying conductivities at room temperature of 2×10^{-4} S cm^{-1}. $Li_4BH_4(NH_2)_3$ reaches values of 1×10^{-3} S cm^{-1} at 370 K; and due to melting and therefore faster lithium motion $Li_2BH_4NH_2$, 6×10^{-2} S cm^{-1} at 378 K.[103] The successful synthesis of these materials and corresponding conductivity data suggests a potential for other mixed anion complex hydrides to display similar conductivity properties. Therefore this range of materials could provide useful solid state lithium ion conductors in the future.

1.6 Project Aims

Research has shown complex hydrides to have promising lithium ion conductivities; therefore opening up the possibility of finding new highly conductive solid state lithium ion conductors. The aim of this project was to synthesise new potential lithium ion conductors within the Li–NH_2–NH–BH_4 phase space.

Although there have been previous studies into the lithium amide-borohydride system, there are potential advantages of incorporating imide anions into these structures and forming new lithium borohydride-imides. One key potential advantage is that lithium imide is known to be a better lithium ion conductor than lithium amide. As mentioned previously, lithium imide has a conductivity of 3×10^{-4} S cm^{-1} at room temperature[72] compared with lithium amide which has a barely detectable lithium ion conductivity at room temperature.[104] Lithium imide also displays superior thermal stability and is less reactive than lithium amide. In synthesising new lithium borohydride-imide phases it would be hoped that these attractive properties seen for lithium imide alone would be replicated.

Initial research will focus of the synthesis of lithium imide, which although previously reported in the literature,[76] still provokes some debate over the optimum conditions to achieve an amide-free product. The project will then go onto to look at the reaction between lithium borohydride and lithium imide, with the aim to improve the purity of any new phases and subsequently characterise them.

Chapter 2 – Experimental

2.1 Solid State Synthesis

The high reactivity of the materials studied in this thesis to oxygen and moisture meant that all samples were handled under inert conditions. Consequently sample preparation was carried out in an argon filled glovebox with typical oxygen and water levels of <10 ppm and <1 ppm respectively.

Samples were weighed out on an analytical balance and ground together using a pestle and mortar. The ground samples were then transferred into sealed reaction vessels; quartz tubes were sealed with a Young's tap T-piece with an Ultra-Torr® fitting (Figure 2.1). The reaction vessels were then removed from the glovebox and clamped in place in vertical tube furnaces (Lenton Furnaces, LTF 12/25/250 fitted with a Eurotherm 3216P1 controller). Gas lines were then attached to either end of the tap allowing argon to flow through. After allowing argon to purge the gas line, the tap was then opened to allow the gas to flow over the sample. The furnace was then ramped up to the desired temperature, typically at a rate of 2 °C min^{-1}, and held for a period of time before being cooled back down to room temperature. The hold temperatures typically used during these experiments ranged from 200 to 600 °C for lithium imide synthesis (Chapter 3), and 100 to 250 °C for lithium borohydride-imide synthesis (Chapter 4). The sample was typically cooled at a rate of approximately 1–2 °C min^{-1}, similar to the heating ramp rate. Once cooled, the Young's tap was sealed and the sample was returned to the glovebox.

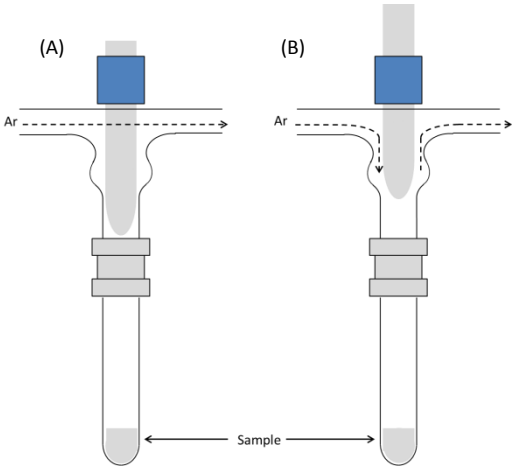

Figure 2.1 – Schematic of reaction vessel, quartz tubes sealed with a Young's tap T-piece with an Ultra-Torr® fitting, where dashed line shows flow of Ar gas (A) tap sealed to allow gas line to be purged (B) tap opened to allow gas to flow over sample

2.1.1 Ball-Milling

Prior to heating, some samples were mechanically ground together in a planetary micro mill. Ball milling is used for both particle size reduction, to enable better mixing of reagents, as well as mechanochemical reactions.[105] A planetary ball mill works by rotating a disk around a central axis, whilst simultaneously rotating attached milling jars to grind the samples (Figure 2.2). The sample particles are impacted with the high speed, high energy milling balls contained within the jars resulting in smaller particle sizes and potentially the formation of new products.

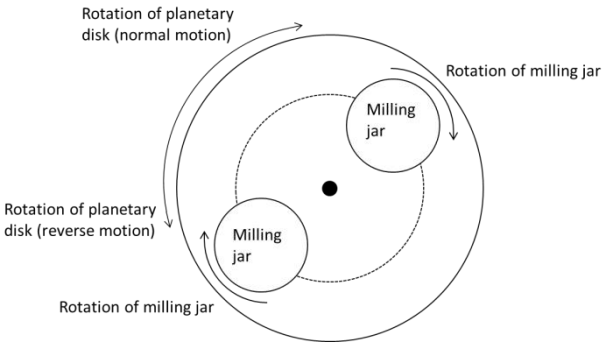

Figure 2.2 – Diagram of planetary ball mill motion (adapted from Burmeister *et al.*[105])

The motion of the balls within the milling jars varies depending on the speed of revolution, the number of milling balls and the ratio of milling balls to powder. Figure 2.3 shows the possible motion of the milling balls which can be: cascading, cataracting or rolling. A slower revolution speed and reduced number of milling balls tends to favour the cascading motion whereas using a high speed and increased number of milling balls results in more of the rolling motion occurring. In the cascading motion the balls move along the wall of the pot then roll along each other back down to the bottom of the cascade. The cataracting motion is similar although rather than rolling back down the other balls; they move at high speed across the milling pot and collide with the other balls on the far side. Finally in the rolling motion the balls simply move around the edge of the jar.[105]

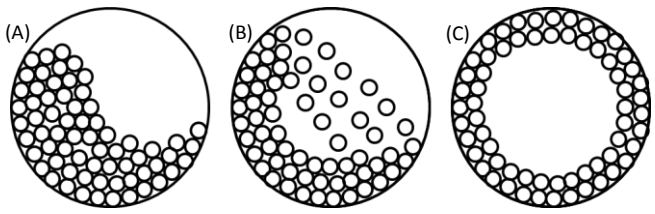

Figure 2.3 – Schematic of ball motion in planetary ball mill pot (A) cascading (B) cataracting (C) rolling (adapted from Burmeister *et al.*[105])

When planning a ball milling experiment there are multiple factors which need to be considered: the speed of revolutions, the total milling time, the duration and frequency of any rest periods, how much sample is contained within the jars and the size and number of milling balls used.[105]

In this thesis the machine used was a Fritsch Pulverisette 7 Premium Line and milling was carried out in 45 ml silicon nitride grinding jars with silicon nitride balls (10 mm, 18 in each jar). Samples were prepared and the milling jars were filled and sealed in an argon filled glovebox. A speed of 200 rpm was used with a cycle of 15 minutes on followed by a 1 minute rest period, totalling 24 hours of grinding time.

2.2 Crystallography

2.2.1 Crystal Structure

Crystallography is the study of atomic arrangements within crystalline materials.[106,107] In this section the fundamentals of crystallographic descriptions of solid state structures are introduced. Solid crystal structures are made up of a regular array of atoms which can be defined in 3 dimensions, known as a lattice. Simplifying the structure down into the smallest possible arrangement of atoms which still contains all the symmetry elements produces the unit cell. The unit cell can then be used as a building block, repeated over and over again to form the whole structure. The unit cell is described by 6 parameters: a, b and c are the lengths of the three edges; and α, β and γ are the angles between those edges (depicted in Figure 2.4).

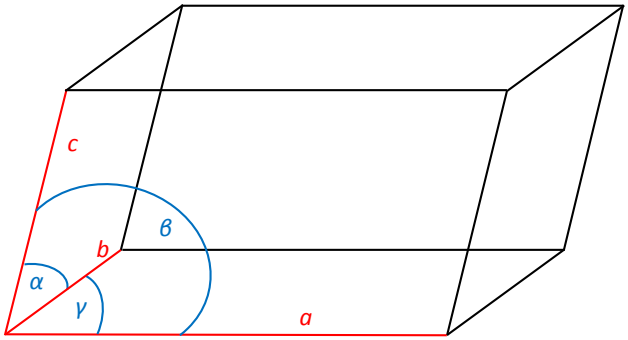

Figure 2.4 – Diagram of a unit cell

Different combinations of the 6 different lattice parameters give rise to 7 different crystal systems: cubic, tetragonal, orthorhombic, hexagonal, rhombohedral, monoclinic and triclinic. Each has specific symmetry essential in forming that unit cell.

The 7 different possible crystal systems can be combined with 4 lattice types: primitive (P), body-centred (I), face-centred (F) and base-centred (C). Primitive is the simplest lattice type; this has a lattice point on the corners of the unit cell. Addition of extra lattice points gives rise to the more complex lattice types. A body-centred lattice (I) is formed by addition of a lattice point to the centre of the unit cell and a face-centred (F) by adding a lattice point to the centre of each face. If a lattice point is only added to the centre of two opposite faces (middle of the *ab* plane) then it becomes a base-centred lattice (C). Not all of the 4 lattice types are compatible with the 7 crystal systems. The allowed combinations are known as Bravais lattices and there are 14 in total.

Table 2.1 – Possible crystal systems and associated Bravais lattices

Crystal System	Unit Cell Lengths	Unit Cell Angles	Essential Symmetry	Allowed Lattices
Triclinic	$a \neq b \neq c$	$\alpha \neq \beta \neq \gamma \neq 90°$	None	P
Monoclinic	$a \neq b \neq c$	$\alpha = \gamma = 90°, \beta \neq 90°$	One twofold axes	P, C
Rhombohedral	$a = b = c$	$\alpha = \beta = \gamma \neq 90°$	One threefold axes	R
Hexagonal	$a = b \neq c$	$\alpha = \beta = 90°$ $\gamma = 120°$	One sixfold axes	P
Orthorhombic	$a \neq b \neq c$	$\alpha = \beta = \gamma = 90°$	Three perpendicular twofold axes	P, I, F, C
Tetragonal	$a = b \neq c$	$\alpha = \beta = \gamma = 90°$	One fourfold axis	P, I
Cubic	$a = b = c$	$\alpha = \beta = \gamma = 90°$	Four Threefold axes in tetrahedral arrangement	P, I, F

To describe a complete crystal structure the lattice parameters, internal symmetry and atomic positions of the cell are all needed. The atomic positions are described through fractional coordinates and give more detail as to structure. The result of combining all of this information together gives 230 possible symmetry combinations, known as space groups.

2.2.2 Lattice Planes

Lattice points are built up to form the 3D lattices which describe solid crystal structures. These points can be connected together to form lattice planes within the overall lattice. Lattice planes are repeated and regularly spaced throughout the structure.

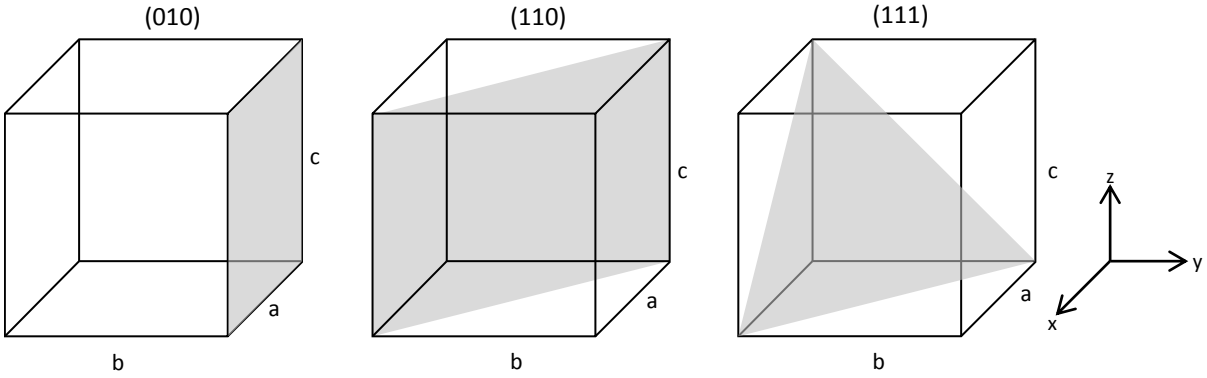

Figure 2.5 – Lattice planes and their associated Miller indices

Figure 2.5 shows examples of lattice planes and how they are described through Miller indices. Miller indices are written as *hkl* values, which are the reciprocals of the fractional intercepts. For example, if a lattice plane intercepted the x-axis a third of the way along, the y-axis halfway along and the z-axis at one, the Miller indices would be written as (321). If the plane is parallel to an axis its intercept is given as infinity and consequently its Miller index is 0. The spacing between the lattice planes remains constant throughout the structure and this distance is referred to as the *d*-spacing (d_{hkl}). This distance can be calculated as shown in Equation 2.1 for the most simple cubic system, where *h*, *k* and *l* are the Miller indices and *a* is the lattice parameter, becoming more complex for the other crystal systems.

$$d_{hkl} = \frac{a}{\sqrt{h^2 + k^2 + l^2}} \qquad (2.1)$$

2.3 X-ray Diffraction

Crystalline materials can be analysed using X-ray diffraction (XRD).[107] A monochromatic beam of X-ray radiation is fired at the sample and X-rays are collected after they interact with the electrons in the sample, producing a diffraction pattern. The

wavelengths of X-rays are similar to the distances between lattice planes in a crystal structure (*d*-spacings), making X-ray diffraction possible.

Bragg's law can be used to understand the interaction of X-rays with a crystal. It can be used to relate the diffracted X-rays detected from the lattice planes to their *d*-spacing via the X-ray wavelength. Figure 2.6 depicts the geometry used to derive Bragg's law, and shows a crystal as layers of atoms.

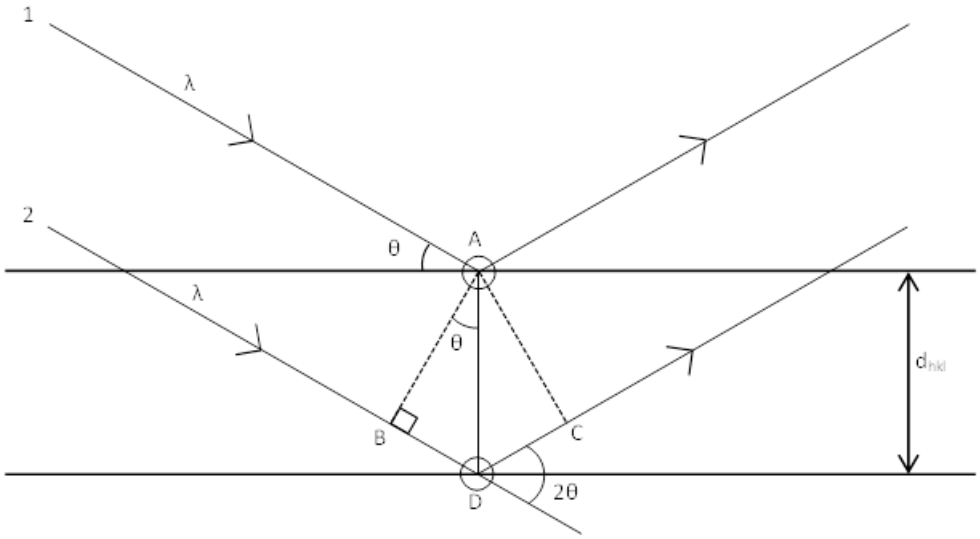

Figure 2.6 – Geometry used in the derivation of Bragg's law

X-rays are fired at the crystal and hit the lattice planes. The first X-ray is reflected at A, at the same angle as the incident beam angle. The second X-ray goes through the first lattice plane and reflects at D, again at the same angle at which it hit. Using the geometry depicted in Figure 2.6, simple trigonometry can then be applied to determine distances within the crystal (Equation 2.2), where λ is the wavelength, d_{hkl} is the *d*-spacing (distance between equivalent lattice planes in the crystal structure) and θ is the diffraction angle. Reflections only appear as a result of constructive interference, where the path-length difference

(distances BD + DC) between the two X-rays is equal to an integer multiple of the incident wavelength, therefore n must be an integer for a Bragg peak to be observed.

$$n\lambda = BD + DC = 2d_{hkl} \sin \theta_{hkl} \quad (2.2)$$

Although this derivation is a simplification of the real situation, where X-rays are scattered from electron clouds around atoms in many thousands of consecutive crystal planes, rather than the planes themselves, the resulting Bragg's law still holds.

2.3.1 Peak Positions

The positions of the peaks in a diffraction pattern are determined by the size, shape and symmetry of a unit cell. As a unit cell increases in size and therefore *d*-spacings increase, peaks shift to lower 2θ values. Peak positions are also determined by the wavelength of the radiation source; instrumental factors such as zero point error can also contribute.

2.3.2 Peak Shape

Peak shapes are affected by both instrument and sample factors. In regards to instrument contributions these can be things like the radiation source and instrument setup e.g. alignment. In terms of the sample factors the main one is crystallite size. Smaller crystallites result in broader peaks as Bragg's law assumes an infinite crystal size. Other sample factors include defects within the structure and local disorder.

2.3.3 Peak Intensity

A diffraction pattern is produced as a result of X-rays being scattered by electrons. Heavier elements which have more electrons are observed more intensely in XRD. However, there are multiple factors which contribute to the intensity of a peak: atomic positions,

thermal motion, phase fractions, lattice plane multiplicities and preferred orientation. There are different types of intensity to be considered: absolute intensity of the pattern as a whole; relative intensities of the different phases and variation of intensities within a phase. Absolute intensity is generally due to instrument factors and experimental factors, such as collection times and scattering power. Relative intensities of the different phases relate to the abundance of the different phases predominantly; changing peak shapes, as a result of crystal size, can also make peaks appear less intense as the intensity is spread out over a greater 2θ range.

Within a phase, peak intensities are down to the type, position and thermal motion of the different atoms within the unit cell. However, preferred orientation can cause disproportionate intensities due to preferential alignment of the different lattice planes with the incident radiation leading to data which is not representative of a randomly orientated powder (see §2.3.4). When considering peak intensities it is important to discuss structure factors.

$$|I_{hkl}| \propto |F_{hkl}|^2 \qquad (2.3)$$

where I_{hkl} is the peak intensity and F_{hkl} is the structure factor. The structure factor can be defined by the equation below, which is a sum over all atoms in the unit cell:

$$F_{hkl} = \sum_{j=1}^{n} f_j \cos\left[2\pi\left(hx_j + ky_j + lz_j\right)\right] + i\sum_{j=1}^{n} f_j \sin\left[2\pi\left(hx_j + ky_j + lz_j\right)\right] \qquad (2.4)$$

f_j = atomic scattering factor

x_j, y_j, z_j = the atomic coordinates for the jth atom

h, k, l = the Miller indices of a particular lattice plane

Structure factors can indicate where Bragg peaks will be observed and where there will be systematic absences as a result of destructive interference. Systematic absences are characteristic of the different crystal systems:

- Primitive – all *hkl* values allowed
- Body centred – $h + k + l$ = even number allowed
- Face centred – *hkl* either all odd or all even allowed
- Base centred – $k + l$ always even

Other systematic absence rules are also characteristic of specific space groups or groups of space groups.

2.3.4 Powder X-ray Diffraction

In a powder sample, all of the crystallites are randomly orientated and therefore each Bragg reflection is observed at azimuthal angles. This results in a cone of reflections, which corresponds to reflections from every possible orientation. 2θ is measured from the centre of the cone out to each ring of the cone and therefore in order to detect in the full 2θ range in a typical diffraction experiment, a slice of the cone is detected to produce a complete powder diffraction pattern.

2.3.4.1 X-ray Generation

X-rays are generated in a laboratory diffractometer by firing electrons at a metal target. The result of this is the formation of a hole as one of the electrons is ejected from a core orbital. X-rays are emitted as the hole is refilled *via* electron decay. Depending on which

metal is chosen as the target a different characteristic wavelength is emitted. Copper is a common choice for laboratory studies and is the target used in the diffractometers used in this thesis. In copper, electron decay occurs as a result of the 2p and 3p electrons dropping down to fill the hole in the 1s orbital, named K_α and K_β.

2.3.4.2 Monochromation

Along with the X-rays emitted at the desired wavelength there is a large amount of background radiation given off too. To isolate a single wavelength a monochromator is used. This is commonly a single crystal, aligned so that only the desired wavelength can satisfy the Bragg equation in the direction of the sample being measured. Consequently only the desired wavelength can be diffracted by the sample.

2.3.4.3 Detection

Scintillation counters are often used as the detector in XRD. They utilise a phosphorescent screen which when hit with X-rays emits photons. A photon multiplier then detects and amplifies the emitted photons, with the signal intensity proportional to the number of photons hitting the detector.

Proportional counters use a metal shell acting as a cathode which is filled with mainly inert gas and containing a thin metal wire acting as an anode. Application of an electric field between the anode and cathode means that as X-rays passing into the gas ionise it, the ion accelerates towards the wire generating further ionisation events as it goes. When this 'avalanche' of ionised particles hits the wire it creates a measurable pulse, which is then detected with read-out electronics.

More modern diffractometers use silicon strip detectors, where X-rays deposit charge within the silicon semiconductor which is then quantified and related to the number of incident X-rays via read-out electronics. Strip detectors can cover larger areas and discriminate between where X-rays are hitting the detector so that multiple 2θ angles can be measured at one time, increasing the speed of a diffraction measurement.

2.3.5 Laboratory X-ray Diffraction

The samples were prepared for analysis on a Siemens D5000 instrument by sealing them in Cole-Parmer polyimide tubing (0.0340 inch internal diameter). The capillaries were prepared by sealing one end with an epoxy resin. They were then filled with sample, which had been ground by hand, in an argon-filled glovebox and the other end was sealed with vacuum grease. The diffractometer was run in transmission mode and uses a germanium monochromator to produce Cu $K_{\alpha 1}$ radiation at a wavelength of 1.54056 Å. The sample capillaries were aligned and rotated perpendicular to the beam to improve powder averaging.

2.3.6 Synchrotron High Resolution X-ray Diffraction

In order to collect high resolution X-ray diffraction data, data were collected at the Diamond Light Source synchrotron facility. A synchrotron (Figure 2.7) is a type of particle accelerator which accelerates electrons and holds them in a circular orbit using a series of bending magnets. High intensity X-rays are subsequently generated over a broad range of wavelengths when the accelerated electrons change velocity. Specific wavelengths can then be selected depending on what is required for a particular type of experiment using a monochromator.[108]

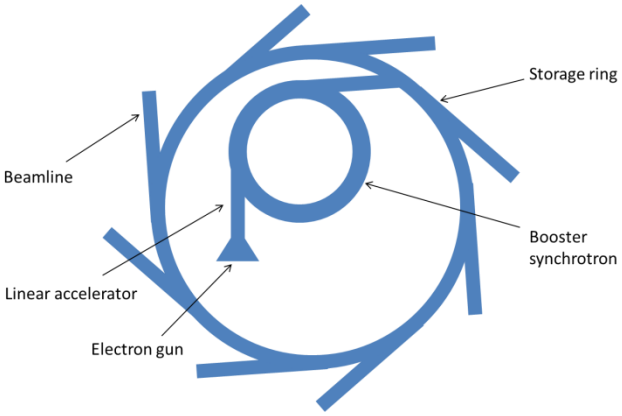

Figure 2.7 – Schematic of a synchrotron[109]

There are several advantages to using synchrotron XRD compared with laboratory methods. The resolution is significantly improved due to better spatial precision. The high intensity of the generated X-rays means that monochromators can be highly selective as there is still sufficient intensity in the monochromatic beam. The intensity of the beam also means that the signal to noise ratio is much improved, with more intense peaks. The tuneable wavelength means fluorescence can be minimised, resulting in a much better peak to background ratio. Finally peak broadening of lower angle peaks can be significantly reduced as the parallel beam means there is not the need for focussing geometry.[110]

Data were collected on the high resolution powder diffraction beam line, I11, using a wavelength of 0.826055 Å (September 2016), 0.826042 Å (May 2017), 0.82492 Å (April 2018), at Diamond Light Source. The samples were prepared in an argon-filled glove box by filling borosilicate capillaries, 0.5 mm in diameter, with pre-ground sample. They were then sealed using an epoxy resin. The sealed capillaries were rotated perpendicular to the X-ray beam during data collection and a hot air blower was used to vary the temperature.

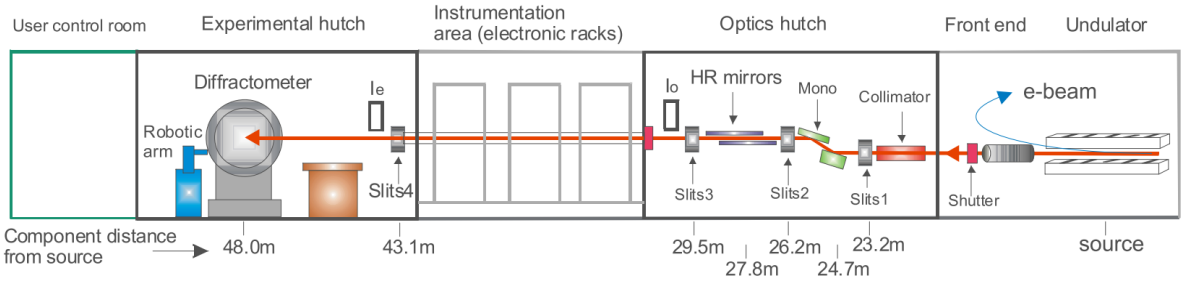

Figure 2.8 – Schematic of I11 beamline at Diamond light source (Thompson *et al.*[111])

Figure 2.8 shows the setup of the I11 beamline, made up of five different sections: the front end, where the synchrotron light is directed into the beamline from the storage ring; the optics hutch where the beam is filtered and focussed; the instrumentation area, housing the electronics racks; the experimental hutch where X-ray beam hits the sample and diffraction is detected; and finally the control room where the experiment is performed from.[109] Data collected on I11 can be collected through two different detector types: a MAC detector made up of five multi-analysing crystals for high resolution data; or a wide angle position sensitive detector (PSD) for time-resolved studies where fast data collection is important.[112]

2.4 Structure Refinement of Powder XRD Data[107,113,114]

The Rietveld refinement method models a proposed crystal structure against experimental data. The crystal structure used in the refinement contains information on atomic positions, occupancies, symmetry and cell parameters. Instrument parameters are also included such as the wavelength of the diffractometer and peak shape. Rietveld refinement uses a least squares method to minimise the difference between the calculated and experimental data. This is shown in Equation 2.5 where the function S_y is minimised.

$$S_y = \sum_i w_i \left(y_{i(obs)} - y_{i(calc)}\right)^2 \quad (2.5)$$

$y_{i(obs)}$ = the observed peak intensity at the i^{th} step,

$y_{i(calc)}$ = the calculated peak intensity at the i^{th} step, with the total sum over all data points. The estimated error is also taken into account through the inclusion of w_i, where typically $w_i = 1/y_i$.

When carrying out a refinement a difference profile is produced giving a good visual indication of how well the experimental data and calculated data agree. If the data sets completely agree, then this will produce a flat line. There are also numerical values which can be used to determine the quality of the fit.

R_{Bragg} compares the observed and calculated intensities at the Bragg positions for a given structure, with a given unit cell. Therefore for this value to be accurate the correct unit cell is important.

$$R_{Bragg} = \frac{\sum_{hkl} |I_{hkl}(obs) - I_{hkl}(calc)|}{\sum_{hkl} |I_{hkl}(obs)|} \quad (2.6)$$

I_{hkl}(obs) = the observed intensity for a given peak,

I_{hkl}(calc) = the calculated intensity for a given peak[115].

R_{wp} is the 'R-weighted profile factor' and gives a good indication of the quality of the fit between the model and the whole diffraction pattern.

$$R_{wp} = \sqrt{\frac{\sum_i w_i \left(y_{i(obs)} - y_{i(calc)}\right)^2}{\sum_i w_i y_i^2}} \quad (2.7)$$

w_i is the weighting given to the i^{th} data point, based on the estimated error in the intensity. Despite this being a good indication of the quality of the fit, absent peaks and a well fitted background can skew the value.

R_{exp} describes the best possible statistical fit:

$$R_{exp} = \left[\frac{(N - C - P)}{\sum_i w_i[y_i(obs)]^2}\right]^{\frac{1}{2}} \quad (2.8)$$

N = number of observed data points,

P = number of refined parameters,

C = number of constraints.

χ^2 combines both R_{wp} and R_{exp} to give a value determining the goodness of fit. For a perfect fit χ^2 equals 1, however, the quality of the data can influence it. For poor quality data a value close to one can be obtained as the structural fit errors can be hidden in a fit to a high, well defined background.

$$\chi^2 = \left[\frac{R_{wp}}{R_{exp}}\right]^2 \quad (2.9)$$

For a large amount of data in this research, atomic positions and occupancies were not refined. The refinements were used to obtain cell parameters and to carry out quantitative phase analysis (QPA) to estimate the weight fraction of the phases present. Calculating the relative weight fraction (W_p) of phase, p, is described in Equation 2.10:

$$W_p = \frac{S_p(ZMV)_p}{\sum_{i=1}^{n} S_i(ZMV)_i} \quad (2.10)$$

S = the scale factor,

Z = the number of formula units per unit cell,

M = the mass of the formula unit (in atomic mass units),

V = the unit cell volume (in Å^3),

n = the total number of phases within the mixture.

In some cases an internal standard, s, is added to the mixture. This can be used to give absolute weight fractions of the different phases. It is particularly useful if an amorphous phase is present in the phase mixture; without the internal standard the weight percentages of the known phases would be overestimated as the amorphous phase would be unaccounted for.

$$W_p = \frac{W_s S_p (ZMV)_p}{S_s (ZMV)_s} \tag{2.11}$$

The errors associated with the reported weight percentages in this thesis consider only the mathematical fit to the data. They were calculated using the software TOPAS and are based on the determined scale factor values. There are other effects which have not been taken into consideration with regards to the errors and thus will have resulted in a slight decrease in accuracy. Crystallite size, preferred orientation, thermal motion, microabsorption and extinction can all have an impact on the measured peak intensities, which in turn will result in variation in the scale factor and subsequently the calculated weight percentages.

Unlike the Rietveld method, the Pawley method,[116] a type of model-independent fit, does not require a whole crystal structural model. The structural data required for this

refinement includes the symmetry (space group) and cell parameters. Therefore, although this method can be used to obtain cell parameters, there is no information about atomic positions or occupancies contained within the output information. This method can consequently be used when the whole crystal structure is unknown. In this research, Pawley refinements have been used to obtain cell parameters and give a visual indication of the presence of unknown products of reactions.

Pawley[116] and Rietveld[114,116] refinements were carried out on the powder XRD data collected using TOPAS computer software.[117]

2.5 Pair Distribution Function Analysis[118,119]

Pair distribution function (PDF) data are used to look at the local structure in a material. This is a useful tool allowing local distortions in a material to be visible and interpreted, as well as showing the overall medium and long-range order of the structure.[119] PDF data combine information from both the Bragg peaks and the diffuse scattering from a sample. Diffuse scattering is not used in standard diffraction experiments; it is removed as part of the background as it lies beneath and between the Bragg peaks.[119] It is the data from diffuse scattering which provides a range of additional information, particularly on the local structure and disorder. PDF is real space data and can provide a whole host of information about a structure. Peak positions can be used to find atomic distances; peak area gives information on coordination number and the type of atom-atom pairings; peak width relates to disorder; and peak damping provides information on the size and shape of the particles (damping being the decay in amplitude with distance, *r*).

In order to produce a PDF, the coherent scattering data from a diffraction measurement is Fourier transformed. Unfortunately coherent data cannot be collected on its own; there are other things which need to be taken into account and corrected for. Combined with the coherent scattering are: container scattering, fluorescence, incoherent scattering, multiple scattering and air scattering. Multiple scattering is when photons are scattered twice or more within the same sample. Fluorescence is when they are absorbed and re-radiated at lower energy; this is highly dependent on composition and energy. Finally Compton scattering is inelastic incoherent scattering which reduces in energy as the angle increases; this is more dominant at higher angles. Hence, prior to analysing the data it needs to be processed, accounting for all of these factors.

Q is momentum transfer, also called the diffraction vector, and the *Q*-range measured is important in determining the data quality (Equation 2.12).

$$Q = \frac{4\pi \sin\theta}{\lambda} \tag{2.12}$$

where λ is the wavelength of the scattered particle, and 2θ is the angle between the incident and diffracted beams.

Ideally Q_{max} should be as high as possible to give the best resolution real space PDF data. The resolution, Δ*r*, of a PDF is approximately $2\pi/Q_{max}$, thus a higher Q_{max} means a better resolution. Obtaining a high Q_{max} means using higher energy radiation and a higher angular coverage detector, and consequently the maximum *Q*-range of coherent scattering data is collected. As $\sin\theta \leq 1$, the maximum *Q* range cannot be greater than $4\pi/\lambda$. Therefore

in order to obtain high quality PDF data to a high *Q*, a high intensity, short wavelength is required.[118]

Equation 2.13 shows how the reciprocal space data is converted into real space PDF data, $G(r)$.[120] Ideally this would be collected over an infinite range but in reality limitations result in collection over a finite *Q* range.

$$G(r) = \frac{1}{(2\pi)^3 \rho_0} \int_0^\infty 4\pi Q^2 F(Q) \frac{sinQr}{Qr} dQ \qquad (2.13)$$

Q = momentum transfer

r = radial distance

ρ_0 = average number density

In the equation, $F(Q)$ refers to the coherent scattering and therefore all other scattering events need to be subtracted prior to Fourier transforming the data. It is also important to normalise the data to the number of photons which hit the sample.

2.5.1 Processing PDF Data

As mentioned in the previous section there are a number of factors to be accounted for before PDF data can be analysed. In this thesis GudrunX[121] was used to background-subtract, correct, normalise and process the data in PDFs. The PDF data from GudrunX were then analysed with TOPAS.[117]

2.5.2 Collecting Synchrotron X-ray PDF Diffraction Data

Data were collected on the X-ray Pair Distribution Function (XPDF) beamline, I15-1, at Diamond Light Source, using a wavelength of 0.161669 Å. The samples were prepared in an

argon-filled glove box by filling borosilicate capillaries, 1.3 mm in diameter, with pre-ground sample. A small amount of glass wool was then placed above the sample to hold it in place before sealing the capillary by inserting a smaller capillary coated in an epoxy resin. The sealed capillaries were rotated perpendicular to the X-ray beam during data collection and a hot air blower was used to vary the temperature. Samples were typically heated up to temperatures between 200 and 300 °C, with data recorded every 25 °C over a 10 minute period.

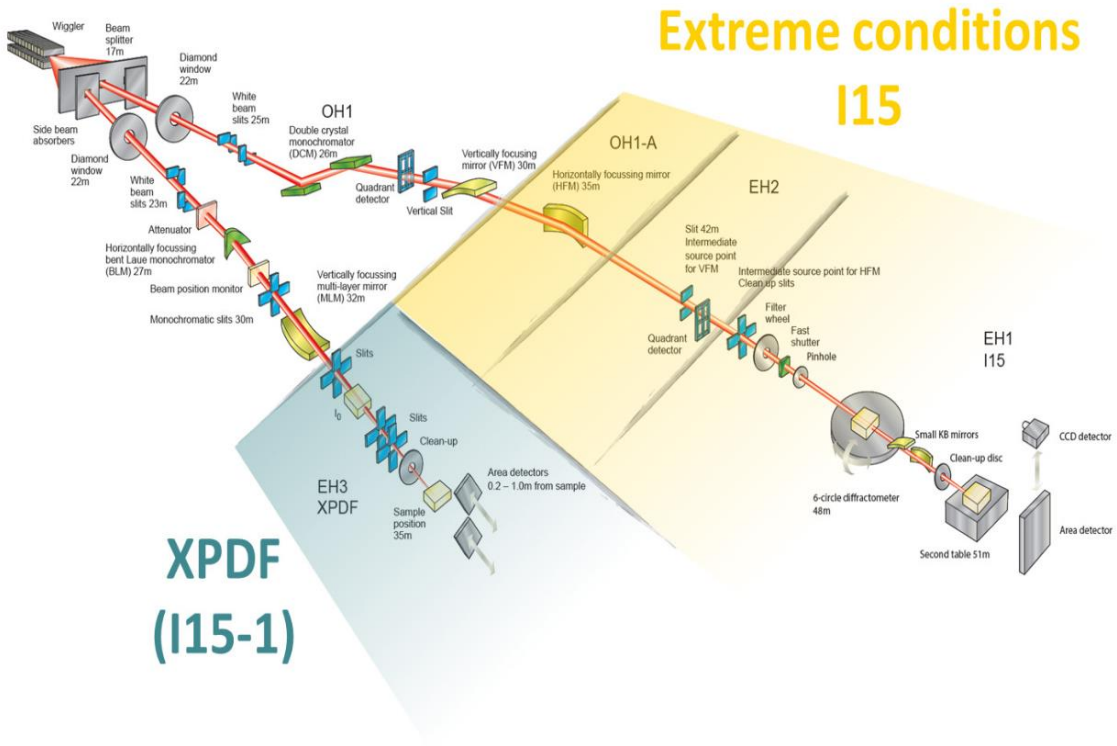

Figure 2.9 – Schematic of I15 and I15-1 beamlines at Diamond light source[122]

I15-1 is a beamline dedicated to collecting X-ray PDF diffraction data which shares the same X-ray source as the I15-1 extreme conditions beamline (Figure 2.9).[123] In order to generate high quality XPDF data the beamline needs to deliver high energy, high flux X-rays.

The XPDF beamline operates with two separate 2D detectors, one is used for collecting PDF data and the other simultaneously collects Bragg data.[123]

2.6 Raman Spectroscopy

Raman spectroscopy is a type of vibrational spectroscopy which measures the scattered light emitted as a molecule is hit with electromagnetic radiation.[124] A monochromatic laser is used to irradiate a sample resulting in excitation of the molecule, and consequently a change in its vibrational state to a higher energy virtual state. The photons emitted as the molecule returns to the vibrational states are then observed. There are 3 different types of scattering which can occur as a result of this: anti-Stokes Raman scattering, Rayleigh scattering and Stokes Raman scattering (Figure 2.10). By far the most common of these is Rayleigh scattering; the absorbed photon and the emitted scattered photon are at the same energy, in other words there is no change in energy. This is due to a return to the same vibrational state the excitation occurred from.

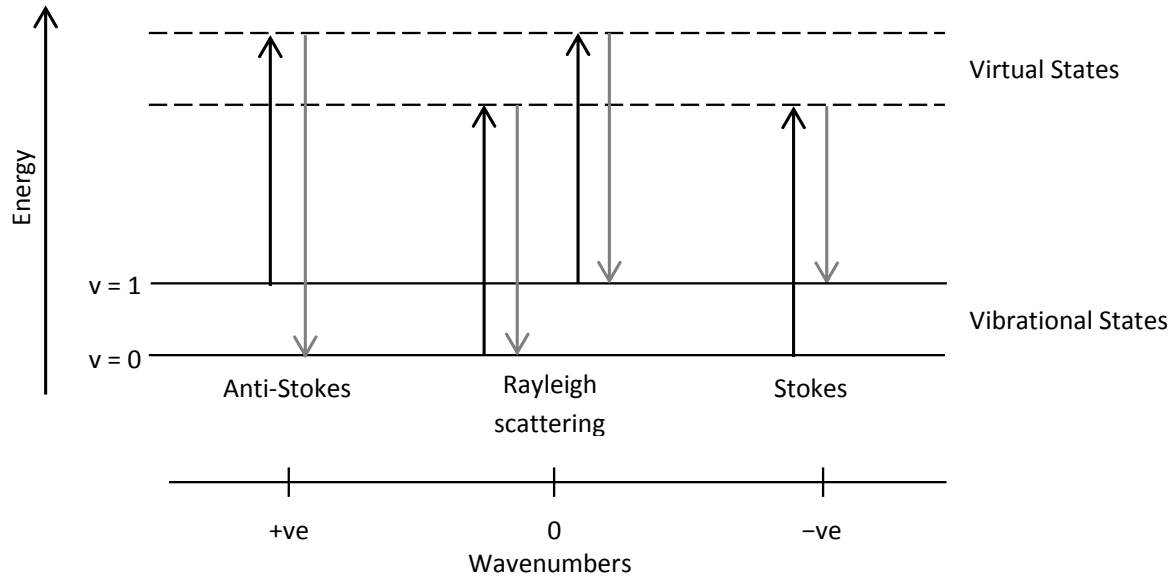

Figure 2.10 – Different scattering processes in Raman spectroscopy

Raman scattering is much less common, but this is the type of scattering important to this technique. Both anti-Stokes and Stokes scattering occur as a result of a change in the vibrational energy state of the molecule as it drops back down from a virtual state. The absorbed photon causes a transition to an excited virtual state and another photon is emitted when the molecule returns to a vibrational state. However, Raman scattering is a type of inelastic scattering; therefore when the molecule returns to a vibrational state it returns to a different vibrational state at a different energy to the initial state from which it was originally excited. The consequence of this difference in energy between the initial and final vibrational states is that there is also an energy difference between the incident photon and the photon emitted as a result of the molecule returning to a vibrational energy state. In the case of Stokes scattering, the molecule returns to a higher vibrational state than it was excited from whereas anti-Stokes scattering is the result of it returning to a lower vibrational state. As Raman scattering measurements are usually carried out at room temperature, Stokes scattering is much more common than anti-Stokes resulting in significantly higher intensity lines. This is due to the majority of molecules being found in the ground state (v = 0) at ambient temperature. As the temperature increases more molecules will be in an excited vibrational state and therefore the ratio of Stokes to anti-Stokes will decrease. An important point about Raman spectroscopy is that only vibrations which result in a change in the polarizability of the molecule are Raman active.

Samples were prepared for analysis on a Renishaw InVia Raman microscope in an argon-filled glovebox. Samples were sealed in an Instec sample cell before being loaded into the Raman microscope. An Ar laser with a wavelength of 488 nm was used to analyse the samples, typically focusing on the region between 3000 and 3500 cm^{-1}. This region was the

main focus in this work as N–H vibrations are observed in this region. The N–H vibrations differ depending on the parent molecule i.e. N–H stretching vibrations in a lithium imide structure are at a lower wavenumber to those in a lithium amide structure. Raman data were therefore important in this work to enable the presence of Li_2NH, $LiNH_2$ and mixed NH^{2-} NH_2^- anion structures to be determined, giving an indication as to the level of purity of a single structure.

2.7 A.C. Impedance Spectroscopy

A.C. impedance spectroscopy is performed by applying an alternating voltage across a sample while measuring the corresponding current, and is a way of measuring the conductivity of a sample. The current is generated as the charge carrying species move through the sample.[125,126] The voltage applied is sinusoidal and can be expressed as in Equation 2.14, and consequently the current output is also sinusoidal. This process is repeated as a function of frequency.

$$e = E \sin \omega t \tag{2.14}$$

where *e* = the observed voltage at time, *t,*

E = input voltage,

ω = frequency (in Hz) × 2π, also known as angular frequency.

Unless the sample is a perfect resistor there will be a phase shift between the input voltage and output current. It is capacitance and inductive effects which cause this shift. This phase shift can be defined by the equation below:

$$i = I \sin(\omega t + \varphi) \tag{2.15}$$

where *i* = current,

I = the maximum amplitude of the current,

φ = the phase angle between the input and the output.

If a sample does act as a perfect resistor, and has no phase separation, then it obeys Ohm's law (*V* = *IR*) and the equation below can be used to determine the current, where *R* is resistance.

$$i = \frac{E}{R}\sin \omega t \tag{2.16}$$

If on the other hand the sample is a pure capacitor it displays the relationship given in Equation 2.17, where X_c is the capacitive reactance and equals $1/\omega C$.

$$i = \frac{E}{X_c}\sin(\omega t + \frac{\pi}{2}) \tag{2.17}$$

In this case the voltage and current vectors are perpendicular to one another. This means that if current were to be plotted along the x-axis then voltage could be plotted on the y axis, giving rise to the equation below, where $j = \sqrt{-1}$:

$$E = -jX_c I \tag{2.18}$$

The capacitance and resistance voltages measured in series will add together to give the overall voltage. This relationship along with Equation 2.18 allows an impedance vector, *Z*, to be defined, given in Equation 2.19.

$$E = I(R - jX_c) = IZ \tag{2.19}$$

Impedance is formed of two parts, a real (resistance, *R*) and imaginary (capacitance, X_c) part:

$$Z = Z_{Re} - jZ_{Im} \tag{2.20}$$

which relates to the phase angle through Equation 2.21.

$$\tan\varphi = \frac{Z_{Im}}{Z_{Re}} = \frac{X_c}{R} \tag{2.21}$$

The imaginary (*Z″*) and real (*Z′*) data can be plotted against each other to give a Nyquist plot, commonly used for displaying impedance data (Figure 2.11). Different magnitudes of capacitance are measured depending on the physical phenomenon being observed. For example bulk capacitance values are in the region of 10^{-12} F whereas capacitance relating to grain boundaries will be somewhere in the region of 10^{-11} to 10^{-8} F. Ideally these would be observed as two different semi circles on the Nyquist plot, but this can vary depending on the samples being studied. The larger semi-circle in Figure 2.11 is representative of when bulk and grain-boundary contributions cannot be resolved.

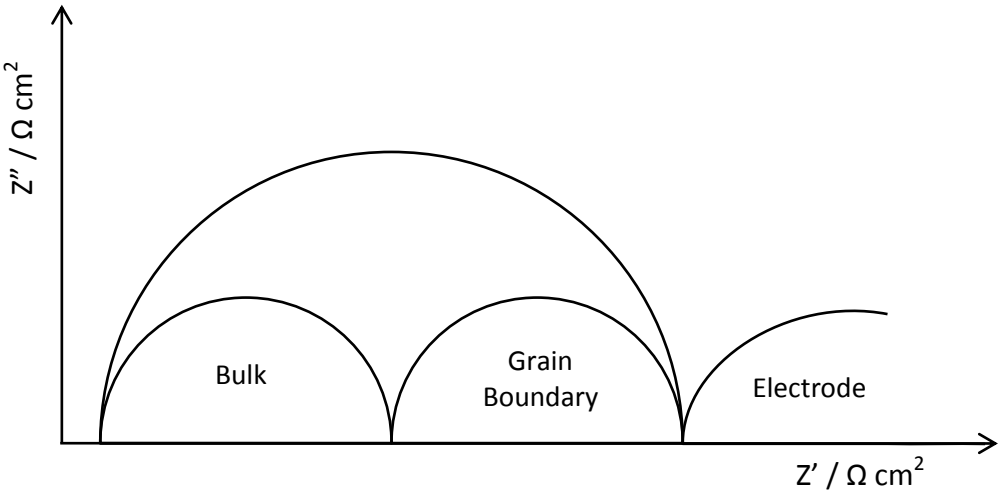

Figure 2.11 – Schematic of a Nyquist plot

The conductivity of the sample (σ) can consequently be determined from the resistance by the following equation:

$$\sigma = \frac{l}{RA} \tag{2.22}$$

where R = resistance,

A = sample surface area (in cm^2),

l = the sample thickness (in cm).

If data are collected over a range of temperatures it is also possible to calculate the activation energy of ion migration through Equation 2.23, as the temperature dependence of the conductivity can be plotted. The Arrhenius relationship allows the activation energy to be calculated from the slope of the graph.

$$\sigma T = Ae^{\frac{-E_a}{RT}} \tag{2.23}$$

In this thesis, impedance data were collected through the following method. Samples were ground and pressed into pellets using a Specac mini-pellet press using an axial force of between 0.5 and 1 tonne. All sample preparation was carried out in an inert argon atmosphere glove box. For the majority of the pellets prepared in this thesis sintering was not performed due to the thermal stability of the samples, with the exception of the Li_2NH samples which were sintered in a quartz tube under an argon gas flow at 400 °C for 12 hours (setup shown in §2.1).

Once the pellets were sintered they were assembled into coin cells. The pellets were sandwiched between two pieces of lithium metal in a CR2032 cell cap. A stainless steel spacer and spring were then placed on top, and finally a CR2032 cell cap with an attached O-ring. In order to hold everything together and ensure the whole system was air-tight a Hohsen Corp coin cell crimper was used to press and seal the cell. A schematic of the

assembly is shown in Figure 2.12.

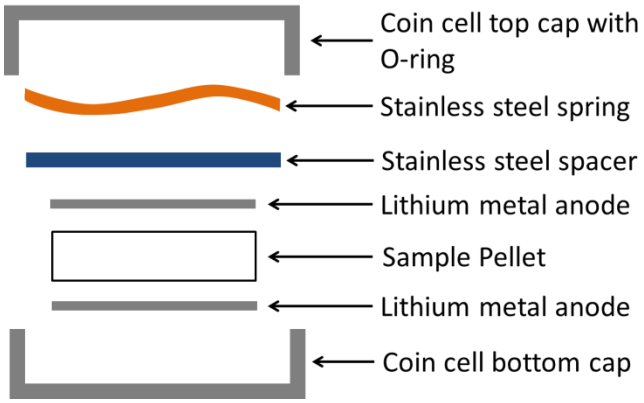

Figure 2.12 – Coin cell assembly

In order to measure impedance, silver wires were attached to either side of the coin cell using silver-electrodag paint (Agar Scientific) and after allowing the paint to dry were suspended in a furnace (Carbolite furnace, MTF 10/38/130 fitted with a Eurotherm 2416 controller) and connected to the analyser. Data were collected on a Solartron 1200 phase-sensitive multimeter with impedance analysis interface, between 1 Hz and 1 MHz.

Once data were collected, analysis was carried out using ZView software.[127] *Z*" was plotted against *Z*' (as in Figure 2.11) and the data were multiplied by A/l (component value) in order to convert resistance to $1/\sigma$, and to enable a direct comparison to be drawn between samples. A semi-circle was then fitted to the data by selecting the data points at either end of the data set and using the in-built "fit circle" tool. The high intercept of the fitted semi-circle on the *x*-axis was then taken to be the bulk $1/\sigma$ value for that sample. The extracted $1/\sigma$ values were then converted to log σ and plotted against 1000/T to determine the activation energy for each of the measured materials.

Chapter 3 – Li–N–H System

3.1 Introduction

There is more than one reported synthesis route to form lithium imide (Li_2NH). One is the direct decomposition of lithium amide ($LiNH_2$) (Equation 3.1); another is through the reaction of lithium amide and lithium hydride (LiH) (Equation 3.2) and finally there is the reaction of lithium nitride and lithium amide (Equation 3.3).

$$2LiNH_2 \rightarrow Li_2NH + H_2 \quad (3.1)$$

$$LiNH_2 + LiH \rightarrow Li_2NH + H_2 \quad (3.2)$$

$$Li_3N + LiNH_2 \rightarrow 2Li_2NH \quad (3.3)$$

Previous work within the group has compared the results of two of these methods: the decomposition of lithium amide and the reaction of lithium amide with lithium hydride.[128] Based on this, the one which produced the best results was the reaction of lithium amide and lithium hydride. Decomposition of lithium amide alone resulted in a much greater oxide content, and in all reactions there was more amide remaining than in the comparative lithium amide + lithium hydride reaction.[128] Within the literature studies have shown an extensive solid solution range exists between lithium imide and lithium amide, and so materials which look structurally like imide may also contain large amounts of amide anions.[76] Consequently there will be more disorder in the system as the structure has to accommodate both amide and imide anions within it. Subsequent reactions carried out required pure imide as a reactant, and therefore the reaction was investigated in detail in

order to optimise the reaction conditions, as well as study the possibility of forming a mixed anion phase.

Researchers have shown that there are different polymorphs of lithium imide. Initially the structure was reported to have a disordered cubic lattice comprised of NH^{2-} in disordered orientations with lithium ions in the tetrahedral holes.[129] This structure was later reported in two different space groups, Ohoyama *et al*. reported the space group as *F*-43*m*,[130] whilst Noritake *et al*. and Balogh *et al*. suggested that Li_2NH adopts a disordered *Fm*-3*m* structure.[131,132] In the *F*-43*m* the hydrogen is considered to randomly occupy a quarter of the 16*e* sites, which form tetrahedra around the nitrogen atoms. Alternatively in the *Fm*-3*m* structure the hydrogen occupy 1/12 of the available 48*h* sites. The *Fm*-3*m* structure is closely related to the $LiNH_2$ structure, which adopts an *a* x *a* x 2*a* ordered supercell of the anti-fluorite Li_2NH structure.

These reported disordered cubic Li_2NH structures have been determined to belong to the high temperature polymorph of lithium imide. In 1971 DTA was used to investigate Li_2NH and it was found that that there is an order-disorder transition which occurs at 83 °C.[133] Although at the time the structures were unknown this is now known to correspond to a transition from a cubic *Fd*-3*m* structure to the earlier reported *Fm*-3*m* structure.[132] The *Fd*-3*m* structure has lattice parameters twice that of the *Fm*-3*m* structure due to a greater level of ordering.

3.2 Experimental

$LiNH_2$ (Sigma Aldrich, 95%) and LiH (Sigma Aldrich, 95%) or $LiNH_2$ (Sigma Aldrich, 95%) and Li_3N (Sigma Aldrich, 99.5%) were ground together and sealed in a quartz tube, with a Young's tap, in an argon-filled glovebox. The samples were then heated in tube furnaces at temperatures between 200 and 600 °C for up to 16 hours. Powder X-ray diffraction (XRD) was carried out on the samples using a Siemens D5000 instrument. Raman data were also collected for the samples from various reaction conditions, using a Renishaw InVia Raman microscope.

3.3 $LiNH_2$ + LiH Synthesis

3.3.1 X-ray Diffraction Characterisation

Initially lithium amide and lithium hydride were heated together in a 1:1 reaction ratio for 12 hours at various temperatures. Laboratory powder XRD data were collected to determine how far the reaction proceeded, as well as to give an initial indication as to which temperatures produced purer lithium imide (Figure 3.1).

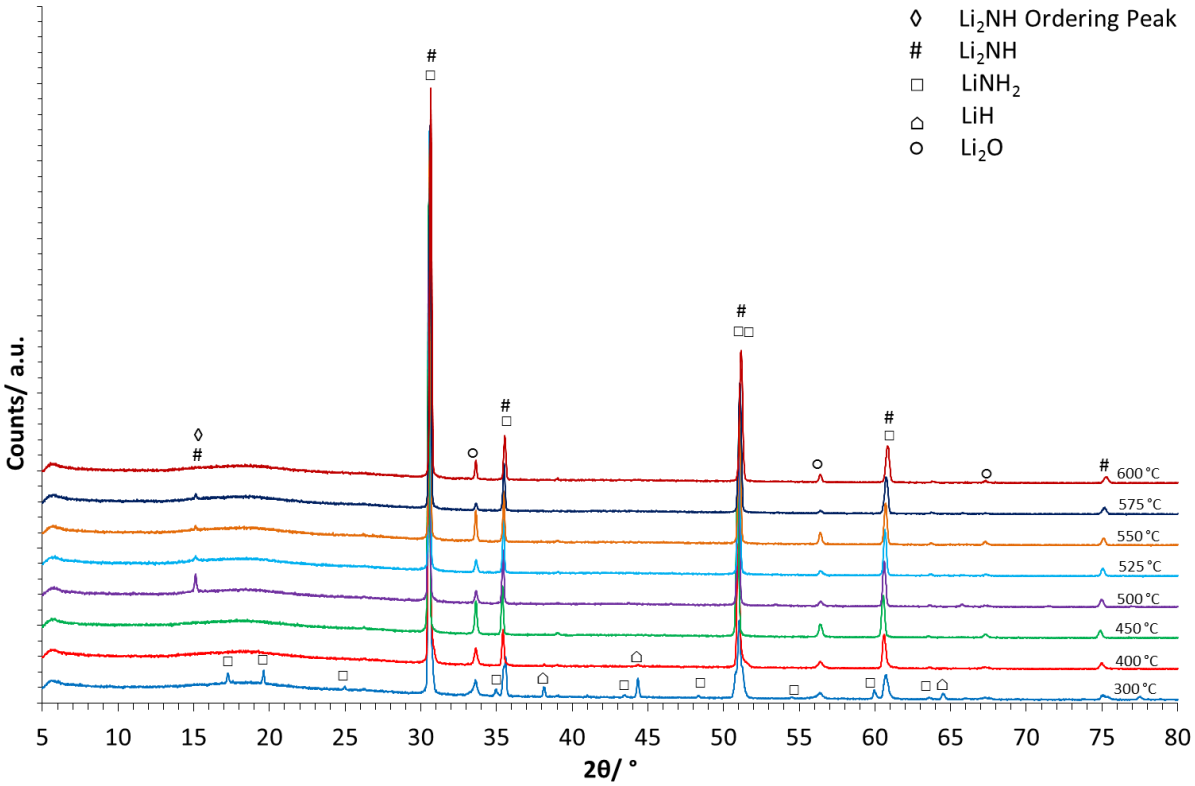

Figure 3.1 – Powder XRD data from the products of the reaction of $LiNH_2$ + LiH at various temperatures for 12 hours. The low angle peaks marked with a square at 17.2 ° and 19.6 ° are characteristic lithium amide peaks corresponding to the (002) and (101)

It is clear from the powder XRD patterns that at 300 °C there was still a significant amount of lithium amide present in the product; therefore this temperature was clearly too low for lithium imide synthesis. There were two low angle peaks at 17.2 ° and 19.6 °, characteristic of the lithium amide structure, corresponding to the (002) and (101) reflections,[134] which quickly disappeared as the temperature increased. The disappearance of these peaks is explained through the formation of the higher symmetry lithium imide structure. Lithium amide has space group *I*-4 which is a tetragonal space group, cell parameters a = 5.04309 Å, c = 10.2262 Å.[76] Lithium imide on the other hand has a cubic unit cell. The space group is often reported as *Fm*-3*m*, with lattice parameter, a, of 5.0742 Å;[131]

this corresponds to the high temperature disordered phase. At low temperature lithium imide has also been reported with the space group *Fd*-3*m* and a lattice parameter of 10.13 Å.[132,135,136] The transition from amide to imide is often determined by the presence or absence of the two low angle peaks at 17.2 ° and 19.6 °.

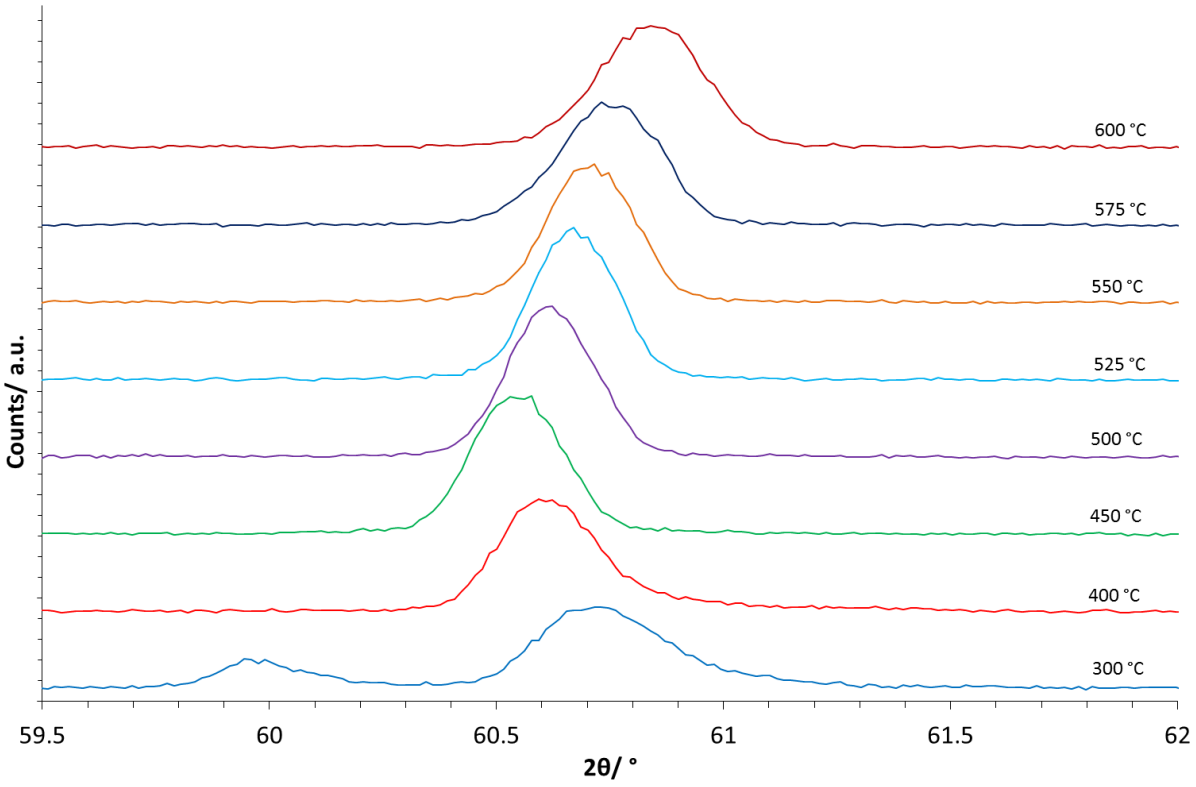

Figure 3.2 – High angle powder XRD data from the products of the reaction of $LiNH_2$ + LiH at various temperatures for 12 hours

In spite of the loss of low angle peaks, indicating imide formation, there was a clear shift in 2θ values as the reaction temperature was changed. This indicates that the composition continued to change as a result of heating at higher temperatures, even after the loss of the low angle peaks. The shift in values was more apparent at higher 2θ values (Figure 3.2), suggesting that the difference was due to a change in the size of the unit cell. A shift to higher 2θ was seen due to a decrease in the size of the unit cell. Comparison of

experimental data against known crystal structure data using pattern matching software, DIFFRAC.EVA, suggested the initial loss of the low angle peaks was due to formation of lithium amide-imide structures. Structurally these materials resemble cubic lithium imide, however, the amount of amide anions still present in the final structure varies.

A low angle peak appeared in some of the higher temperature reactions, marked with a diamond in Figure 3.1. This peak appeared as a result of the increased ordering in the *Fd*-3*m* higher symmetry space group. *Fd*-3*m* corresponds to a doubling of the unit cell, so instead of having 4 formula units per unit cell, this value is increased up to 32. This increase in the size of the unit cell occurs due to a greater lithium ordering. Makepeace *at al*. have discussed the appearance of this peak and suggested it is only present for pure stoichiometric lithium imide at room temperature; the stoichiometry has to be greater than 1.9Li.[83] Any amide anions present within the structure will reduce the symmetry and cause the structure to adopt the *Fm*-3*m* space group, this is due to the need for more structural disorder to accommodate the amide anions.

As the temperature is increased from 500 °C up to 600 °C the intensity of the supercell peak starts to decrease; this may be due to disorder being reintroduced into the structure. One possible explanation for this is that at these temperatures lithium could being leaching out into the quartz tube; alternatively the higher temperatures may start to favour the formation of nitride/ nitride-hydride and therefore these could become incorporated into the structure resulting in increased disorder.

3.3.1.1 Lattice Parameter Comparison

Structure fitting using laboratory Powder XRD data was performed through Rietveld refinement using the TOPAS software[117,137] to investigate changes in lattice parameters and presence of different structures. Refinements using the various imide data sets were carried out using both the *Fm*-3*m* and *Fd*-3*m* space groups. Where the ordering peak at *ca* 15 ° was present the *Fd*-3*m* space group was fitted to the data and where it was absent the *Fm*-3*m* space group was used. Rietveld refinement allows the lattice parameter, *a*, to vary, altering the structural model to fit it to the experimental data. In order to directly compare the lattice parameters from both space groups, the values for *Fd*-3*m* are reported as *a*/2.

The XRD data from lower temperature synthesis at 300 °C indicate both the reported tetragonal lithium amide and cubic lithium imide structures are present, demonstrating that at this temperature the lithium amide had not reacted completely. Figure 3.3 shows the fit of both phases to the experimental data; the cubic lithium imide phase fits to the main peak intensity and another phase, the amide phase fits to the shoulders. The peak at 2θ *ca* 52 ° shows some peak overlap, with two slight shoulders either side of the peak, Figure 3.4 shows this peak in more detail.

At various higher temperatures the data were consistent with the presence of just cubic lithium imide. Any asymmetry in these peaks would have suggested a range of stoichiometry being present. However, although not all displayed the ordering peak and consequently were not pure lithium imide, the peaks appeared to be symmetrical and thus indicated only one stoichiometry was present at a given temperature (Appendix 9.1).

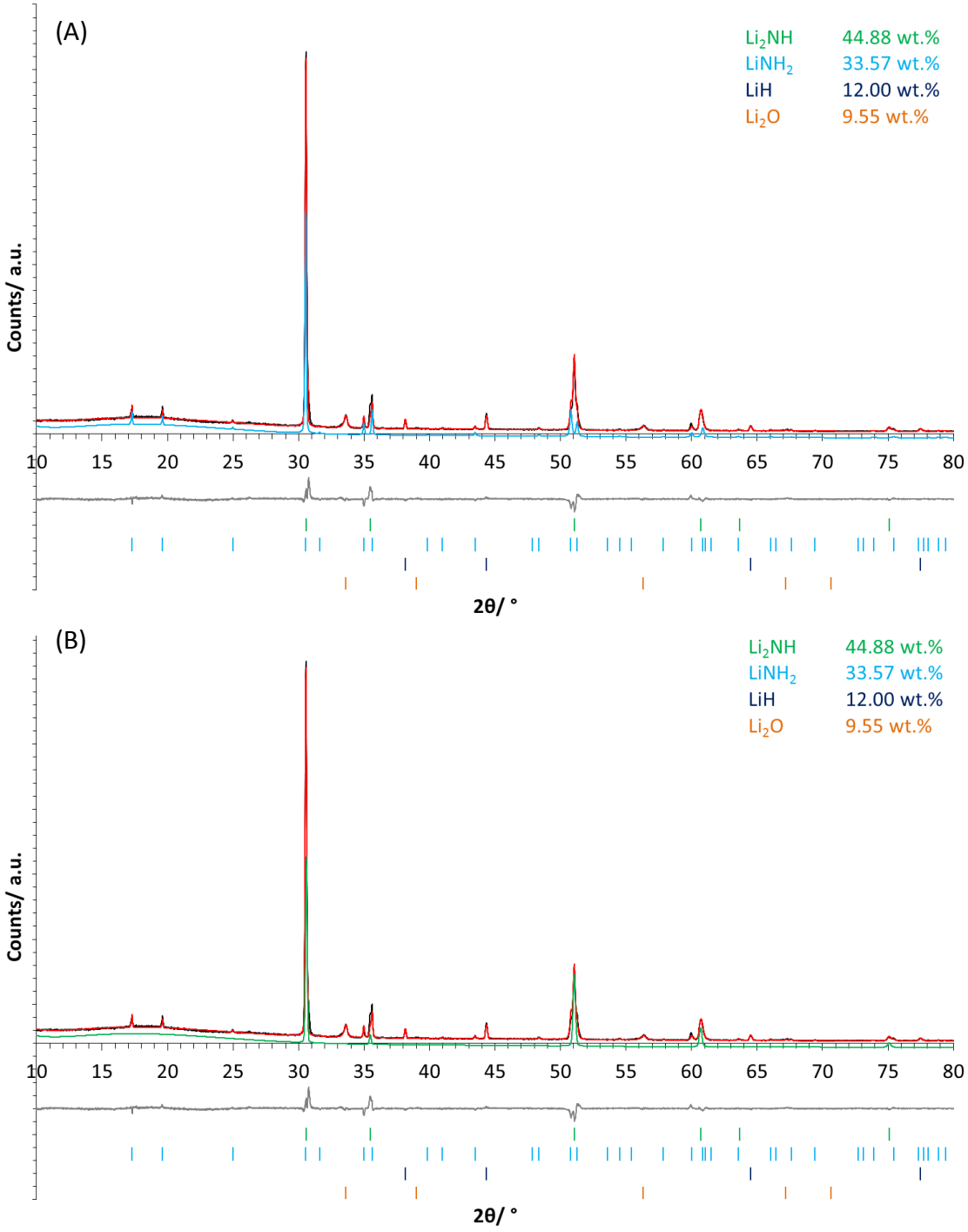

Figure 3.3 – Refinement plot showing the products of heating $LiNH_2$ + LiH at 300 °C for 12 hours. Green tick marks = Li_2NH, light blue tick marks = $LiNH_2$, dark blue tick marks = LiH, orange tick marks = Li_2O. (A) Shows the tetragonal $LiNH_2$ phase fit plotted in light blue (B) shows the cubic Li_2NH phase fit plotted in green

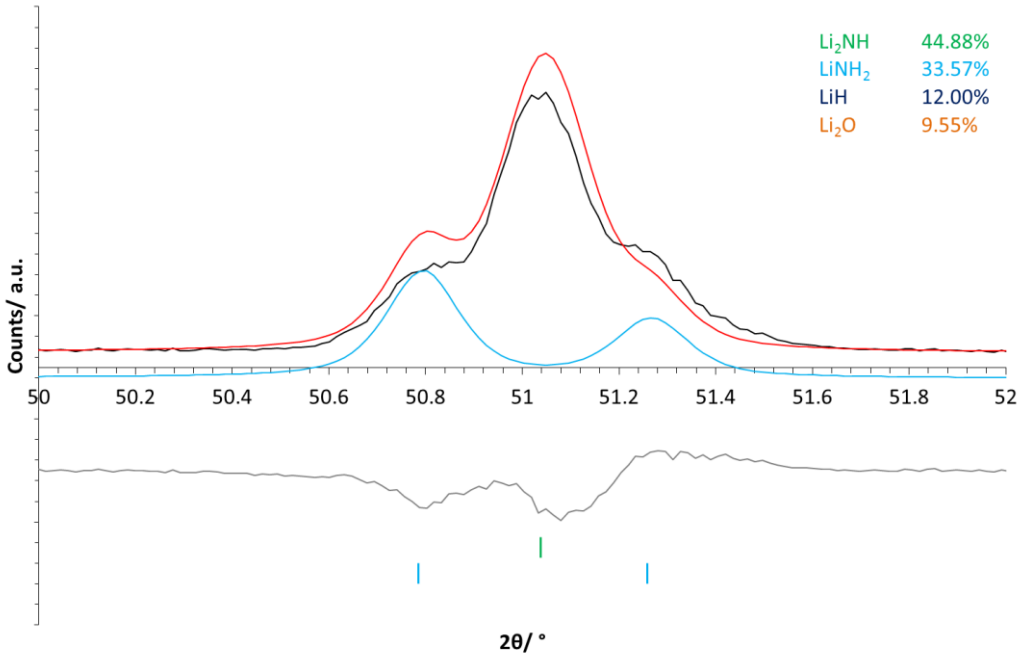

Figure 3.4 – Zoomed in refinement plot showing the products of heating $LiNH_2$ + LiH at 300 °C for 12 hours. Green tick marks = Li_2NH, light blue tick marks = $LiNH_2$. The cubic Li_2NH phase fit is plotted in green and the tetragonal $LiNH_2$ phase fit is plotted in light blue

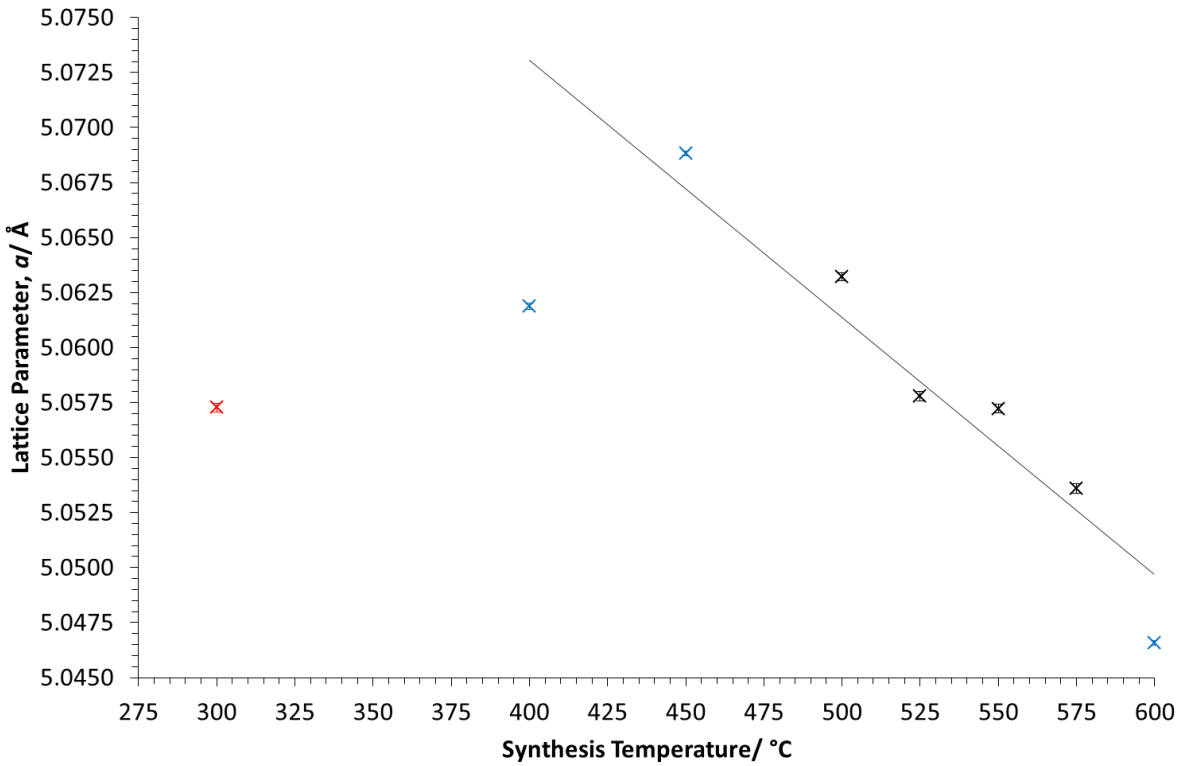

Figure 3.5 – Lattice parameters determined from Rietveld refinement of cubic imide synthesised at various temperatures, the point in red at 300 °C still contains $LiNH_2$, the points in black are fitted to *Fd*-3*m* and *a*/2 is reported and the points in blue have been fitted to *Fm*-3*m* and *a* is reported. Error bars are included but are smaller than the data point symbols

The trend in cell parameters obtained from the refinement data, shown in Figure 3.5, agrees with a decrease in the size of the unit cell with increasing temperature observed in Figure 3.2 by a shift in 2θ. The 300 °C sample clearly still contains lithium amide, therefore was not deemed suitable for onward synthesis. The lithium imide cell parameter calculated for this sample, is significantly lower than at 400 °C with a value of 5.05736(26) Å (shown in red in Figure 3.5), more in line with notably higher synthesis temperatures around 525 °C. One possible explanation for this is the refinement itself. Fitting both the lithium amide and lithium imide phases could have affected the cell parameters for the lithium imide phase.

The XRD patterns of both structures are very similar and there is a large degree of peak overlap, with the phases being indistinguishable at some 2θ values. Consequently the inclusion of lithium amide may have resulted in a greater error in the imide cell parameter values. Although it is important to consider that the low angle amide peaks will fix the higher angle amide peaks in position, preventing the amide lattice parameter from fluctuating as a result of the overlapping peaks. An alternative explanation is when two phases form at lower temperature a stoichiometric lithium imide phase is formed alongside an amide rich phase. Heating at different temperatures may then result in formation of a mixed phase, until at a higher temperature the stoichiometric imide forms.

Reports of lithium imide structure, space group *Fm*-3*m*, states the cell parameter, *a*, to be 5.0742(2) Å.[131] This is comparable to the cell parameter obtained for synthesis at 400 °C. This discrepancy between the reported parameters and those obtained through these refinements may be due to the hydrogen content of the lithium imide being synthesised, as Raman data (see below) suggest that at lower temperatures amide anions were still present. In addition to this it is important to note that previous reports have found that *a*/2 for *Fd*-3*m* is slightly smaller than *a* for *Fm*-3*m*,[83] thus this is something which must also be considered when comparing lattice parameters.

3.3.2 Raman Characterisation

The bulk of work reporting the synthesis of lithium imide from lithium amide does not include IR or Raman data. The spectrum of lithium amide on the other hand has been well studied and characterised. There are three fundamental vibrations of the amide anion: asymmetric stretch, symmetric stretch and bending vibration,[138] corresponding to three

Raman peaks. The observed peaks for the stretching modes in $LiNH_2$ are between 3000 and 3500 cm^{-1}. The symmetric stretch is observed as just one sharp peak at 3269 cm^{-1}. The asymmetric stretch is split and seen as two separate sharp peaks, one at 3321 cm^{-1} and one at 3332 cm^{-1}.[138,139] Kojima and Kawai observed that in lithium imide these peaks are shifted to 3180 cm^{-1} and 3250 cm^{-1}.[134] The presence of multiple N–H stretching modes does, however, suggest that there are amide anions contained within the cubic lithium imide structure – an asymmetric stretch cannot be present with just one N–H bond. They also reported peak broadening which was attributed to smaller crystallite size, a more disordered crystallite system or both.[134]

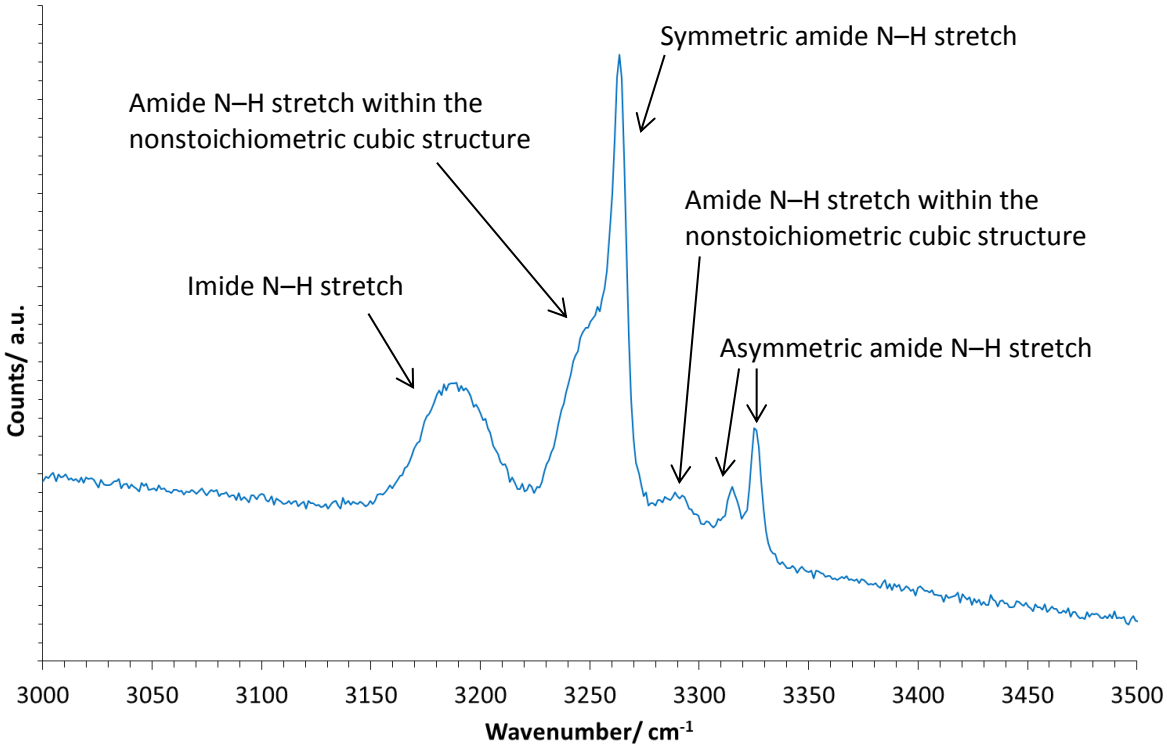

Figure 3.6 – Raman spectrum of the products of $LiNH_2$ + LiH after heating at 300 °C for 12 hours

The Raman spectrum for the sample synthesised at 300 °C (Figure 3.6) shows lithium amide was still present. The characteristic sharp amide peaks can be seen at 3260 cm^{-1} and

3315 cm^{-1}. The presence of these sharp peaks is important as it suggests that the lithium amide structure itself was still present, not just amide anions remaining within the cubic lithium imide structure consistent with XRD. However, the appearance of broader peaks is indicative of the formation of other phases. The broad peaks above 3200 cm^{-1} are likely to be amide anions within the mixed anion cubic structure and the peak below 3200 cm^{-1} is suggested to be due to the stretching vibration of the imide anion. The difference in widths of the various peaks gives an indication of the amount of disorder in a structure. It is clear looking at Figure 3.6 that the imide structure has much more disorder than the amide structure. If there are still some amide anions within the cubic imide structure this level of disorder is only increased.

The increased disorder in imide over amide is reflected in the reported conductivities for the two structures. Lithium amide is known to be a very poor lithium ion conductor whereas lithium imide has a reported lithium ion conductivity of 3×10^{-4} S cm^{-1} at room temperature.[72]

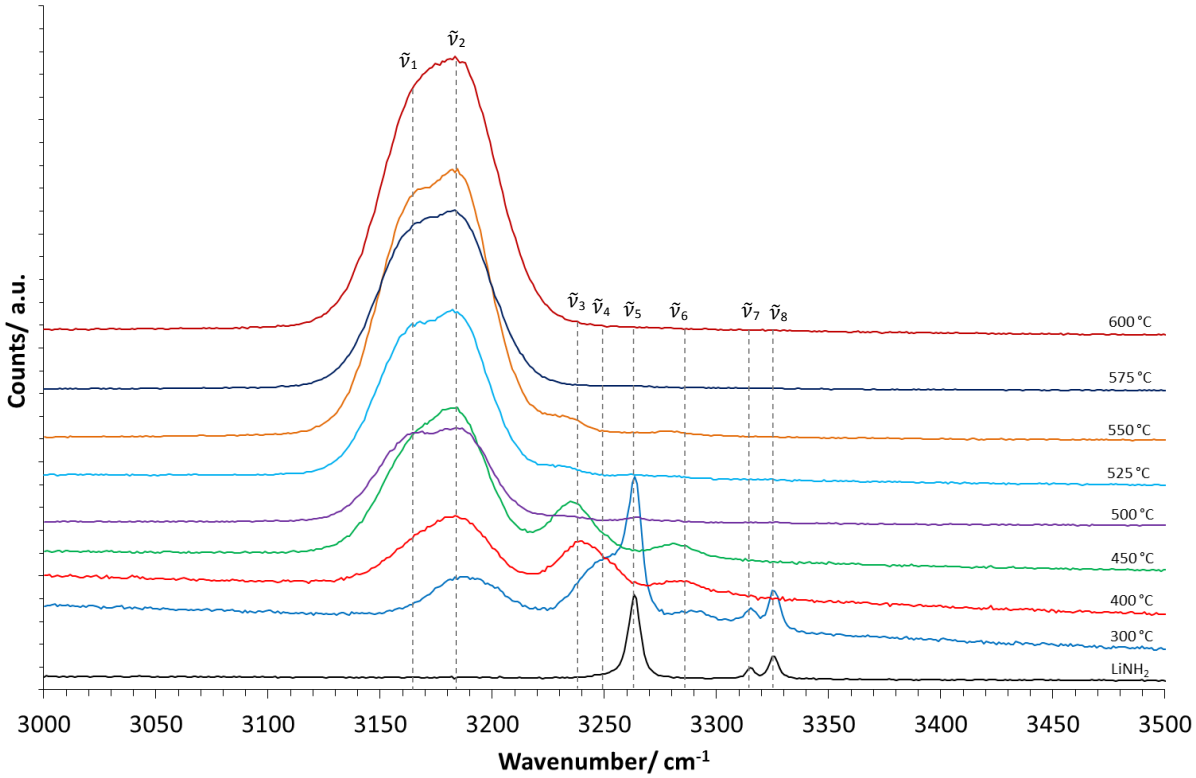

Figure 3.7 – Raman spectrum of the products of the reaction of $LiNH_2$ + LiH after heating at various temperatures for 12 hours

Table 3.1 – Raman stretching modes and assignments of the products of the reaction of $LiNH_2$ + LiH after heating at various temperatures for 12 hours

Synthesis Temperature/ °C	Peak	$\tilde{\nu}$/ cm^{-1}	Relative Intensity	Assignment
300	$\tilde{\nu}_2$	3190	29410	$\tilde{\nu}_s(NH^{2-})$
	$\tilde{\nu}_4$	3250	33129	$\tilde{\nu}_s(NH_2^-)$ non-stoichiometric
	$\tilde{\nu}_5$	3263	47422	$\tilde{\nu}_s(NH_2^-)$
	$\tilde{\nu}_6$	3292	23878	$\tilde{\nu}_s(NH_2^-)$ non-stoichiometric
	$\tilde{\nu}_7$	3316	23965	$\tilde{\nu}_{as}(NH_2^-)$
	$\tilde{\nu}_8$	3326	27347	$\tilde{\nu}_{as}(NH_2^-)$
400	$\tilde{\nu}_2$	3183	32537	$\tilde{\nu}_s(NH^{2-})$
	$\tilde{\nu}_3$	3239	28119	$\tilde{\nu}_s(NH_2^-)$ non-stoichiometric
	$\tilde{\nu}_6$	3283	21130	$\tilde{\nu}_s(NH_2^-)$ non-stoichiometric
450	$\tilde{\nu}_2$	3184	36511	$\tilde{\nu}_s(NH^{2-})$
	$\tilde{\nu}_3$	3235	20135	$\tilde{\nu}_s(NH_2^-)$ non-stoichiometric
	$\tilde{\nu}_6$	3281	12714	$\tilde{\nu}_s(NH_2^-)$ non-stoichiometric
500	$\tilde{\nu}_1$	3165	19159	$\tilde{\nu}_s(NH^{2-})$
	$\tilde{\nu}_2$	3186	19999	$\tilde{\nu}_s(NH^{2-})$
525	$\tilde{\nu}_1$	3165	33213	$\tilde{\nu}_s(NH^{2-})$
	$\tilde{\nu}_2$	3182	35794	$\tilde{\nu}_s(NH^{2-})$
550	$\tilde{\nu}_1$	3167	46819	$\tilde{\nu}_s(NH^{2-})$
	$\tilde{\nu}_2$	3184	50405	$\tilde{\nu}_s(NH^{2-})$
575	$\tilde{\nu}_1$	3167	3092	$\tilde{\nu}_s(NH^{2-})$
	$\tilde{\nu}_2$	3183	32702	$\tilde{\nu}_s(NH^{2-})$
600	$\tilde{\nu}_2$	3183	52204	$\tilde{\nu}_s(NH^{2-})$

Figure 3.7 and Table 3.1 show the Raman spectra after heating $LiNH_2$ and LiH at various temperatures for 12 hours. Sharp peaks disappeared in the spectra and multiple broad peaks formed with increasing temperature. Three clear broad peaks were observed in

the patterns for both 400 and 450 °C. Upon increasing the synthesis temperature further up to 500 °C, the imide peak became dominant. There were very small peaks still present, which appear to correspond to residual amide, although they were very minor compared with the major imide peak.

However, it was only when the temperature reached 600 °C that a single peak was observed. Between 500 °C and the upper temperature there appeared to be two peaks present in the imide peak region ($\tilde{\nu}_1$ and $\tilde{\nu}_2$), and even at the lower temperatures there looked to be some asymmetry in the imide peak. This suggests that there was also peak overlap at the lower temperatures and therefore across all samples there was not just a single N–H imide stretch being observed. One possible explanation is there being imperfect imide environments within the structure, hence different imide anions display slightly different stretching properties to one another and consequently multiple peaks and asymmetry is observed. The presence of amide anions still in the final structure would explain the observation of more than one N–H environment in the spectra and the subsequent peak splitting and asymmetry.

Although this observation would suggest the ideal temperature for synthesising lithium imide to be 600 °C, the product of this synthesis was discoloured. Rather than being a white solid there was a slight yellow colour to the product. This discolouration suggests a side-reaction, such as with the quartz tubes used for the reaction, had occurred or a nitride had formed. Consequently a lower temperature appeared to be more suitable for imide formation. Initial studies of lithium imide synthesis at various temperatures from lithium amide and lithium hydride found the best conditions to be between 500 and 550 °C. There

appeared to be very little difference in the Raman spectra and from 550 °C some discolouration of the product began to appear suggesting there could have been some lithium nitride hydride forming. Previous work by Zhang *et al.*[140] suggested decomposition of lithium imide begins to occur at 550 °C, which corresponds to the discolouration seen above that temperature and consequently the conclusion is that it is due to the formation of lithium nitride hydride. However, it is important to note that although the splitting of the imide peak and asymmetry at some of the lower temperatures may be due to the presence of amide anions as previously mentioned, it is also possible that in some cases there may have been other anions present i.e. N^{3-} and H^{-}, due to some decomposition beginning to occur. Consequently, where there is splitting or asymmetry in the imide peak region it is possible that there are other anions present, N^{3-} NH_2^{-} or H^{-}, and the sample is not simply a pure cubic imide structure.

3.3.3 Reannealing

At the lower synthesis temperatures, based on the Raman spectra, there were a significant number of amide anions still present within the cubic imide structure, as shown in Figure 3.7. In order to determine whether or not the reaction could proceed any further at these temperatures and whether there could be a further reduction in the amount of amide anions, regrinding and reheating was attempted at 400, 450, 500 and 550 °C. Both XRD and Raman were used to compare the reannealed samples.

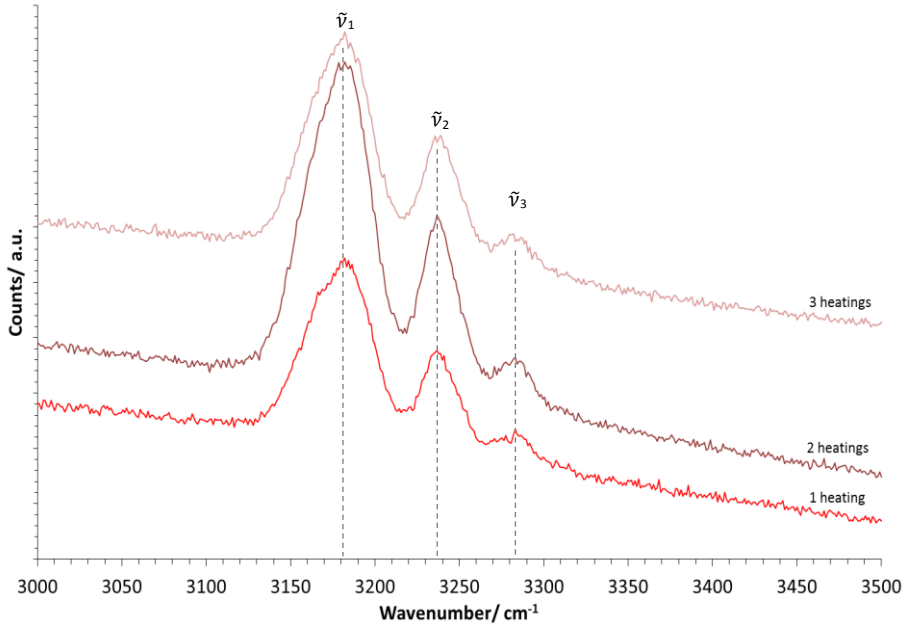

Figure 3.8 – Raman spectrum of the products of $LiNH_2$ + LiH after heating and reannealing at 400 °C

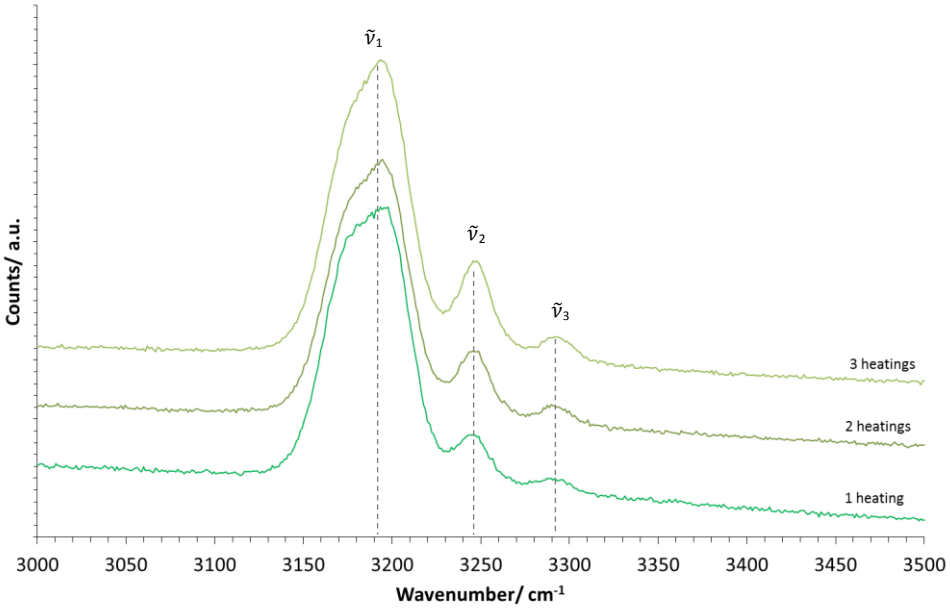

Figure 3.9 – Raman spectrum of the products of $LiNH_2$ + LiH after heating and reannealing at 450 °C

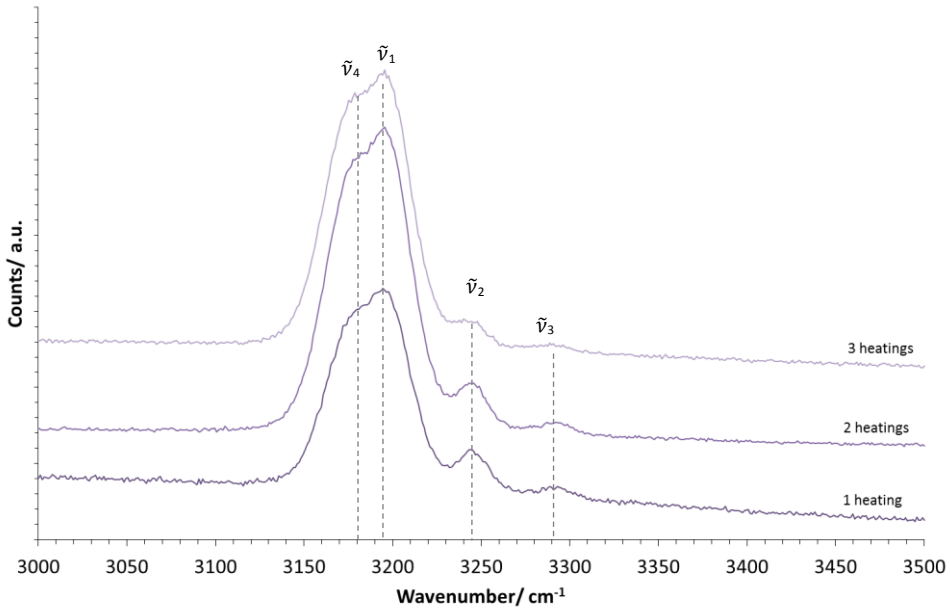

Figure 3.10 – Raman spectrum of the products of $LiNH_2$ + LiH after heating and reannealing at 500 °C

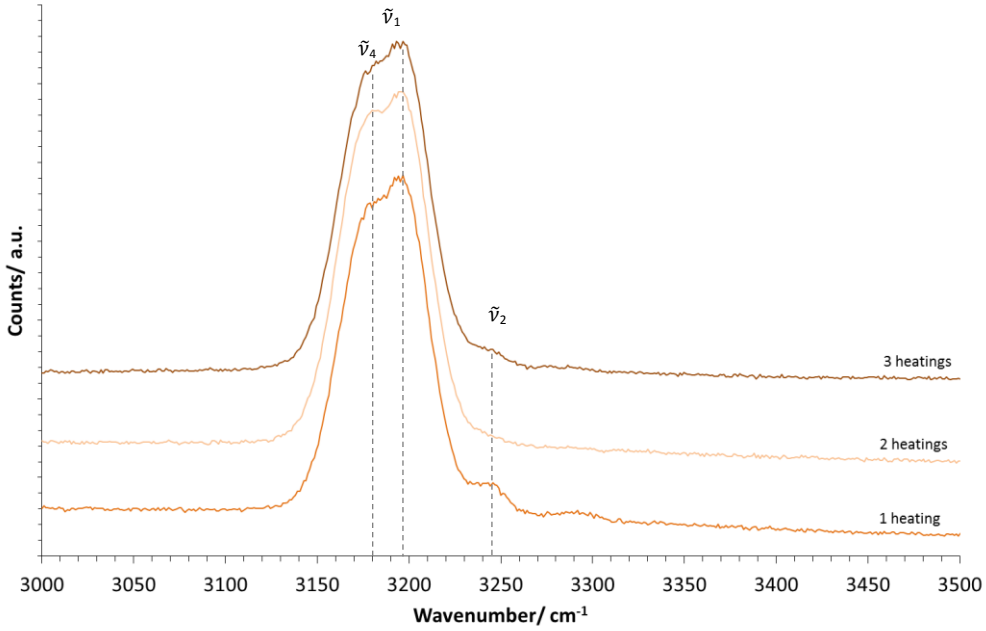

Figure 3.11 – Raman spectrum of the products of $LiNH_2$ + LiH after heating and reannealing at 550 °C

Table 3.2 – Raman stretching modes and assignments of the products of $LiNH_2$ + LiH after heating and reannealing at various temperatures

Synthesis Temperature / °C	Peak	$\tilde{\nu}$/ cm^{-1}	Relative Intensity			Assignment
			Heating cycle			
			1	2	3	
400	$\tilde{\nu}_1$	3183	18565	25817	18813	$\tilde{\nu}_s(NH^{2-})$
	$\tilde{\nu}_2$	3240	15410	19810	15172	$\tilde{\nu}_s(NH_2^-)$ non-stoichiometric
	$\tilde{\nu}_3$	3284	12673	15054	11549	$\tilde{\nu}_s(NH_2^-)$ non-stoichiometric
450	$\tilde{\nu}_1$	3193	35967	31810	34440	$\tilde{\nu}_s(NH^{2-})$
	$\tilde{\nu}_2$	3249	16525	15755	17400	$\tilde{\nu}_s(NH_2^-)$ non-stoichiometric
	$\tilde{\nu}_3$	3294	12775	11030	10971	$\tilde{\nu}_s(NH_2^-)$ non-stoichiometric
500	$\tilde{\nu}_4$	3180	21125	22099	22048	$\tilde{\nu}_s(NH^{2-})$
	$\tilde{\nu}_1$	3194	22400	24150	23664	$\tilde{\nu}_s(NH^{2-})$
	$\tilde{\nu}_2$	3244	11901	7296	7294	$\tilde{\nu}_s(NH_2^-)$ non-stoichiometric
	$\tilde{\nu}_3$	3292	9474	4694	5896	$\tilde{\nu}_s(NH_2^-)$ non-stoichiometric
550	$\tilde{\nu}_4$	3180	25113	26323	23173	$\tilde{\nu}_s(NH^{2-})$
	$\tilde{\nu}_1$	3193	27133	27125	24699	$\tilde{\nu}_s(NH^{2-})$
	$\tilde{\nu}_2$	3247	5041	5560	5128	$\tilde{\nu}_s(NH_2^-)$ non-stoichiometric

Figure 3.8, Figure 3.9, Figure 3.10 and Figure 3.11 show the Raman spectra of the products of reannealing compared with a single heating at 400, 450, 500 and 550 °C respectively (peaks assigned in Table 3.2). It is clear from these data that the amide anions are not fully removed from the cubic imide structure at 400, 450 or 500 °C. The presence of the non-stoichiometric amide stretch at *ca* 3250 cm^{-1} is evidence of this. Although the peak remains present, it did notably reduce in the 500 °C series data, suggesting reheating does help to remove additional amide anions. It is important to note that at these elevated

temperatures, reannealing is likely to have been causing decomposition of $LiNH_2$ in addition to facilitating the reaction of $LiNH_2$ and LiH. At 550 °C the non-stoichiometric amide peak almost completely disappears, however, there is clearly some asymmetry in the imide peak at *ca* 3200 cm^{-1}. This asymmetry indicates there are imperfect imide environments and thus it is not a perfect cubic structure, despite reannealing.

In order to support the Raman data collected, the reported cubic crystal structure of lithium imide was refined against the experimental data, using the Rietveld method. This allowed the lattice parameters of each of the products to be determined and consequently see how they changed with repeated heating.

On refining the lattice parameters there was a clear trend, showing a decrease in lattice parameters with additional regrinding and reheating cycles (Figure 3.12). The decrease in lattice parameters suggests that, by regrinding and reannealing, the amount of amide anions in the final structure did decrease, thus forming a structure closer to the pure lithium imide.

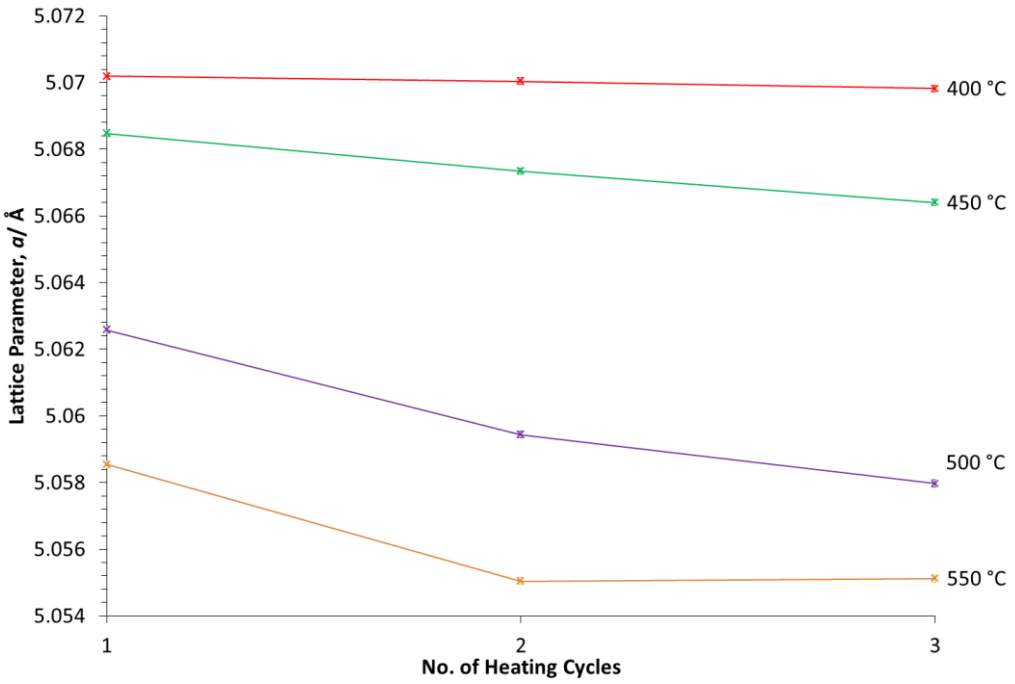

Figure 3.12 – Lattice parameter changes observed as a result of regrinding and reannealing products of the $LiNH_2$ + LiH reaction determined through Rietveld refinement. Error bars are included but are smaller than the data point symbols

Although Rietveld refinements did show a decrease in cell parameters with an increased number of heating cycles, the choice of synthesis temperature is still very important. It is clear from these data, that regrinding and reheating makes a greater difference at higher temperature. At 450 °C a difference of *ca* 0.04% (0.002 Å) was seen after three heating cycles, compared with just 0.008% (0.0004 Å) at 400 °C. On the other hand, reannealing at 500 and 550 °C just once (two heating cycles) resulted in differences of *ca* 0.06% (0.003 Å) and 0.07% (0.003 Å), respectively. These trends indicate that, based on lattice parameters, combining both reheating and higher temperatures is the most effective method to form a purer lithium imide product, with less amide anions present.

Although overall the data supports this idea, it is still important to note the plateau in the 550 °C data in Figure 3.12. This potentially highlights the limit in reannealing and agrees with the Raman data collected (Figure 3.11). In the Raman data there appeared to be very little difference between the data collected after two heating cycles and the data collected after three heating cycles at 550 °C. The peak corresponding to a symmetric NH^{2-} stretch in a non-stoichiometric cubic structure ($\tilde{\nu}_2$) did not appear visible after just two heating cycles. Therefore, it could be that after two heating cycles at 550 °C all additional amide anions have been removed and as a result additional reannealing resulted in no change in lattice parameters.

As a result of these reannealing experiments, and based on lattice parameter data, heating and reannealing at 500 °C was determined to be the best method for synthesising Li_2NH. Reannealing resulted in the removal of additional amide anions from the structure, whilst keeping the temperature at 500 °C prevented any discolouration occurring which may have been as a result of nitride formation. Despite the smaller lattice parameters for the imide synthesised at 550 °C, discolouration was an issue and therefore the presence of nitride could not be discounted.

3.3.4 Excess Hydride Series

In addition to varying the temperature and heating times, reactions were carried out with an excess of LiH. Initially reactions were performed at 450, 480 and 500 °C using a $2LiNH_2 + 3LiH$ ratio. Powder XRD data show the result of these reactions to be the formation of two separate phases (Figure 3.13), seen in the splitting and asymmetry of the imide peaks.

The appearance of the low angle ordering peak at *ca* 15 ° also suggests one of those phases may be pure Li_2NH.

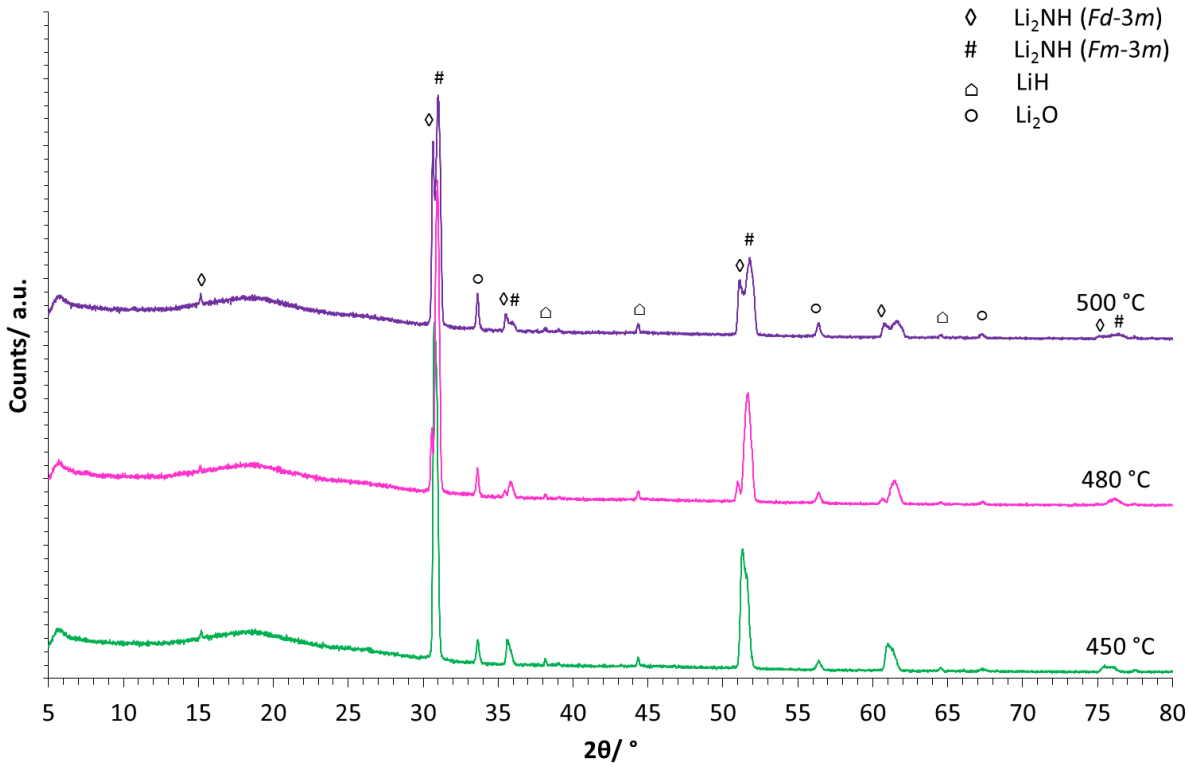

Figure 3.13 – Powder XRD data of the products of the reaction of $2LiNH_2$ + 3LiH at various temperatures for 12 hours

Initial comparison with data from known structures suggested that two different structures form with differing amounts of amide anions present. The data were analysed in more detail through Rietveld refinement, fitting two Li_2NH phases against the experimental data. One of the lithium imide phases fitted was the disordered *Fm*-3*m*, the other *Fd*-3*m* (previously observed when lithium content is greater than 1.9).[83] These two structures fit well to the data and thus suggested an excess of lithium hydride may produce both a structure close to pure Li_2NH and a disordered cubic imide structure alongside it (Figure 3.14, Figure 3.15 and Figure 3.16).

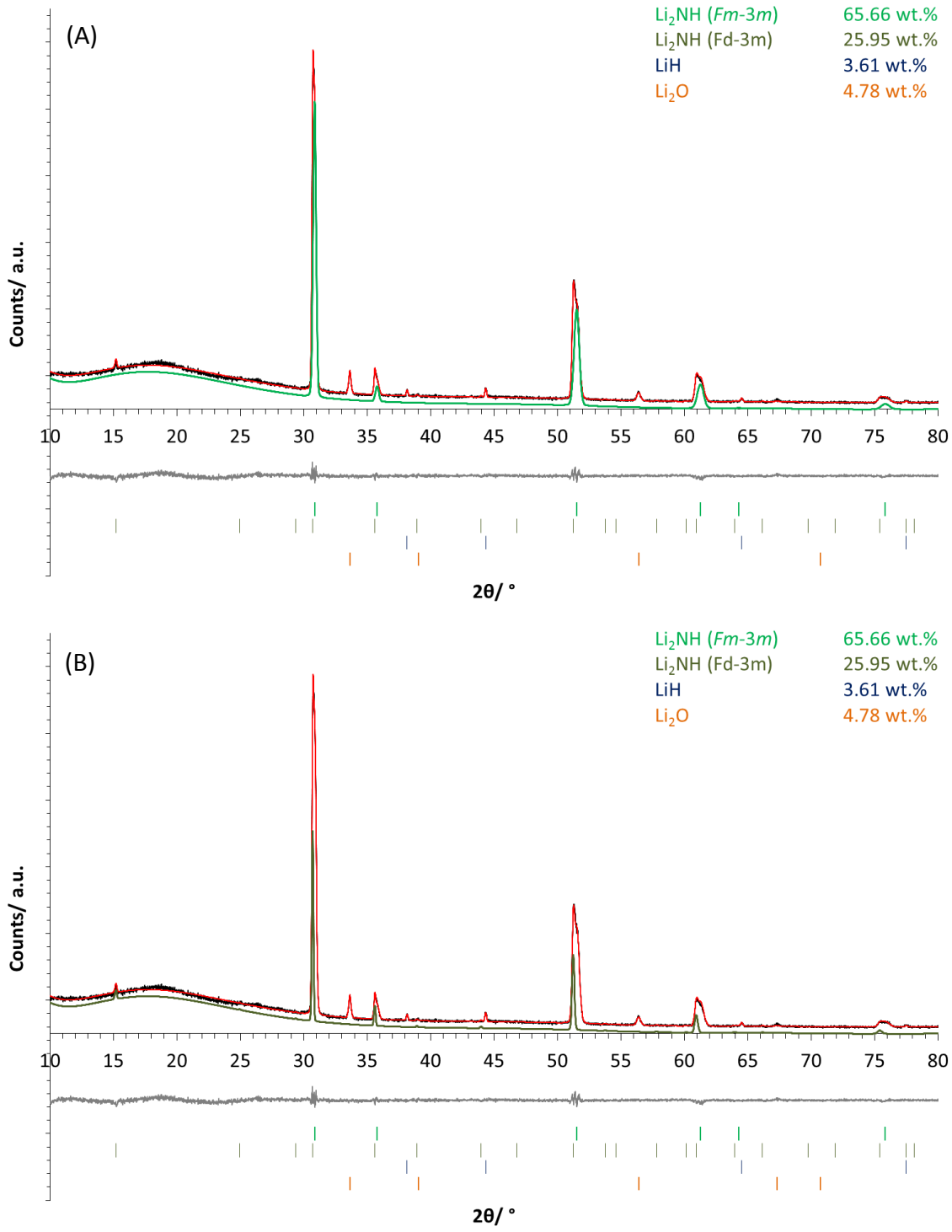

Figure 3.14 – Refinement plot showing the products of heating $2LiNH_2 + 3LiH$ at 450 °C for 12 hours. Green tick marks = Li_2NH (Fm-3m), dark green tick marks = Li_2NH (Fd-3m), dark blue tick marks = LiH, orange tick marks = Li_2O. (A) Shows the Li_2NH (*Fm*-3*m*) phase fit plotted in green (B) shows the Li_2NH (*Fd*-3*m*) phase fit plotted in dark green

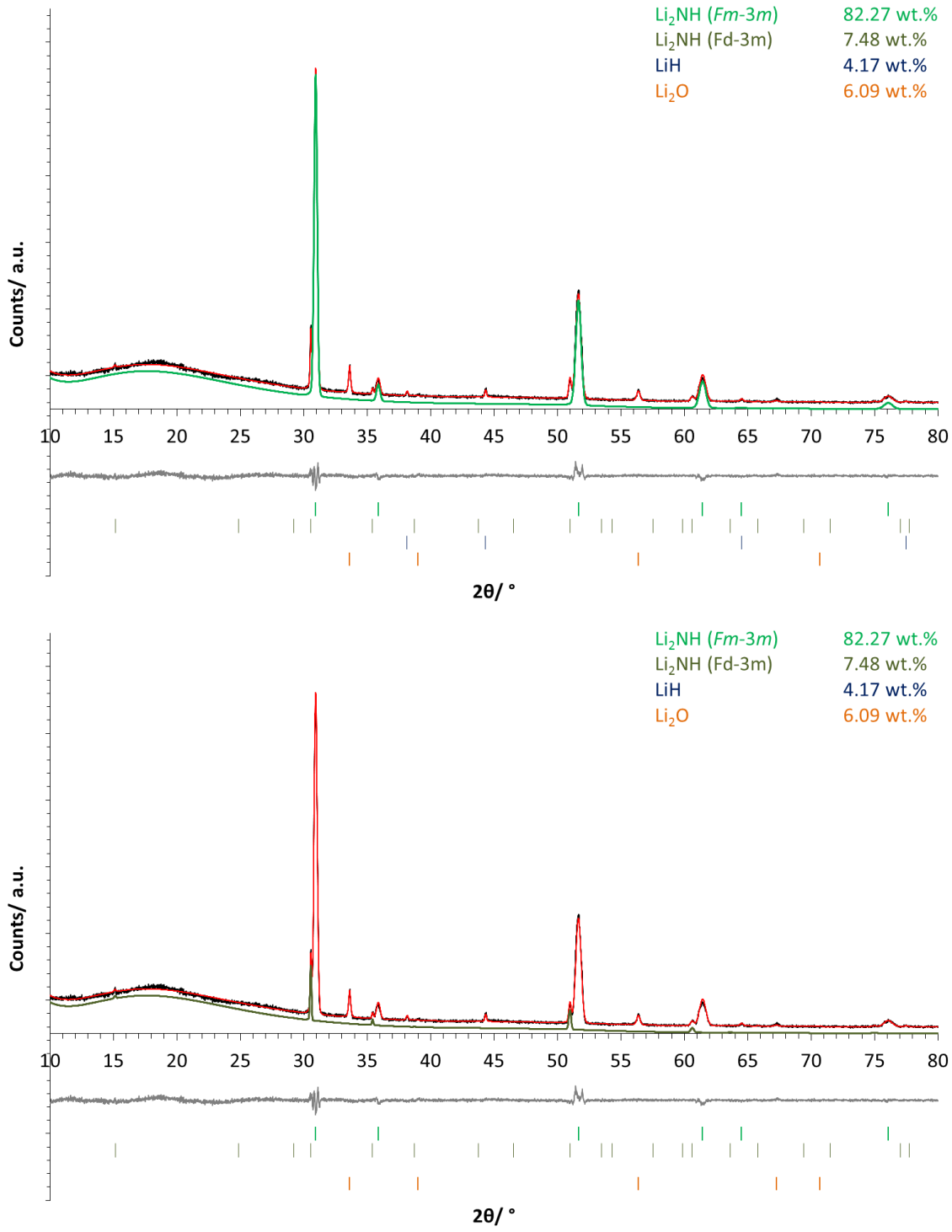

Figure 3.15 – Refinement plot showing the products of heating $2LiNH_2 + 3LiH$ at 480 °C for 12 hours. Green tick marks = Li_2NH (Fm-3m), dark green tick marks = Li_2NH (Fd-3m), dark blue tick marks = LiH, orange tick marks = Li_2O. (A) Shows the Li_2NH (*Fm*-3*m*) phase fit plotted in green (B) shows the Li_2NH (*Fd*-3*m*) phase fit plotted in dark green

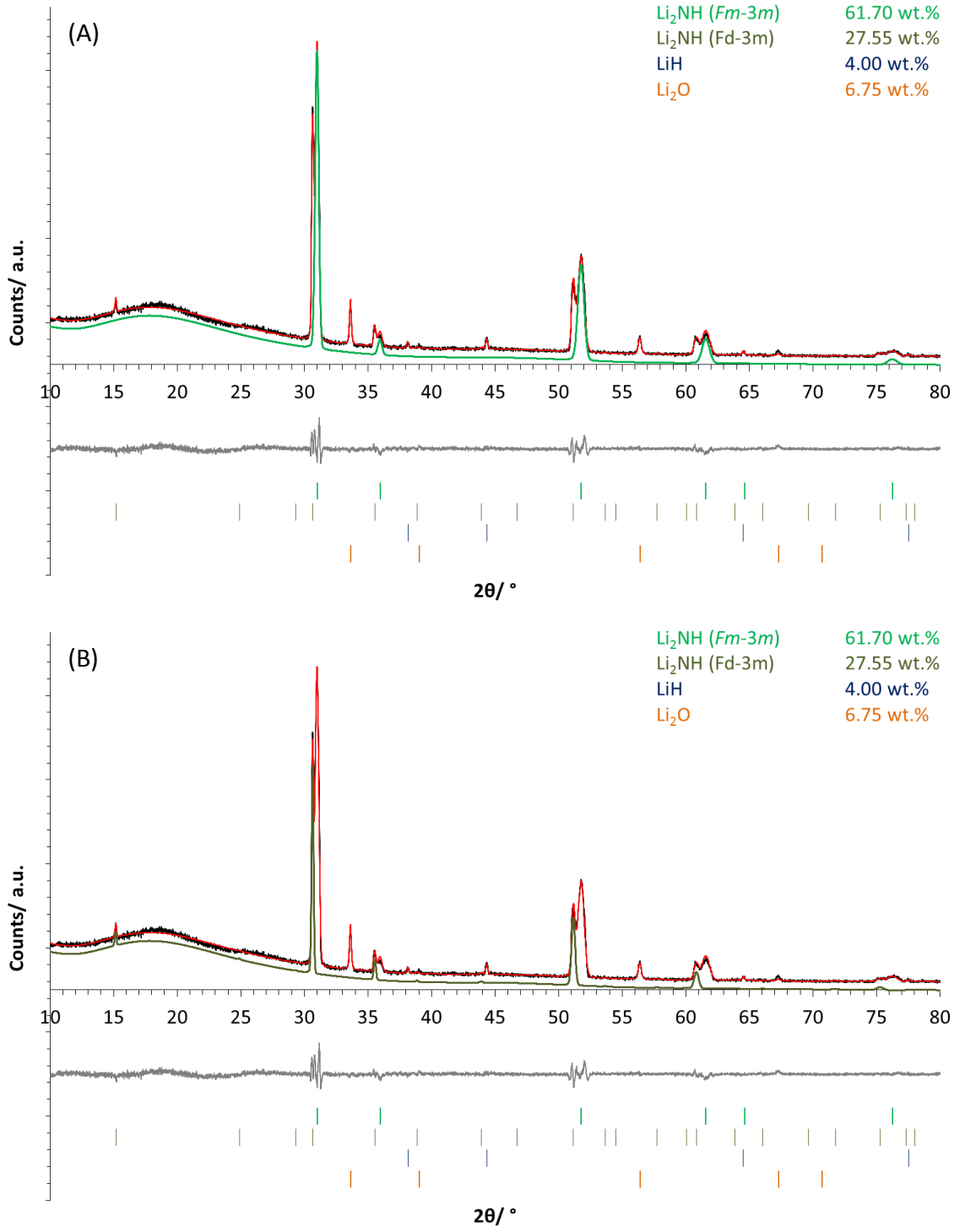

Figure 3.16 – Refinement plot showing the products of heating $2LiNH_2 + 3LiH$ at 500 °C for 12 hours. Green tick marks = Li_2NH (Fm-3m), dark green tick marks = Li_2NH (Fd-3m), dark blue tick marks = LiH, orange tick marks = Li_2O. (A) Shows the Li_2NH (*Fm*-3*m*) phase fit plotted in green (B) shows the Li_2NH (*Fd*-3*m*) phase fit plotted in dark green

The lattice parameters determined from these refinements are reported in Table 3.3. All the disordered *Fm*-3*m* structures had smaller unit cells than the 1:1 reactions at the same temperatures. The smallest lattice parameter determined from the 1:1 reaction was 5.0466(1) Å, notably higher than the smallest lattice parameters determined for the reactions carried out with excess lithium hydride, 4.9902(3) Å. This decrease in the lattice parameters compared with the 1:1 reaction indicates a compositional difference between the structures.

Table 3.3 – Lattice parameters of products of the $1LiNH_2$ + 1.5LiH reaction, heated at various temperatures for 12 hours, determined from Rietveld refinement

Synthesis Temperature/ °C	Lattice Parameter / Å	
	Lower angle Li_2NH (*Fd*-3*m*, *a*/2)	Higher angle Li_2NH (*Fm*-3*m*, *a*)
450	5.0384(4)	5.0137(3)
480	5.0626(5)	5.0013(2)
500	5.0450(6)	4.9902(3)

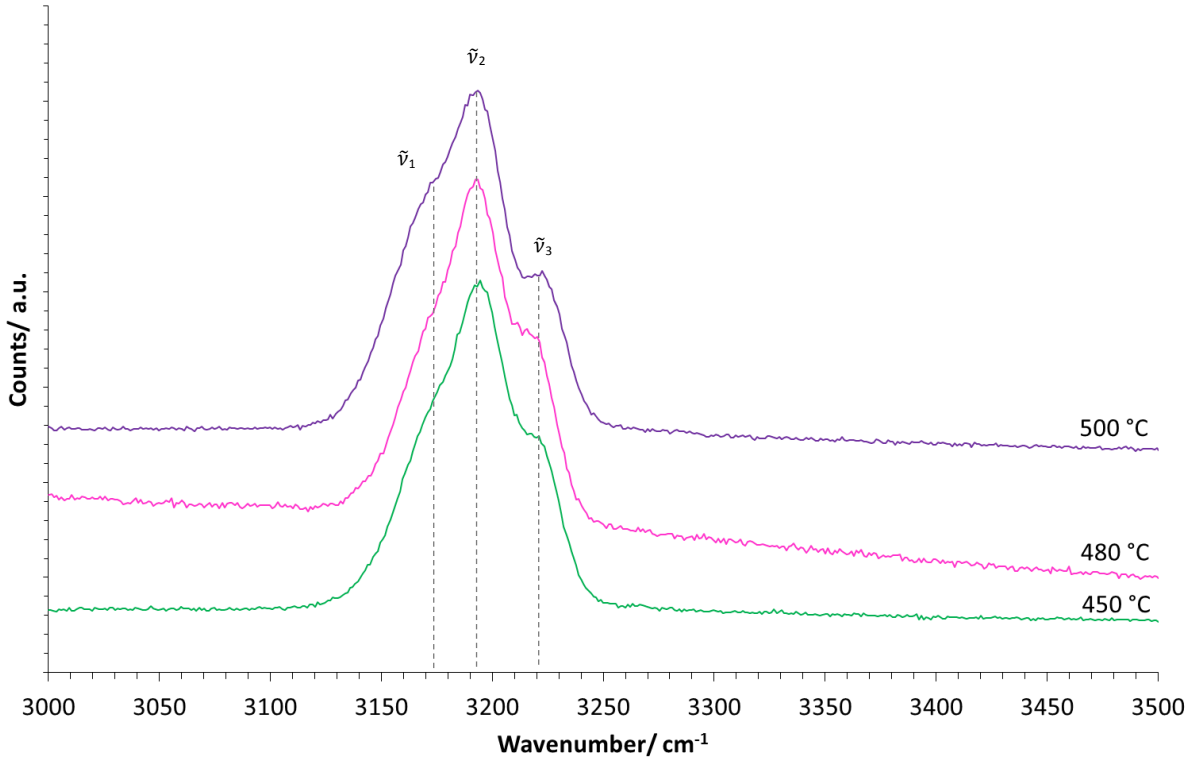

Figure 3.17– Raman spectra of the products of the reaction of $1LiNH_2$ + 1.5LiH at various temperatures for 12 hours

Table 3.4 – Raman stretching modes and assignments of the products of the reaction of $1LiNH_2$ + 1.5LiH at various temperatures for 12 hours

Synthesis Temperature / °C	Peak	$\tilde{\nu}$/ cm^{-1}	Relative Intensity	Assignment
450	$\tilde{\nu}_1$	3173	14279	$\tilde{\nu}_s(NH^{2-})$/ $\tilde{\nu}_s(NH_2^-)$ non-stoichiometric
	$\tilde{\nu}_2$	3195	20602	$\tilde{\nu}_s(NH^{2-})$/ $\tilde{\nu}_s(NH_2^-)$ non-stoichiometric
	$\tilde{\nu}_3$	3224	11874	$\tilde{\nu}_s(NH^{2-})$/ $\tilde{\nu}_s(NH_2^-)$ non-stoichiometric
480	$\tilde{\nu}_1$	3173	23837	$\tilde{\nu}_s(NH^{2-})$/ $\tilde{\nu}_s(NH_2^-)$ non-stoichiometric
	$\tilde{\nu}_2$	3195	30426	$\tilde{\nu}_s(NH^{2-})$/ $\tilde{\nu}_s(NH_2^-)$ non-stoichiometric
	$\tilde{\nu}_3$	3224	20597	$\tilde{\nu}_s(NH^{2-})$/ $\tilde{\nu}_s(NH_2^-)$ non-stoichiometric
500	$\tilde{\nu}_1$	3173	17745	$\tilde{\nu}_s(NH^{2-})$/ $\tilde{\nu}_s(NH_2^-)$ non-stoichiometric
	$\tilde{\nu}_2$	3195	22126	$\tilde{\nu}_s(NH^{2-})$/ $\tilde{\nu}_s(NH_2^-)$ non-stoichiometric
	$\tilde{\nu}_3$	3224	12854	$\tilde{\nu}_s(NH^{2-})$/ $\tilde{\nu}_s(NH_2^-)$ non-stoichiometric

Raman data were collected for the products of the reactions at the three different temperatures (Figure 3.17 and Table 3.4). For all three samples there were multiple overlapping peaks in the imide stretch region and the amide-imide region, which appeared to be more defined as the synthesis temperature was increased. The peak at the highest wavenumber appeared to shift to a higher wavenumber with increasing temperature; there also appeared to be a reduction in the intensity of this peak.

The increased separation in the Raman peaks agreed with the XRD data which displays two clearly defined cubic structures, suggesting the presence of a more amide-rich cubic structure and a separate more imide-rich cubic structure. The reduction in the peak at the more amide-rich end of the region (higher wavenumber) also agreed with the XRD data (Table 3.3) which demonstrated a shift to higher 2θ for both peaks, suggesting a decrease in the amount of amide anions.

Although reducing the amount of amide anions in the structure and hence observing shifting in the Raman is one theory, there is also the possibility that hydride and/or nitride anions became incorporated into these structures. The lattice parameters determined for the *Fm*-3*m* unit cell, suggested to be the disordered amide-imide, are much smaller than the cubic phase synthesised at the even higher temperature of 600 °C when using a 1:1 ratio. This significant difference suggests there may be other anions in the structure causing this discrepancy.

Lithium nitride hydride, Li_4NH, forms a tetragonal structure with lattice parameters, *a* = 4.877 Å and *c* = 9.877 Å.[141], and is formed during the decomposition of Li_2NH. However, Zhang and Hu have reported that during decomposition, Li_4NH forms a solid solution with

Li_2NH and in that Li_4NH has a cubic structure similar to Li_2NH. Rather than observing two phases in the XRD data there was a shift to higher 2θ as decomposition occurred and the solid solution was formed. The unit cell of this structure is reported to be 5.033 Å. They concluded that the tetragonal structure is formed only once the cubic structure can no longer stabilise Li_4NH.[140]

Independently, Bull *et al.* conducted research into the hydrogenation of Li_3N. During hydrogenation Li_2NH and Li_4NH are formed and subsequently go on to form $Li_{4-2x}NH$, a cubic structure referred to as a quasi-imide.[142] This work highlights how the cubic structure can accommodate both N^{3-} and H^-.[140,142] Similar research has also been carried out on other metal N-H systems, for example Santoru *et al.* have reported a solid solution of KNH_2 and KH, forming a cubic $K(NH_2)_xH_{(1-x)}$ structure with variable lattice parameters.[143] Consequently it is possible that adding an excess of LiH to the $LiNH_2$ + LiH reaction may cause hydride anions to become embedded in the cubic structure, subsequently reducing the lattice parameter.

Having varied temperature with a constant excess of LiH, the excess amount of LiH was then varied at a constant temperature to see if a trend was apparent as the amount of LiH was increased. The additional data could also provide more information on whether hydride or nitride anions were being incorporated into the cubic imide structure.

$LiNH_2$ and LiH were ground together and heated in a 1:1 ratio. The reaction products were then ground together with additional LiH (0.25, 0.5, 0.75 and 1 mole) and reheated. The series was repeated at 500 and 535 °C and a similar trend was seen at both temperatures. Multiple phases appeared to be present which all fit to the cubic *Fm*-3*m*

imide structure. As the amount of LiH was increased the lowest angle peak decreased in size and the higher angle, smaller unit cell seemed to dominate (Figure 3.18 and Figure 3.19, Figure 3.20 shows zoomed in plot between 29 and 33 °).

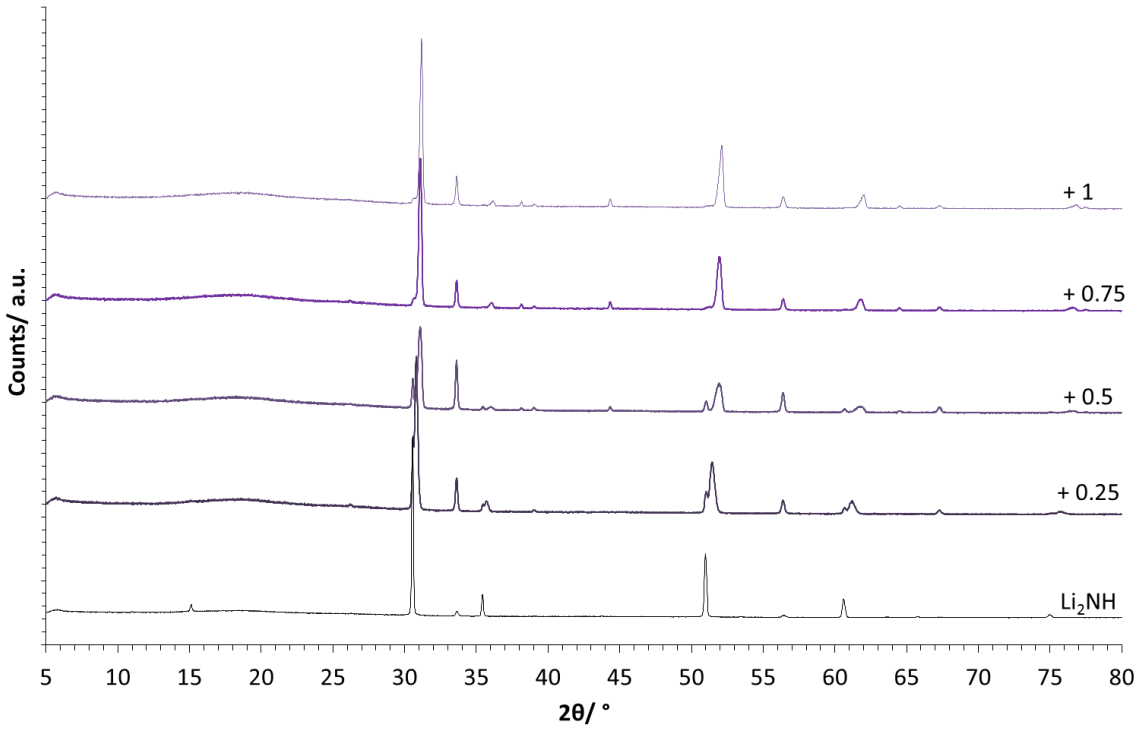

Figure 3.18 – Powder XRD data of the products of the reaction of $1Li_2NH + xLiH$ at various values of *x*, where the total values of *x* = 1.25, 1.5, 1.75 and 2, with the initial Li_2NH data for reference, heated at 500 °C for 12 hours

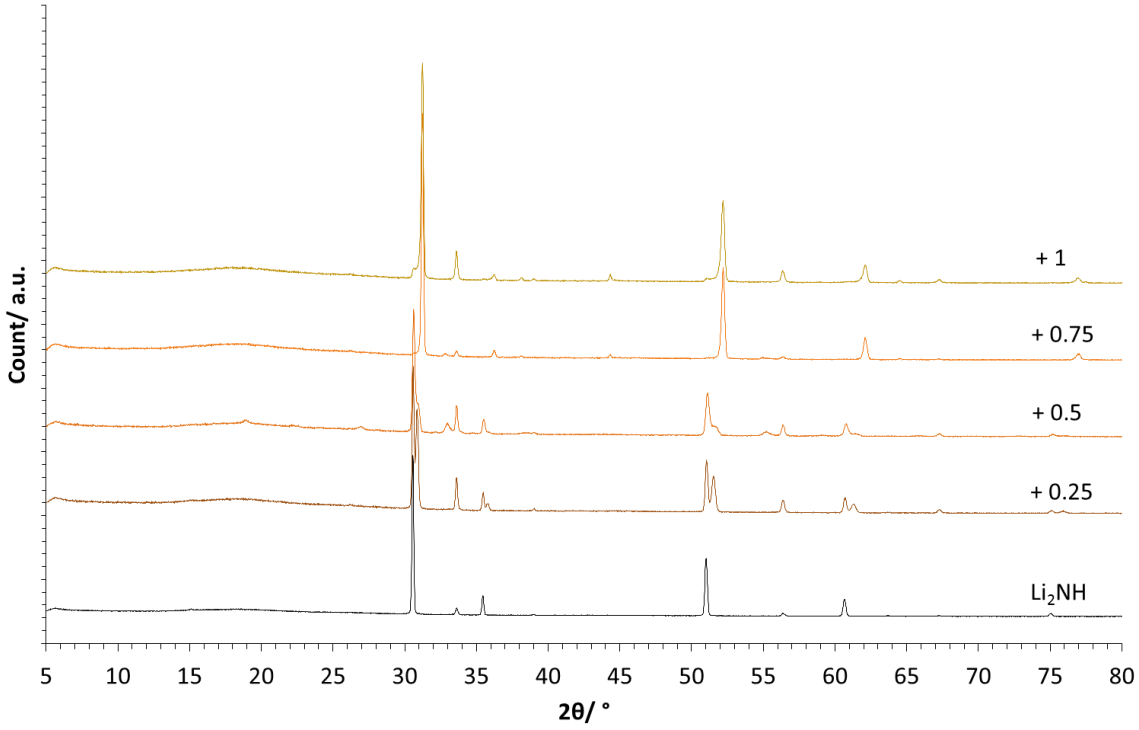

Figure 3.19 – Powder XRD data of the products of the reaction of $1Li_2NH + xLiH$ at various values of *x*, where the total values of *x* = 1.25, 1.5, 1.75 and 2, with the initial Li_2NH data for reference, heated at 535 °C for 12 hours

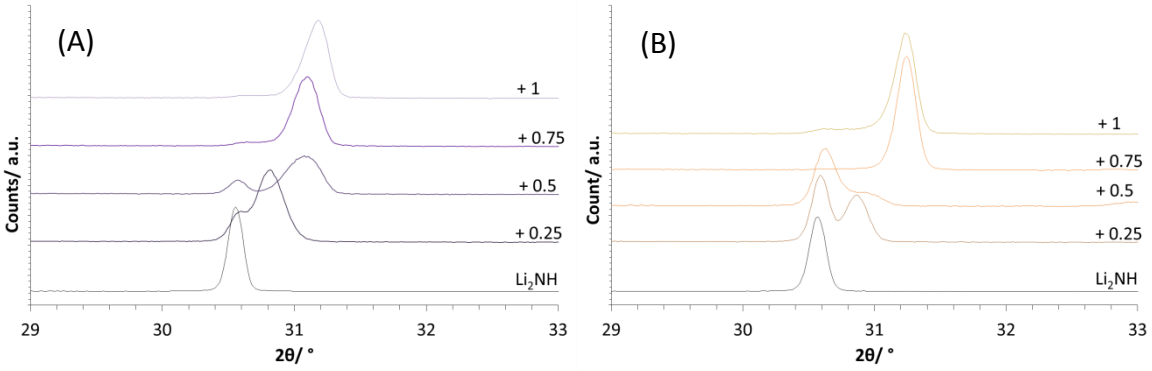

Figure 3.20 – Zoomed in plots of powder XRD data of the products of the reaction of $1Li_2NH + xLiH$ at various values of x, with the initial Li_2NH data for reference, heated at (A) 500 °C and (B) 535 °C for 12 hours

Table 3.5 – Lattice parameters of the products of the 1Li_2NH + *x*LiH reaction, heated at 500 and 535 °C, determined from Rietveld refinement, with initial Li_2NH lattice parameter for comparison

Excess LiH, *x*	Lattice Parameters/ Å		
	1st Li_2NH phase	2nd Li_2NH phase	3rd Li_2NH phase
500 °C			
Initial Li_2NH	5.0632(2)		
+0.25	5.0585(2)	5.0182(2)	–
+ 0.5	5.0575(2)	4.9797(2)	–
+ 0.75	5.0200(29)	4.9752(2)	–
+1	5.0495(10)	4.9773(11)	4.9592(3)
535 °C			
Initial Li_2NH	5.0582(1)		
+0.25	5.0550(1)	5.0114(1)	–
+0.5	5.0387(7)	4.9802(19)	4.9570(3)
+0.75	–	–	4.9518(1)
+1	5.0460(10)	4.9730(6)	4.6123(2)

Rietveld refinements were carried out on both temperature sets of XRD data in order to compare the lattice parameters (Table 3.5). Both data sets showed a general decrease in lattice parameters with temperature, although the number of Li_2NH phases which were fitted varied. On the whole these data show that increasing the LiH excess resulted in smaller unit cells. However, while a smaller unit cell suggests amide anions have been removed, the major decrease in lattice parameters resulting in unit cells smaller than 5 Å, suggests, as with the previous series, there may be more going on than simply removal of NH_2^-. There is also the added issue of an excess of LiH remaining in the final products.

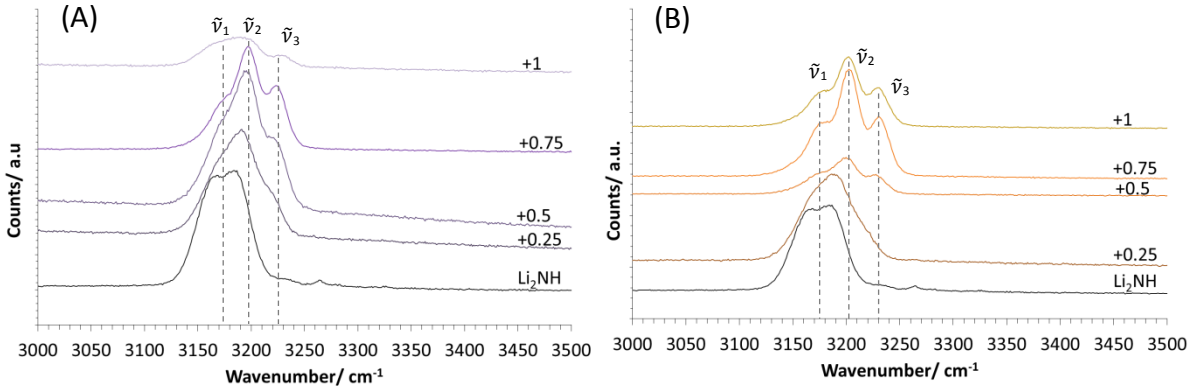

Figure 3.21 – Raman data of the products of the reaction of 1Li_2NH + *x*LiH at various values of x, with the initial Li_2NH data for reference, heated at (A) 500 and (B) 535 °C for 12 hours

Table 3.6 – Raman stretching modes and assignment of the products of the reaction of $1Li_2NH + xLiH$ at various values of x

Synthesis Temperature / °C	*x*	Peak	$\tilde{\nu}$/ cm^{-1}	Relative Intensity	Assignment
500	+0.25	$\tilde{\nu}_2$	3190	23758	$\tilde{\nu}_s(NH^{2-})$
		$\tilde{\nu}_3$	3220	14821	$\tilde{\nu}_s(NH_2^-)$ non-stoichiometric
	+0.5	$\tilde{\nu}_2$	3197	31000	$\tilde{\nu}_s(NH^{2-})$
		$\tilde{\nu}_3$	3222	21465	$\tilde{\nu}_s(NH_2^-)$ non-stoichiometric
	+0.75	$\tilde{\nu}_1$	3178	9836	$\tilde{\nu}_s(NH^{2-})$
		$\tilde{\nu}_2$	3197	16633	$\tilde{\nu}_s(NH^{2-})$
		$\tilde{\nu}_3$	3224	11130	$\tilde{\nu}_s(NH_2^-)$ non-stoichiometric
	+1	$\tilde{\nu}_2$	3194	7937	$\tilde{\nu}_s(NH^{2-})$
		$\tilde{\nu}_3$	3231	5318	$\tilde{\nu}_s(NH_2^-)$ non-stoichiometric
535	+0.25	$\tilde{\nu}_1$	3185	23941	$\tilde{\nu}_s(NH^{2-})$
	+0.5	$\tilde{\nu}_1$	3175	6255	$\tilde{\nu}_s(NH^{2-})$
		$\tilde{\nu}_2$	3199	9212	$\tilde{\nu}_s(NH^{2-})$/ $\tilde{\nu}_s(NH_2^-)$ non-stoichiometric
		$\tilde{\nu}_3$	3230	5673	$\tilde{\nu}_s(NH^{2-})$/ $\tilde{\nu}_s(NH_2^-)$ non-stoichiometric
	+0.75	$\tilde{\nu}_1$	3188	14306	$\tilde{\nu}_s(NH^{2-})$
		$\tilde{\nu}_2$	3208	20899	$\tilde{\nu}_s(NH^{2-})$/ $\tilde{\nu}_s(NH_2^-)$ non-stoichiometric
		$\tilde{\nu}_3$	3231	14125	$\tilde{\nu}_s(NH^{2-})$/ $\tilde{\nu}_s(NH_2^-)$ non-stoichiometric
	+1	$\tilde{\nu}_1$	3179	9207	$\tilde{\nu}_s(NH^{2-})$
		$\tilde{\nu}_2$	3202	15802	$\tilde{\nu}_s(NH^{2-})$/ $\tilde{\nu}_s(NH_2^-)$ non-stoichiometric
		$\tilde{\nu}_3$	3231	9723	$\tilde{\nu}_s(NH^{2-})$/ $\tilde{\nu}_s(NH_2^-)$ non-stoichiometric

In order to investigate the concentration of imide and amide anions within the product mixtures, Raman data were collected (Figure 3.21 and Table 3.6). As in the previous series (Figure 3.17) there appeared to be multiple imide environments which could again support the theory that hydride and potentially nitride anions were being introduced into

the cubic imide structure. The reactions performed at both 500 and 535 °C, in particular for the data collected on the 535 °C products, there appeared to be a shift of the peaks away from the pure imide region and more clearly defined, separate peaks were present. Logic would dictate that adding a greater excess of LiH would introduce more hydride, therefore more disorder and more imide environments. The peaks do, however, appear to be sharper with increasing LiH content, suggesting more defined vibrations and therefore a more specific range of N–H environments.

Although addition of excess LiH seemed to allow the ratio of amide to imide anions to be varied, supported by both XRD and Raman data, there was an issue with the purity of these phases and the potential introduction of hydride and nitride anions. A range of phases appeared to form alongside an excess of LiH remaining in the higher LiH reactions, limiting the possible use of this as a method to tune anion ratios.

3.4 $LiNH_2 + Li_3N$ Synthesis

Although a suitable route to forming Li_2NH was found through the reaction of $LiNH_2$ and LiH, the reaction of $LiNH_2$ and Li_3N was also investigated for comparison.

3.4.1 X-ray Diffraction Characterisation

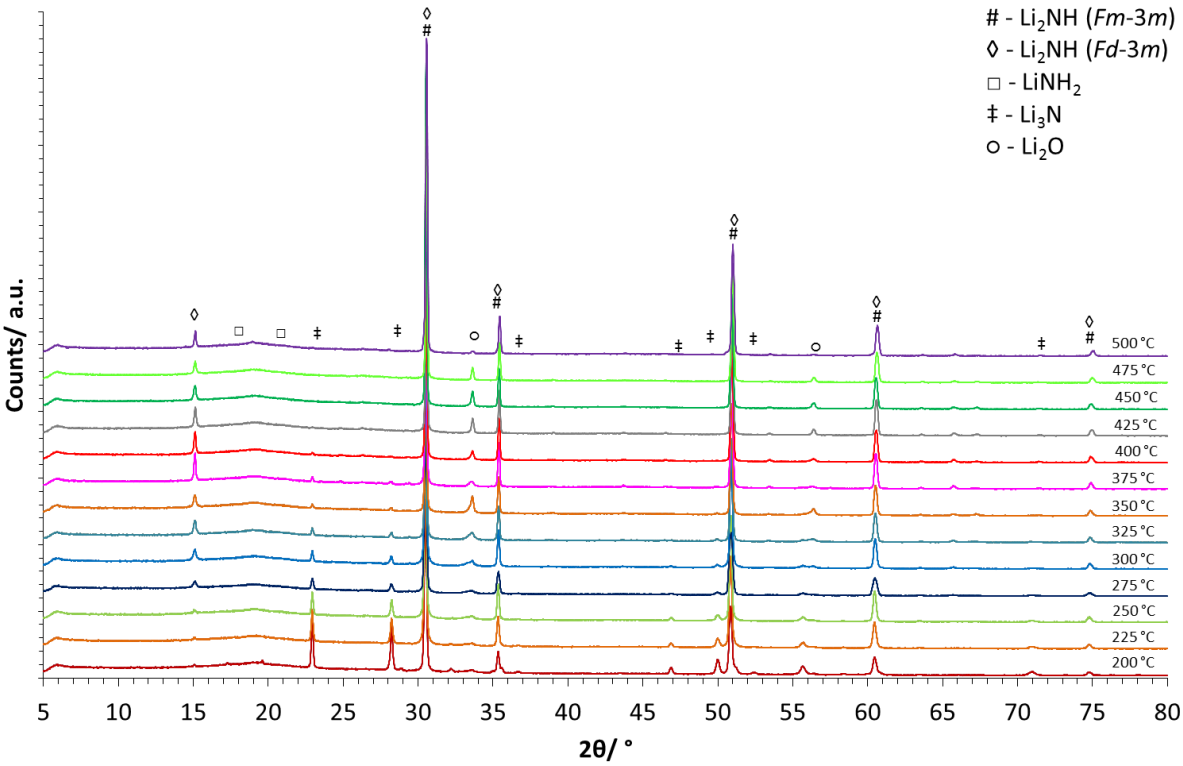

Figure 3.22 – Powder XRD data from the products of the reaction of $LiNH_2$ + Li_3N at various temperatures for 12 hours

The reaction was carried out at a range of temperatures in 25 °C increments from 200 °C up to 500 °C (Figure 3.22). There are characteristic amide peaks at 200 °C (15 ° and 17.5 °), however, these quickly disappeared as the tetragonal structure was lost and an overall cubic structure was adopted. Unlike the $LiNH_2$ + LiH reaction where the low angle amide peaks were still present at 300 °C, for the $LiNH_2$ + Li_3N reaction the cubic structure was formed at a significantly lower temperature. Despite the formation of the cubic structure at *ca* 225 °C, there was still Li_3N present at much higher temperatures, up to *ca* 425 °C. Consequently based on initial observations of the XRD data, 425 °C was deemed a suitable temperature for Li_2NH formation *via* this reaction.

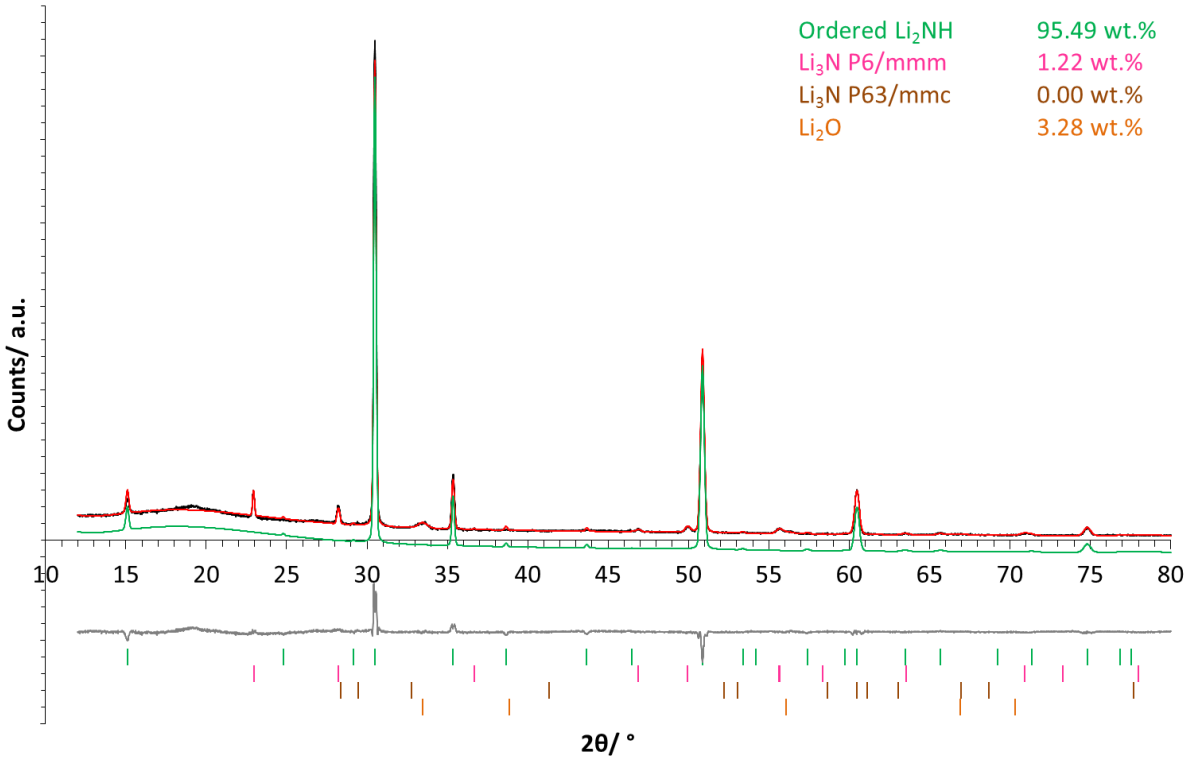

Figure 3.23 – Rietveld refinement plot showing the products of heating $LiNH_2$ + Li_3N at 375 °C for 12 hours. Green tick marks = Li_2NH, pink tick marks = Li_3N *P*6/*mmm*, brown tick marks = Li_3N *P*63/*mmc*, orange tick marks = Li_2O, with the ordered Li_2NH *Fd*-3*m* phase highlighted in green

Again as with the $LiNH_2$ + LiH reaction, a low angle peak at *ca* 15 ° was present, suggesting the formation of an ordered *Fd*-3*m* Li_2NH supercell.[136] For this reaction the additional ordering peak was present at all temperatures, although with varying intensity. This variation in intensity suggested that there may have been a mixture of both the *Fm*-3*m* and *Fd*-3*m* structures of Li_2NH present in some of the samples. At 375 °C the relative intensity of the peak at 15 ° was greatest, which suggests this temperature may be where the highest proportion of ordered imide phase was formed. Figure 3.23 shows the fit of the *Fd*-3*m* supercell to the collected data. Despite some small discrepancies in the intensities;

overall the structure fitted well to the data. Based on conclusions from the $LiNH_2$ + LiH reaction results (§3.3), this would suggest 375 °C to be the ideal synthesis temperature for the formation of Li_2NH, however, the Li_3N peaks are not lost until a higher temperature of 425 °C, indicating a slightly higher temperature is required to ensure all Li_3N has been reacted.

Lithium nitride exists in three different polymorphs.[144] The α-Li_3N polymorph (*P*6/*mmm*) is the form which is stable at room temperature and pressure; it is a layered structure with alternating Li_2N^- and Li^+ layers. There is then the β-Li_3N polymorph (*P*6$_3$/*mmc*) which forms from α-Li_3N at a relatively low pressure of 0.6 GPa and adopts a Na_3As structure.[145] Then finally there is the γ-Li_3N polymorph which is the high pressure structure and forms when β-Li_3N under pressures of between 35 and 45 GPa.[144] In commercial Li_3N there is often a mixture of α-Li_3N and β-Li_3N, this is due to the low pressure required to form the β polymorph, which can be formed simply through grinding preparation methods.[146] Consequently these reactions were performed using a mixture of α-Li_3N and β-Li_3N, both of which are present in the product mixtures of the lower temperature reactions. However, the exothermal transformation of the β to the α polymorph occurs on heating above 200 °C and therefore at the higher temperatures β-Li_3N is no longer present.[145]

3.4.1.1 Lattice Parameter Comparison

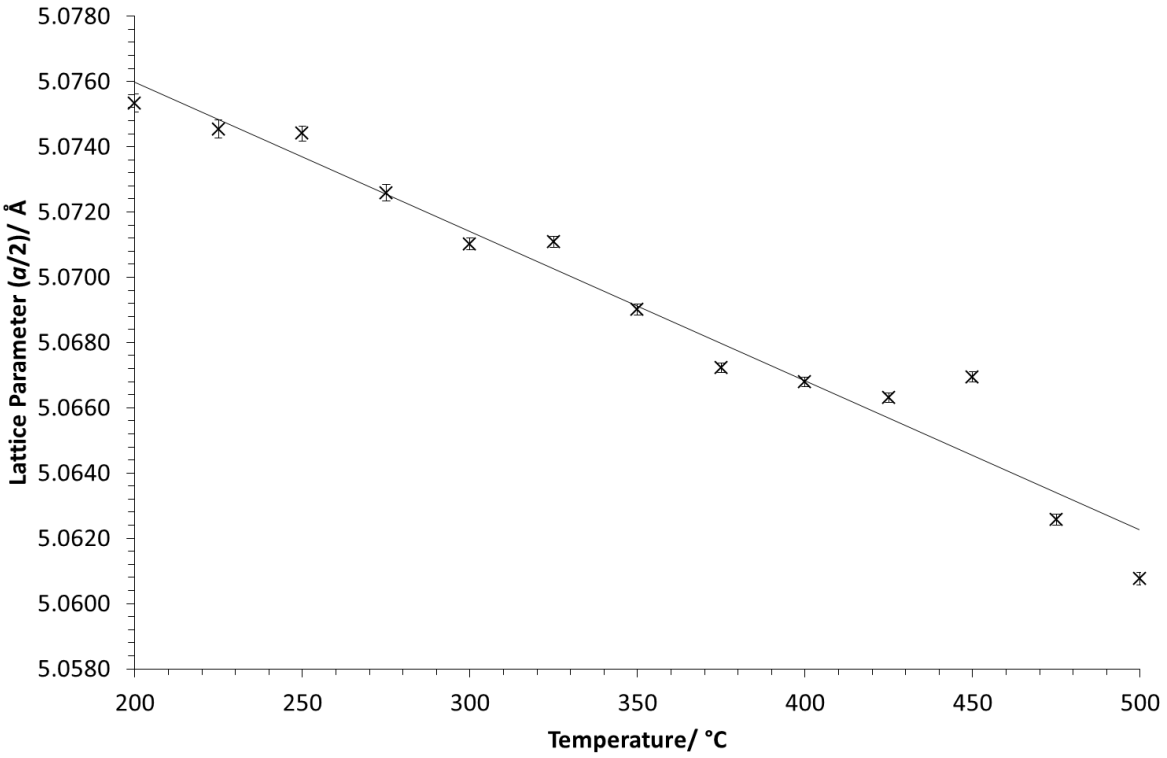

Figure 3.24 – Lattice parameters of the products of the $LiNH_2$ + Li_3N reaction heated at various temperatures, determined from Rietveld refinement of the *Fd*-3*m* structure

Using Rietveld refinement the lattice parameters of the Li_2NH structure were refined for each synthesis temperature sample. These refinements were carried out using the *Fd*-3*m* space group, including the additional ordering peak. In order to be able to draw a clear comparison between different data sets containing both space group stretches, the ordered superstructure lattice parameter values are reported as $a/2$.

Figure 3.24 shows how the lattice parameter, $a/2$, changed with synthesis temperature. There is a clear trend of decreasing lattice parameter with increasing temperature. At 425 °C a lattice parameter of 5.0664(1) Å was refined; however, a smaller structure still has been refined for 500 °C with a lattice parameter of 5.0608(2) Å. The trend

observed in these lattice parameters follows a similar trend to that observed for the $LiNH_2$ + LiH reaction (data summarised in Table 3.7). However, there is a slight difference between the two (§3.3, Table 3.8), with slightly smaller lattice parameters as a result of the $LiNH_2$ + Li_3N reaction, with the exception of the sample at 300 °C where $LiNH_2$ was also present alongside Li_2NH.

Table 3.7 – Summary of the products of the reaction of $LiNH_2$ and Li_3N performed at various temperatures

Temp/ °C	Li_2NH Lattice Parameter ($a/2$)/ Å	Weight Percent				
		Li_2NH	Li_3N (*P*6/*mmm*)	Li_3N (*P*6$_3$/*mmc*)	Li_2NH	Li_2O
200	5.0757(2)	43.1(6)	22.7(3)	5.8(3)	24.5(5)	3.9(4)
225	5.0746(2)	85.2(4)	12.1(2)	0	0	2.7(4)
250	5.0744(1)	87.8(5)	8.5(2)	0	0	3.7(5)
275	5.0725(2)	90.8(5)	5.4(3)	0	0	3.8(4)
300	5.0709(1)	91.4(4)	3.6(2)	0	0	5.0(3)
325	5.0711(1)	90.3(3)	2.6(2)	0	0	7.2(3)
350	5.0690(1)	88.0(2)	1.3(2)	0	0	10.7(2)
375	5.0672(1)	95.5(3)	1.2(1)	0	0	3.3(2)
400	5.0668(1)	94.7(2)	0.5(1)	0	0	4.8(2)
425	5.0664(1)	94.4(1)	0	0	0	5.6(1)
450	5.0670(1)	92.8(2)	0	0	0	7.2(2)
475	5.0627(1)	95.2(2)	0	0	0	4.8(2)
500	5.0608(1)	99.0(2)	0	0	0	1.0(2)

Table 3.8 – Comparison of the lattice parameters determined from Rietveld refinement of $LiNH_2$ + LiH and $LiNH_2$ + Li_3N reactions

Synthesis Temperature/ °C	Lattice Parameter, *a*/ Å	
	$LiNH_2$ + LiH Reaction	$LiNH_2$ + Li_3N Reaction
300	5.0574(2)	5.0710(2)
400	5.0706(1)	5.0668(2)
425	—	5.0663(1)
450	5.0688(1)	5.0669(2)
500	5.0632(2)	5.0608(2)

As the additional peak at *ca* 15 ° in the *Fd*-3*m* structure is an indication of the level of order in the structure, the ratio between that peak and the highest intensity imide peak was determined. This was to highlight which structure was likely to be the most ordered, and consequently which temperature may be the most suitable for synthesising the most pure imide structure.

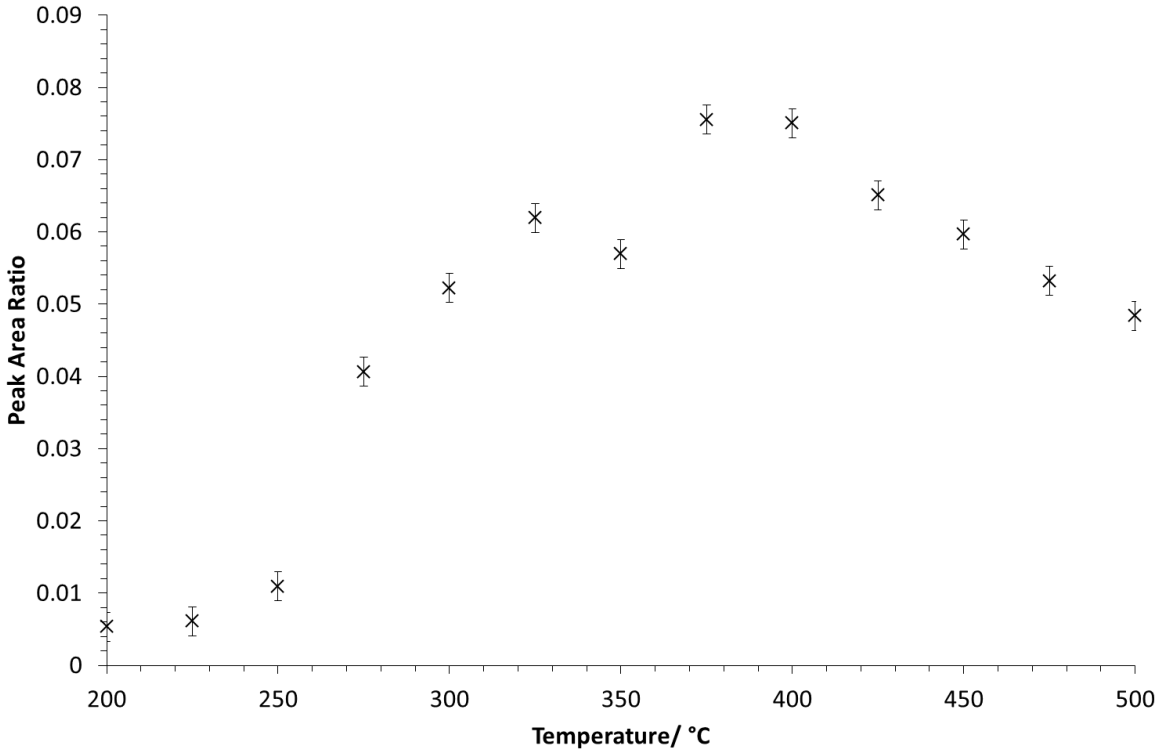

Figure 3.25 – Peak area ratio of ordering peak at *ca* 15 ° to most intense imide peak at *ca* 30 ° from the $LiNH_2$ + Li_3N reaction heated at various temperatures

Figure 3.25 shows the ratio between these two peaks and shows the area of the ordering peak increasing relative to the main imide peak, as the temperature is increased up to *ca* 375 – 400 °C. After reaching a maximum between those two temperatures the area of the ordering peak then begins to drop off again. Consequently, these observations suggest the imide structure was most ordered when formed between 375 and 400 °C.

3.4.2 Raman Characterisation

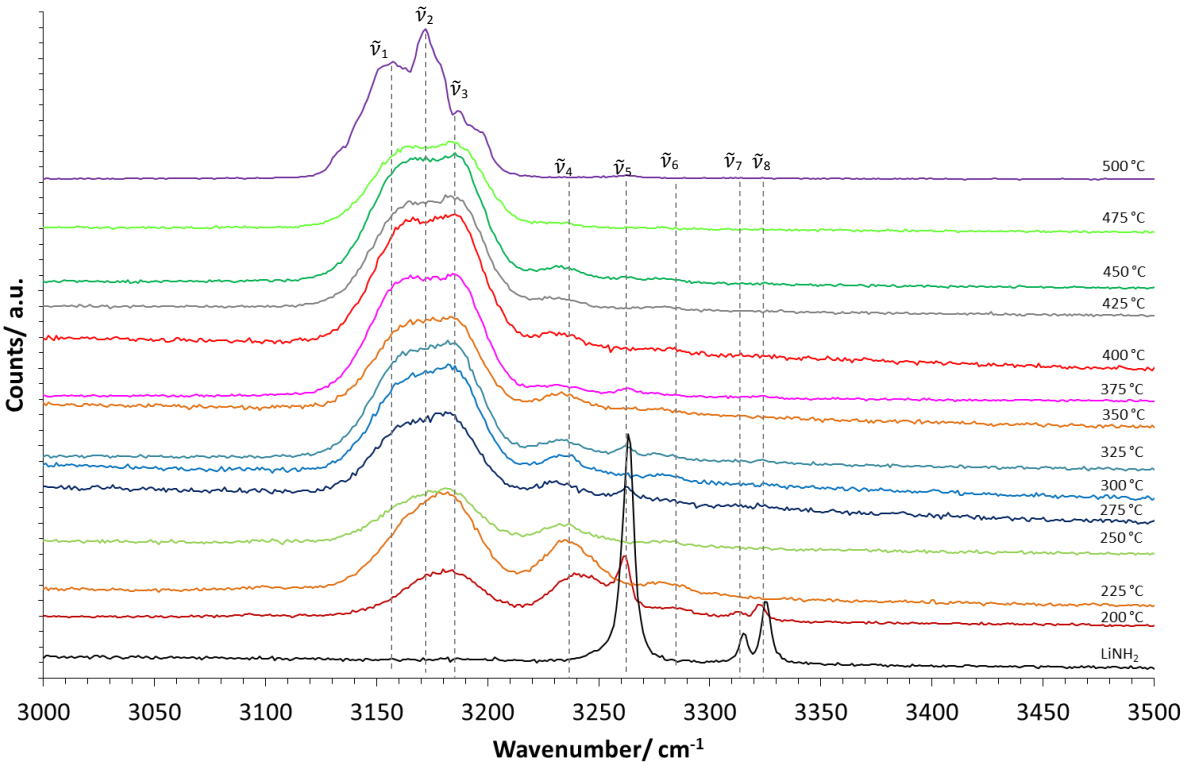

Figure 3.26 – Raman data from the products of the reaction of $LiNH_2$ + Li_3N at various temperatures for 12 hours

Table 3.9 – Raman stretches and assignment of the products of the reaction of $LiNH_2$ + Li_3N at various temperatures for 12 hours

Synthesis Temperature/ °C	Peak	$\tilde{\nu}$/ cm^{-1}	Relative Intensity	Assignment
200	$\tilde{\nu}_3$	3183	4994	$\tilde{\nu}_s(NH^{2-})$
	$\tilde{\nu}_4$	3242	4666	$\tilde{\nu}_s(NH_2^-)$ non-stoichiometric
	$\tilde{\nu}_5$	3262	5829	$\tilde{\nu}_s(NH_2^-)$
	$\tilde{\nu}_6$	3285	2447	$\tilde{\nu}_s(NH_2^-)$ non-stoichiometric
	$\tilde{\nu}_7$	3314	2235	$\tilde{\nu}_{as}(NH_2^-)$
	$\tilde{\nu}_8$	3323	2719	$\tilde{\nu}_{as}(NH_2^-)$
225	$\tilde{\nu}_3$	3182	9992	$\tilde{\nu}_s(NH^{2-})$

	$\tilde{\nu}_4$	3237	6764	$\tilde{\nu}_s(NH_2^-)$ non-stoichiometric
	$\tilde{\nu}_6$	3284	4079	$\tilde{\nu}_s(NH_2^-)$ non-stoichiometric
250	$\tilde{\nu}_3$	3182	6191	$\tilde{\nu}_s(NH^{2-})$
	$\tilde{\nu}_4$	3237	3951	$\tilde{\nu}_s(NH_2^-)$ non-stoichiometric
	$\tilde{\nu}_6$	3283	2825	$\tilde{\nu}_s(NH_2^-)$ non-stoichiometric
275	$\tilde{\nu}_1$	3163	11472	$\tilde{\nu}_s(NH^{2-})$
	$\tilde{\nu}_3$	3184	12112	$\tilde{\nu}_s(NH^{2-})$
	$\tilde{\nu}_4$	3229	7744	$\tilde{\nu}_s(NH_2^-)$ non-stoichiometric
	$\tilde{\nu}_5$	3262	7354	$\tilde{\nu}_s(NH_2^-)$
300	$\tilde{\nu}_1$	3163	12279	$\tilde{\nu}_s(NH^{2-})$
	$\tilde{\nu}_3$	3184	12931	$\tilde{\nu}_s(NH^{2-})$
	$\tilde{\nu}_4$	3234	7321	$\tilde{\nu}_s(NH_2^-)$ non-stoichiometric
325	$\tilde{\nu}_1$	3163	9599	$\tilde{\nu}_s(NH^{2-})$
	$\tilde{\nu}_3$	3184	10331	$\tilde{\nu}_s(NH^{2-})$
	$\tilde{\nu}_4$	3234	3909	$\tilde{\nu}_s(NH_2^-)$ non-stoichiometric
	$\tilde{\nu}_5$	3263	3552	$\tilde{\nu}_s(NH_2^-)$
350	$\tilde{\nu}_1$	3163	9790	$\tilde{\nu}_s(NH^{2-})$
	$\tilde{\nu}_3$	3184	10333	$\tilde{\nu}_s(NH^{2-})$
	$\tilde{\nu}_4$	3237	5294	$\tilde{\nu}_s(NH_2^-)$ non-stoichiometric
375	$\tilde{\nu}_1$	3163	8995	$\tilde{\nu}_s(NH^{2-})$
	$\tilde{\nu}_3$	3184	9091	$\tilde{\nu}_s(NH^{2-})$
	$\tilde{\nu}_5$	3264	1745	$\tilde{\nu}_s(NH_2^-)$
400	$\tilde{\nu}_1$	3163	14597	$\tilde{\nu}_s(NH^{2-})$
	$\tilde{\nu}_3$	3184	14970	$\tilde{\nu}_s(NH^{2-})$
	$\tilde{\nu}_4$	3234	7253	$\tilde{\nu}_s(NH_2^-)$ non-stoichiometric
425	$\tilde{\nu}_1$	3163	8795	$\tilde{\nu}_s(NH^{2-})$
	$\tilde{\nu}_3$	3184	9111	$\tilde{\nu}_s(NH^{2-})$
	$\tilde{\nu}_4$	3231	2562	$\tilde{\nu}_s(NH_2^-)$ non-stoichiometric
450	$\tilde{\nu}_1$	3163	9323	$\tilde{\nu}_s(NH^{2-})$
	$\tilde{\nu}_3$	3184	9924	$\tilde{\nu}_s(NH^{2-})$
	$\tilde{\nu}_4$	3234	2621	$\tilde{\nu}_s(NH_2^-)$ non-stoichiometric
475	$\tilde{\nu}_1$	3163	6321	$\tilde{\nu}_s(NH^{2-})$

	$\tilde{\nu}_3$	3184	6632	$\tilde{\nu}_s(NH^{2-})$
500	$\tilde{\nu}_1$	3157	7812	$\tilde{\nu}_s(NH^{2-})$/ $\tilde{\nu}_s(NH_2^-)$ non-stoichiometric
	$\tilde{\nu}_2$	3172	9900	$\tilde{\nu}_s(NH^{2-})$/ $\tilde{\nu}_s(NH_2^-)$ non-stoichiometric
	$\tilde{\nu}_3$	3189	3927	$\tilde{\nu}_s(NH^{2-})$/ $\tilde{\nu}_s(NH_2^-)$ non-stoichiometric

In order to compare the ratio of amide to imide anions within the synthesis products at the various temperatures, Raman data were collected (Figure 3.26, Table 3.9). At 200 °C there were sharp amide peaks, agreeing with the presence of the characteristic $LiNH_2$ peaks in the XRD and thus the presence of pure $LiNH_2$. As the temperature was increased the second broad peak at *ca* 3240 cm^{-1} decreased, which has been identified as a mixed amide-imide peak. This observation supports the formation of a purer imide phase with increasing temperature, as expected from the XRD data (Figure 3.22). At 425 °C, the temperature at which Li_3N appeared to have all reacted based on XRD data, there was only a very small residual amide-imide peak. The residual amide was observed at all temperatures up to 500 °C; however, at 500 °C the single imide peak became multiple overlapping peaks suggesting the presence of multiple vibrations in the imide region.

At temperatures below 500 °C there was a small amount of asymmetry in the imide peak, suggesting more than one N–H stretch. However, the presence of residual amide would explain this asymmetry and was also present in the products of the $LiNH_2$ + LiH reaction.

The synthesis products from the $LiNH_2$ + Li_3N reaction did not vastly differ from the products of the $LiNH_2$ + LiH reaction. Synthesis at 400 °C appeared to be the most promising. The *Fd-3m* cubic imide ordering peak was most intense for synthesis at 375 and 400 °C,

however all Li_3N was removed by 425 °C according to the XRD data. Raman data for all three samples also showed only residual amide presence. Consequently, based on the different data sets, 400 °C provides a good compromise between removing all starting materials and having the most ordered cubic imide structure. Although there was a drop in lattice parameter by increasing the temperature up to 500 °C, that came alongside the presence of unidentified vibrations in the Raman spectra and consequently the higher temperature was not deemed suitable for imide synthesis.

Moving forward the reaction of $LiNH_2$ + LiH heated at 500 °C, heated for 12 hours and annealed for a further 12 hours was determined to be suitable to use in further synthesis. Consequently later work contained within this thesis used this as the Li_2NH preparation method.

3.5 Amide-imide Synthesis

Once suitable synthesis conditions for Li_2NH formation were determined, mixed anion amide-imide phases were then studied. The aim of this work was to investigate whether the ratio of anions could be tuned and subsequently carried forward into other work with borohydride-imides discussed later in this thesis. Previous work by Makepeace et *al*.[77,83] demonstrated that a solid solution exists between Li_2NH and $LiNH_2$, supported by the varying lattice parameters and Raman data reported earlier in this chapter.

3.5.1 Varying Synthesis Temperature

Initially Li_2NH and $LiNH_2$ were ground together and heated in a 1:1 ratio at various temperatures between 200 and 350 °C for 12 hours, with the aim of producing a single mixed anion phase. The samples were heated under flowing argon and a ramp rate of 2 °C

min^{-1} was used to reach the desired temperature, the samples were then allowed to cool with the furnace back to room temperature. XRD and Raman data were subsequently collected for analysis.

3.5.1.1 XRD Characterisation

Figure 3.27 shows the XRD data of the products of these reactions. XRD was used to help determine whether or not there were two distinct phases and whether or not there was still pure $LiNH_2$ present. The samples heated at 200, 250 and 300 °C all have the characteristic $LiNH_2$ peaks at 17.2 ° and 19.6 °, suggesting there may have been some pure $LiNH_2$ still contained within the samples.

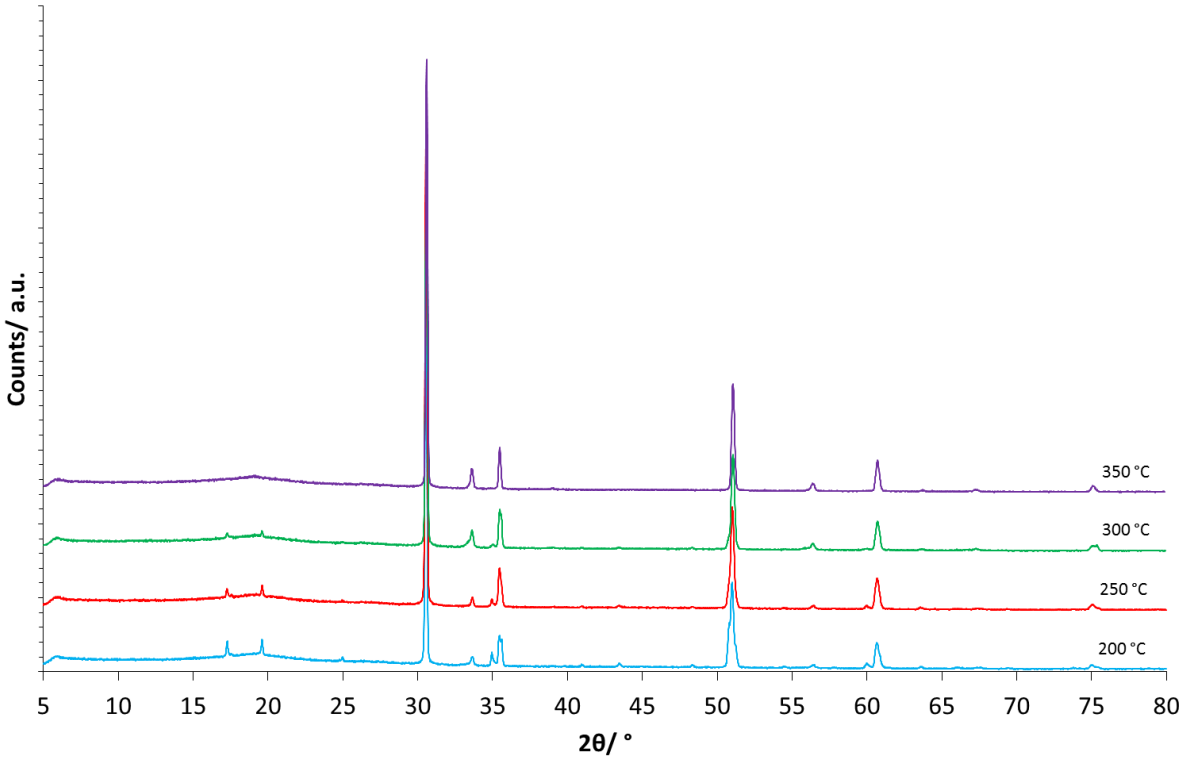

Figure 3.27 – Powder XRD data from the products of the reaction of Li_2NH + $LiNH_2$ at various temperatures for 12 hours

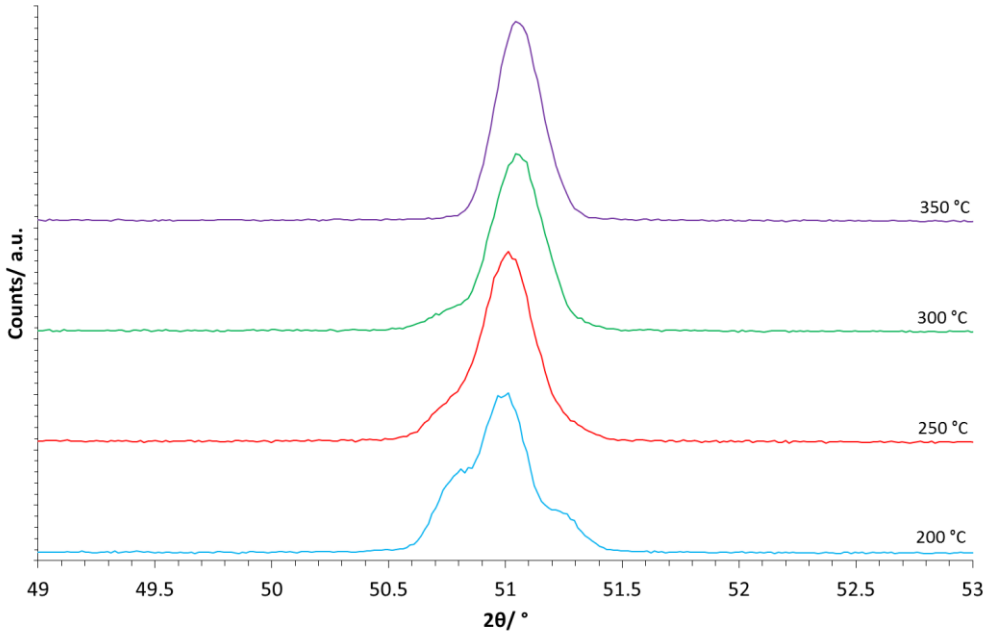

Figure 3.28 – High angle powder XRD data from the products of the reaction of Li_2NH + $LiNH_2$ at various temperatures for 12 hours

One of the other key observations is the shape of the peak at *ca* 51 ° (Figure 3.28); any asymmetry in this peak would suggest two different peaks were overlapping and consequently two different phases were present. From these XRD data 350 °C seemed to be the most suitable temperature to produce a single phase, and Raman was used to support this finding.

3.5.1.2 Raman Characterisation

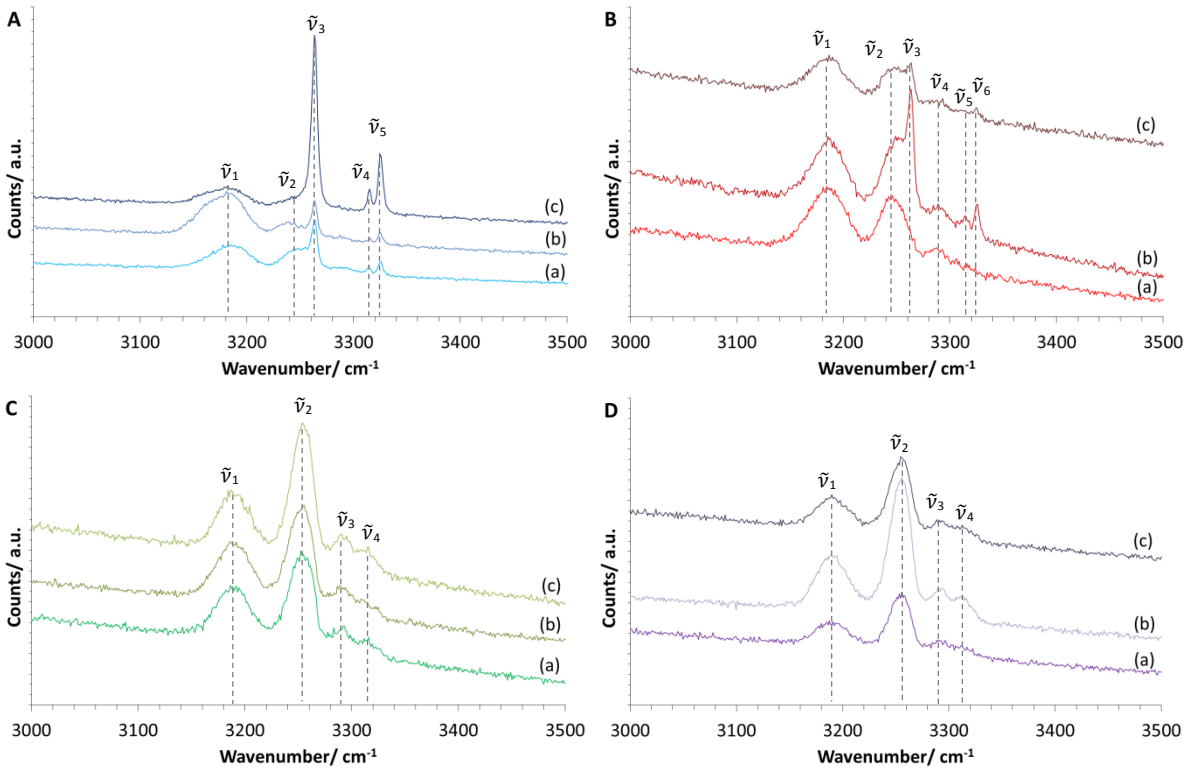

Figure 3.29 – Raman data from the products of the reaction of Li_2NH + $LiNH_2$ at various temperatures for 12 hours (A) Reaction at 200 °C (B) Reaction at 250 °C (C) Reaction at 300 °C (D) Reaction at 350 °C. (a), (b) and (c) correspond to different scans of the same sample

Table 3.10 – Raman stretching modes and assignment of the products of the reaction of Li_2NH + $LiNH_2$ at various temperatures for 12 hours

Synthesis Temperature / °C	Peak	$\tilde{\nu}$/ cm^{-1}	Relative Intensity			Assignment
			Sample			
			a	b	c	
200	$\tilde{\nu}_1$	3182	5758	8456	6510	$\tilde{\nu}_s(NH^{2-})$
	$\tilde{\nu}_2$	3241	5257	5934	5654	$\tilde{\nu}_s(NH_2^-)$ non-stoichiometric
	$\tilde{\nu}_3$	3263	7837	7880	18725	$\tilde{\nu}_s(NH_2^-)$
	$\tilde{\nu}_4$	3315	4000	4813	–	$\tilde{\nu}_{as}(NH_2^-)$
	$\tilde{\nu}_5$	3325	4452	5127	8867	$\tilde{\nu}_{as}(NH_2^-)$
250	$\tilde{\nu}_1$	3186	8985	12365	8143	$\tilde{\nu}_s(NH^{2-})$
	$\tilde{\nu}_2$	3244	8531	12075	7586	$\tilde{\nu}_s(NH_2^-)$ non-stoichiometric
	$\tilde{\nu}_3$	3262	7394	14139	7738	$\tilde{\nu}_s(NH_2^-)$
	$\tilde{\nu}_4$	3289	6619	9862	6232	$\tilde{\nu}_s(NH_2^-)$ non-stoichiometric
	$\tilde{\nu}_5$	3315	–	9380	–	$\tilde{\nu}_{as}(NH_2^-)$
	$\tilde{\nu}_6$	3325	–	9867	5991	$\tilde{\nu}_{as}(NH_2^-)$
300	$\tilde{\nu}_1$	3189	8595	8256	10233	$\tilde{\nu}_s(NH^{2-})$
	$\tilde{\nu}_2$	3254	9839	9638	12963	$\tilde{\nu}_s(NH_2^-)$ non-stoichiometric
	$\tilde{\nu}_3$	3292	7055	6548	8438	$\tilde{\nu}_s(NH_2^-)$ non-stoichiometric
	$\tilde{\nu}_4$	3316	6630	5849	8133	$\tilde{\nu}_s(NH_2^-)$ non-stoichiometric
350	$\tilde{\nu}_1$	3190	5127	6854	6222	$\tilde{\nu}_s(NH^{2-})$
	$\tilde{\nu}_2$	3256	6403	9906	7680	$\tilde{\nu}_s(NH_2^-)$ non-stoichiometric
	$\tilde{\nu}_3$	3290	4479	5611	5131	$\tilde{\nu}_s(NH_2^-)$ non-stoichiometric
	$\tilde{\nu}_4$	3313	4309	5218	5028	$\tilde{\nu}_s(NH_2^-)$ non-stoichiometric

Raman data collected on each of the 1:1 ratio samples are displayed in Figure 3.29 (detailed in Table 3.10). The aim of this analysis was to get an indication of the ratio of imide to amide anions in each sample and also, by collecting data from different areas of the

samples, to determine whether or not the samples were homogeneous. Samples heated at both 200 and 250 °C contain sharp peaks characteristic of pure $LiNH_2$. In addition the samples were not homogeneous, with the peaks present varying depending on the area of the sample being observed; thus they were not deemed suitable temperatures to produce a single phase. On the other hand, at both 300 and 350 °C the samples appear to be homogeneous, with all three areas of the sample producing comparable spectra. Consequently, due to these results the Li_2NH to $LiNH_2$ ratio was varied and heated at both 300 and 350 °C to compare the results.

These data sets clearly demonstrate the level of disorder in the newly formed phases compared with the *I*-4 amide structure. The amide anions in the pure *I*-4 phase are in distinct ordered environments and therefore a sharp peak is observed due to the minimal amount of variation in the wavenumber. The peak *ca* 3200 cm^{-1} is considered to be due to imide anions as discussed earlier in this chapter (§3.3.2). The peaks at higher wavenumber are therefore due to amide anions within either the *Fm*-3*m* or *I*-4 structure. The peaks corresponding to amide anions in the cubic *Fm*-3*m* structure are significantly broader than amide anions in the *I*-4 structure. This illustrates how different the level of disorder is in the *Fm*-3*m* structure compared with the *I*-4 structure.

3.5.2 Varying the Ratio

Various ratios of Li_2NH and $LiNH_2$ were ground together and heated at 300 °C and 350 °C under argon. The temperature was ramped at a rate of 2 °C min^{-1} and then held for 12 hours at the target temperature, before being allowed to cool back down to room

temperature with the furnace. Li_2NH to $LiNH_2$ ratios were varied using the equation below, where x = 0, 0.25, 0.33, 0.42, 0.5, 0.58, 0.66, 0.75 or 1.

$$x\mathrm{Li_2NH} + (1-x)\mathrm{LiNH_2} \rightarrow \mathrm{Li_{(1+x)}(NH_2)_{(1-x)}(NH)_x} \qquad (3.4)$$

3.5.2.1 Synthesis at 300 °C

The reaction at 300 °C was studied first. It is clear from the XRD data (Figure 3.30) that there was still $LiNH_2$ present, as again the characteristic low angle peaks were observed (17 and 19.5 °). Therefore although Raman data suggested there may be a complete reaction happening at 300 °C there still appeared to be two different phases.

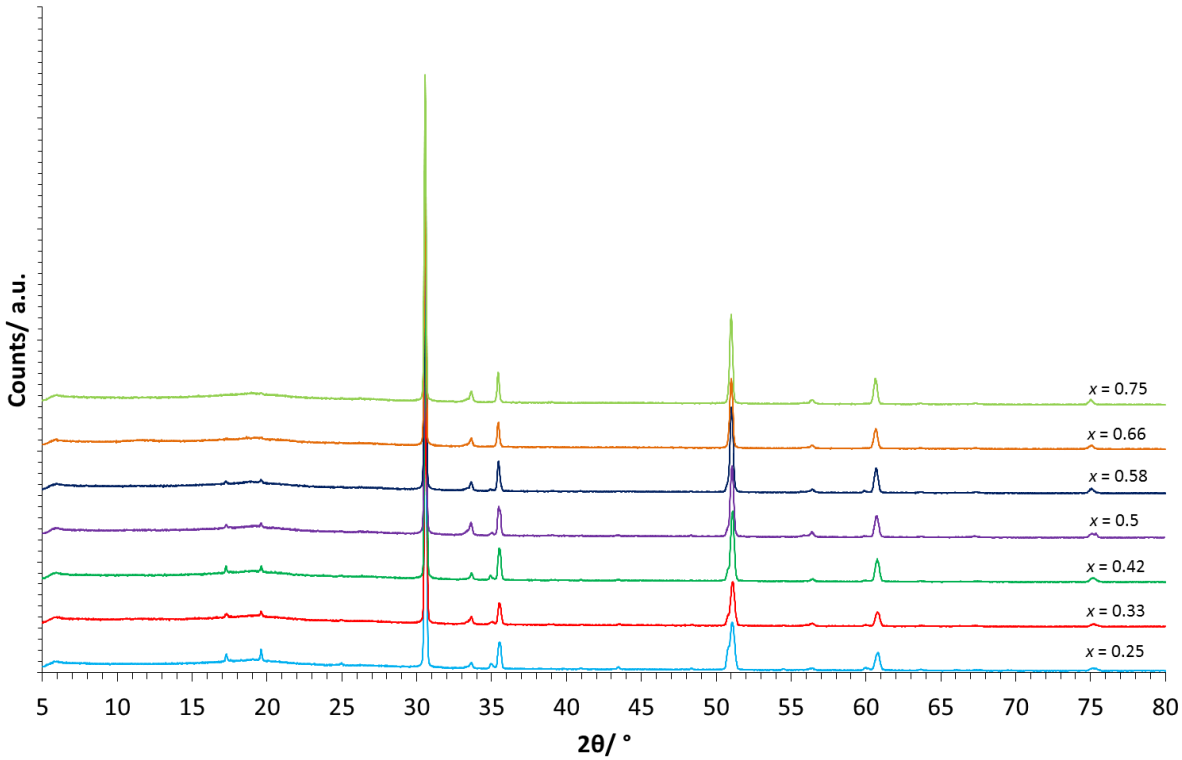

Figure 3.30 – Powder XRD data from the products of the reaction of $x\mathrm{Li_2NH} + (1-x)\mathrm{LiNH_2}$ at various values of x heated at 300 °C for 12 hours

Figure 3.31 highlights the imide peaks at higher angle, showing that there is clearly asymmetry in the peak at *ca* 52 °. This asymmetry confirms the presence of multiple phases and is in accordance with the presence of amide ordering peaks, which also indicate the presence of pure $LiNH_2$. Only for the reactions where x = 0.66 and 0.75 were the asymmetry and the characteristic tetragonal amide peaks (17 and 19.5 °) not visible, suggesting that only with a high imide content could a single phase be formed. However, it is important to note that in a Li_2NH-rich reaction, although $LiNH_2$ may have been present the low intensity amide peaks at 17 and 19.5 °may not have been detectable in the data. Consequently, the data collected for the reactions performed at 300 °C indicated that this was not a suitable temperature for the formation of a single amide-imide phase.

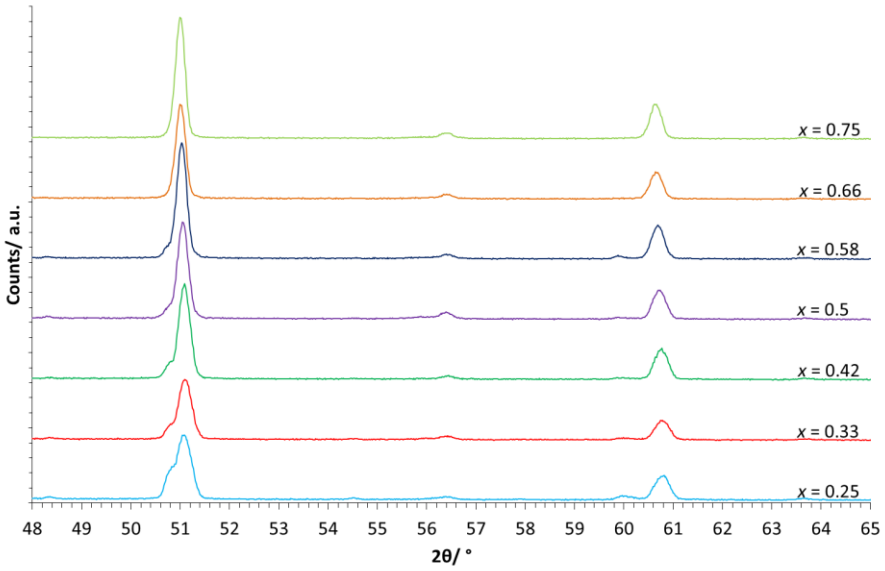

Figure 3.31 – High angle powder XRD data from the products of the reaction of $x$$Li_2NH$ + (1 – x)$LiNH_2$ at various values of x heated at 300 °C for 12 hours

3.5.2.2 Synthesis at 350 °C

After unsuccessful synthesis of a single phase from heating at 300 °C, the reactions were repeated at a higher temperature of 350 °C and the final products compared. At the higher synthesis temperature the asymmetry in the peaks is no longer visible (Figure 3.32 and Figure 3.33), suggesting the formation of a single phase for some values of *x*.

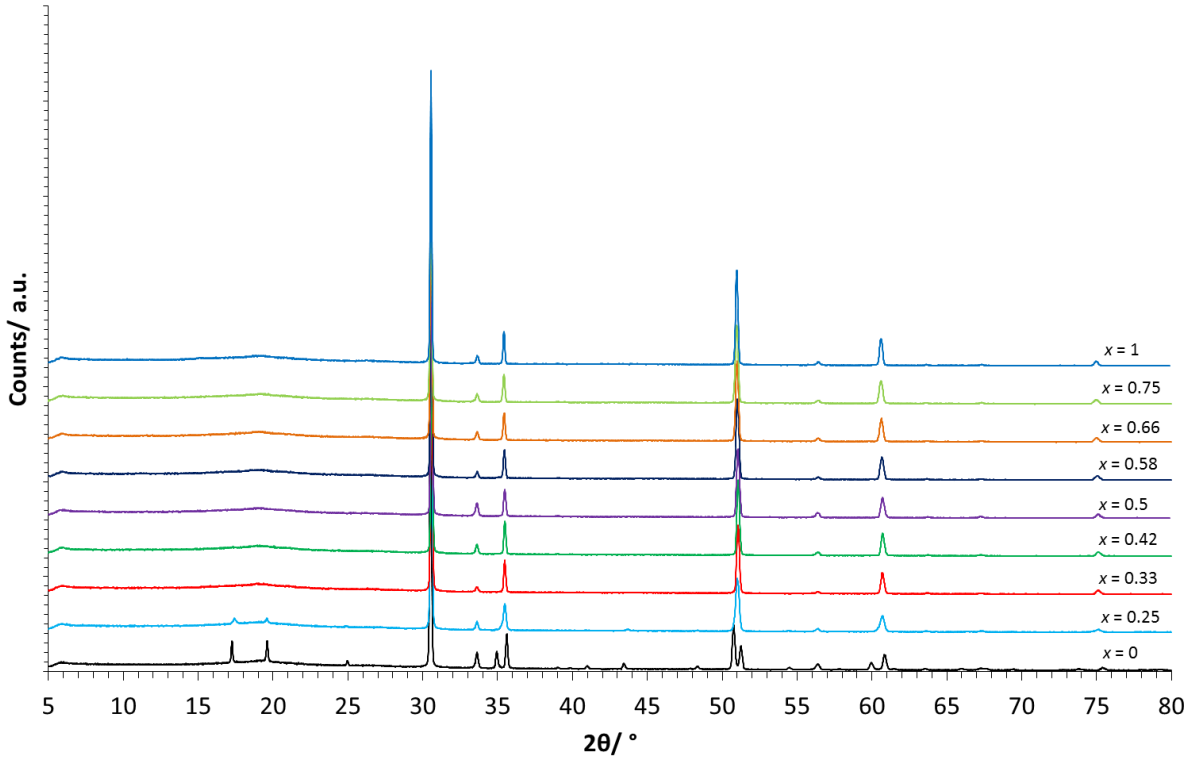

Figure 3.32 – Powder XRD data from the products of the reaction of xLi$_2$NH + (1 – x)LiNH$_2$ at various values of x heated at 350 °C for 12 hours

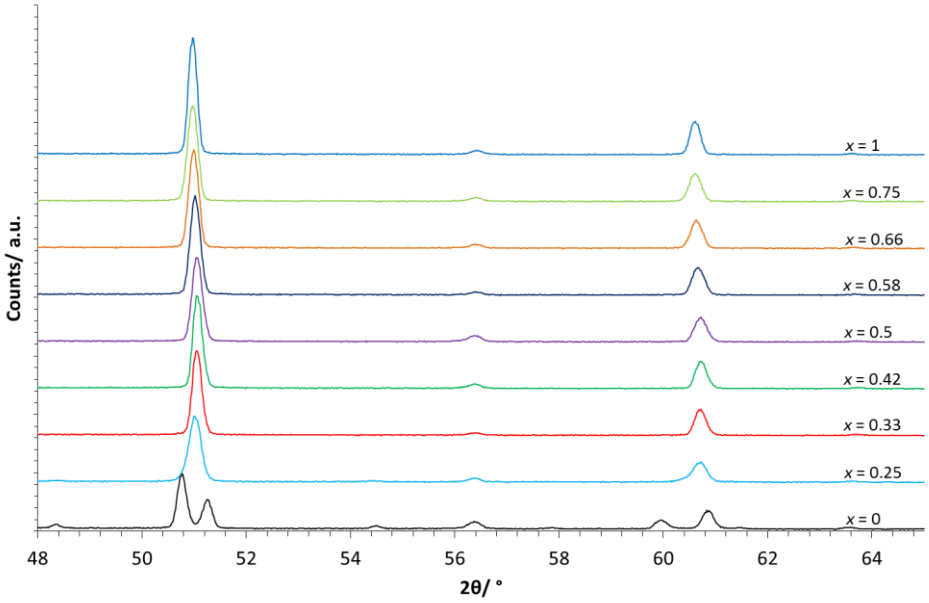

Figure 3.33 – High angle powder XRD data from the products of the reaction of *x*Li_2NH + (1 – *x*)$LiNH_2$ at various values of *x* heated at 350 °C for 12 hours

The characteristic $LiNH_2$ peaks (17 and 19.5 °) were visible in the x = 0.25 and x = 0.33 patterns, indicating that $LiNH_2$ was present in these samples. Where x > 0.33 these peaks were no longer visible and therefore the samples appeared to be single phase. These observations suggest that although a single phase can be formed at 350 °C this is only the case in more imide-rich reactions. With the successful synthesis of single phase products, Rietveld refinements were performed to determine the lattice parameters of the amide-imide phase at each of the different reactant ratios. The cubic Li_2NH structure was refined against the data and the lattice parameter, a is reported in Figure 3.34. The general trend is an increase in a with increasing Li_2NH in the starting mixture. As mentioned previously, the XRD data of the first two ratios, x = 0.25 and 0.33, both contain amide peaks. This could explain the intial dip in the lattice parameter as the cubic structure was refined alongside the tetragonal amide structure in each of these refinements. Alternatively it may be that a

compositional limit exists, and despite an increase in the amount of $LiNH_2$ in the starting mixture, relative to Li_2NH, no more NH_2^- anions can be accommodated within the cubic structure. The products of the reactions where x = 0.33, 0.42 and 0.5 had similar lattice parameters, therefore it is possible that x = 0.5 is close to the compositional limit under these synthesis conditions. Consequently, where x < 0.5 more than one phase may be present as excess of $LiNH_2$ exists alongside the mixed anion cubic phase.

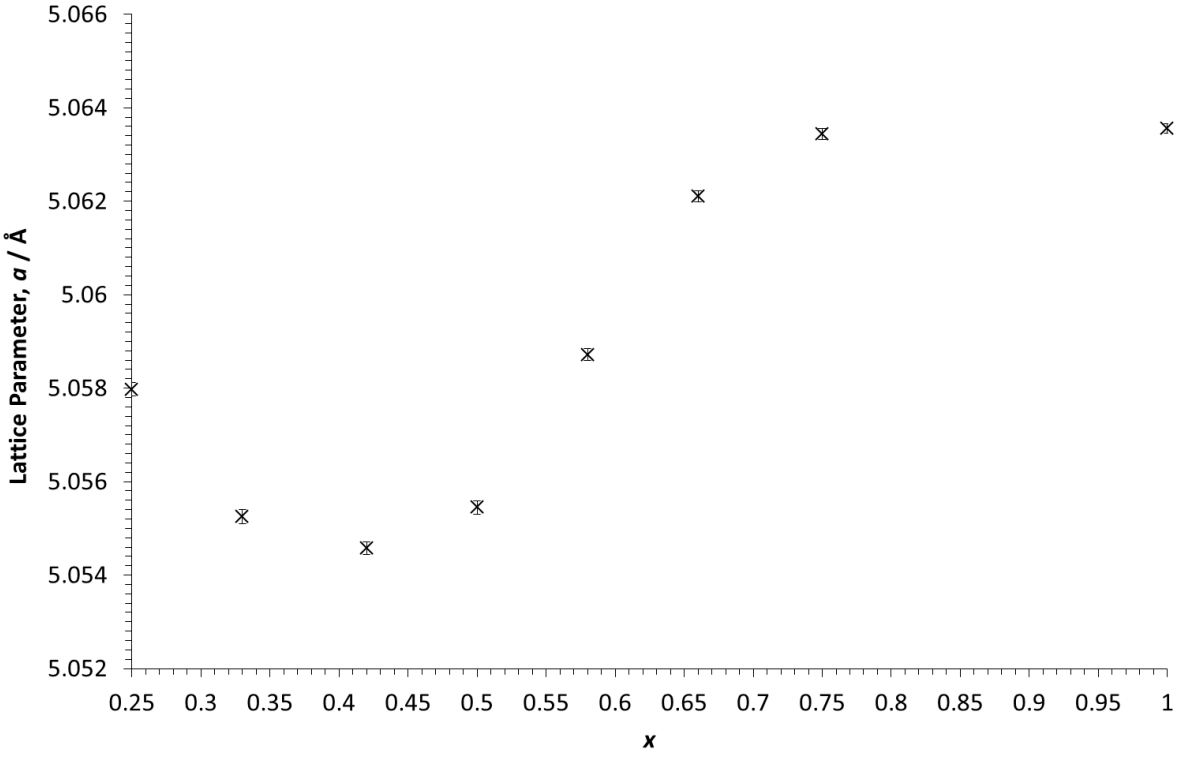

Figure 3.34 – Lattice parameters determined through Rietveld refinement for different values of x for the reaction xLi$_2$NH + (1 – x)LiNH$_2$

The upward trend observed suggests a greater concentration of imide anions results in a larger unit cell. This is contradictory to much of the earlier work in this chapter which suggests a smaller unit cell means a reduced number of amide anions and a structure closer to pure Li_2NH. Interestingly, Makepeace *et al*. have seen similarly contradicting trends when

changing their synthesis method from the reaction of $LiNH_2$ and LiH to the reaction of Li_3N and $LiNH_2$.[77,83] They claim that different preparation methods affect the microstructure of these materials, thus, the reported lattice parameters are different due to potentially different defect structures.[83]

Raman data were also collected to give an indication of the imide to amide anion ratio. Multiple data sets were collected for each sample and all had the same relative intensities, thus confirming the samples to be homogeneous. Figure 3.35 shows Raman data for each of the different ratios in which there is a clear trend of the imide anion peak (peak below 3200 cm^{-1}) increasing with *x* (details in Table 3.11). Simultaneously the peak *ca* 3250 cm^{-1} decreased with *x*. This peak is likely to be due to an amide N–H stretch within the cubic structure and thus its reduction agrees with a decreasing number of amide anions within the cubic structure. For $x = 0.25$ there still appeared to be peaks which are notably sharper than the other samples. The sharp peaks as shown in $x = 0$ (pure $LiNH_2$) are characteristic $LiNH_2$ peaks and correspond to stretching of the NH_2^- anion. Therefore their presence in the $x = 0.25$ sample could suggest some pure amide was still present in the sample, which would agree with the presence of $LiNH_2$ peaks in the XRD (Figure 3.32).

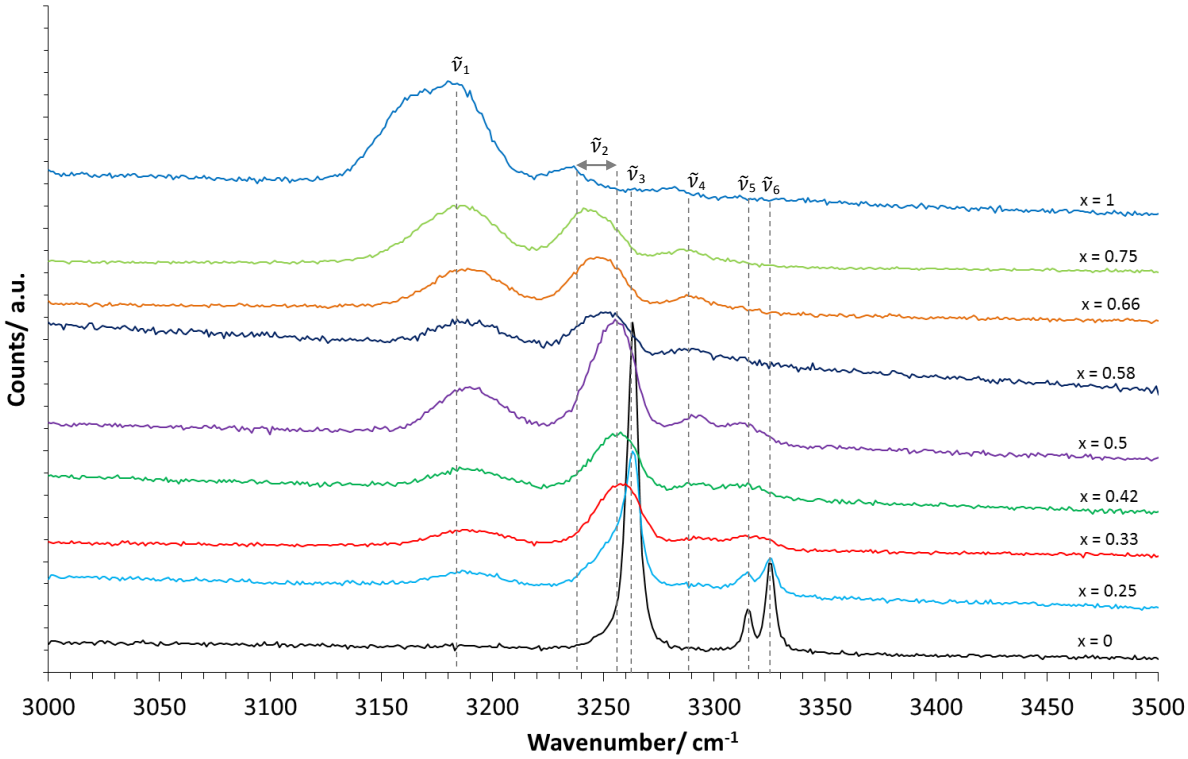

Figure 3.35 – Raman data of the products of the reaction of xLi$_2$NH + (1 – x)LiNH$_2$ at various values of x heated at 350 °C for 12 hours

Table 3.11 – Raman stretches and assignment of the products of the reaction of xLi$_2$NH + (1 – x)LiNH$_2$ at various values of x heated at 350 °C for 12 hours

x	Peak	$\tilde{\nu}$/ cm^{-1}	Relative Intensity	Assignment
0	$\tilde{\nu}_3$	3263	17752	$\tilde{\nu}_s(NH_2^-)$
	$\tilde{\nu}_5$	3316	4859	$\tilde{\nu}_{as}(NH_2^-)$
	$\tilde{\nu}_6$	3325	6919	$\tilde{\nu}_{as}(NH_2^-)$
0.25	$\tilde{\nu}_1$	3190	4563	$\tilde{\nu}_s(NH^{2-})$
	$\tilde{\nu}_3$	3263	9962	$\tilde{\nu}_s(NH_2^-)$
	$\tilde{\nu}_5$	3316	4532	$\tilde{\nu}_{as}(NH_2^-)$
	$\tilde{\nu}_6$	3327	5140	$\tilde{\nu}_{as}(NH_2^-)$
0.33	$\tilde{\nu}_1$	3189	2444	$\tilde{\nu}_s(NH^{2-})$
	$\tilde{\nu}_2$	3259	4499	$\tilde{\nu}_s(NH_2^-)$ non-stoichiometric

	$\tilde{\nu}_4$	3294	2064	$\tilde{\nu}_s(NH_2^-)$ non-stoichiometric
	$\tilde{\nu}_5$	3319	2157	$\tilde{\nu}_s(NH_2^-)$ non-stoichiometric
0.42	$\tilde{\nu}_1$	3199	5184	$\tilde{\nu}_s(NH^{2-})$
	$\tilde{\nu}_2$	3258	6817	$\tilde{\nu}_s(NH_2^-)$ non-stoichiometric
	$\tilde{\nu}_4$	3291	4493	$\tilde{\nu}_s(NH_2^-)$ non-stoichiometric
	$\tilde{\nu}_5$	3315	4523	$\tilde{\nu}_s(NH_2^-)$ non-stoichiometric
0.5	$\tilde{\nu}_1$	3190	6854	$\tilde{\nu}_s(NH^{2-})$
	$\tilde{\nu}_2$	3255	9906	$\tilde{\nu}_s(NH_2^-)$ non-stoichiometric
	$\tilde{\nu}_4$	3294	5570	$\tilde{\nu}_s(NH_2^-)$ non-stoichiometric
	$\tilde{\nu}_5$	3312	5262	$\tilde{\nu}_s(NH_2^-)$ non-stoichiometric
0.58	$\tilde{\nu}_1$	3188	8908	$\tilde{\nu}_s(NH^{2-})$
	$\tilde{\nu}_2$	3251	9225	$\tilde{\nu}_s(NH_2^-)$ non-stoichiometric
	$\tilde{\nu}_4$	3286	7600	$\tilde{\nu}_s(NH_2^-)$ non-stoichiometric
0.66	$\tilde{\nu}_1$	3189	4185	$\tilde{\nu}_s(NH^{2-})$
	$\tilde{\nu}_2$	3249	4654	$\tilde{\nu}_s(NH_2^-)$ non-stoichiometric
	$\tilde{\nu}_4$	3292	2941	$\tilde{\nu}_s(NH_2^-)$ non-stoichiometric
0.75	$\tilde{\nu}_1$	3188	4008	$\tilde{\nu}_s(NH^{2-})$
	$\tilde{\nu}_2$	3241	3921	$\tilde{\nu}_s(NH_2^-)$ non-stoichiometric
	$\tilde{\nu}_4$	3287	2043	$\tilde{\nu}_s(NH_2^-)$ non-stoichiometric
1	$\tilde{\nu}_1$	3179	9624	$\tilde{\nu}_s(NH^{2-})$
	$\tilde{\nu}_2$	3234	5727	$\tilde{\nu}_s(NH_2^-)$ non-stoichiometric
	$\tilde{\nu}_4$	3281	4870	$\tilde{\nu}_s(NH_2^-)$ non-stoichiometric

It is interesting to note the relative intensities of the imide and amide peaks. For example in the *x* = 0.5 sample where there was a 1:1 imide to amide ratio the amide anion peak is significantly more intense than the imide anion peak. This discrepancy highlights why it is difficult to remove all trace of amide anions from the Raman spectra, even for close to pure Li_2NH.

This study demonstrates that, although there was some discrepancy for the very amide-rich sample, a single mixed amide-imide phase can be synthesised by heating a mixture of Li_2NH and $LiNH_2$ at 350 °C. The ability to synthesise a mixed anion phase could prove useful in forming more complex mixed anion hydride systems, such as addition of a borohydride anion which is discussed later in this thesis (§4.6).

3.6 Conclusions

This chapter looks at the Li–N–H phase space, in particular the formation of Li_2NH and the possibility of forming mixed anion $Li_{(1+x)}(NH_2)_{(1-x)}(NH)_x$ phases. Studying two different synthetic routes for forming a pure lithium imide phase has enabled a reliable synthesis method to be determined to be used for further work, discussed later in this thesis. Data collected with the aim of forming a pure Li_2NH sample has also enabled a more detailed look into varying the anion content to be carried out. Varying the anion content of the amide-imide structure opens up the possibility of tuning the lithium content of the structures, important for later studies on the conductivity of these materials.

Chapter 4 – nLi$_2$NH + (1 – n)LiBH$_4$: Synthesis of New Phases

4.1 Introduction

Hewett performed some preliminary investigations into the reaction of lithium imide with lithium borohydride.[81] The resulting product consisted of two unknown phases: an orthorhombic phase with proposed space group *Pnma* and cell parameters a = 10.1459(9) Å, b = 11.483(1) Å, c = 7.0302(4) Å and a cubic phase, proposed space group *P*23, where a = 5.609(2) Å. The orthorhombic phase had the same proposed space group as lithium borohydride, but a unit cell volume just under four times the size, 819.056 Å^3 compared with 216.685 Å^3.[81,86] From observations, Hewett suggested that the orthorhombic phase may adopt a similar structure to lithium borohydride, and that the relative sizes of the borohydride and imide anions may account for why the unit cell volumes are not exact multiples of each other.[81] A lithium borohydride formula unit is 54.171 Å^3 whereas a lithium imide formula unit is only 32.714 Å^3. However, the reported cell parameters of lithium borohydride, where a = 7.17858 Å, b = 4.43686 Å and c = 6.80321 Å,[86] are not simple factors of the lithium borohydride-imide orthorhombic phase unit cell. Therefore the relationship between these two structures may be more complex than originally thought. The cubic phase on the other hand seems to have a similar structure to lithium imide. Although it is significantly larger than Li$_2$NH (176.464 Å^3 compared with 130.857 Å^3), the substitution of the larger borohydride ion for imide anion would be expected to result in a larger unit cell.[81]

From the previous study,[81] synthesis carried out using a 1:1 reactant ratio at 125 °C heating for 12 hours seemed to favour the formation of the orthorhombic phase, whereas a

higher temperature of 200 °C and a 1:1 reactant ratio, heating for 12 hours, seemed to favour the formation of the cubic phase.[81] However, neither the cubic nor the orthorhombic phase were prepared pure. Further investigation was needed to look into the phase space in more detail, to study how changes in the synthesis conditions affected the resulting products and to determine whether those changes would result in the formation of additional previously unknown structures.

4.2 Experimental

Various ratios of lithium borohydride (Sigma Aldrich, 90% purity) and lithium imide (synthesised using the optimum reaction conditions determined previously, §3.3.3) were ground together and sealed in a quartz tube, with a Young's tap, in an argon-filled glovebox. The samples were then heated in tube furnaces at various temperatures for up to 12 hours and analysed through powder X-ray diffraction using a Siemens D5000 instrument. This procedure was also repeated for various ratios of lithium borohydride (Sigma Aldrich, 90% purity) and lithium amide-imide (synthesised using the optimum reaction conditions determined previously, §3.5). See §2.1 for more detailed synthetic information.

4.3 Temperature Series – 1:1 Ratio

Initially lithium borohydride and lithium imide were heated together in a 1:1 ratio for 12 hours. The lithium imide used was synthesised at 500 °C, heating lithium amide and lithium hydride together in a 1:1 ratio twice for 12 hours, the conditions determined from work reported in the previous chapter (§3.3.3). The Li$_2$NH + LiBH$_4$ reaction was carried out at temperatures between 100 and 250 °C in 25 °C increments. The powder XRD patterns of the resulting products are plotted in Figure 4.1, with the 21 to 36 ° range shown in Figure 4.2.

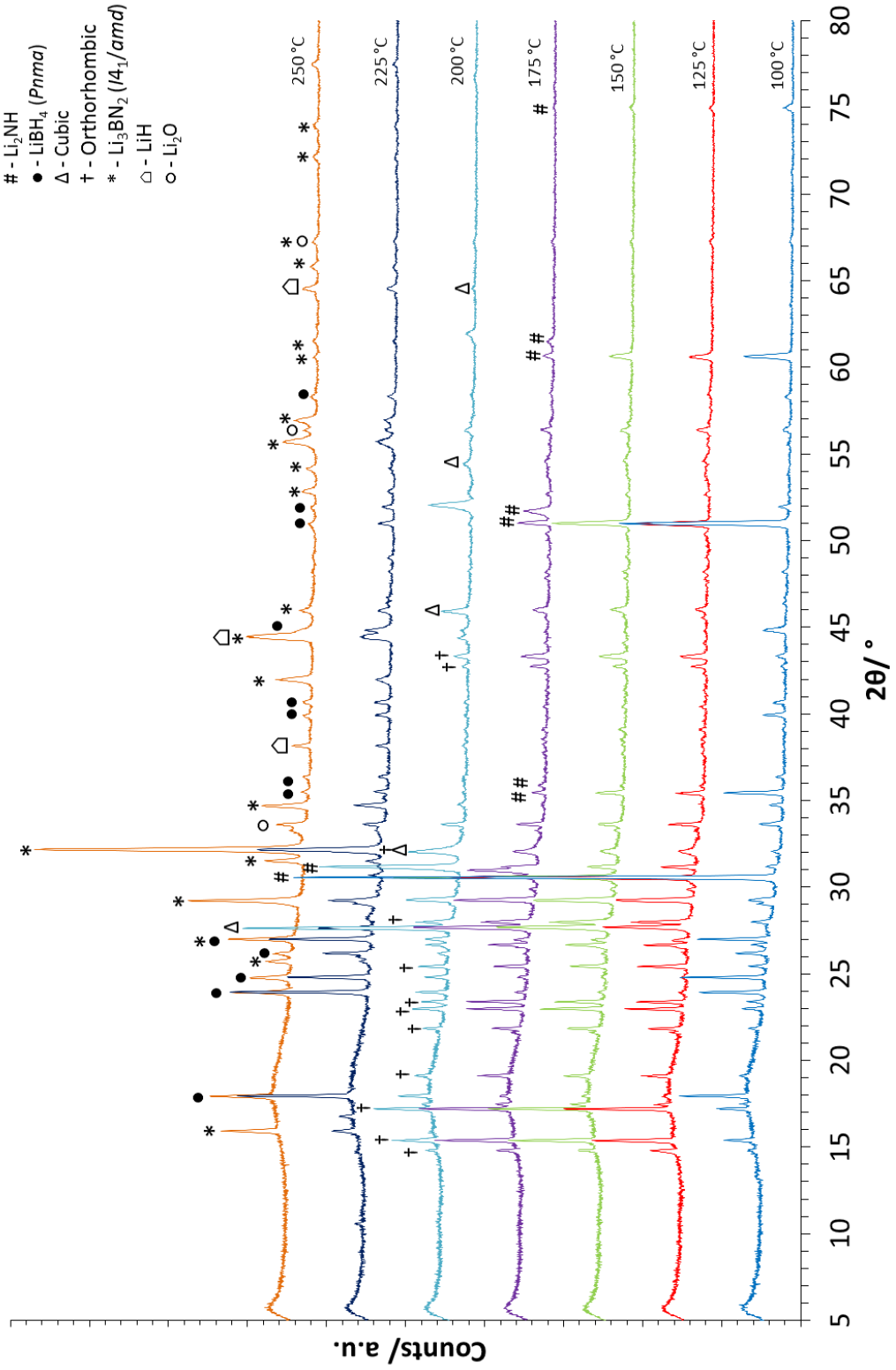

Figure 4.1 – Powder XRD data of the products of the reaction of Li_2NH + $LiBH_4$ at various temperatures for 12 hours in a 1:1 ratio, where # = Li_2NH, ● = $LiBH_4$ (*Pnma*), Δ = cubic phase, † = orthorhombic phase, * = Li_3BN_2 (*I*4$_1$/*amd*), ⌂ = LiH and ○ = Li_2O

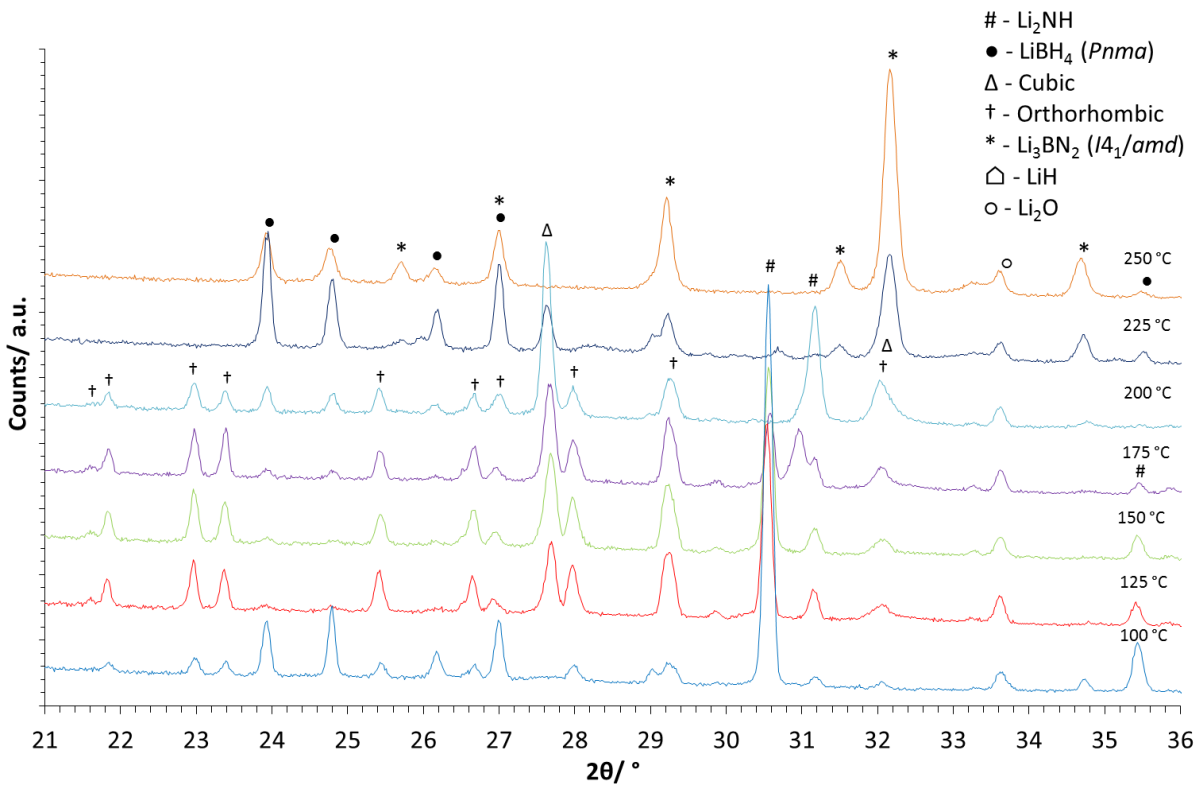

Figure 4.2 – Zoomed in plot of powder XRD data of the products of the reaction of Li$_2$NH + LiBH$_4$ at various temperatures for 12 hours in a 1:1 ratio, where # = Li$_2$NH, ● = LiBH$_4$ (*Pnma*), Δ = cubic phase, † = orthorhombic phase, * = Li$_3$BN$_2$ (*I*4$_1$/*amd*), ⌂ = LiH and ○ = Li$_2$O

The XRD data collected from the initial series showed the formation of both the orthorhombic and cubic phases. The data suggested that the orthorhombic phase was favoured at lower temperatures and that the cubic phase was favoured at higher temperatures. However, one thing to note is that at all temperatures there were still starting materials present. Nevertheless, the observed ratios between the starting materials, in the product mixture, provided valuable information as they could indicate the true anion ratio in each of the two product phases. For example, an excess of Li$_2$NH in the final product mixture suggests a more LiBH$_4$-rich ratio would be favoured, and vice versa.

Rietveld refinements were carried out on the XRD data in order to extract weight percentages of each phase through quantitative phase analysis (QPA); the QPA results are presented in Table 4.1. The phase fractions of the cubic and orthorhombic phases were obtained based on structural models discussed in the following chapter (§5.3 and §5.4) with the formulae Li_3BH_4NH and $Li_5(BH_4)_3NH$, respectively.

Table 4.1 – Weight percentages of the different components of the product mixture of a 1:1 Li_2NH and $LiBH_4$ reaction at various temperatures heated for 12 hours, determined from Rietveld refinement

Synthesis Temp/ °C	Weight Percent						
	Li_2NH	$LiBH_4$ (*Pnma*)	Cubic	Orthorhombic	Li_3BN_2 ($I4_1/amd$)	LiH	Li_2O
100	48.6(4)	32.9(4)	0	16.1(5)	0	0	2.3(1)
125	21.7(3)	2.4(4)	25.5(4)	47.6(5)	0	0	2.8(2)
150	21.8(2)	4.3(4)	24.9(3)	46.6(4)	0	0	2.4(1)
175	19.8(5)	5.2(4)	26.3(4)	46.4(5)	0	0	2.4(1)
200	14.6(1)	11.1(2)	34.0(3)	24.1(3)	11.7(3)	2.0(2)	2.4(1)
225	0	49.0(4)	10.2(3)	0	30.5(3)	6.1(3)	4.2(2)
250	0	29.8(3)	0	0	55.8(3)	9.2(3)	5.1(1)

The weight percentages obtained from QPA were also converted into mole percentages of lithium and are displayed in Figure 4.3. As weight percentage values are dominated by the heavier fractions, converting wt.% values into mol% Li improved the weighting of the lighter phase fractions and gave a clearer picture of the product mixtures.

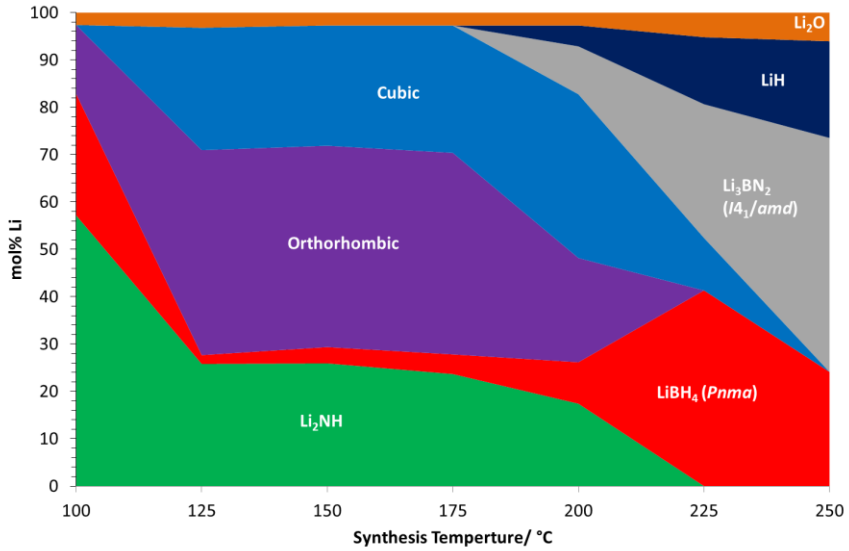

Figure 4.3– Mole percentage lithium in the different components of the product mixture of a 1:1 Li_2NH and $LiBH_4$ reaction at various temperatures heated for 12 hours

The results of the QPA clearly show that the orthorhombic phase forms at temperatures as low as 100 °C, however, at this temperature the product mixture was still dominated by unreacted starting materials. When the synthesis temperature was increased up to 125 °C there was a significant increase in the weight percentage of orthorhombic phase; concurrently there was a significant decrease in the amount of $LiBH_4$. Between 125 and 175 °C there continued to be a large amount of orthorhombic phase and a relatively small amount of $LiBH_4$ present in the final product mixture. This observed behaviour of both the orthorhombic phase and $LiBH_4$ suggested that the orthorhombic phase may be borohydride-rich compared with the 1:1 reaction stoichiometry.

The cubic phase was identified in the product mixture of the reaction performed at 125 °C, and the amount present was fairly consistent up to 200 °C. At 200 °C there was a decrease in the amount of orthorhombic phase, however, this was alongside the formation of some Li_3BN_2 and LiH decomposition products. Increasing the reaction temperature from

200 °C up to 225 °C and then subsequently up to 250 °C resulted in significant decomposition, with a huge increase in the amount of Li_3BN_2 and LiH present. Possible reactions which may be occurring in the system are given in Equations 4.1, 4.2, 4.3 and 4.4.

$$2Li_5(BH_4)_3NH \rightarrow Li_3BN_2 + 5LiBH_4 + 2LiH + 2H_2 \quad (4.1)$$

$$Li_5(BH_4)_3NH \rightarrow Li_3BH_4NH + 2LiBH_4 \quad (4.2)$$

$$2Li_3BH_4NH \rightarrow Li_3BN_2 + LiBH_4 + 2LiH + 2H_2 \quad (4.3)$$

$$2Li_2NH + LiBH_4 \rightarrow Li_3BN_2 + 2LiH + 2H_2 \quad (4.4)$$

4.4 The Orthorhombic Phase

In order to fully investigate the structure and properties of the orthorhombic phase a range of synthetic strategies were investigated to determine the most favourable conditions for its formation, and to determine the effect different reaction conditions had on the final product mixture.

4.4.1 Synthesis at 100 °C

4.4.1.1 Reannealing

The initial Li_2NH and $LiBH_4$ reactions (§4.3) suggested that orthorhombic phase formation was favoured at lower temperatures; at 100 °C it was formed without the cubic phase present alongside it (Figure 4.1). However, one of the main issues with this low synthesis temperature was the large amounts of starting materials remaining, which is perhaps unsurprising due to relatively slow reaction kinetics at lower temperatures. Reannealing was employed in an attempt to reduce the amount of starting materials present and to maximise the amount of orthorhombic phase formed. Figure 4.4 shows the XRD data

obtained after one heating cycle and after a second; the sample was re-ground thoroughly between each heating cycle in order to improve the atomic mixture between phases present.

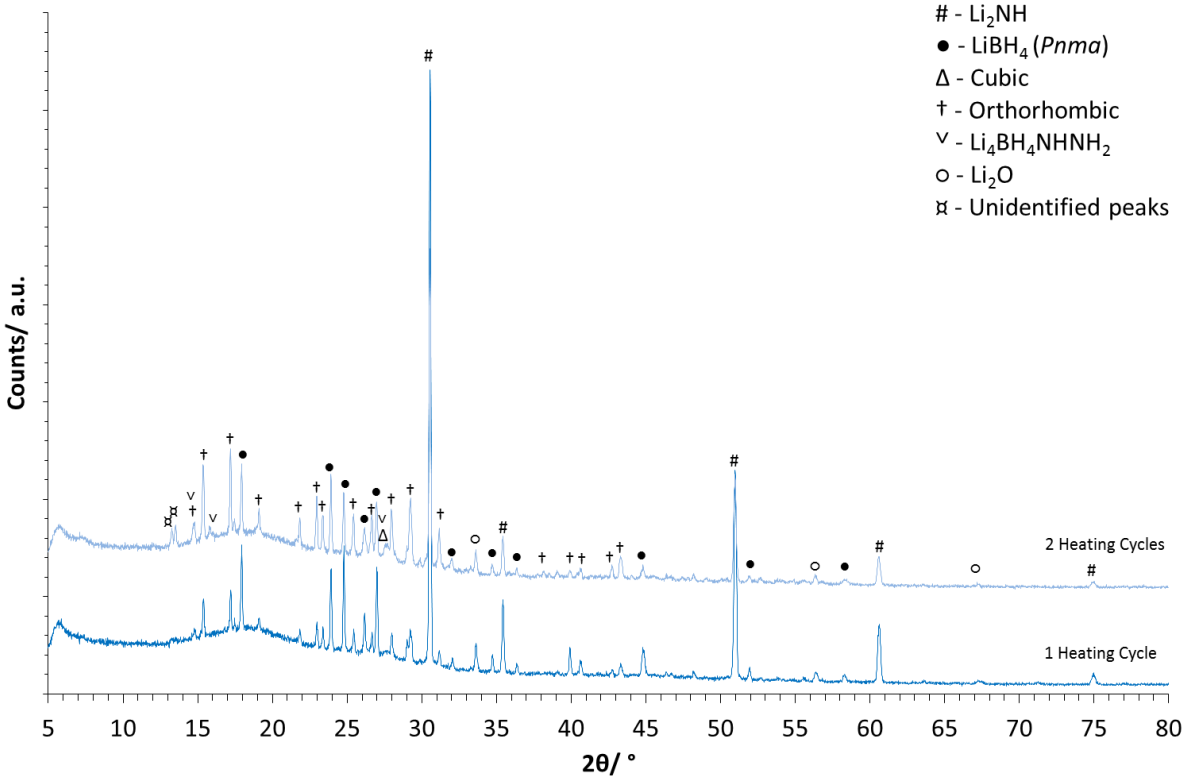

Figure 4.4 – Powder XRD data of the products of the reaction of Li$_2$NH + LiBH$_4$ after regrinding and reheating at 100 °C for 12 hours, where # = Li$_2$NH, ● = LiBH$_4$ (*Pnma*), Δ = cubic phase, † = orthorhombic phase, ᵛ = Li$_4$BH$_4$NHNH$_2$, ○ = Li$_2$O and ¤ = unidentified peaks

Rietveld refinements with QPA were carried out to calculate the weight percentages of the phases present; the results are given in Table 4.2. From these data it is clear there was a notable increase in the amount of orthorhombic phase present after a second heating, and there was also a concurrent decrease in the amount of both Li$_2$NH and LiBH$_4$.

Table 4.2 – Weight percentages of the different components of the product mixture of a 1:1 Li_2NH + $LiBH_4$ reaction determined from Rietveld refinement after one and two heating cycles at 100 °C

Heating Cycles/ hrs	Weight Percent					
	Li_2NH	$LiBH_4$ (*Pnma*)	Cubic	Orthorhombic	$Li_4BH_4NHNH_2$	Li_2O
1 × 12	48.6(4)	32.9(4)	0	16.1(5)	0	2.3(1)
2 × 12	25.6(3)	25.7(4)	5.3(7)	33.8(5)	7.8(5)	1.9(1)

Although after one 12 hour heating there appeared to be no cubic phase present, after regrinding and reannealing there was a small broad peak at *ca* 27.5 °. This is where the most intense reflection of the cubic phase is located and therefore suggested some of the cubic phase may have formed. As it is the most intense peak, its presence resulted in a notable increase in the amount of cubic phase determined from Rietveld refinement. However, as no other cubic reflections were observable, this was only a possibility; it may have been due to the formation of another unidentified phase or a highly disordered structure relating to the cubic phase.

There was also the formation of another phase upon reannealing, demonstrated by the appearance of new peaks at *ca* 14.5 ° and 16 °. Again due to the presence of only two small peaks it could not be unambiguously identified; however, they are considered to be due to a new hexagonal lithium amide-borohydride-imide phase, $Li_4BH_4NHNH_2$ (discussed in more detail in §4.6 and §5.5). $Li_4BH_4NHNH_2$ is thought to be a thermodynamically stable phase and thus appeared as an impurity phase in some of the Li_2NH + $LiBH_4$ reactions. Its appearance in this instance was possibly as a result of a small amount of residual NH_2 being present in the lithium imide starting material. The presence of this phase is also important to

consider alongside the cubic phase. The (1 0 −4) reflection of the $Li_4BH_4NHNH_2$ phase overlaps with the main cubic reflection therefore adding an additional complication to determining the presence of the cubic phase.

The appearance of two additional unidentified peaks at *ca* 14 ° (*d* = 6.67 Å and *d* = 6.54 Å) confirmed there was also another unknown phase present; however, due to the high number of overlapping reflections for the various phases, no other peaks could be unambiguously attributed to the same unknown phase.

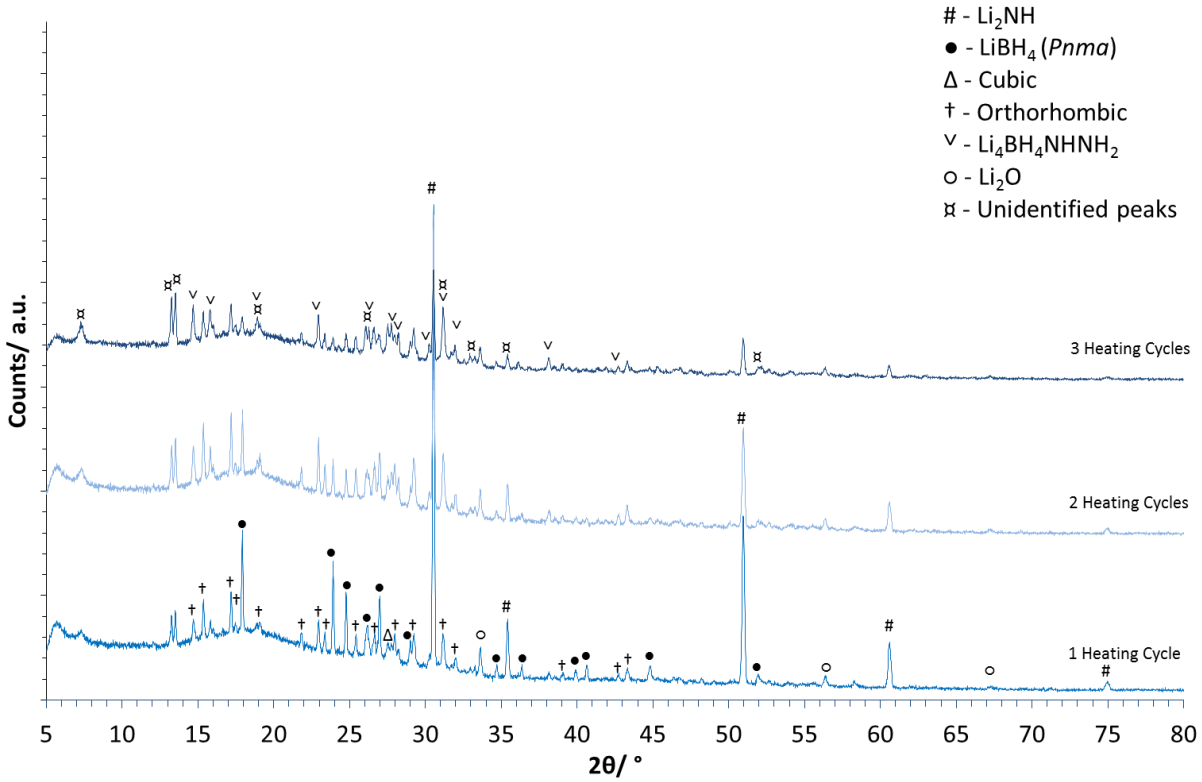

Figure 4.5 – Powder XRD data of the products of the reaction of Li_2NH + $LiBH_4$ after regrinding and reheating at 100 °C for 12 hours, where # = Li_2NH, ● = $LiBH_4$ (*Pnma*), Δ = cubic phase, † = orthorhombic phase, ᵛ = $Li_4BH_4NHNH_2$, ○ = Li_2O and ¤ = unidentified peaks

A second sample of Li_2NH + $LiBH_4$ was treated with three lots of grinding and 12 hour heating cycles. Although the first attempt seemed promising (Figure 4.4), there were

significantly more unidentified peaks associated with the second sample (Figure 4.5). This time, the two low angle peaks from the first heating cycle were present (13.3 and 13.6 °), along with multiple other unidentified peaks. In addition to the unidentified peaks there was a significant increase in the amount of the hexagonal $Li_4BH_4NHNH_2$ phase, however, the amount present was unlikely to be due to simply residual NH_2 contained within the lithium imide lattice. The amount present suggested a more complex reaction process may have been taking place, possibly one in which some of the Li_2NH was reduced to $LiNH_2$ by $LiBH_4$, a phenomenon suggested by Hewett when performing similar reactions.[81]

This low temperature reaction was repeated multiple times using the same conditions and the intensity of both the hexagonal $Li_4BH_4NHNH_2$ phase (§4.6, §5.5) and the low angle unidentified peaks varied between the different samples. Lithium hydroxide, lithium hydride and lithium boron nitride have all been eliminated as possible causes of the unidentified peaks. The inconsistency in the observation of them could support the hypothesis of a slow oxidation of products as the seal of the different reaction vessels may vary slightly and subsequently cause a lesser or greater level of oxidation. An alternative explanation could be that the low angle peaks correspond to a new borohydride-imide phase which is yet to be identified, potentially related to either the cubic or orthorhombic phase through some additional ordering. These results and the repeated appearance of unidentified low angle peaks and the hexagonal $Li_4BH_4NHNH_2$ phase suggests that regrinding and reheating for 12 hours at 100 °C are not the most suitable conditions for isolating the orthorhombic phase.

4.4.1.2 Sealed Tube

In order to investigate longer synthesis times and the possibility of the unknown peaks appearing as a result of slow oxidation, Li_2NH and $LiBH_4$ were ground together and sealed in a quartz tube under vacuum. The sample was heated at 100 °C for 90 hours and the XRD data collected from the products are shown in Figure 4.6. These conditions eliminated the possibility of a small leak in the gas flow which may have resulted in oxidation over longer reaction times. The unidentified peaks at *ca* 13 ° were still observed in the sealed tube reaction, although they were lower in intensity than for the reannealed samples. This suggested that these peaks were due to the presence of another unidentified phase, instead of slow oxidation of the sample.

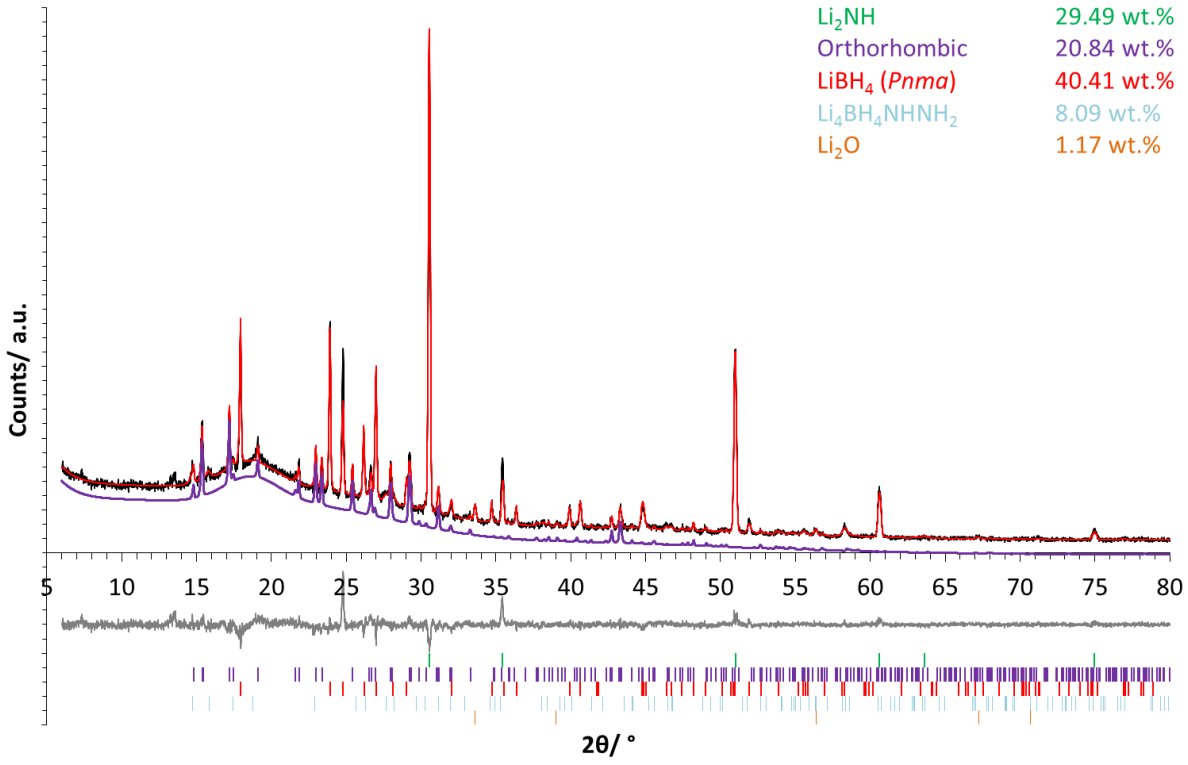

Figure 4.6 – Rietveld refinement plot of Li_2NH + $LiBH_4$ heated at 100 °C for 90 hours in a sealed tube where black = observed data, red = calculated data and grey = difference, highlighting the

orthorhombic phase in purple. Green tick marks = Li_2NH, purple tick marks = orthorhombic phase, light blue tick marks = $Li_4BH_4NHNH_2$, red tick marks = $LiBH_4$ (*Pnma*) and orange tick marks = Li_2O

The longer heating times for this sealed tube reaction (90 hours) did not increase the yield of the orthorhombic phase; QPA gave a weight percent of 20.8(3)% which is between the values obtained for 1 and 2 heating cycles for 12 hours under argon. Consequently these conditions do not appear to be to optimum for the formation of the orthorhombic phase.

4.4.2 Synthesis at 125 °C

At 125 °C both the cubic and orthorhombic phases were formed. Initial analysis of the XRD data showed a large amount of the orthorhombic phase was formed with a smaller proportion of cubic phase. Figure 4.7 and Figure 4.8 highlight the peaks corresponding to the orthorhombic and cubic phases, respectively. Rietveld refinement with QPA using the reactant phases showed that there was a large amount of lithium imide still present in the reaction product and that very little lithium borohydride remained. As previously mentioned (§4.3), the ratio of starting materials remaining in the product mixture suggested that the orthorhombic phase may be more borohydride rich than the 1:1 reaction stoichiometry.

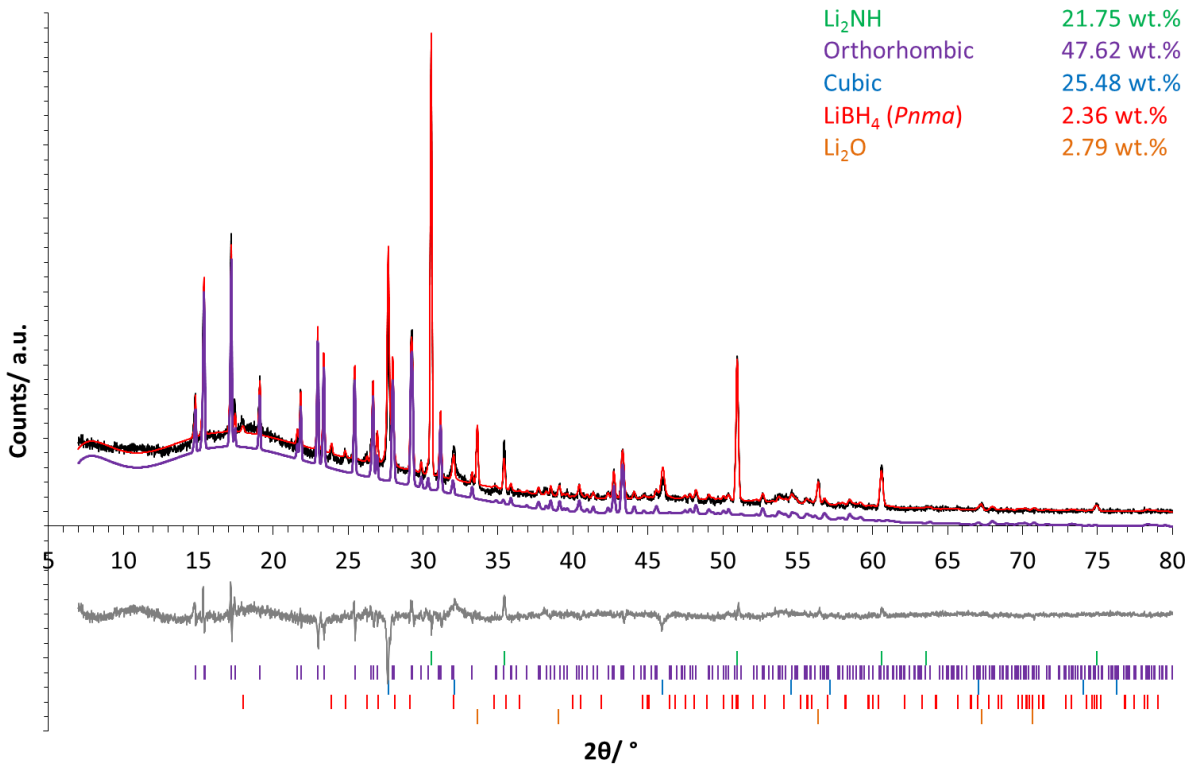

Figure 4.7 – Rietveld refinement plot of the products of Li_2NH + $LiBH_4$ heated at 125 °C for 12 hours, where black = observed data, red = calculated data and grey = difference, highlighting the orthorhombic phase in purple. Green tick marks = Li_2NH, purple tick marks = orthorhombic phase, blue tick marks = cubic phase, red tick marks = $LiBH_4$ (*Pnma*) and orange tick marks = Li_2O

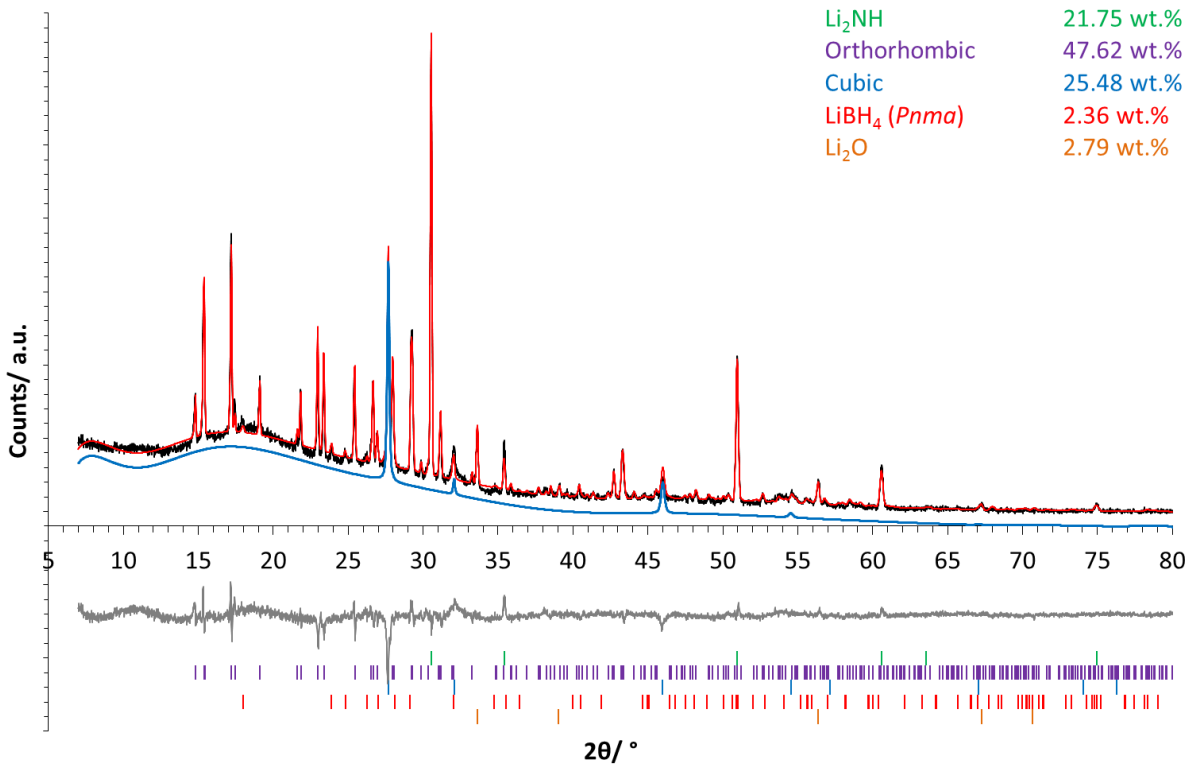

Figure 4.8 – Rietveld refinement plot of the products of Li_2NH + $LiBH_4$ heated at 125 °C for 12 hours, where black = observed data, red = calculated data and grey = difference, highlighting the cubic phase in blue. Green tick marks = Li_2NH, purple tick marks = orthorhombic phase, blue tick marks = cubic phase, red tick marks = $LiBH_4$ (*Pnma*) and orange tick marks = Li_2O

4.4.2.1 Varying the Reactant Ratio

The lithium imide to lithium borohydride ratio was then investigated to determine whether varying this could result in a greater amount of orthorhombic phase. Lithium borohydride rich reaction stoichiometries of 4:5, 2:3, 4:7, 1:2, 2:5, 1:3 and 1:4 (n = 0.44, 0.4, 0.36, 0.33, 0.29, 0.25 and 0.2, respectively) were used; samples were heated at 125 °C for 12 hours. Figure 4.9 shows the XRD data collected on the products of those reactions, where n corresponds to the reactant ratio using the equation nLi$_2$NH + (1 – n)LiBH$_4$. Figure 4.10 shows the range 14 to 34 ° for the same data.

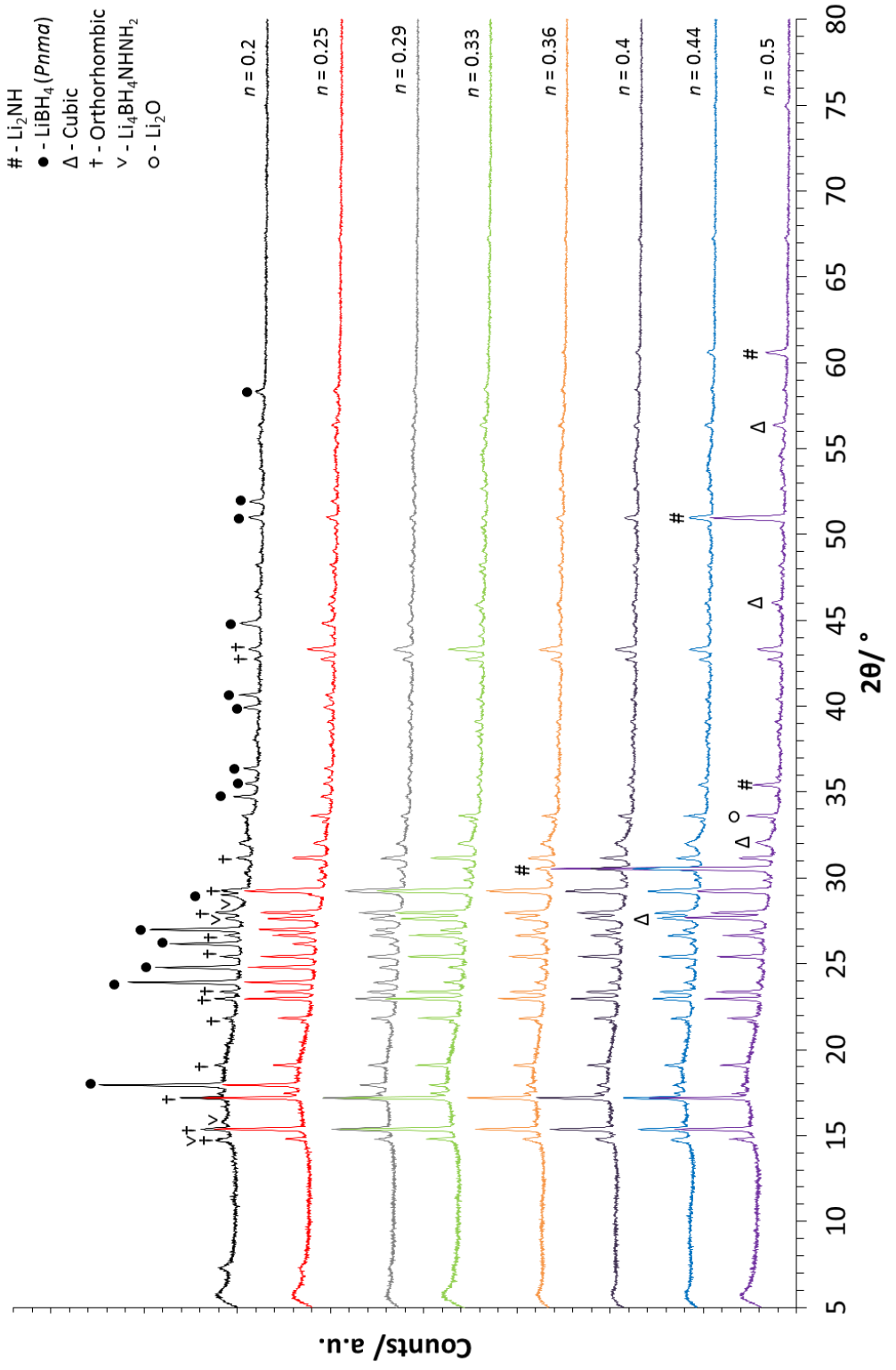

Figure 4.9 – Powder XRD data of the products of the reaction of Li$_2$NH + LiBH$_4$ at 125 °C for 12 hours in various LiBH$_4$-rich reaction conditions, where # = Li$_2$NH, ● = LiBH$_4$ (*Pnma*), Δ = cubic phase, † = orthorhombic phase, ᵛ = Li$_4$BH$_4$NHNH$_2$ and ○ = Li$_2$O

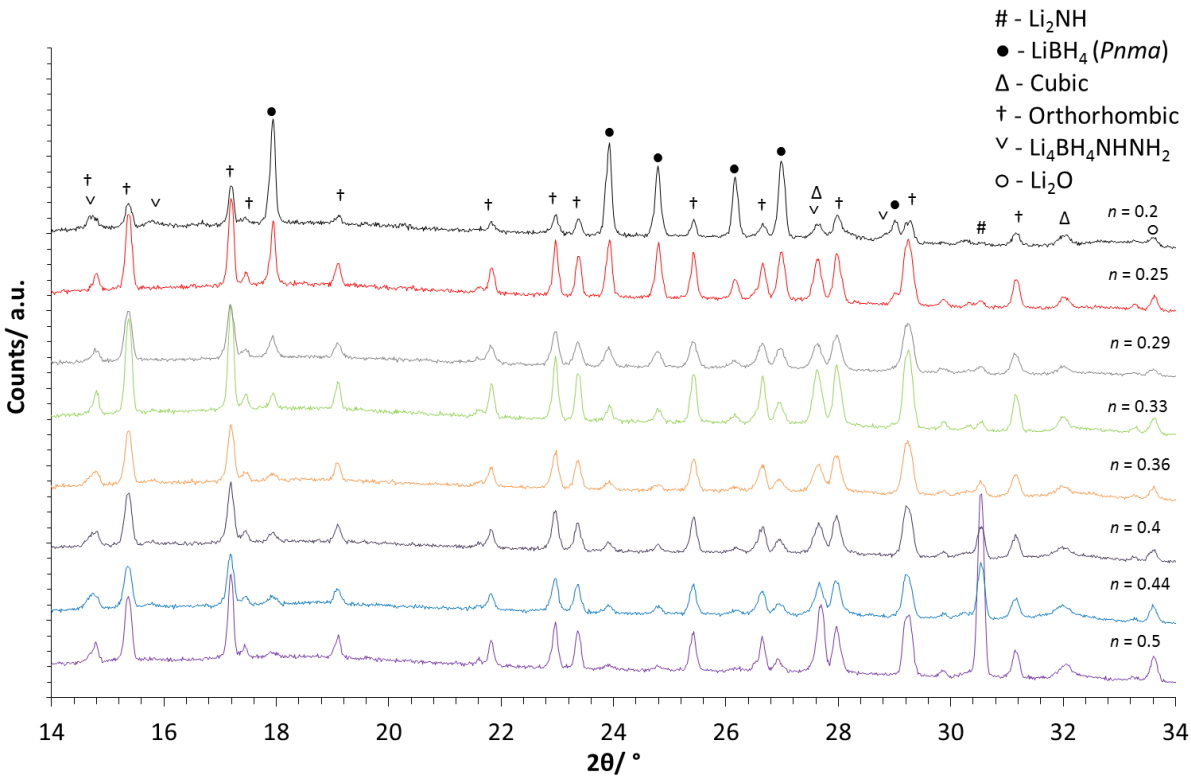

Figure 4.10 – Zoomed in plot of powder XRD data of the products of the reaction of Li_2NH + $LiBH_4$ at 125 °C for 12 hours in various $LiBH_4$-rich reaction conditions, where # = Li_2NH, ● = $LiBH_4$ (*Pnma*), Δ = cubic phase, † = orthorhombic phase, ᵛ = $Li_4BH_4NHNH_2$ and ○ = Li_2O

Initially the reaction was carried out in 1:1, 1:2, 1:3 and 1:4 Li_2NH:$LiBH_4$ reactant ratios (n = 0.5, 0.33, 0.25, and 0.2, respectively) and, through Rietveld refinement with QPA, weight percentages were obtained. The initial reaction ratios suggested the best ratio may lie somewhere between 1:1 and 1:2. Consequently ratios between 1:1 and 1:2 were investigated more closely. In all of these samples there was still cubic phase present alongside the orthorhombic phase; however, the orthorhombic phase was the dominant product. The weight percentages obtained from all of those reactions are reported in Table 4.3 and the mole percentages of lithium are depicted in Figure 4.11.

Table 4.3 – Weight percentages of the different components of the product mixture from the reaction of Li_2NH + $LiBH_4$ at 125 °C for 12 hours with various reactant ratios, where *n* refers to $nLi_2NH + (1 - n)LiBH_4$

Li_2NH:$LiBH_4$ Ratio	*n*	Weight Percent					
		Li_2NH	$LiBH_4$ (*Pnma*)	Cubic	Orthorhombic	$Li_4BH_4NHNH_2$	Li_2O
1:1	0.5	21.7(3)	2.4(4)	25.5(4)	47.6(5)	0	2.8(2)
4:5	0.44	8.8(2)	6.0(5)	13.6(6)	56.0(8)	12.3(8)	3.4(2)
2:3	0.4	5.3(2)	7.6(7)	18.3(5)	66.5(7)	0	2.2(2)
4:7	0.36	2.5(2)	6.3(7)	19.7(6)	69.1(7)	0	2.5(2)
1:2	0.33	0.7(1)	9.6(5)	19.4(3)	68.0(5)	0	2.3(1)
2:5	0.29	1.0(2)	18.0(5)	15.7(4)	63.2(6)	0	2.1(2)
1:3	0.25	0.6(1)	31.8(4)	12.9(3)	52.8(4)	0	1.9(1)
1:4	0.2	0	57.5(6)	4.7(3)	21.9(5)	12.2(7)	3.6(1)

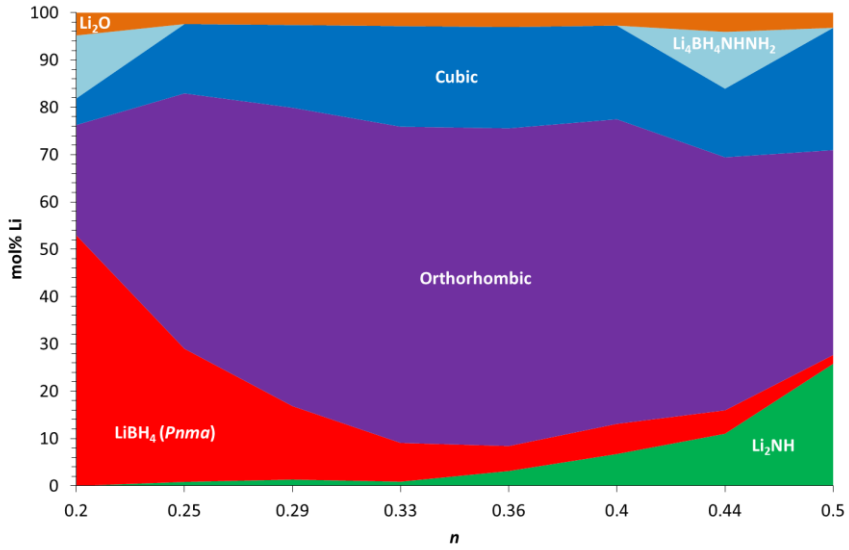

Figure 4.11 – Mole percentage lithium of the different components of the product mixture from the reaction of Li_2NH + $LiBH_4$ at 125 °C for 12 hours with various reactant ratios, where *n* refers to $nLi_2NH + (1 - n)LiBH_4$

The results of the QPA illustrated that varying the ratio did have an effect on the amount of orthorhombic phase formed; for example at the most LiBH$_4$-rich end there was a significant decrease in the amount of orthorhombic phase present, as LiBH$_4$ began to dominate the pattern. However, between n = 0.29 and n = 0.44 the amount of both the orthorhombic phase and cubic phase remained fairly consistent.

This LiBH$_4$-rich series suggested that a reactant ratio slightly more LiBH$_4$-rich than a simple 1:1 ratio may have been preferred when forming the orthorhombic phase. However, in order to compare this against the other end of the scale, reactions were carried out across the whole range: 3:9, 4:8, 5:7, 6:6, 7:5, 8:4 and 9:3 (n = 0.25, 0.33, 0.42, 0.5, 0.58, 0.66 and 0.75, respectively). LiBH$_4$-rich conditions all the way through to Li$_2$NH-rich conditions were investigated, based on the equation nLi$_2$NH + (1 – n)LiBH$_4$. The XRD data collected from these samples are presented in Figure 4.12.

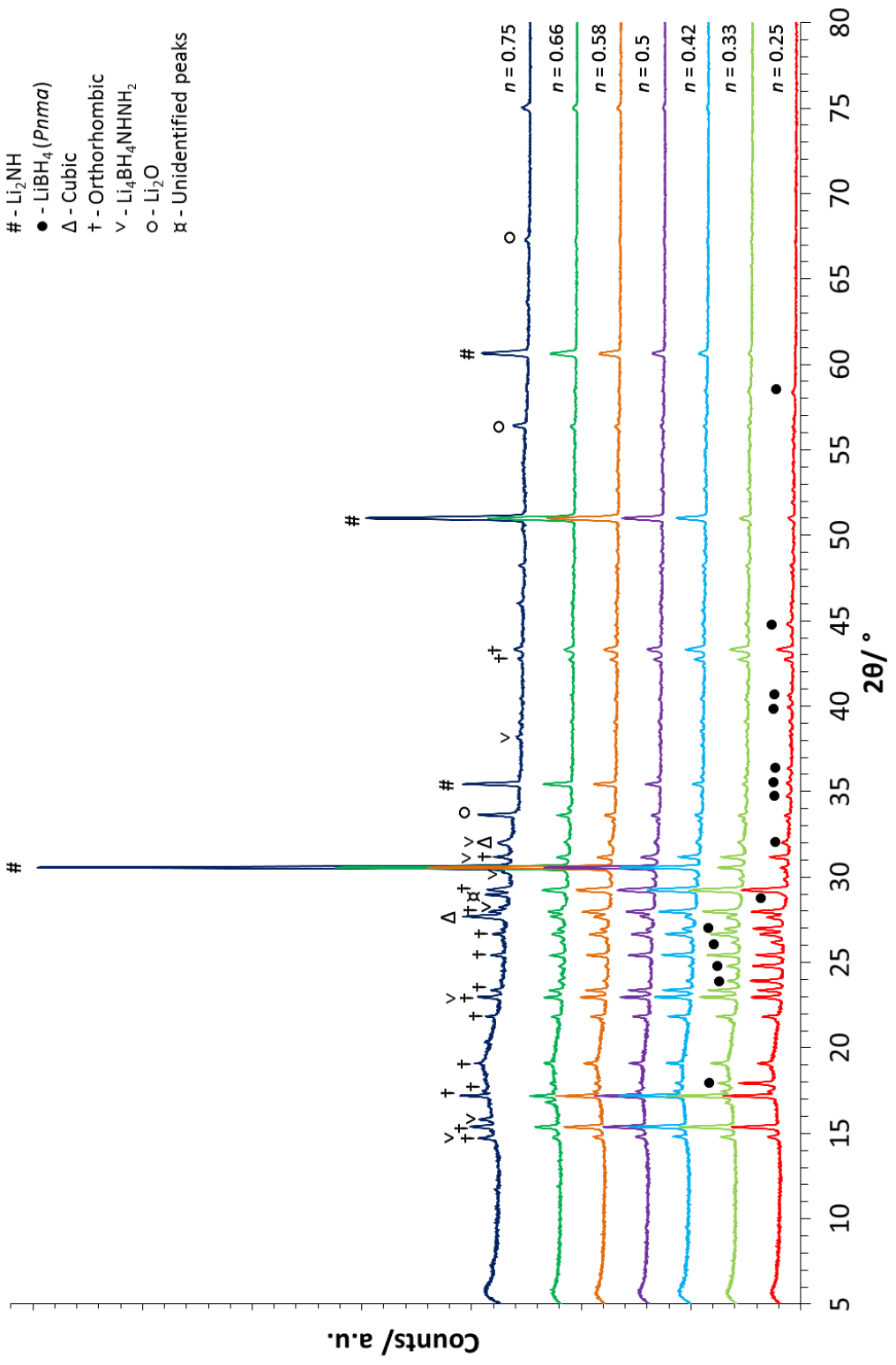

Figure 4.12 – Powder XRD data of the products of the reaction of nLi$_2$NH + (1 – n) LiBH$_4$ at 125 °C for 12 hours with various values of n, where # = Li$_2$NH, ● = LiBH$_4$ (*Pnma*), Δ = cubic phase, † = orthorhombic phase, ᵛ = Li$_4$BH$_4$NHNH$_2$, ○ = Li$_2$O and ¤= unidentified peaks

As with the previous data Rietveld refinements with QPA were carried out to quantify the observed data; weight percentages are reported in Table 4.4 and mole percentages of lithium are depicted in Figure 4.13.

Table 4.4 – Weight percentages of the different components of the product mixture of the nLi$_2$NH + (1 – n) LiBH$_4$ reaction at 125 °C for 12 hours with various values of n

Li$_2$NH:LiBH$_4$ Ratio	n	Weight Percent					
		Li$_2$NH	LiBH$_4$ (*Pnma*)	Cubic	Orthorhombic	Li$_4$BH$_4$NHNH$_2$	Li$_2$O
3:9	0.25	1.4(1)	33.3(4)	9.1(3)	55.2(4)	0	1.0(1)
4:8	0.33	5.5(2)	11.7(4)	8.9(4)	72.2(5)	0	1.7(1)
5:7	0.42	15.8(2)	8.3(4)	7.9(4)	66.7(4)	0	1.3(1)
6:6	0.5	26.0(3)	3.7(4)	9.5(4)	59.1(4)	0	1.7(1)
7:5	0.58	39.5(3)	3.5(4)	10.2(4)	45.0(4)	0	1.9(1)
8:4	0.66	50.6(5)	5.3(4)	9.7(5)	31.5(5)	0	2.9(1)
9:3	0.75	51.4(5)	0	9.4(5)	20.6(5)	12.1(6)	6.6(2)

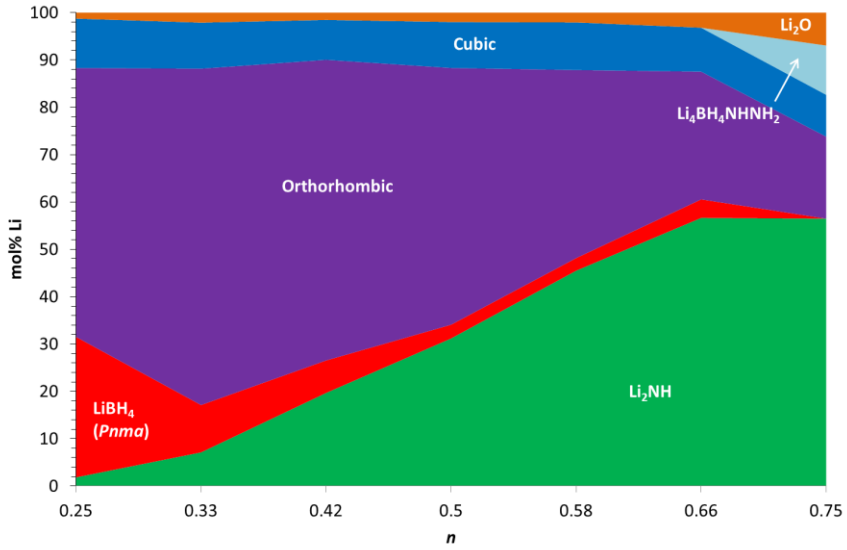

Figure 4.13 – Mole percent lithium of the different components of the product mixture of the nLi$_2$NH + (1 – n) LiBH$_4$ reaction at 125 °C for 12 hours with various values of n

From these data it appeared that a 4:8 ratio (n = 0.33), gave the greatest proportion of orthorhombic product. As well as having the greatest amount of orthorhombic phase, there was also the lowest combined amount of remaining starting materials. However, the remaining starting materials were both present in large enough quantities that potentially reannealing could improve the product ratios further still. This is discussed in more detail later in this chapter (§4.4.2.3).

With the aim of more easily comparing all the different ratios investigated, both data sets were combined into a plot, as well as additional repeats which were carried out, to enable the trends to be observed. Figure 4.14 shows the weight percentages with all the different reactant ratios heated at 125 °C for 12 hours.

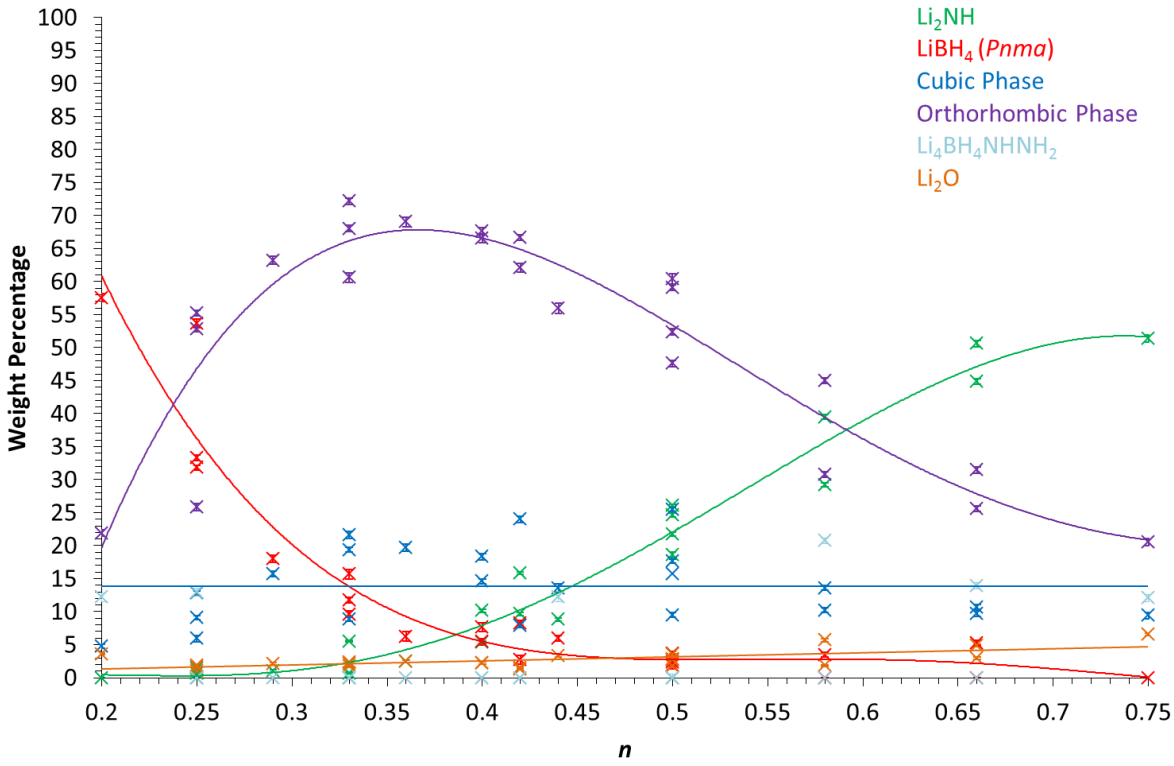

Figure 4.14 – Weight percentages determined from Rietveld refinement of the reaction of nLi$_2$NH + (1 – n)LiBH$_4$ with various values of n, heated at 125 °C for 12 hours. The solid lines are a polynomial fit and are intended to guide the eye only. Error bars are included but are smaller than the data point symbols

From the data presented in Figure 4.14 it is clear the orthorhombic phase was favoured between a ratio of 2:5 (n = 0.29) and 4:5 (n = 0.44) signifying a LiBH$_4$-rich reactant ratio is optimal for orthorhombic synthesis. Although a 4:8 ratio (n = 0.33) resulted in the greatest weight percentage of orthorhombic phase, repetition of the reaction resulted in a slightly lower weight percentages, below both the 4:7 (n = 0.36) and 5:7 (n = 0.42) ratios. Consequently, 4:8 (n = 0.33) cannot be determined to be the ideal reactant ratio. The amount of cubic phase, on the other hand, appears to have remained relatively consistent between samples fluctuating at *ca* 15 wt.%. There were some samples with slightly more

cubic phase present; however, repeats of the same conditions gave rise to samples with slightly less cubic phase and consequently these values averaged out to *ca* 15 wt.%. There was also hexagonal $Li_4BH_4NHNH_2$ (§4.6, §5.5) present in several samples across the series. However, there was a significant amount of fluctuation in the weight percentages and therefore its presence may have been affected by other sample preparation conditions e.g. grinding times, time between synthesis and data collection and the batch of Li_2NH used as a starting material amongst others.

One other point to note is the shape of the $LiBH_4$ and Li_2NH trend lines. Whilst Li_2NH steadily increased in abundance from *ca* n = 0.33, there was a much sharper decline in $LiBH_4$ with increasing n. The initial sharp decline mirrors the sharp increase in the orthorhombic phase. This trend is characteristic of a material which contains a greater proportion of one species compared with the other. Thus, as previously mentioned, it seemed likely that the orthorhombic phase contains more borohydride than imide.

4.4.2.2 Varying the Heating Times

For all of the previous reactions the heating period was kept constant at 12 hours while the temperatures and ratios were varied. In order to study the effect heating times had on the products of the nLi$_2$NH + (1 – n)LiBH$_4$ reaction, a series of different reaction times were investigated with both a 3:9 (n = 0.25) and a 2:3 (n = 0.4) reactant ratio. The 3:9 (n = 0.25) reactant ratio was chosen as it was the ratio of imide to borohydride anions in the orthorhombic model at the time – subsequently determined to be the true anion ratio in the structure (§5.3). The 2:3 (n = 0.4) reactant ratio was chosen as it lay within the reactant ratio

region of interest, producing a product mixture with one of the highest weight percentages of the orthorhombic phase.

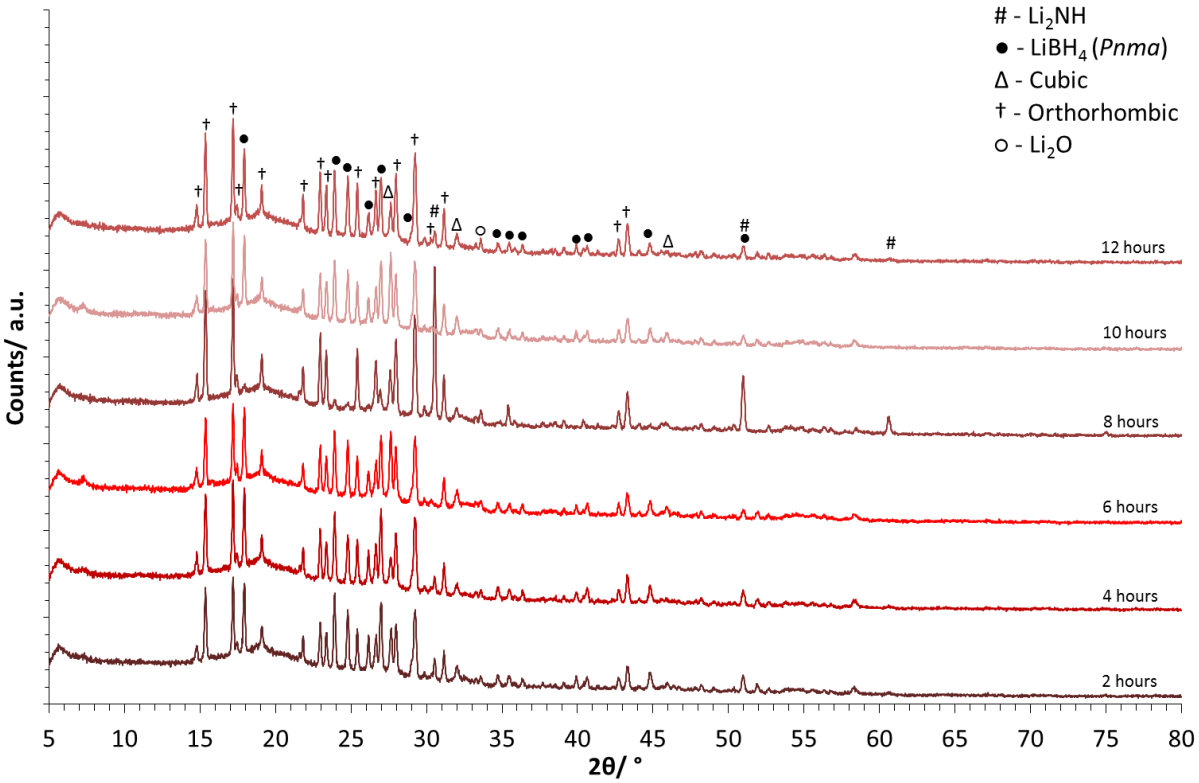

Figure 4.15 – Powder XRD data of the products of the reaction of nLi$_2$NH + (1 – n)LiBH$_4$, where n = 0.25, at 125 °C heated for various times, where # = Li$_2$NH, ● = LiBH$_4$ (*Pnma*), Δ = cubic phase, † = orthorhombic phase and ○ = Li$_2$O

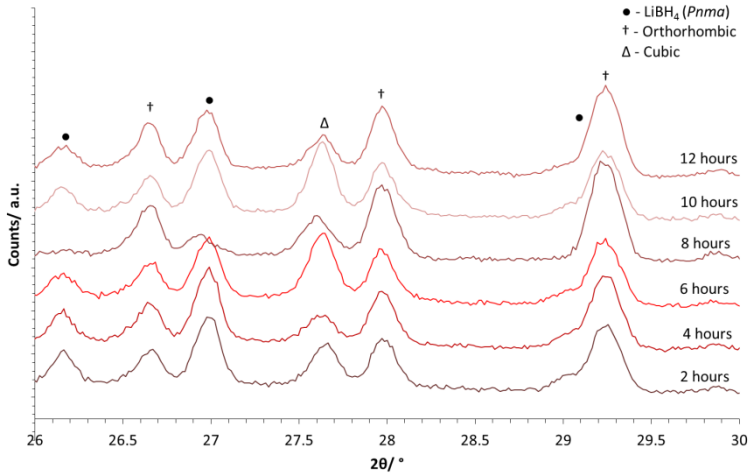

Figure 4.16 – Zoomed in XRD data of the products of the reaction of nLi$_2$NH + (1 – n)LiBH$_4$, where n = 0.25, at 125 °C heated for various times, where ● = LiBH$_4$ (*Pnma*), Δ = cubic phase and † = orthorhombic phase

Figure 4.15 shows the XRD data collected for the 3:9 (n = 0.25) series. The two overlapping peaks at *ca* 28 ° (highlighted in Figure 4.16) give a good indication of the cubic to orthorhombic ratio, as that is where the most intense of the cubic peaks is located. Based on the ratio of these two peaks, there did not seem to be a clear trend with increased heating time. The ratio of the peaks appeared to fluctuate randomly suggesting potentially other factors, such as grinding time, may have contributed to the presence of different phase ratios. Again, in order to quantify the ratios of the different phases Rietveld refinements with QPA were carried out; Table 4.5 contains the results of those refinements.

Table 4.5 – Weight percentages of the different components of the product mixture of the nLi$_2$NH + (1 – n)LiBH$_4$ reaction, where n = 0.25, heated at 125 °C for various times, determined from Rietveld refinement

Heating Time/ hrs	Weight Percent				
	Li$_2$NH	LiBH$_4$ (*Pnma*)	Cubic	Orthorhombic	Li$_2$O
2	2.0(1)	40.4(4)	12.0(3)	45.0(4)	0.7(1)
4	1.7(1)	38.5(3)	9.5(3)	49.8(4)	0.6(1)
6	0	35.5(4)	17.3(3)	45.6(4)	1.6(1)
8	16.3(2)	3.9(4)	11.5(3)	67.1(4)	1.2(1)
10	0	32.3(5)	18.2(3)	48.8(4)	0.8(1)
12	1.4(2)	33.3(4)	9.1(3)	55.2(4)	1.0(1)

As one of the reasons for the random fluctuations in weight percentages was suggested to be grinding time, the series was repeated with the grinding of the reagents timed for 5 minutes, to ensure consistency between all the samples. The XRD data for these samples are presented in Figure 4.17.

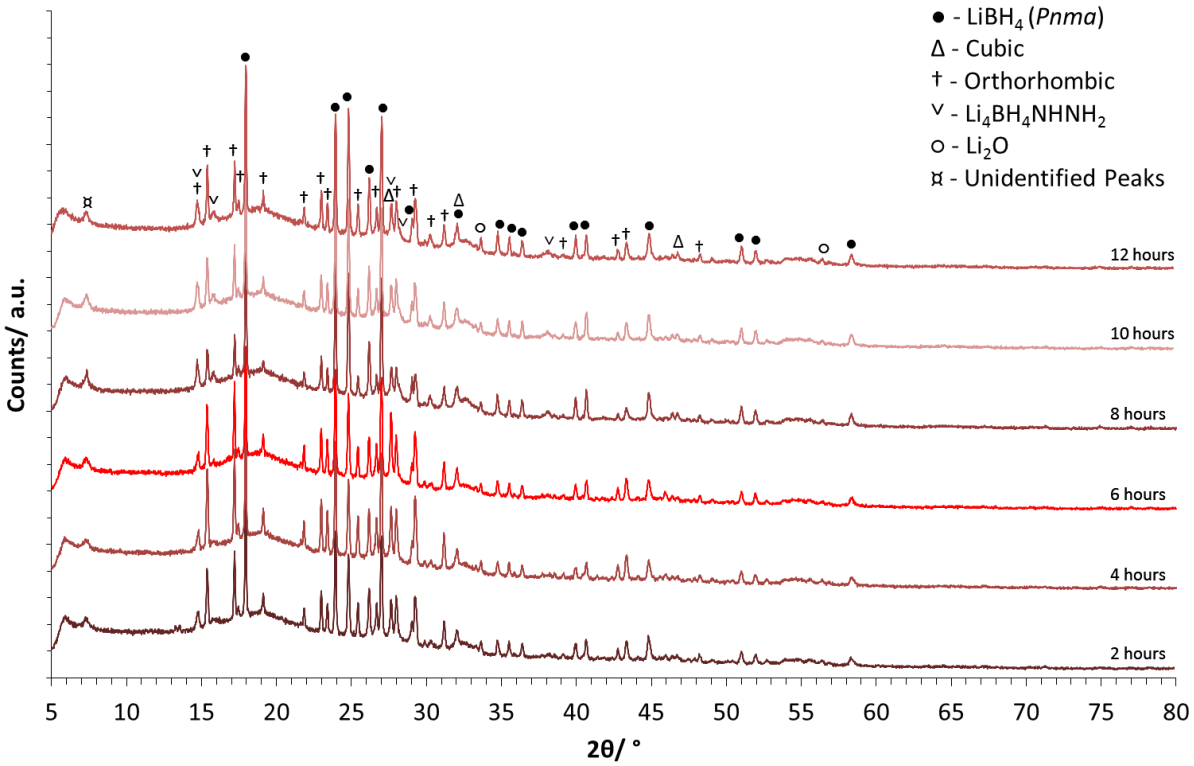

Figure 4.17 – Powder XRD data of the products of the reaction of nLi$_2$NH + (1 – n)LiBH$_4$, where n = 0.25, with a fixed 5 minute grinding time, heated at 125 °C for various times, where ● = LiBH$_4$ (*Pnma*), Δ = cubic phase, † = orthorhombic phase, ᵛ = Li$_4$BH$_4$NHNH$_2$, ○ = Li$_2$O and ¤ = unidentified peaks

Although the spike in Li$_2$NH at 8 hours was not seen for this repeated series and the data were much more consistent there were still some fluctuations. The results of the QPA are given in Table 4.6. The increased consistency suggested that grinding time does play a part in determining the abundance of different phases. However, the lack of a clear trend suggests that there may be additional factors which also contributed to the observed fluctuations, for example one possibility is furnace cooling times.

Table 4.6 – Weight percentages of the different components of the product mixture of the nLi$_2$NH + (1 – n)LiBH$_4$ reaction (repeated with consistent grinding times), where n = 0.25, heated at 125 °C for various times, determined from Rietveld refinement

Heating Time/ hrs	Weight Percent					
	Li_2NH	$LiBH_4$ (*Pnma*)	Cubic	Orthorhombic	$Li_4BH_4NHNH_2$	Li_2O
2	0	50.6(5)	11.7(4)	36.1(5)	0	1.6(2)
4	0	43.7(4)	11.8(3)	43.2(4)	0	1.3(1)
6	0	46.0(4)	16.2(3)	36.4(4)	0	1.4(2)
8	0	59.0(7)	5.9(6)	18.5(6)	14.8(6)	1.7(2)
10	0	53.2(6)	6.2(5)	25.2(5)	13.7(6)	1.8(2)
12	0	53.6(6)	6.0(5)	25.8(6)	13.0(6)	1.6(1)

Interestingly the weight percentages of the orthorhombic phase, determined through QPA of the repeated data set, are all lower than even the lowest recorded weight percent for the first repeated heating series (Table 4.5). The decrease in the orthorhombic phase occurred alongside an increase in the amount of $LiBH_4$ present. This suggests that slight increases in grinding time can reduce the amount of orthorhombic phase formed, and the simultaneous increase in $LiBH_4$ supports the theory that the orthorhombic phase is richer in borohydride than imide. In addition, the appearance of more $Li_4BH_4NHNH_2$ impurity peaks, thought to be a more thermodynamically stable phase, alongside a decrease in the amount of orthorhombic phase with longer heating times suggests that the orthorhombic phase may not be thermodynamically stable, the more intimate mixing consequently resulting in a reduction in the yield of the orthorhombic phase.

Figure 4.18 shows the XRD data collected for the 2:3 (n = 0.40) series. As with the 3:9 (n = 0.25) series it is the two overlapping peaks at *ca* 28 ° (highlighted in Figure 4.19) that

give a good indication of the cubic to orthorhombic phase ratio, although in this case the presence of hexagonal $Li_4BH_4NHNH_2$ (§4.6, §5.5) also needs to be considered as it overlaps with the cubic peak. Based on the observed peak intensities as the time was increased the amount of cubic phase appeared to increase, in particular for the 10 hour sample.

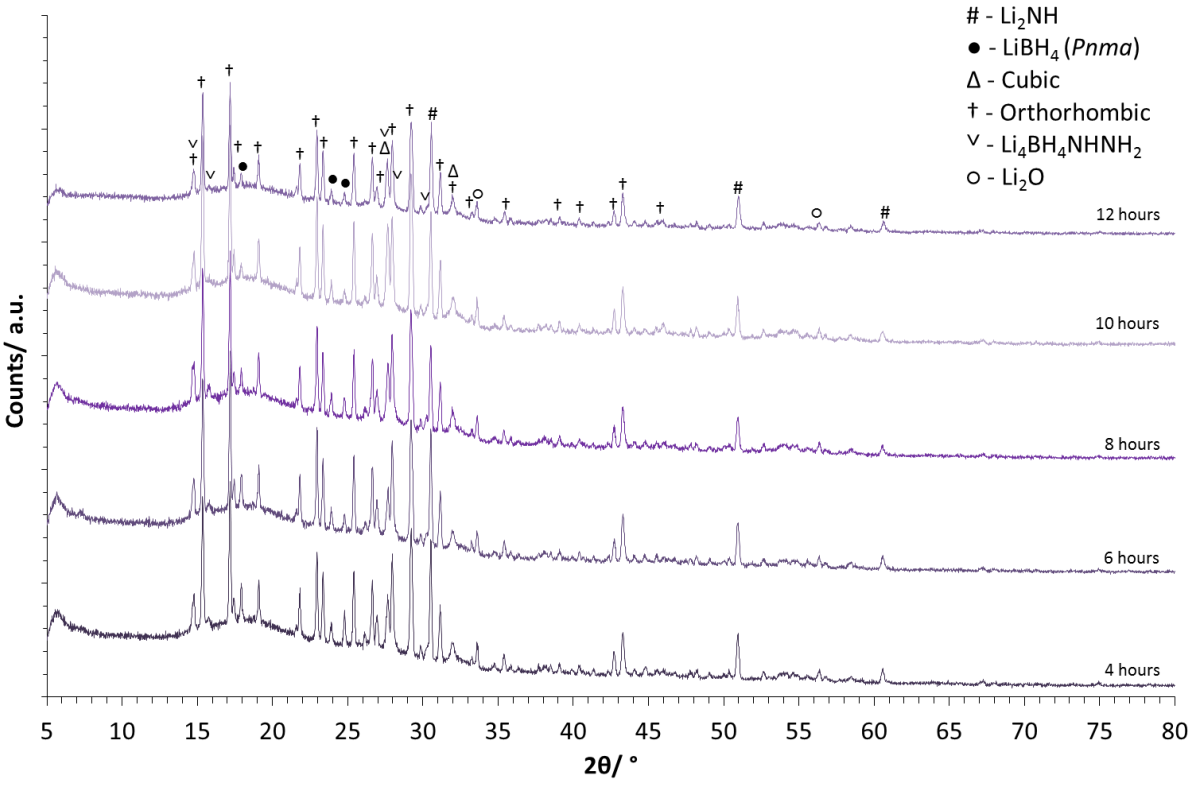

Figure 4.18 – Powder XRD data of the products of the reaction of 2Li$_2$NH + 3LiBH$_4$ (n = 0.4) at 125 °C heated for various reaction times, where # = Li$_2$NH, ● = LiBH$_4$ (*Pnma*), Δ = cubic phase, † = orthorhombic phase, ᵛ = Li$_4$BH$_4$NHNH$_2$ and ○ = Li$_2$O

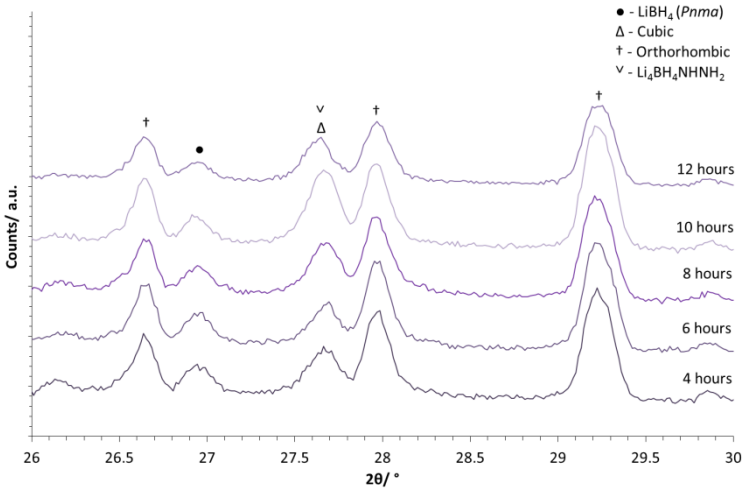

Figure 4.19 – Zoomed in powder XRD data of the products of the reaction of 2Li$_2$NH + 3LiBH$_4$ (n = 0.4) at 125 °C heated for various reaction times, where ● = LiBH$_4$ (*Pnma*), Δ = cubic phase, † = orthorhombic phase and ᵛ = Li$_4$BH$_4$NHNH$_2$

Again Rietveld refinements were carried out to quantify the observations. Table 4.7 shows the weight percentages obtained from those QPA refinements. The refinement data appear to show relatively consistent values for all of the different weight percentages, with the exception of Li$_4$BH$_4$NHNH$_2$ which was present in only two of the samples. The weight percentage of orthorhombic phase fluctuated between *ca* 59 and 69 wt.%. There was not a clear trend associated with this temperature data, as with the 3:9 (n = 0.25) data, however, there were smaller variations in the weight percentages than for the 3:9 data. The consistency between samples undergoing different length heat treatments suggests that varying the heating times between 4 and 12 hours has minimal impact on the yield of the orthorhombic phase.

Table 4.7 – Weight percentages of the different components of the product mixture of the 2Li$_2$NH + 3LiBH$_4$ (n = 0.40) reaction heated at 125 °C for various reaction times, determined from Rietveld refinement

Heating Time/ hrs	Weight Percent					
	Li$_2$NH	LiBH$_4$ (*Pnma*)	Cubic	Orthorhombic	Li$_4$BH$_4$NHNH$_2$	Li$_2$O
4	8.0(2)	9.9(5)	13.8(4)	66.4(5)	0	1.9(2)
6	7.6(2)	10.3(4)	7.4(4)	62.0(6)	10.9(6)	1.9(1)
8	5.8(2)	9.4(5)	10.7(4)	59.3(6)	12.9(6)	1.9(1)
10	6.8(2)	5.3(5)	18.1(4)	68.9(5)	0	1.8(1)
12	10.1(2)	5.5(5)	14.6(4)	67.6(5)	0	2.2(2)

Due to the fluctuation in weight percentages and the decline in the orthorhombic phase in the repeated 3:9 (n = 0.25) series (Table 4.6), it was determined that further studies were needed. In order to understand more fully the effects of intimate mixing on the yield of the orthorhombic phase, both ball-milling and reannealing were investigated.

4.4.2.3 Reannealing

Regrinding and reannealing were carried out on the products of the 2Li$_2$NH + 3LiBH$_4$ (n = 0.4) reactions performed over various heating times, and heating was repeated in the same time frame (i.e. 2 × 4 hours, 2 × 6 hours, 2 × 8 hours, 2 × 10 hours, and 2 × 12 hours). For every sample the repeated heating resulted in a greater amount of cubic phase in the XRD data of the product mixture. There was also a significant decrease in the intensity of reflections due to lithium imide. These changes in intensity were accompanied by very little change in peaks due to the orthorhombic phase and only a slight decrease in the intensity of lithium borohydride reflections (Figure 4.20). In addition the hexagonal Li$_4$BH$_4$NHNH$_2$ phase

(§4.6, §5.5) was present in the reannealed sample as a small impurity phase, demonstrating that the phase was clearly introduced after reannealing.

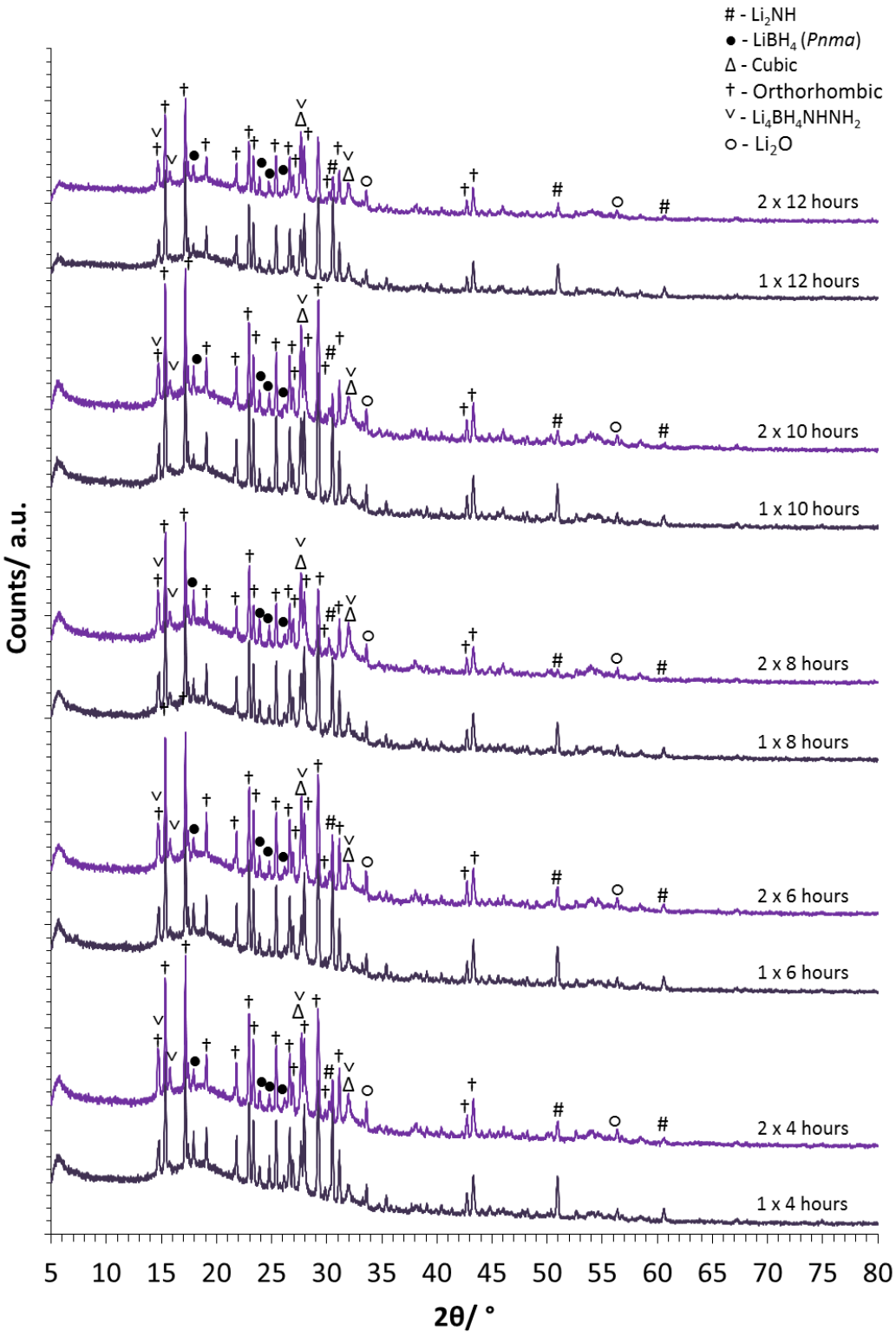

Figure 4.20 – Powder XRD data of the products of the reaction of 2Li$_2$NH + 3LiBH$_4$ (n = 0.4) at 125 °C heated for various times and reannealed, where # = Li$_2$NH, ● = LiBH$_4$ (*Pnma*), Δ = cubic phase, † = orthorhombic phase, ᵛ = Li$_4$BH$_4$NHNH$_2$ and ○ = Li$_2$O

In order to quantify the observations, Rietveld refinements with QPA were carried out; Table 4.8 contains the results of those refinements. From these data a consistent decrease in Li_2NH was confirmed with reannealing, accompanied by a consistent decrease in the weight percentage of orthorhombic phase and increase in the weight percentage of the hexagonal $Li_4BH_4NHNH_2$ phase. The weight percentages of $LiBH_4$ and the cubic phase are not as clear. For the 4 and 6 hour cycles a decrease in the amount of $LiBH_4$ was observed, however, for the other heating cycles an increase was seen. The cubic phase was observed displaying similar behaviour, fluctuating weight percentages across the series.

Table 4.8 – Weight percentages of the different components of the product mixture of the $2Li_2NH + 3LiBH_4$ (n = 0.40) reaction heated and reannealed at 125 °C for various reaction times, determined from Rietveld refinement

Heating Time/ hrs	Weight Percent					
	Li_2NH	$LiBH_4$ (*Pnma*)	Cubic	Orthorhombic	$Li_4BH_4NHNH_2$	Li_2O
4	8.0(2)	9.9(5)	13.8(4)	66.4(5)	0	1.9(2)
2 × 4	2.7(1)	8.2(5)	8.1(3)	58.0(6)	20.7(5)	2.2(2)
6	7.6(2)	10.3(4)	7.4(4)	62.0(6)	10.9(6)	1.9(1)
2 × 6	3.6(2)	7.9(5)	9.7(4)	58.9(6)	17.8(6)	2.2(1)
8	5.8(2)	9.4(5)	10.7(4)	59.3(6)	12.9(6)	1.9(1)
2 × 8	0	13.4(5)	15.5(5)	50.4(7)	18.7(6)	2.0(2)
10	6.8(2)	5.3(5)	18.1(4)	68.0(5)	0	1.8(1)
2 × 10	1.5(2)	10.5(4)	12.6(4)	55.8(7)	17.7(7)	2.0(2)
12	10.1(2)	5.5(5)	14.6(4)	67.6(5)	0	2.2(2)
2 × 12	3.0(2)	10.1(5)	14.3(4)	53.6(7)	16.7(7)	2.4(2)

The QPA data suggests that reannealing favours formation of the new hexagonal $Li_4BH_4NHNH_2$ phase over both the orthorhombic phase and the cubic phase, despite the

reaction being between lithium imide and lithium borohydride. Considering the XRD patterns the main cubic phase appeared to consistently grow with reannealing, however, the weight percentages determined fluctuate. This was due to the main cubic reflection overlapping with a $Li_4BH_4NHNH_2$ phase reflection (27.5 °) and therefore it is likely that the accuracy of the cubic weight percentages were reduced as there was no isolated cubic reflection and only a single unique reflection for $Li_4BH_4NHNH_2$. Although it is clear that $Li_4BH_4NHNH_2$ formed on reannealing, the difficulty in detecting a trend in the cubic phase may be in part due to these issues.

After studying the effects of reannealing using a $2Li_2NH$ to $3LiBH_4$ ratio (n = 0.4), reannealing experiments were then performed using different reactant ratios. Figure 4.21 and Figure 4.22 compare reannealing with a 4:8 (n = 0.33) and a 5:7 (n = 0.42) ratio, respectively; both were chosen due to their presence in the region most preferable for orthorhombic phase formation.

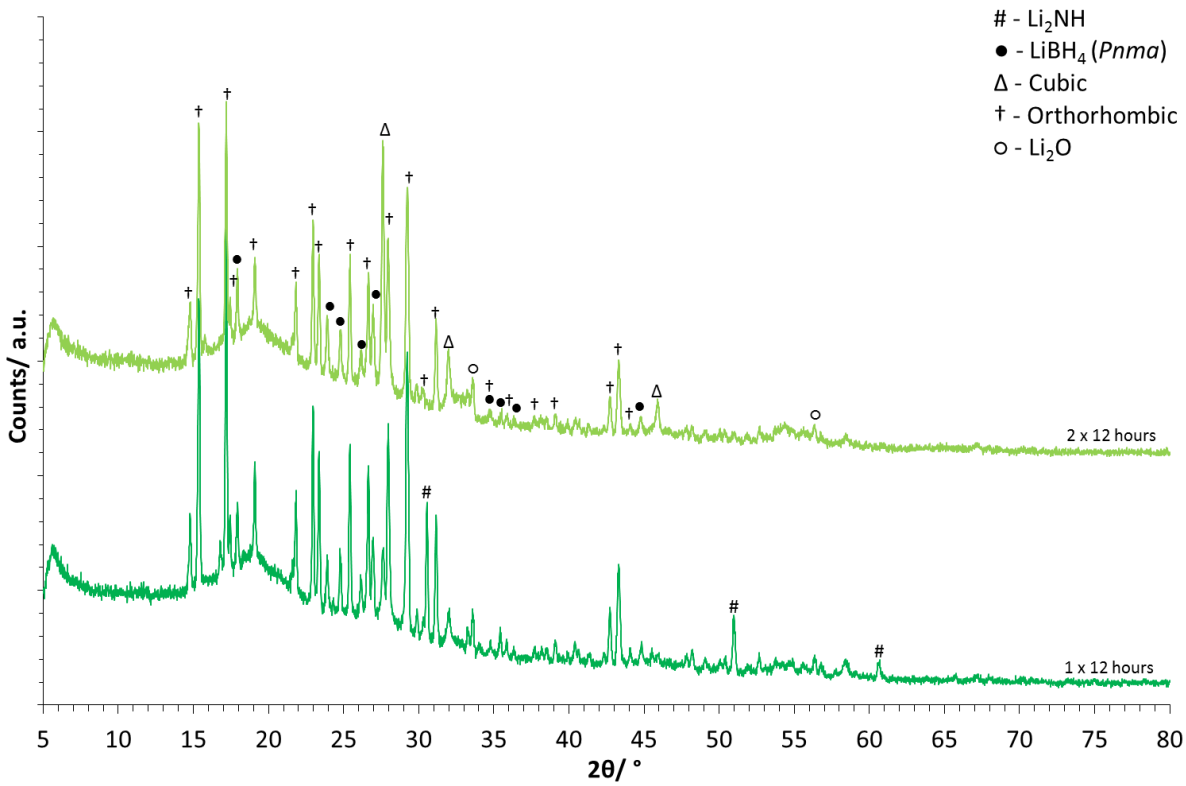

Figure 4.21 – Powder XRD data of the products of the reaction of nLi$_2$NH + (1 – n)LiBH$_4$, where n = 0.33, at 125 °C heated for 12 hours and reannealed, where # = Li$_2$NH, ● = LiBH$_4$ (*Pnma*), Δ = cubic phase, † = orthorhombic phase and ○ = Li$_2$O

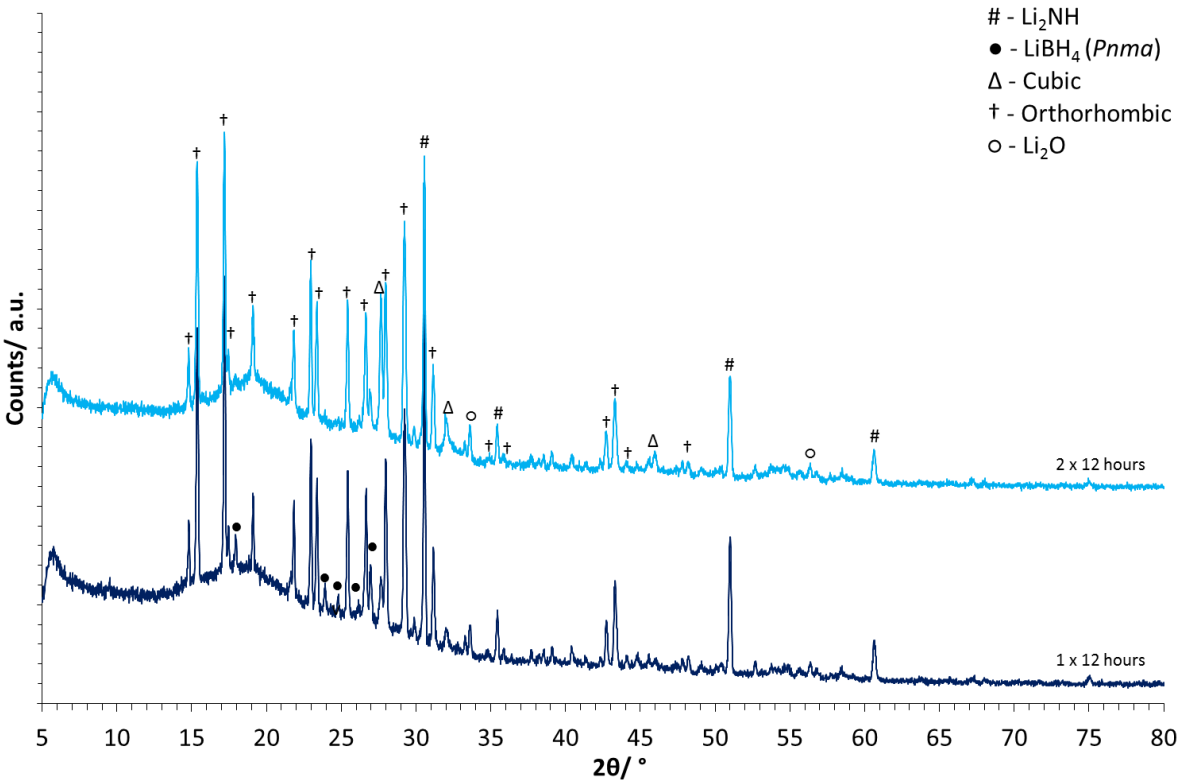

Figure 4.22 – Powder XRD data of the products of the reaction of nLi$_2$NH + (1 – n)LiBH$_4$, where n = 0.42, at 125 °C heated for 12 hours and reannealed, where # = Li$_2$NH, ● = LiBH$_4$ (*Pnma*), Δ = cubic phase, † = orthorhombic phase and ○ = Li$_2$O

Table 4.9 – Weight percentages of the different components of the product mixture of the nLi$_2$NH + (1 – n)LiBH$_4$ reaction, heated and reannealed for 12 hours at 125 °C, using various values of n

n	Heating Time/ hrs	Weight Percent				
		Li$_2$NH	LiBH$_4$ (*Pnma*)	Cubic	Orthorhombic	Li$_2$O
0.33	12	5.5(2)	11.7(4)	8.9(4)	72.2(5)	1.7(1)
0.33	2 × 12	0	14.9(5)	25.6(4)	57.7(5)	1.8(2)
0.42	12	15.8(2)	8.3(4)	7.9(4)	66.7(4)	1.3(1)
0.42	2 × 12	14.5(2)	0	17.1(3)	67.0(4)	1.4(1)

One key point of interest in these two studies is the presence of the different starting materials. A ratio of 4:8 (n = 0.33) showed a clear absence of Li_2NH after reannealing and for a 5:7 ratio (n = 0.42) there was an absence of $LiBH_4$. This suggests that a ratio without either starting material may be found between these two ratios. Table 4.9 contains the results of the Rietveld refinements with QPA of the XRD data. In these data there was both an increase in cubic phase and decrease in the orthorhombic phase. However, the possibility of removing both starting materials appeared to be possible as one sample was absent of $LiBH_4$ and one of Li_2NH. Consequently a ratio between these two was investigated, $19Li_2NH:31LiBH_4$ (n = 0.38), with the hopes of removing both starting materials. Shorter heating times were also used as the data collected for the 2:3 (n = 0.4) series clearly showed that shorter heating times favoured the orthorhombic phase over the cubic phase. The XRD data for the n = 0.38 samples are displayed in Figure 4.23 and Figure 4.24.

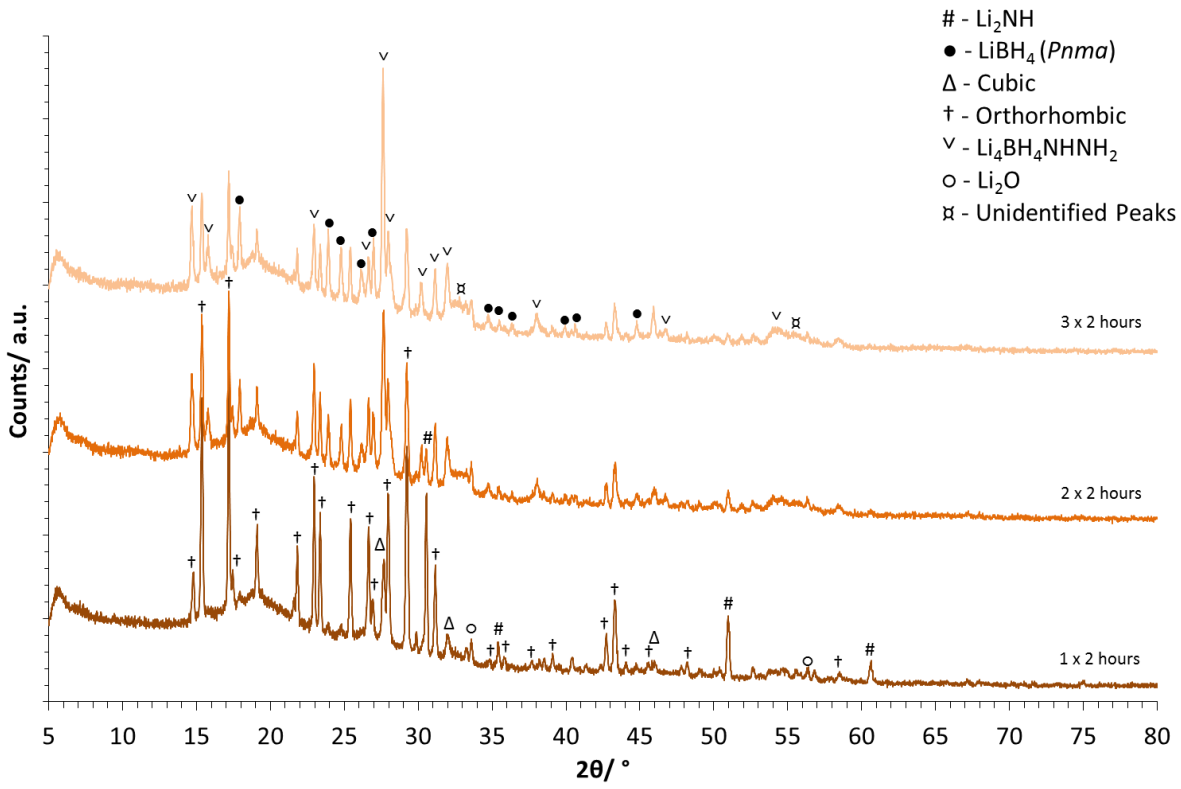

Figure 4.23 – Powder XRD data of the products of the reaction of nLi$_2$NH + (1 – n)LiBH$_4$, where n = 0.38, heated and reannealed in 2 hour heating cycles at 125 °C, where # = Li$_2$NH, ● = LiBH$_4$ (*Pnma*), Δ = cubic phase, † = orthorhombic phase, ᵛ = Li$_4$BH$_4$NHNH$_2$, ○ = Li$_2$O and ¤ = unidentified peaks

Initially the 19:31 (n = 0.38) reaction mixture was heated in 2 hour cycles (Figure 4.23). The data clearly show an increase in cubic phase and decrease in orthorhombic phase with repeated heating cycles, similar to what was observed previously for the 4:8 (n = 0.33) and 5:7 (n = 0.42) series (Table 4.9). There also seemed to be an increase in LiBH$_4$ and decrease in Li$_2$NH, again consistent with previous samples. However, there was also a dramatic increase in the amount of the hexagonal Li$_4$BH$_4$NHNH$_2$ phase (§4.6, §5.5), as well as the appearance of very broad unidentified peaks, supporting conclusions previously drawn about the orthorhombic phase not being thermodynamically stable.

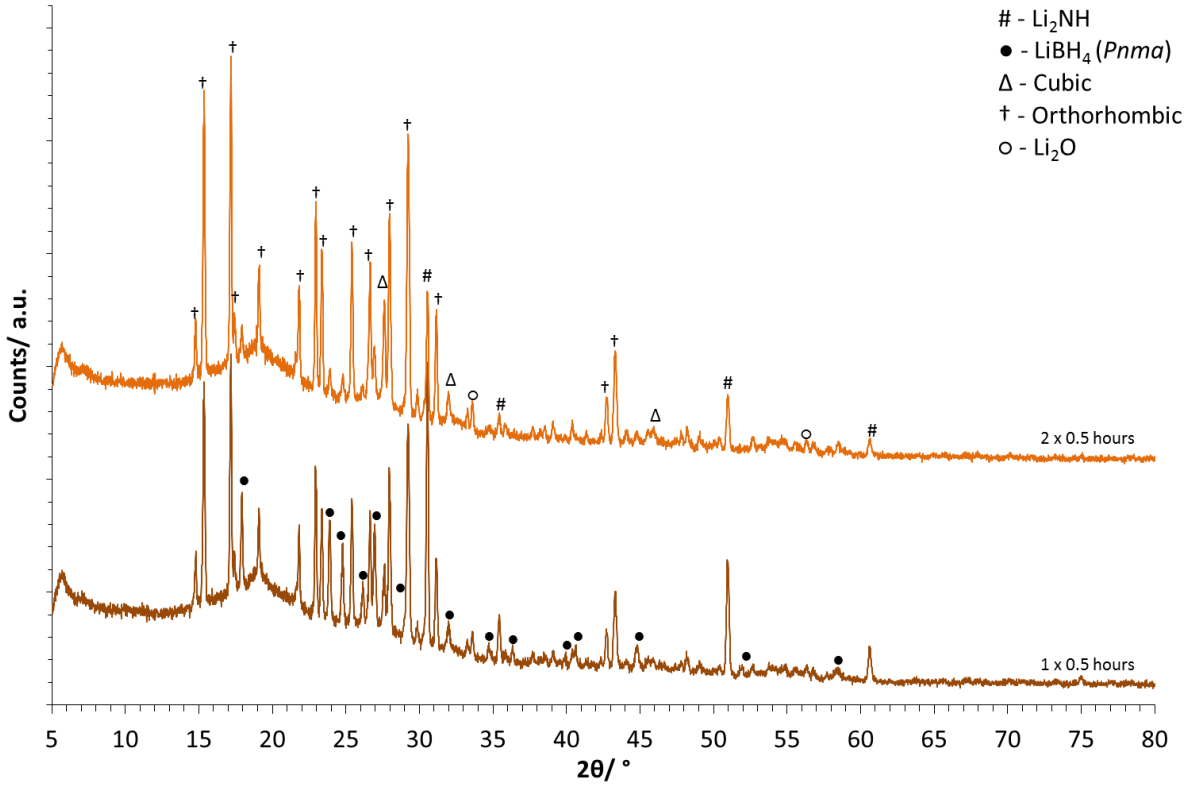

Figure 4.24 – Powder XRD data of the products of the reaction of nLi$_2$NH + (1 – n)LiBH$_4$, where n = 0.38, heated and reannealed in 0.5 hour heating cycles at 125 °C, where # = Li$_2$NH, ● = LiBH$_4$ (*Pnma*), Δ = cubic phase, † = orthorhombic phase and ○ = Li$_2$O

As the sample heated for 2 hours produced unidentified peaks and a significant amount of the hexagonal $Li_4BH_4NHNH_2$ phase, and reannealing still resulted in a decrease in the orthorhombic phase, an even shorter heating time was investigated. Figure 4.24 shows the results of heating and reannealing for half an hour. Between the first and second heating there was a big drop in the amount of $LiBH_4$, alongside a smaller drop in Li_2NH. There was also an increase in the amount of the orthorhombic phase, although this was concurrent with an increase in cubic phase. The results of Rietveld refinements with QPA for both the 2 hour heating and 0.5 hour heating on the 19:31 (n = 0.38) series are displayed in Table 4.10. The results quantify the reported observations and support the shorter heating time of half

an hour and reannealing to be promising as a means to synthesise a larger amount of orthorhombic phase, despite this occurring alongside an increase in the cubic phase.

Table 4.10 – Weight percentages of the different components of the product mixture of the nLi$_2$NH + (1 – n)LiBH$_4$ reaction where n = 0.38, heated and reannealed at 125 °C for various times

Heating Time/ hrs	Weight Percent					
	Li$_2$NH	LiBH$_4$ (*Pnma*)	Cubic	Orthorhombic	Li$_4$BH$_4$NHNH$_2$	Li$_2$O
2	9.1(1)	2.7(3)	13.7(3)	73.3(4)	0	1.2(1)
2 × 2	1.5(1)	14.6(5)	17.4(5)	42.1(5)	22.4(5)	1.9(1)
3 × 2	0	18.3(5)	22.6(4)	34.0(5)	23.4(5)	1.8(1)
0.5	12.8(2)	20.1(3)	7.8(3)	58.1(4)	0	1.2(1)
2 × 0.5	6.0(1)	6.0(4)	12.2(3)	74.4(4)	0	1.3(1)

4.4.2.4 Ball-Milling

During the course of this project Wang *et al.* and Wolczyk *et al.* published their work on the orthorhombic phase, and in both cases the orthorhombic phase was synthesised through ball milling followed by annealing.[147,148] Consequently, ball-milling was investigated in order to better understand the effects of more intimate mixing of the two reagents and subsequently the effect of that mixing on the final product mixtures after heating. Both authors reported using a planetary ball mill, as was used in this study. Wolczyk *et al.* used a Fritsch Pulverisette 7 (the same model used in this research) and Wang *et al.* used a Retsch PM400.

In the research performed by Wang *et al*., Li$_2$NH and LiBH$_4$ were ball-milled in various different ratios starting with 1:1 and then increasing the amount of LiBH$_4$ up to ratios of 2:3, 1:2 and 3:8. The authors found that they formed the orthorhombic phase after ball-

milling for 24 hours at 200 rpm, although this was alongside some starting material. This work was subsequently replicated in order to determine whether this may have been a more effective synthesis method.

Initially Li_2NH and $LiBH_4$ were ball-milled in 2:3 (n = 0.4) and 1:3 (n = 0.25) ratios. The 2:3 ratio was chosen as it proved the most promising ratio in Wang and Wolczyk's work as well as being the anion ratio favoured in many of the reactions in this work.[147,148] The 1:3 ratio was chosen as it is the anion ratio in the current orthorhombic phase model (§5.3.4.2). The samples were milled for 24 hours in a planetary micro mill, using a 15 minutes on, 1 minute rest cycling programme. The XRD data collected from the products of ball-milling showed that no reaction had taken place as both samples contained only starting materials.

As no reaction had taken place from ball-milling alone, the samples were heated to try and form the desired product. They were heated at both 125 °C and 150 °C for 2 hours. The XRD patterns of the products of those reactions are presented in Figure 4.25

At the 1:3 ratio (n = 0.25) the products were dominated by $LiBH_4$, other than that and a small Li_2O impurity there were a few, mostly broad unidentified peaks. The peak at *ca* 7 ° was seen previously in some of the non-ball-milled reactions, however, in all of those cases it was only as a very small peak. It appeared, based on this study, that whatever phase that peak is associated with was more suited to ball-milled conditions. The very broad unidentified peaks have also been observed in some reactions carried out at higher temperature (detailed in §4.5.1). The broad peaks are potentially due to a highly disordered additional phase which was present in a range of compositions; alternatively they may have been due to varied composition and disorder in one of the known phases.

Once the ratio was changed to 2Li$_2$NH:3LiBH$_4$ (n = 0.4) the orthorhombic phase was formed, more abundantly in the sample heated at 125 °C compared with 150 °C. However, this was still alongside LiBH$_4$, the cubic phase, the hexagonal Li$_4$BH$_4$NHNH$_2$ phase (§4.6, §5.5) and several unknown peaks.

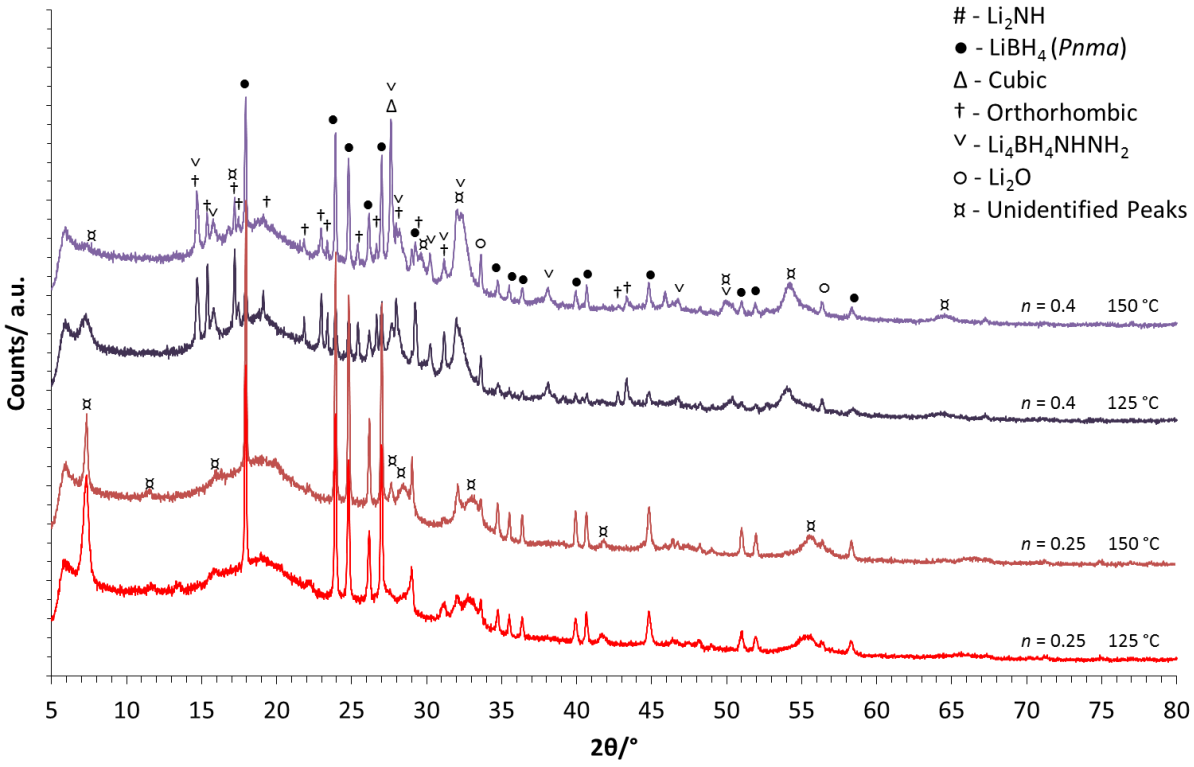

Figure 4.25 – Powder XRD data of the nLi$_2$NH + (1 – n)LiBH$_4$ reaction with various values of n, ball-milled for 24 hours and heated for 2 hours at either 125 or 150 °C, where † = orthorhombic phase, Δ = cubic phase, ● = LiBH$_4$ (*Pnma*), # = Li$_2$NH, ○ = Li$_2$O, ᵛ = Li$_4$BH$_4$NHNH$_2$ and ¤ = unidentified peaks

As replicating the work carried out by Wang *et al.* work did not produce promising results, the higher speed reported by Wolczyk *et al.* of 500 rpm was not replicated. Ball-milling studies performed within this body of work suggested that more intimate mixing is not the best way of forming the orthorhombic phase.

As has been suggested throughout this chapter the orthorhombic phase is unlikely to be the most thermodynamically stable phase in the lithium borohydride-imide phase space. The results of this ball-milling investigation support the conclusions drawn when consistently timed hand grinding was implemented (§4.4.2.2), that more intimate mixing results in less orthorhombic phase. As a result of ball milling substantially less orthorhombic phase was formed, only a small amount in the 2:3 (n = 0.4) series and none in the 1:3 (n = 0.25) series. Consequently ball-milling combined with heating was not deemed to be a suitable method for the synthesis of the orthorhombic phase.

4.4.3 Best Conditions for Orthorhombic Phase Synthesis

The different investigations into the orthorhombic phase have provided a more detailed understanding of the formation of the orthorhombic phase, even though synthesis of a pure phase was unsuccessful. These studies have demonstrated the orthorhombic phase to favour a lower temperature and shorter heating time. Reannealing has been shown to provide mixed results, yet reannealing can enable the amount of starting materials to be reduced, and with very short heating times enabling a greater proportion of orthorhombic phase to be formed.

Studies so far have shown the best synthetic conditions for the orthorhombic phase are 125 °C heating for half an hour and reannealing for a further half an hour again at 125 °C, using a reactant ratio of 19Li$_2$NH to 31LiBH$_4$ (n = 0.38 for nLi$_2$NH + (1 – n)LiBH$_4$). This reaction gave a weight percent of orthorhombic phase of 74.4(4) wt.% and the lattice parameters from that refinement were a = 10.1437(4), b = 11.4731(5) and c = 6.9986(3) Å. Figure 4.26 shows the Rietveld refinement plot of the product of that reaction.

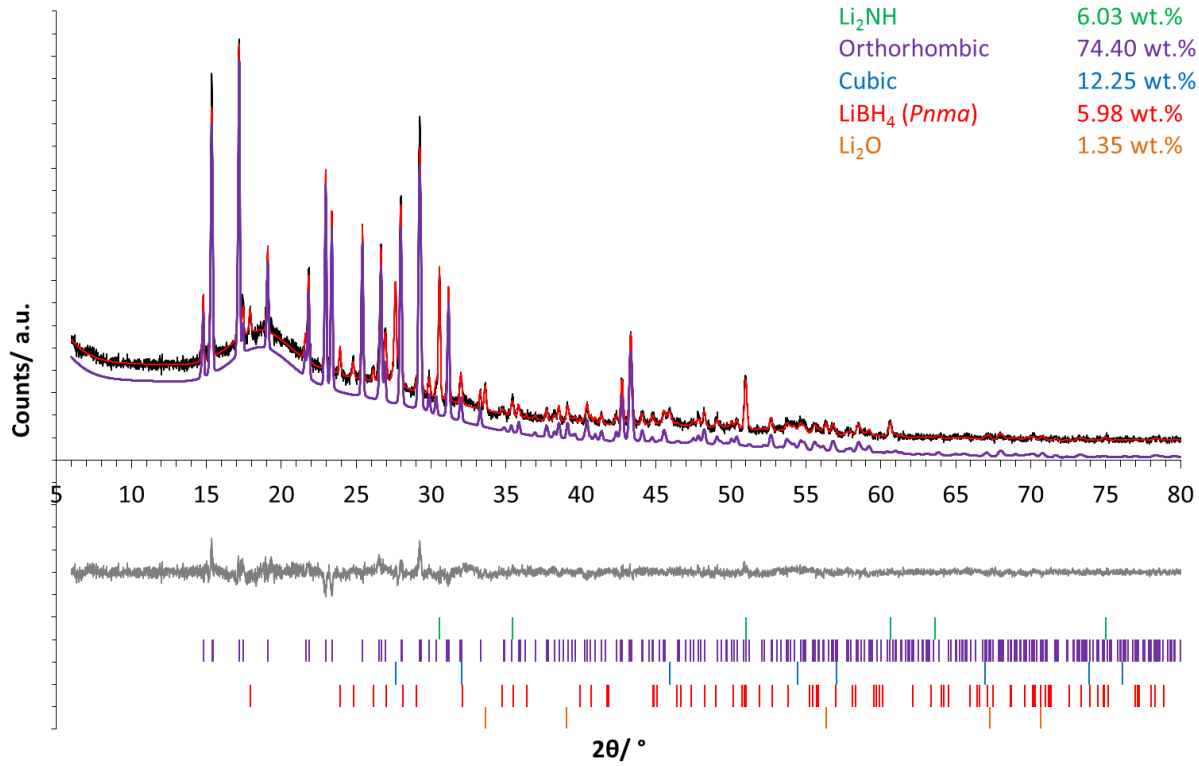

Figure 4.26 – Rietveld refinement plots of the products of the nLi$_2$NH + (1 – n)LiBH$_4$ reaction, where n = 0.38, carried out at 125 °C for 2 × 0.5 hours, where black = observed data, red = calculated data and grey = difference, highlighting the orthorhombic phase in purple. Green tick marks = Li$_2$NH, purple tick marks = orthorhombic phase, blue tick marks = cubic phase, red tick marks = LiBH$_4$ (*Pnma*) and orange tick marks = Li$_2$O

4.5 Higher Temperature Synthesis

Aside from the orthorhombic phase, there was another new lithium borohydride-imide, referred to as the cubic phase. From the initial series of reactions (Figure 4.1) the cubic phase appeared to be most abundant at 200 °C. Below 200 °C, although there was cubic phase present from 125 °C, there was still a significant proportion of orthorhombic phase. At 200 °C some Li$_3$BN$_2$ and LiH decomposition products had formed, however, upon increasing the temperature up to 225 °C or 250 °C there was a significant increase in Li$_3$BN$_2$

and LiH.[149] Consequently a more detailed investigation into the formation of products at the higher temperature of 200 °C was carried out, as this was determined to contain the lowest combined amount of the orthorhombic phase, Li_3BN_2 and LiH.

The initial 1:1 (n = 0.5) reaction of lithium imide and lithium borohydride performed at 200 °C resulted in a mixture of products and remaining starting materials. The most abundant product under those reaction conditions was the cubic phase; Figure 4.27 highlights the cubic phase in the final product. This fit is based on the formula Li_3BH_4NH, the structure which is discussed in detail in §5.4. The main cubic peak at *ca* 27.5 ° is the greatest in intensity and therefore was often used as the key identifying peak for the cubic phase throughout this work.

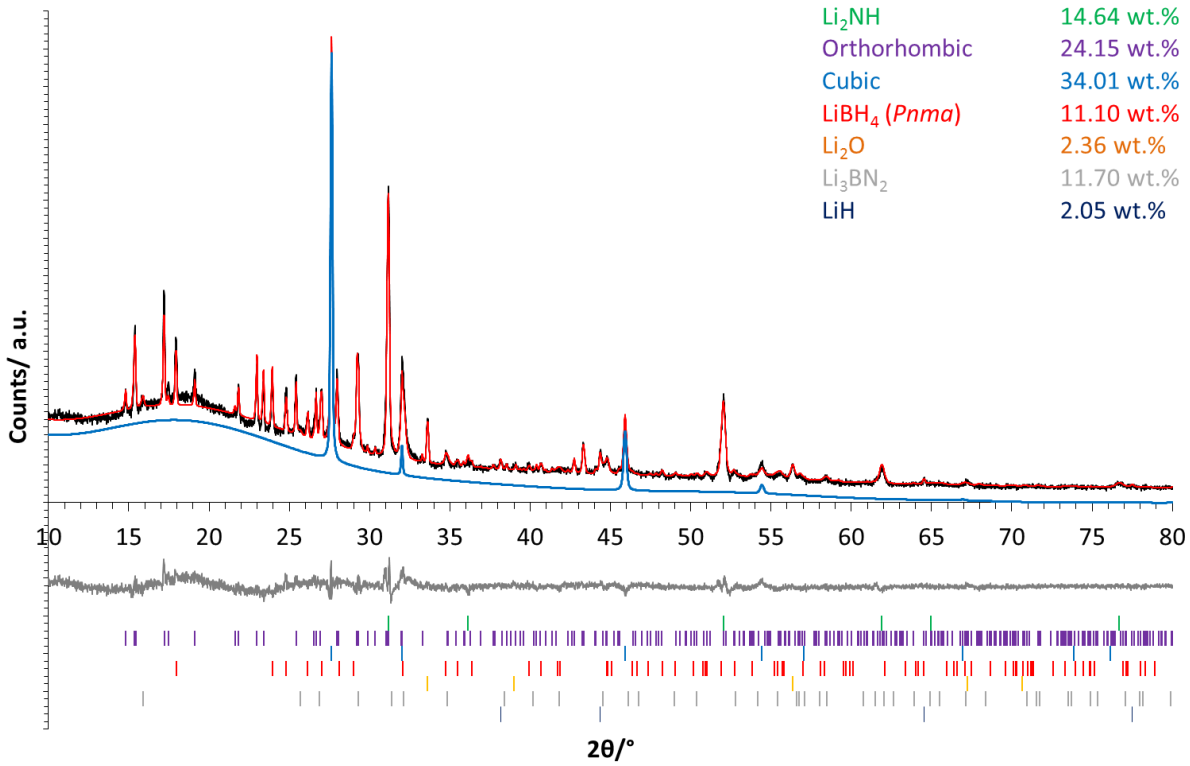

Figure 4.27 – Rietveld refinement plots of the products of the Li$_2$NH + LiBH$_4$ reaction carried out at 200 °C for 12 hours, where black = observed data, red = calculated data and grey = difference, highlighting the cubic phase in blue. Green tick marks = Li$_2$NH, purple tick marks = orthorhombic phase, blue tick marks = cubic phase, red tick marks = LiBH$_4$ (*Pnma*), orange tick marks = Li$_2$O, grey tick marks = Li$_3$BN$_2$ (*I*4$_1$/*amd*) and dark blue tick marks = LiH

4.5.1 Varying the Reactant Ratio

As was discussed at the start of this chapter (§4.3), at the higher temperatures, where the cubic phase was favoured, there was more lithium borohydride present in the final product mixture compared with the products of lower temperature syntheses. This observation suggested that a less LiBH$_4$-rich reaction mixture, in other words a more Li$_2$NH-rich mixture, may result in a greater amount of cubic phase. In order to test this theory a series of Li$_2$NH-rich reactions were carried out at 200 °C varying the Li$_2$NH:LiBH$_4$ ratio; from

1:1 up to 4:1. The ratios used were: 1:1, 5:4, 3:2, 7:4, 2:1, 5:2, 3:1 and 4:1 (n = 0.5, 0.56, 0.6, 0.64, 0.66, 0.71, 0.75 and 0.8, respectively). The powder XRD patterns of the resulting products are plotted in Figure 4.28.

The data presented show lithium imide was present in the product mixture across the whole ratio range. Increasing the amount of Li_2NH in the starting mixture seemed to predominantly increase the amount of Li_2NH in the final product mixture. However, as the amount of Li_2NH was increased relative to the amount of $LiBH_4$ (the reaction became more Li_2NH-rich), there was a decrease in the amount of orthorhombic phase, yet more evidence for the conclusions drawn earlier in this chapter (§4.4) that the orthorhombic phase is favoured by a more $LiBH_4$-rich reaction.

In addition to the known phases there were also several other peaks in the sample data, in particular at the more Li_2NH-rich end of the series. Initially when carrying out this study these peaks were unknown. However, further studies of the phase space identified the new hexagonal lithium amide-borohydride-imide phase, $Li_4BH_4NHNH_2$ (discussed in more detail in 4.6, §5.5), also identified as an impurity in the lower temperature work (§4.4), which matched to the majority of those peaks.

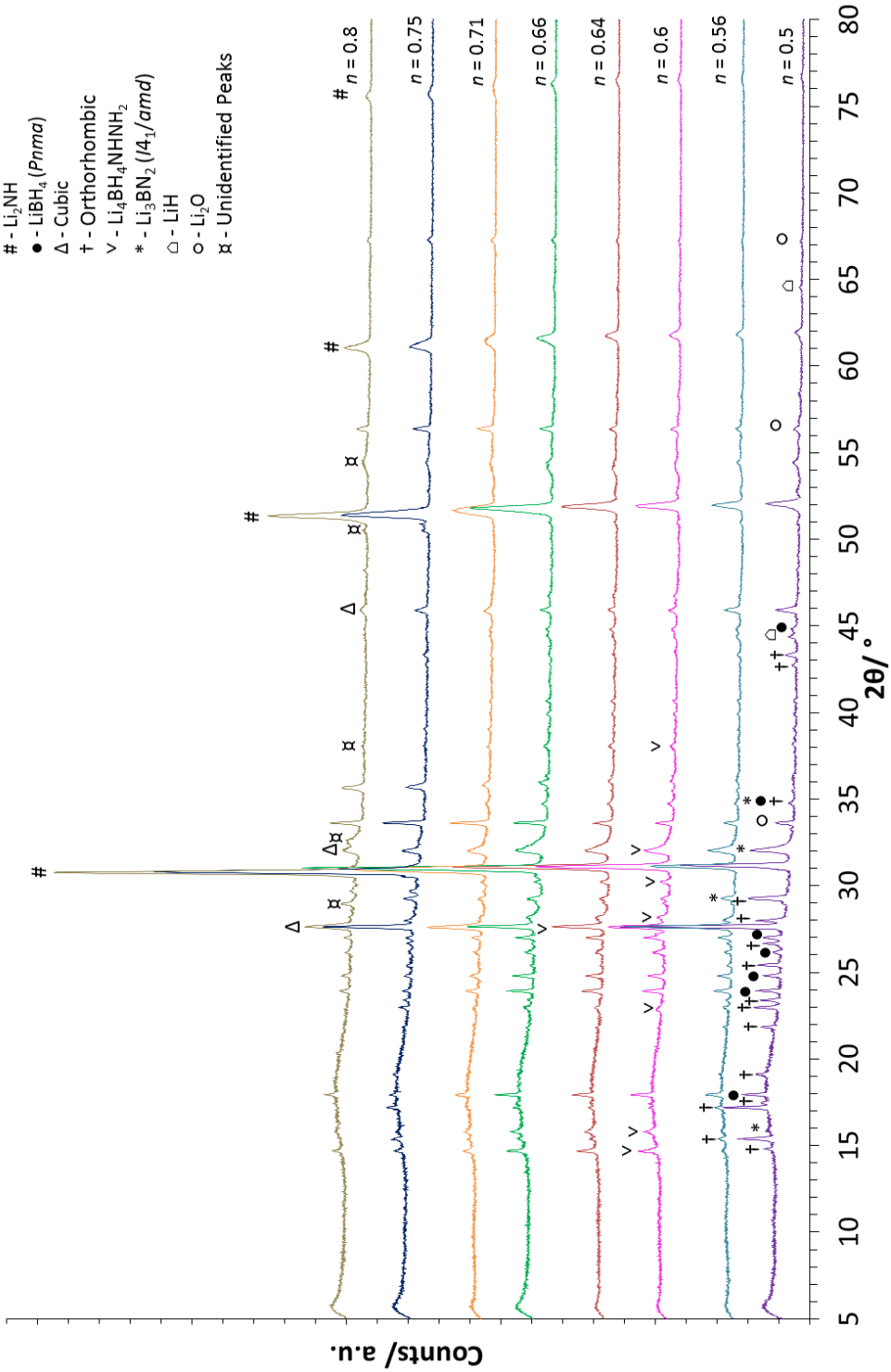

Figure 4.28 – Powder XRD data of the products of the reaction of Li$_2$NH + LiBH$_4$ at 125 °C for 12 hours in various Li$_2$NH-rich reaction conditions, where # = Li$_2$NH, ● = LiBH$_4$ (*Pnma*), Δ = cubic phase, † = orthorhombic phase, ᵛ = Li$_4$BH$_4$NHNH$_2$, * = Li$_3$BN$_2$ (*I*4$_1$/*amd*), ⌂ = LiH, ○ = Li$_2$O and ¤ = unidentified peaks

In order to quantify the data observed in Figure 4.28, Rietveld refinements were carried out with QPA, the results of which are displayed in Table 4.11 and Figure 4.29.

Table 4.11 – Weight percentages of the different components of the product mixture from the reaction of Li_2NH + $LiBH_4$ at 200 °C for 12 hours with various reactant ratios, where *n* refers to $nLi_2NH + (1 - n)LiBH_4$

	Weight Percent							
n	**Li_2NH**	**$LiBH_4$ (*Pnma*)**	**Cubic**	**Ortho**	**Li_3BN_2 (*I*4$_1$/*amd*)**	**LiH**	**$Li_4BH_4NHNH_2$**	**Li_2O**
0.5	14.6(1)	11.1(2)	34.0(3)	24.1(3)	11.7(3)	2.0(2)	0	2.4(1)
0.56	17.5(3)	12.3(4)	32.5(4)	7.1(4)	15.6(4)	1.2(3)	9.8(6)	4.2(2)
0.6	24.8(3)	18.5(4)	17.1(3)	0	18.2(4)	0	17.5(5)	3.9(2)
0.64	32.0(3)	16.1(4)	13.8(3)	0	15.3(4)	0	18.8(5)	4.0(2)
0.66	37.2(5)	12.8(4)	13.7(3)	3.8(5)	13.8(5)	0	15.1(5)	3.6(1)
0.71	33.3(4)	10.7(4)	20.4(4)	2.5(3)	16.4(4)	0	8.6(5)	8.1(2)
0.75	45.9(5)	5.8(5)	19.8(4)	9.1(4)	7.1(4)	0	7.3(6)	5.1(1)
0.8	62.3(6)	5.5(6)	21.8(5)	0	5.2(2)	0	0	5.2(2)

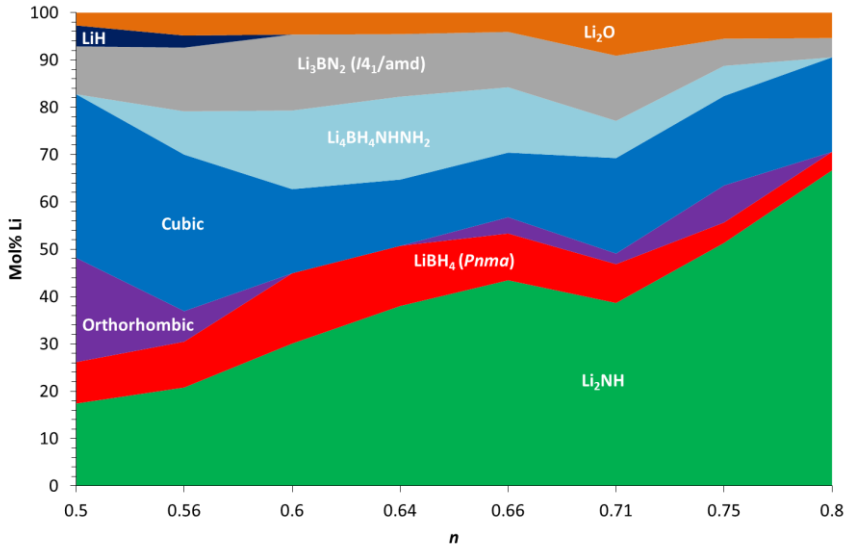

Figure 4.29 – Mole percentage lithium for the different components of the product mixture from the reaction of Li$_2$NH + LiBH$_4$ at 200 °C for 12 hours with various reactant ratios, where *n* refers to *n*Li$_2$NH + (1 – *n*)LiBH$_4$

The results of the refinements show there was an increase in the amount of Li$_2$NH in the final products as *n* was increased, until it dominated the product mixture at the most Li$_2$NH-rich end of the scale. Despite an increase in the amount of Li$_2$NH in the reactant mixture, an increase in the amount of cubic phase forming did not occur as was initially expected. The cubic phase was in fact more abundant at the 1:1 end of the investigated range. Therefore, in order to gain a clearer understanding of the impact of the reactant ratio on the products of the reaction at 200 °C, a series of reactions were performed across the entire composition range using various Li$_2$NH:LiBH$_4$ ratios. Both Li$_2$NH and LiBH$_4$-rich reaction conditions were investigated: 3:9, 4:8, 5:7, 6:6, 7:5, 8:4 and 9:3 (n = 0.25, 0.33, 0.42, 0.5, 0.58, 0.66 and 0.75, respectively); the reactions were performed according to the equation nLi$_2$NH + (1 – n)LiBH$_4$. The powder XRD patterns of the products of those reactions are shown in Figure 4.30.

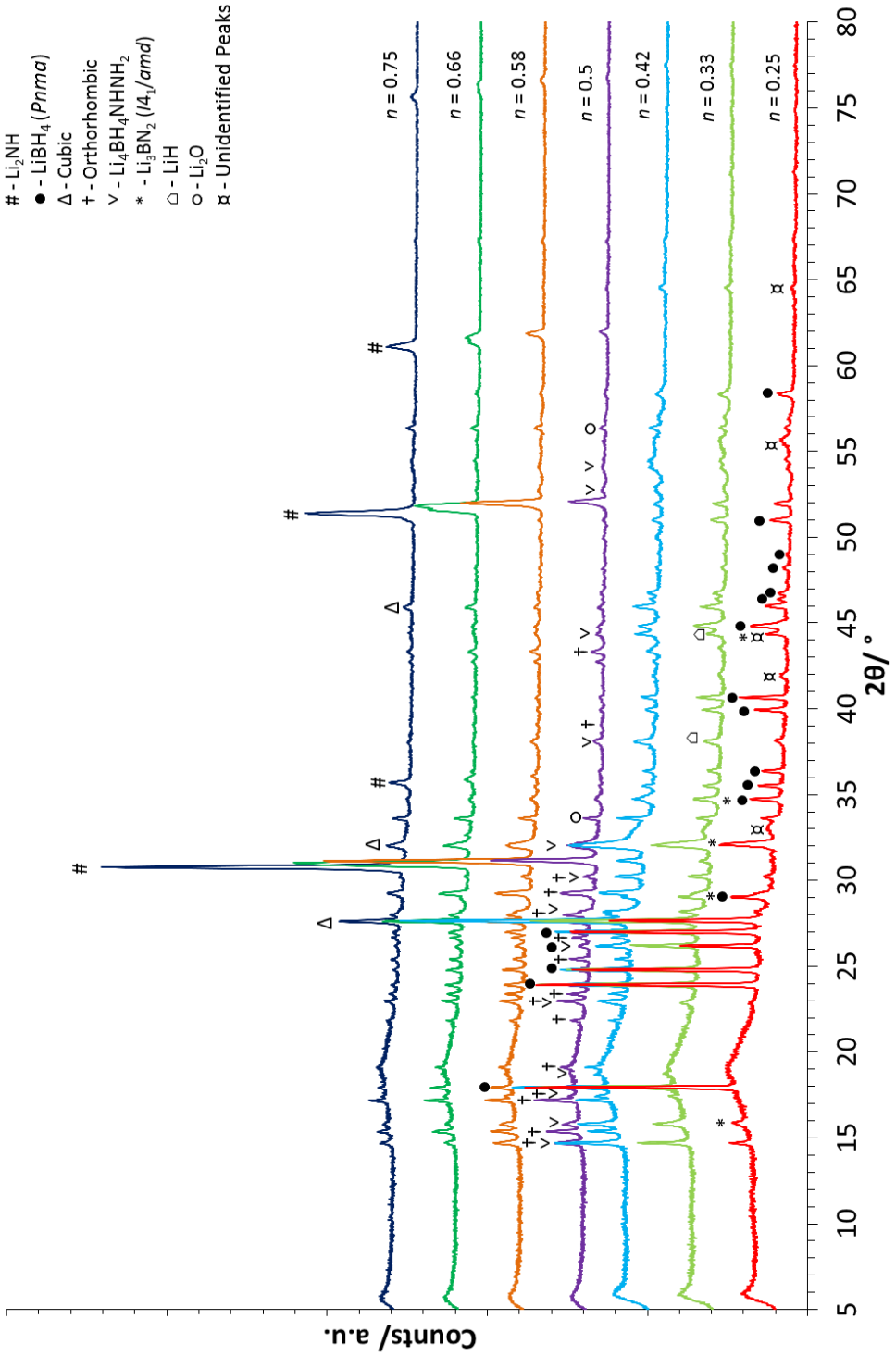

Figure 4.30 – Powder XRD data of the products of the reaction of nLi$_2$NH + (1 – n) LiBH$_4$ at 200 °C for 12 hours with various values of n, where # = Li$_2$NH, ● = LiBH$_4$ (*Pnma*), Δ = cubic phase, † = orthorhombic phase, ᵛ = Li$_4$BH$_4$NHNH$_2$, * = Li$_3$BN$_2$ (*I*4$_1$/*amd*), ⌂ = LiH, ○ = Li$_2$O and ¤ = unidentified peaks

Again as in the Li$_2$NH-rich series, Rietveld refinements were used to quantify the collected XRD data. Table 4.12 shows the weight percentages determined from the Rietveld refinements and Figure 4.31 the mole percentages of lithium.

Table 4.12 – Weight percentages of the different components of the product mixture from the reaction of nLi$_2$NH + (1 – n)LiBH$_4$ at 200 °C for 12 hours with various values of n

	Weight Percent							
n	**Li_2NH**	**$LiBH_4$ (*Pnma*)**	**Cubic**	**Ortho**	**Li_3BN_2 ($I4_1/amd$)**	**LiH**	**$Li_4BH_4NHNH_2$**	**Li_2O**
0.25	0	61.6(5)	19.2(3)	0	10.6(3)	0	7.5(4)	1.2(1)
0.33	0	45.6(4)	18.3(3)	0	13.2(3)	3.2(3)	17.1(4)	2.5(2)
0.42	0	23.9(4)	21.6(3)	10.4(3)	18.5(4)	3.8(3)	19.5(4)	2.4(1)
0.5	14.5(2)	15.4(4)	10.3(3)	25.5(4)	12.1(4)	2.3(4)	18.0(5)	1.9(1)
0.58	31.7(3)	13.7(4)	10.2(3)	18.3(4)	8.9(3)	1.0(3)	14.4(4)	2.0(1)
0.66	42.3(5)	9.4(3)	16.9(3)	14.3(4)	7.6(3)	0	7.5(6)	2.0(1)
0.75	57.3(5)	4.1(3)	15.1(3)	8.8(4)	5.0(3)	0	7.7(5)	1.9(1)

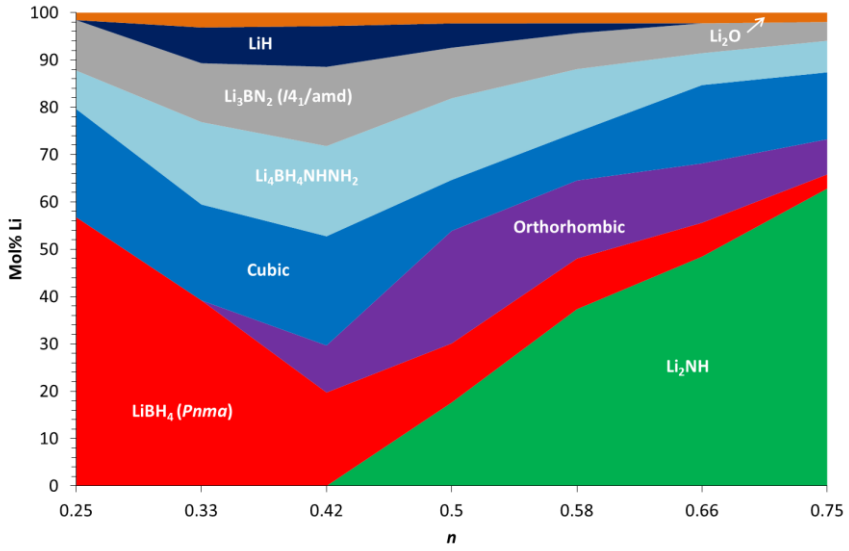

Figure 4.31 – Mole percentages lithium for the different components of the product mixture from the reaction of Li$_2$NH + LiBH$_4$ at 200 °C for 12 hours with various reactant ratios, where *n* refers to *n*Li$_2$NH + (1 – *n*)LiBH$_4$

As was to be expected the amount of Li$_2$NH increased and the amount of LiBH$_4$ decreased with increasing *n*. However, despite the clear trends in the starting materials there were no clear patterns in the products. The amount of cubic phase increased up to 5:7 (*n* = 0.42) where it peaked and then fluctuated as the reaction became more LiBH$_4$-rich. The orthorhombic phase was entirely absent until the 5:7 (*n* = 0.42) reaction, increasing only for the 6:6 (*n* = 0.5) before decreasing as the sample became more Li$_2$NH-rich. Finally, the hexagonal Li$_4$BH$_4$NHNH$_2$ phase (§4.6, §5.5) behaved similarly to the cubic phase, increasing up to a 5:7 ratio before decreasing again as more Li$_2$NH was added.

In order to try and observe any trends across the whole *n* range, and to take into account the Li$_2$NH-rich series, both data sets (Table 4.11 and Table 4.12) were plotted together in Figure 4.32. By including the additional points from the Li$_2$NH-rich series it is clear that there was a significant amount of fluctuation in the composition of the product

mixture. For example for the 6:6 (n = 0.5) ratio there are two data sets: in one the weight percent of cubic phase was 10.3(3)% and in the other 34.0(3) %. This is alongside a similar discrepancy in the amount of the hexagonal lithium amide-borohydride-imide phase.

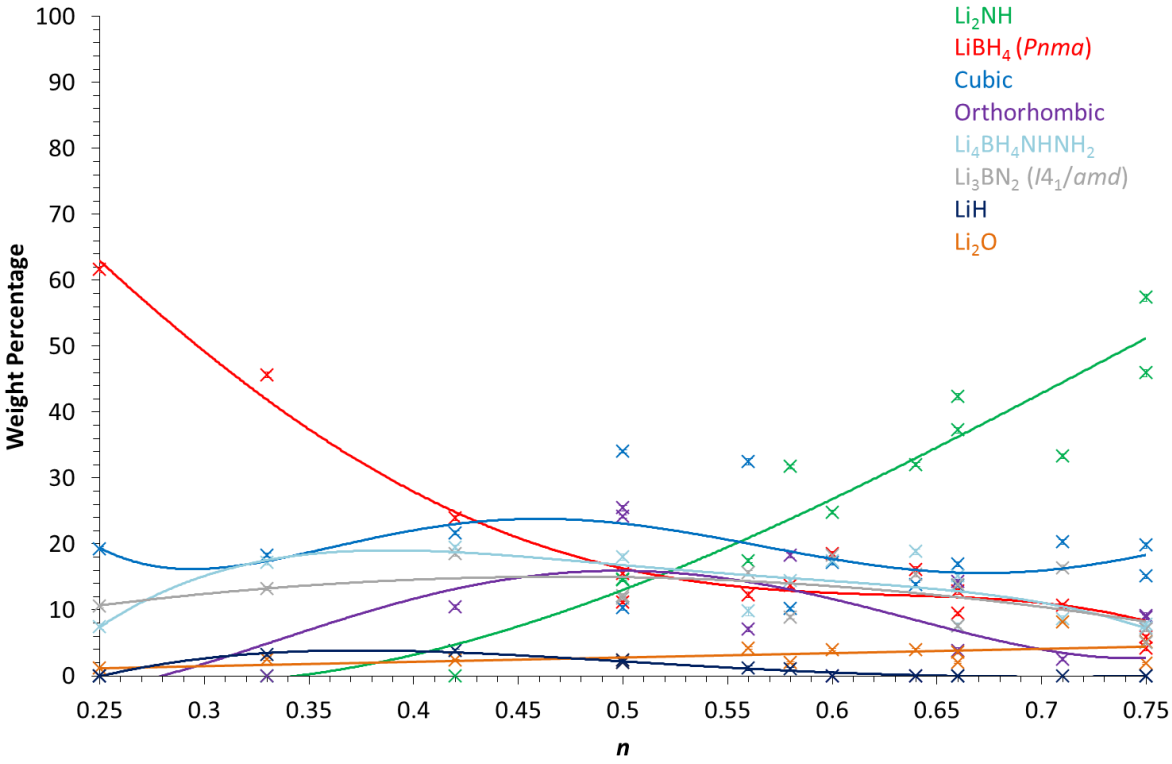

Figure 4.32 – Weight percentages determined from Rietveld refinement of the reaction of nLi$_2$NH + (1 – n)LiBH$_4$ with various values of n, heated at 200 °C for 12 hours. The solid lines are a polynomial fit and are intended to guide the eye only. Error bars are included but are smaller than the data point symbols

The variations in the formation of both the orthorhombic phase and cubic phase are quite significant and neither phase closely follows a path which would make it clear as to how the Li$_2$NH:LiBH$_4$ ratio affects their presence. Moreover there is the added complication of the lithium amide-borohydride-imide phase which again does not seem to follow a clear trend.

Due to the lack of a clear trend and amount of variation in the initial data (Figure 4.32) the series was repeated in order to try and determine whether the results were at all reproducible. The powder XRD data from the repeated series is presented in Figure 4.33. Unfortunately, repetition of the series resulted in more impurity phases, including the presence of multiple unknown broad peaks. There are multiple possibilities for the appearance of these phases, including the cooling rates of the furnace which may have affected crystallisation, and the time between the reactions and collecting the XRD data. These factors may have caused an issue depending on the stability of the products, as more stable products would favour slower cooling rates. Also with an increased period of time between any reaction and data collection, more stable phases may begin to form in the stored product mixture replacing any unstable phases.

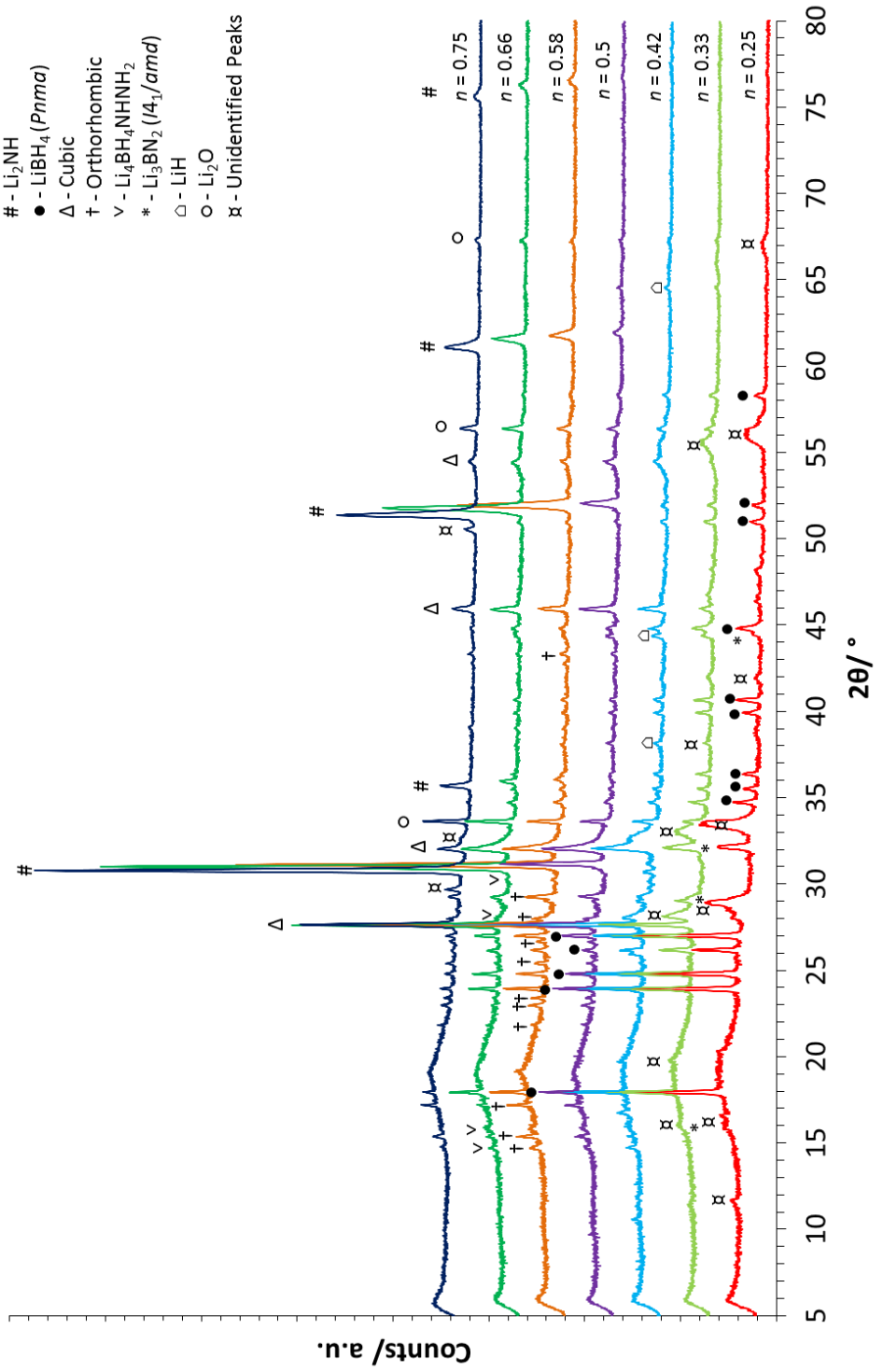

Figure 4.33 – Powder XRD data of the products of the repeated reaction series of nLi$_2$NH + (1 – n) LiBH$_4$ at 200 °C for 12 hours with various values of n, where # = Li$_2$NH, ● = LiBH$_4$ (*Pnma*), Δ = cubic phase, † = orthorhombic phase, ᵛ = Li$_4$BH$_4$NHNH$_2$, * = Li$_3$BN$_2$ (*I*4$_1$/*amd*), ⌂ = LiH, ○ = Li$_2$O and ¤ = unidentified peaks

When samples that were heated to 200 °C were removed from the furnace they did not appear the same as samples heated up to only 125 °C. Unlike the lower temperature samples, which were easily removed from the quartz reaction tube as a powder, the samples heated to 200 °C were stuck to the tube. Once removed from the tubes the samples appeared to have formed a solid block of material and were shiny in nature; they were also much more difficult to grind than the lower temperature samples. The appearance of the samples formed at 200 °C suggested that potentially these samples were melting. This could help to explain the lack of a clear trend in the data and the appearance of additional very broad unknown peaks, as the reliability of the formation of phases from a melt is much more difficult to predict.

In order to test this theory lithium imide and lithium borohydride were ground together and sealed in a glass capillary, repeated for both a 3:9 (n = 0.25) and a 4:8 (n = 0.33) ratio. The samples were then observed using a melting point apparatus as they were heated up to 200 °C. This study confirmed the formation of a melt as the samples were observed to melt between 134 and 140 °C. However, the slight opaqueness of the samples after melting suggested there may have been a solid component to the sample still. A more detailed study into the *in-situ* behaviour of these materials is discussed in §6.3.

Confirmation that a melt formed when the samples were heated up to 200 °C helped to explain the lack of a trend and difficulties with reproducibility when samples were heated to this higher temperature. Due to the nature of the crystallisation process small variations in the conditions, such as the cooling rate of the furnace, can have a notable impact on the materials which form.

The unidentified peaks were noticeably asymmetric and looked as though they may be due to the presence of multiple overlapping peaks. One possibility is that the peaks corresponded to a highly disordered phase, the broadness of the peaks being a result of the varying levels of disorder within the system causing the peaks to shift. Unfortunately, due to the lack of reflections and the width of the peaks indexing was not possible. It is likely that the peaks corresponded to a cubic structure as there were only a small number of reflections present. In particular the peak at *ca* 33 ° overlaps with the (200) peak corresponding to the known lithium borohydride-imide cubic phase (§5.4.2). Consequently it is possible that its presence was due to a high level of disorder and distortion in the already identified lithium borohydride-imide cubic phase.

In order to determine the stability of these phases – both the cubic and the unknown phase(s) – powder XRD data were collected four months after the initial data were collected to see if there were any observable changes. During that time the samples were stored in a sealed jar, contained within an argon-filled glove box, and were not exposed to the atmosphere at any time. The data are displayed in Figure 4.34.

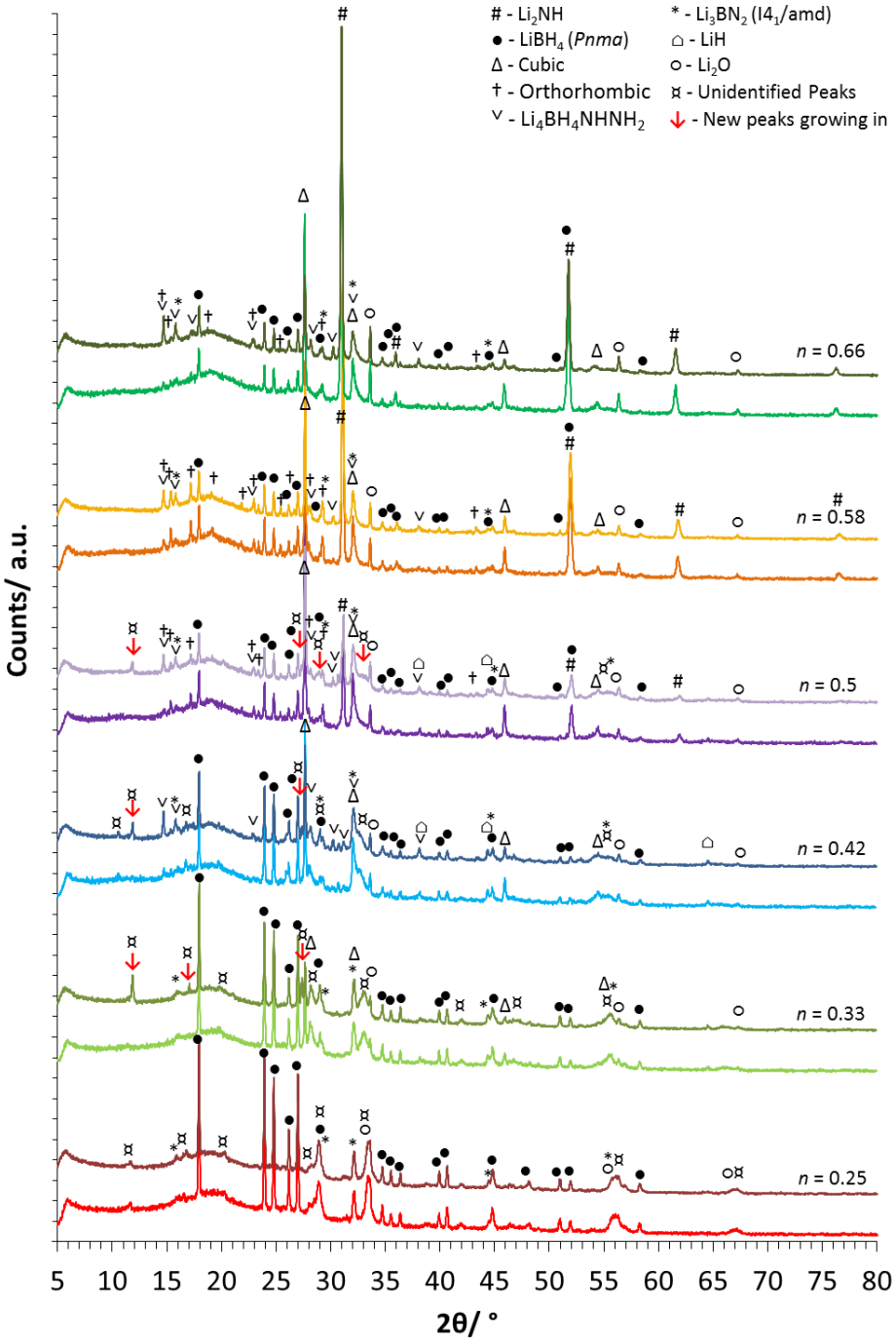

Figure 4.34 – Powder XRD data of the products of the repeated reaction series of nLi$_2$NH + (1 – n) LiBH$_4$ at 200 °C for 12 hours with various values of n, collected 4 months after initial synthesis, where # = Li$_2$NH, ● = LiBH$_4$ (*Pnma*), Δ = cubic phase, † = orthorhombic phase, ᵛ = Li$_4$BH$_4$NHNH$_2$, * = Li$_3$BN$_2$ (*I*4$_1$/*amd*), ⌂ = LiH, ○ = Li$_2$O, ¤ = unidentified peaks and new peaks which grew in are highlighted with a red arrow

One of the initial points to note is that although there were some changes in the samples over the course of the four months, there was not a complete breakdown of the products. Other than the two most borohydride-rich samples (n = 0.25 and n = 0.33) in which there was no hexagonal $Li_4BH_4NHNH_2$ (§4.6, §5.5) initially, the lithium amide-borohydride-imide phase became more dominant. The increase in the amount of $Li_4BH_4NHNH_2$ present was a clear indication that it is a thermodynamically stable phase. On the other hand the peaks corresponding to the cubic phase itself, which was initially the most dominant phase, decreased in intensity. This suggests that although the cubic phase was thought to be a more thermodynamically stable phase, due to its increased abundance through reannealing at lower temperatures (§4.4.2.3), it may not in fact be the case. The decline in the amount present alongside an increase in the amount of $Li_4BH_4NHNH_2$ suggests that the $Li_4BH_4NHNH_2$ phase may be the more thermodynamically favoured of the two.

In addition to the changes in intensity of the cubic phase and $Li_4BH_4NHNH_2$ phase peaks, there were additional peaks which appeared between the two scans, highlighted in Figure 4.34 by red arrows. These new peaks appeared in the 4:8 (n = 0.33), 5:7 (n = 0.42) and 6:6 (n = 0.5) samples, although only two peaks were consistently in all three, with an additional one in the 4:8 (n = 0.33) sample and another two appearing in the 6:6 (n = 0.5) sample. None of these peaks corresponded to any known phases, however, owing to the lack of reflections it may be that they were due to additional ordering of one of the other phases present; alternatively, they may have been due to another unknown phase.

4.5.2 Varying the Cooling Rates

Due to the decrease in the amount of cubic phase present after the samples were stored for four months, there was debate over the thermodynamic stability of the cubic phase. Previous data collected at the lower synthesis temperature of 125 °C (§4.4.2.3) suggested that in some cases reannealing favoured the cubic phase and thus contradicted the data collected four months after initial synthesis. Consequently, cooling rates were investigated in order to try and clarify this and to gain a greater understanding of the phase space.

A series of reactions were carried out using a 3Li$_2$NH:2LiBH$_4$ (n = 0.6) reactant ratio heated at 200 °C for 12 hours. This ratio was deemed an appropriate starting point as it was the reverse ratio to what was determined to be most suited to synthesising the orthorhombic phase. Initial conclusions had been that the cubic phase may adopt a more imide-rich structure compared to the borohydride-rich orthorhombic structure. This was based on the reduced amount of Li$_2$NH present at higher synthesis temperatures where the cubic phase formed more abundantly (§4.3). In addition it was considered that moving away from the optimum ratio for synthesising the orthorhombic phase would reduce its presence in the final product mixture. The first sample was removed from the furnace and quenched in air and cooling times were increased throughout the series up to a cooling rate of 0.05 °C min^{-1} for the final sample (Figure 4.35).

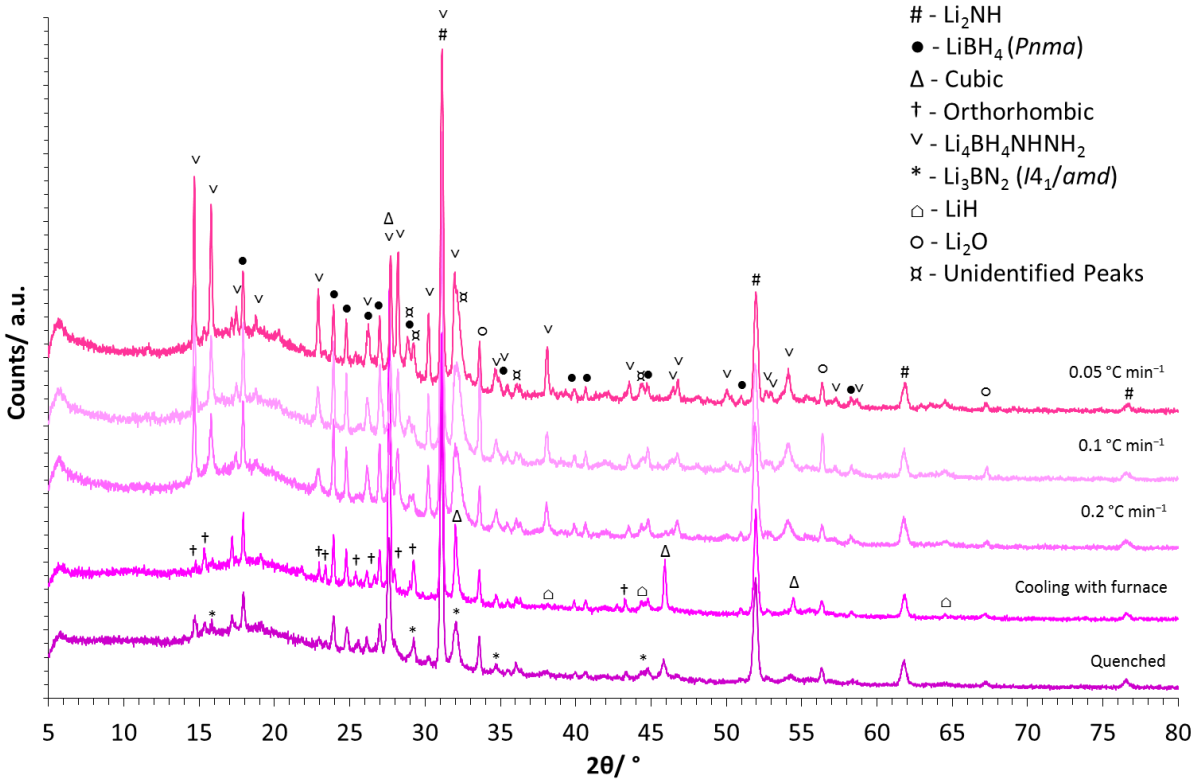

Figure 4.35 – Powder XRD data of the nLi$_2$NH + (1 – n)LiBH$_4$ reaction where n = 0.60, heated at 200 °C and cooled at various rates (quenched sample cooled in air), where # = Li$_2$NH, ● = LiBH$_4$ (*Pnma*), Δ = cubic phase, † = orthorhombic phase, ᵛ = Li$_4$BH$_4$NHNH$_2$, * = Li$_3$BN$_2$ (*I*4$_1$/*amd*), ⌂ = LiH, ○ = Li$_2$O and ¤ = unidentified peaks

The initial comparison of a sample quenched in air versus a sample cooled with the furnace supported the theory that the cubic phase is thermodynamically stable, as the slower cooling resulted in an increase in the amount of cubic phase. However, when this theory was tested further, and the cooling rates were slowed down below that achieved simply by turning off the furnace, there was a very different picture. Although the cubic phase was still present at all cooling rates, the hexagonal Li$_4$BH$_4$NHNH$_2$ phase (§4.6, §5.5), initially identified as an impurity in some of the earlier samples, began to dominate the diffraction pattern. This trend was a clear indication that the hexagonal Li$_4$BH$_4$NHNH$_2$ phase

was the more thermodynamically stable of the two. Table 4.13 and Figure 4.36 detail the results of QPA.

Table 4.13 – Weight percentages of the different components of the product mixture from the reaction of nLi$_2$NH + (1 – n)LiBH$_4$ where n = 0.60, heated at 200 °C and cooled at various rates

Cooling Rate /°C min^{-1}	Weight Percent							
	Li$_2$NH	LiBH$_4$ (*Pnma*)	Cubic	Ortho	Li$_3$BN$_2$ (*I*4$_1$/*amd*)	LiH	Li$_4$BH$_4$NHNH$_2$	Li$_2$O
Quenched in air	30.9(4)	16.9(4)	23.4(4)	5.6(4)	11.9(3)	0	8.6(6)	2.8(1)
Cooled with furnace	24.4(2)	14.5(3)	35.3(3)	8.1(3)	14.2(3)	1.0(2)	0	1.5(1)
0.2	26.1(4)	19.0(4)	4.1(6)	0	16.8(5)	0	32.1(5)	1.8(1)
0.1	22.1(3)	19.7(5)	0	0	21.6(5)	0	33.1(5)	3.6(1)
0.05	20.9(3)	13.8(5)	0	0	21.8(5)	0	41.5(5)	2.0(1)

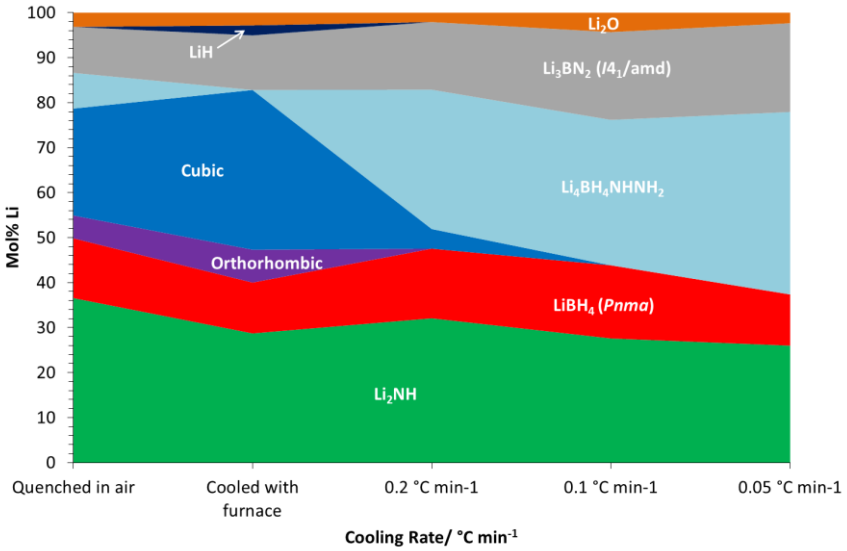

Figure 4.36 – Mole percentage lithium of the different components of the product mixture from the reaction of nLi$_2$NH + (1 – n)LiBH$_4$ where n = 0.60, heated at 200 °C and cooled at various rates

Studies carried out at the higher synthesis temperature of 200 °C have provided more information on the complexity of the phase space and of the cubic phase itself. Although initial conclusions suggested an imide-rich anion ratio, these studies have indicated that the true anion ratio of the cubic phase could be closer to 1:1. Despite this, it is clear that significant fluctuations in the final product ratios can be observed across the entire reactant ratio range. The discovery that the reaction mixture is molten at 200 °C helps to explain these disparities as cooling rates would have played a significant role in the crystallisation of products.

Investigations into the stability of the cubic phase after a period of four months showed that it was actually the lithium amide-borohydride-imide phase which became more abundant, whilst the cubic phase became less so. These changes were alongside the appearance of some unknown peaks in the XRD data suggesting there may be other unknown phases which are thermodynamically stable. The data collected as a result of changing the cooling rates seemed to be the clearest indicator that the $Li_4BH_4NHNH_2$ phase (§4.6, §5.5), and not the cubic phase, is likely to be the most thermodynamically stable structure in the phase space.

4.6 Amide-imides + Borohydride

After studying the synthesis of the two borohydride-imide phases, it was then considered whether a mixed lithium amide-imide could be used to form a similar phase or phases with lithium borohydride. It was also thought that any new phases synthesised in these lithium amide-imide + lithium borohydride reactions may also help to identify unknown peaks appearing in some of the borohydride-imide reactions. This was proven to

be the case with the appearance of hexagonal $Li_4BH_4NHNH_2$ phase (§5.5) peaks in various samples throughout the lithium borohydride-imide synthesis work which consequently appeared to be more thermodynamically stable than either the orthorhombic or cubic phase. This conclusion was based on several observations of the behaviour of the $Li_4BH_4NHNH_2$ phase in various different reactions. Firstly, the increase in the amount of $Li_4BH_4NHNH_2$ when a sample was reground and reannealed (§4.4.2.3); the increase in the amount of $Li_4BH_4NHNH_2$ present in a sample after being stored in an inert atmosphere for an extended period of time, alongside a decline in the amount of the cubic borohydride-imide phase (Figure 4.34); and finally the preferential formation of $Li_4BH_4NHNH_2$ over the cubic borohydride-imide phase with slower cooling rates (§4.5.2).

In the reactions reported in this section, lithium amide-imide was synthesised, as in §3.5, using a 1:1 Li_2NH to $LiNH_2$ ratio, heated at 350 °C for 12 hours to form "$Li_{1.5}(NH_2)_{0.5}(NH)_{0.5}$". This was then heated in various different ratios with $LiBH_4$ using the equation $nLi_{1.5}(NH_2)_{0.5}(NH)_{0.5}$ + (1 – n)$LiBH_4$. These reactions were carried out at the preferred synthesis temperatures for the orthorhombic and cubic phase, 125 °C and 200 °C, respectively, for 12 hours.

4.6.1 Synthesis at 125 °C

Synthesis was first carried out at 125 °C using ratios of lithium amide-imide to lithium borohydride: 3:9, 4:8, 5:7, 6:6, 7:5, 8:4 and 9:3 – n = 0.25, 0.33, 0.42, 0.5, 0.58, 0.66 and 0.75, respectively using the equation $nLi_{1.5}(NH_2)_{0.5}(NH)_{0.5}$ + (1 – n)$LiBH_4$. The XRD data collected from these samples are shown in Figure 4.37.

These reactions resulted in the formation of $Li_4BH_4(NH_2)_3$, a lithium amide-borohydride previously studied in the group by Chater[97] and Hewett,[81] as well as several unidentified peaks. Some of these peaks were determined to belong to a new hexagonal phase, initially observed as a side product in the Li_2NH + $LiBH_4$ reaction performed under various conditions. The new phase was indexed and found to have the space group $P3_221$ and lattice parameters, a = 6.9483(1) Å and c = 15.1981(7) Å (§5.5). The orthorhombic and cubic phases observed in the Li_2NH-$LiBH_4$ syntheses were not present in the products of these reactions.

The main product phases of these reactions, $Li_4BH_4(NH_2)_3$ and the hexagonal $Li_4BH_4NHNH_2$ phase (§5.5) are clearly highlighted in Figure 4.37. However, it is important to note that alongside these two products and the starting materials there were some additional unidentified peaks, in particular at the more lithium borohydride-rich end of the series. Interestingly the sharp pair of peaks at *ca* 13.3 °, which were present in the low temperature (100 °C) reannealing series of the lithium imide and lithium borohydride reaction (§4.4.1.1), were also present in this series. Another unidentified peak from the nLi$_2$NH + (1 – n)LiBH$_4$ reactions was a broad peak at *ca* 7 °. Initially this was thought to possibly be an additional ordering peak for one of the borohydride-imide phases. However, its appearance in these reactions, alongside the absence of either the cubic or orthrhombic phase, suggests it belongs to another phase entirely. This new phase could be another lithium borohydride-imide or alternatively a new lithium amide-borohydride-imide phase.

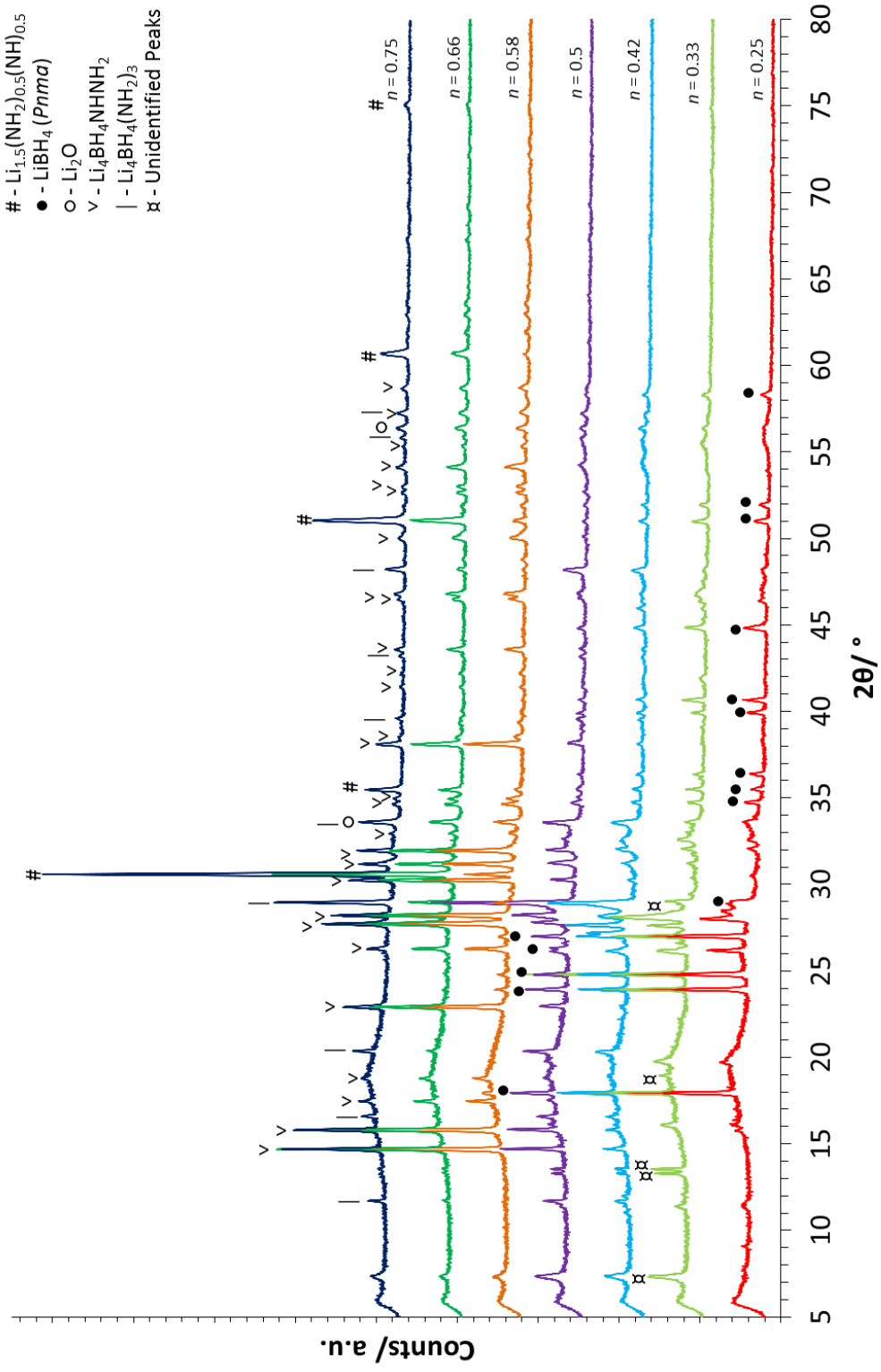

Figure 4.37 – Powder XRD data of the nLi$_{1.5}$(NH$_2$)$_{0.5}$(NH)$_{0.5}$ + (1 – n)LiBH$_4$ reaction with various values of n, heated at 125 °C for 12 hours, where # = Li$_{1.5}$(NH$_2$)$_{0.5}$(NH)$_{0.5}$, ● = LiBH$_4$ (*Pnma*), | = Li$_4$BH$_4$(NH$_2$)$_3$, ᵛ = Li$_4$BH$_4$NHNH$_2$ phase, ○ = Li$_2$O and ¤ = unidentified peaks

In order to quantify the data and determine the best conditions for synthesis of the new hexagonal $Li_4BH_4NHNH_2$ phase (§5.5), Rietveld refinements with QPA were carried out. However, it is important to note that that the results presented in Figure 4.38 do not consider the presence of unidentified peaks, of which there were a few at the $LiBH_4$-rich end of the series. They do still provide an overview of the different phases and the most favourable reaction conditions.

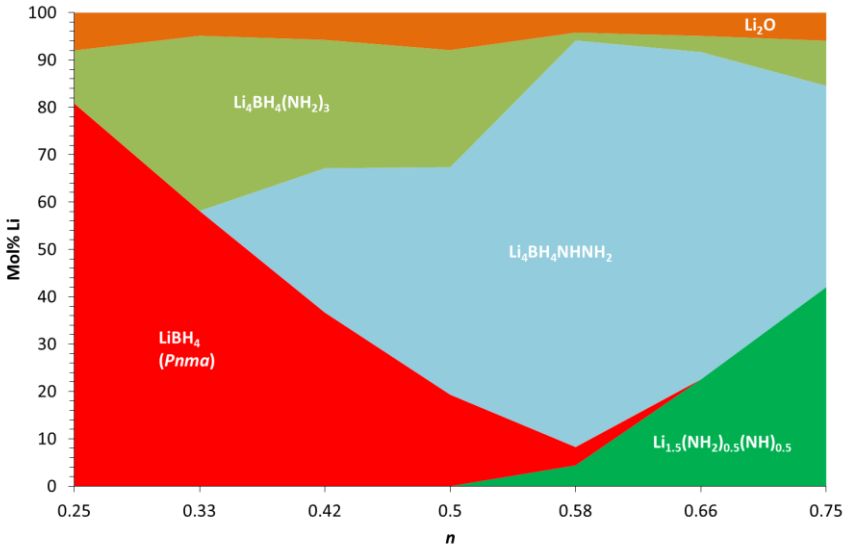

Figure 4.38 – Mole percentage lithium determined through Rietveld refinement for the nLi$_{1.5}$(NH)$_{0.5}$(NH$_2$)$_{0.5}$ + (1 – n)LiBH$_4$ reaction with various values of n, heated at 125 °C for 12 hours

The results given in Figure 4.38 show that in the $LiBH_4$-rich region there was a fairly consistent amount of $Li_4BH_4(NH_2)_3$, however, as the reaction became more Li_2NH-rich the $Li_4BH_4NHNH_2$ phase began to dominate the product mixture. The data show the new hexagonal $Li_4BH_4NHNH_2$ phase was favoured in more amide-imide-rich reaction conditions, with the maximum amount forming at a ratio of 7:5 (n = 0.58). At this reactant ratio there were similar weight percentages of $LiBH_4$ and $Li_{1.5}(NH_2)_{0.5}(NH)_{0.5}$ remaining in the product

mixture. Thus, it is possible that through reannealing or longer heating times they could be removed or at least the amount present could be reduced forming a pure product.

4.6.2 Synthesis at 200 °C

The nLi$_{1.5}$(NH$_2$)$_{0.5}$(NH)$_{0.5}$ + (1 – n)LiBH$_4$ reaction was then repeated at a higher temperature of 200 °C using various different reaction ratios: 3:9, 4:8, 5:7, 6:6, 7:5, 8:4 and 9:3 (n = 0.25, 0.33, 0.42, 0.5, 0.58, 0.66 and 0.75, respectively). The results of these reactions are shown in Figure 4.39.

Despite the fact that the hexagonal Li$_4$BH$_4$NHNH$_2$ phase (§5.5) appeared more frequently as a product of the Li$_2$NH + LiBH$_4$ reaction at 200 °C rather than 125 °C, the powder XRD patterns in Figure 4.39 shows that Li$_4$BH$_4$(NH$_2$)$_3$ was the most dominant phase in the Li$_{1.5}$(NH$_2$)$_{0.5}$(NH)$_{0.5}$ + LiBH$_4$ reaction at 200 °C. The Li$_4$BH$_4$NHNH$_2$ lithium amide-borohydride-imide phase only began to form at the most amide-imide-rich end of the reaction series and was present in the products of the n = 0.66 and n = 0.75 reactions. The cubic borohydride-imide phase was also found in both the n = 0.5 and n = 0.58 reactions.

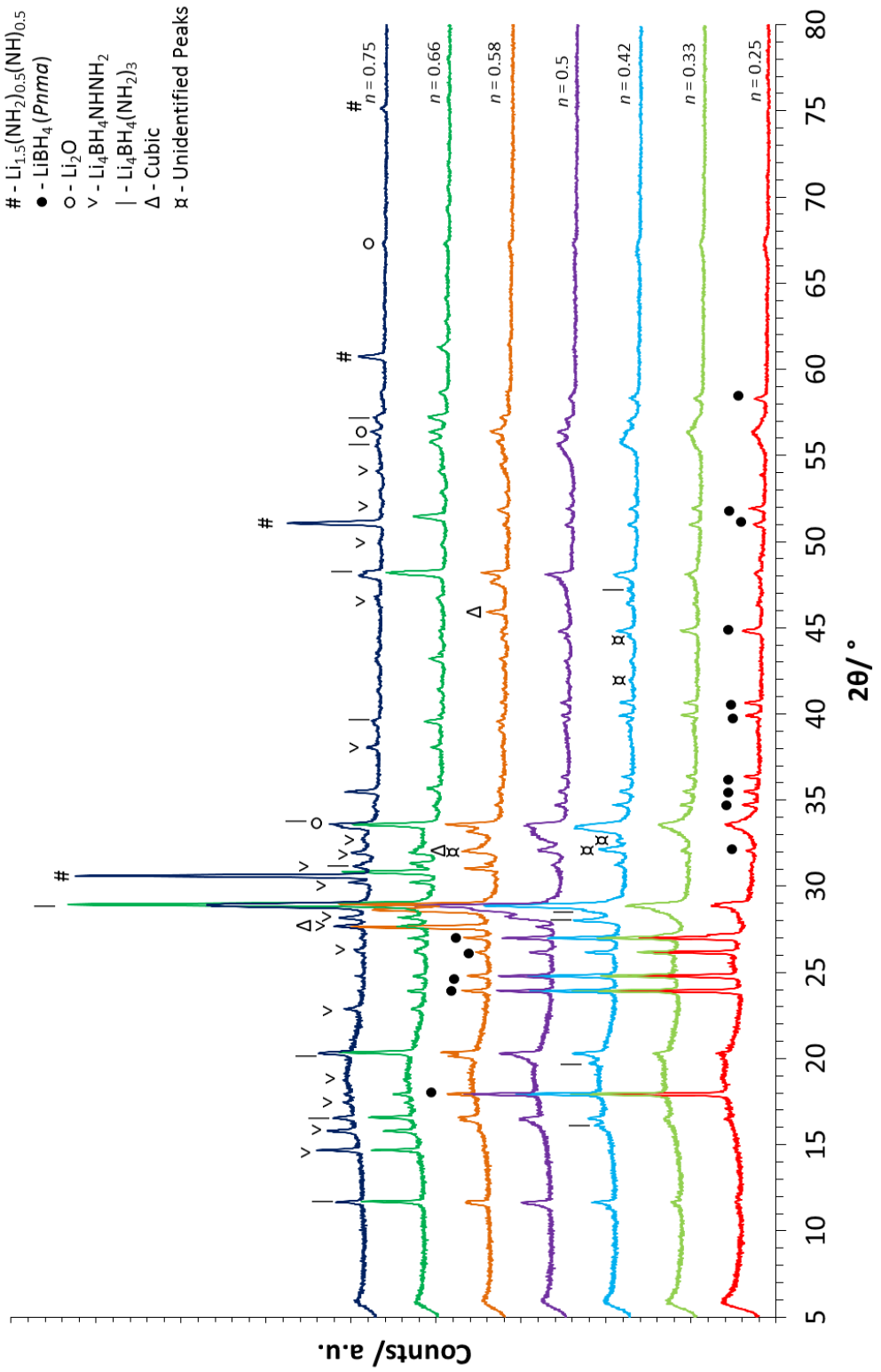

Figure 4.39 – Powder XRD data of the nLi$_{1.5}$(NH$_2$)$_{0.5}$(NH)$_{0.5}$ + (1 – n)LiBH$_4$ reaction with various values of n, heated at 200 °C for 12 hours, where # = Li$_{1.5}$(NH$_2$)$_{0.5}$(NH)$_{0.5}$, ● = LiBH$_4$ (*Pnma*), ᵛ = Li$_4$BH$_4$NHNH$_2$ phase, | = Li$_4$BH$_4$(NH$_2$)$_3$, ○ = Li$_2$O and ¤ = unidentified peaks

$Li_4BH_4(NH_2)_3$ has been reported as a thermodynamically stable structure synthesised at 190 °C by reacting $3LiNH_2 + 1LiBH_4$, and is also formed from a melt.[100] The formation of $Li_4BH_4(NH_2)_3$ over the $Li_4BH_4NHNH_2$ phase at these higher temperatures suggests that the $Li_4BH_4(NH_2)_3$ structure may be more favourable. However, under $Li_2NH + LiBH_4$ reaction conditions it is possible there was insufficient hydrogen for its formation but a sufficient amount for the $Li_4BH_4NHNH_2$ phase (§5.5) to form.

There were some unidentified peaks in this series, in particular at the more $LiBH_4$-rich end of the scale. Some of the unidentified peaks were quite broad and in some cases they were very close to the reflections for other known phases. For example, the most intense Li_2O peak at *ca* 33.5 ° appeared to be very broad and quite high in intensity. However, the (400) reflection of the $Li_4BH_4(NH_2)_3$ phase does overlap with the (111) of the Li_2O, and the broadness and asymmetry of the peak suggests that there may have been other reflections there too. The n = 0.5 sample quite clearly shows there were multiple peaks in this region (30 to 34 °) as in this sample splitting was observed. One explanation is the possibility of NH^{2-} anions being incorporated into the $Li_4BH_4(NH_2)_3$ structure and consequently causing some distortions. Alternatively there may have been another unknown phase present.

Other methods which could help in the identification of the products of these reactions are FTIR and Raman spectroscopy. These techniques are useful to look at the difference in bonding between materials, and to identify the anions present and their environments. The assignment of Li_2NH Raman data, has been discussed in the literature[83] and is discussed extensively in Chapter 3. NH_2^- and NH^{2-} vibrations occur in Raman data between 3000 and 3500 cm^{-1} with the NH^{2-} vibrations appearing at a lower wavenumber

(§Figure 3.6). The difference between these peaks can help to determine the ratio of these two anions.

FTIR and Raman spectra of both $LiBH_4$ and $LiNH_2$ have been more conclusively assigned in the literature.[138,150,151] Therefore, comparisons can be made against data collected on any new crystal structures and can help in identifying changing environments and bonding in a material. Previous research in the group used this strategy to look at the bonding in $Li_4BH_4(NH_2)_3$,[97] with the absence of some vibrations indicating higher levels of symmetry and more constrained environments, compared with the parent materials. The shifting of peaks to lower wavenumbers also indicated a weakening of B–H and N–H bonds. Consequently, in future work it may also prove useful to do a similar study comparing the products of these reactions to data collected on the parent materials and $Li_4BH_4(NH_2)_3$.

Rietveld refinements with QPA were carried out againt the data from the reaction series at 200 °C, the results of which are shown in Figure 4.40. From this analysis it was determined that there were up to three different $Li_4BH_4(NH_2)_3$ phases in each sample. This indicates that although there may have been a stoichiometric $Li_4BH_4(NH_2)_3$ phase, there were also likely to have been other non-stoichiometric phases. These may have been due to the introduction of NH^{2-} anions or alternatively from forming a more borohydride-rich structure. Only at the most amide-imide-rich end of the series where n = 0.66 and n = 0.75 did a single $Li_4BH_4(NH_2)_3$ phase form.

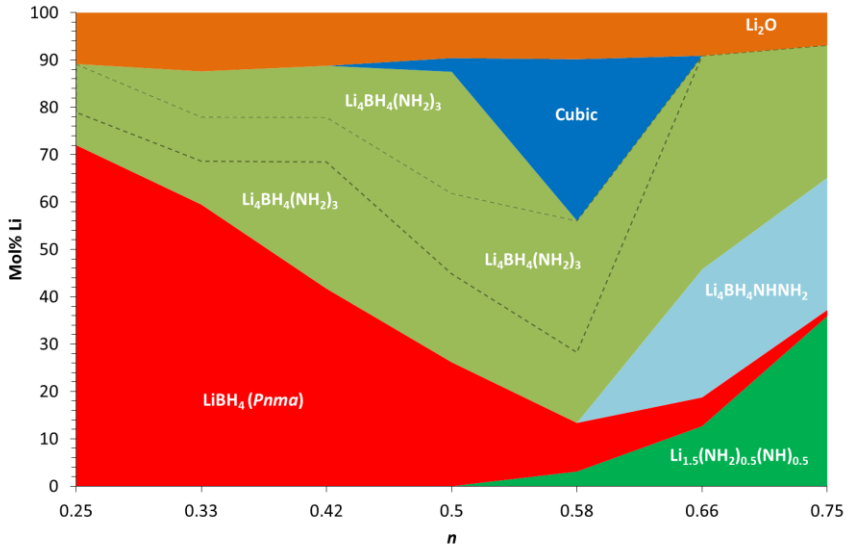

Figure 4.40 – Mole percentage lithium determined through Rietveld refinement for the nLi$_{1.5}$(NH)$_{0.5}$(NH$_2$)$_{0.5}$ + (1 – n)LiBH$_4$ reaction with various values of n, heated at 200 °C for 12 hours

Lattice parameters determined from the different Li$_4$BH$_4$(NH$_2$)$_3$ phases showed significant variation (Figure 4.41). When comparing the different structures synthesised at 125 °C there seemed to be little variation in the lattice parameters from n = 0.42 up to n = 0.75, however, at the most borohydride-rich end of the series the values jumped up to *ca* 11 Å. Chater *et al.* reported that an increase in lattice parameters could be observed if the ratio became more borohydride-rich, for Li$_4$(BH$_4$)$_{(1+x)}$(NH$_2$)$_{(3-x)}$, where x = 0.326, a lattice parameter of a = 10.8296(8) Å was reported.[100] Although this value is not as high as those determined in this series, it may be that introduction of NH^{2-} and consequently a higher level of disorder resulted in a larger unit cell.

At 200 °C, although there were multiple structures present, the lattice parameter of one of those structures remained close to the stoichiometric lattice parameter across the series. This suggests that a stoichiometric structure may have been favoured but excess BH$_4$

or NH was perhaps incorporated into a non-stoichiometric structure or structures resulting in the larger unit cells reported.

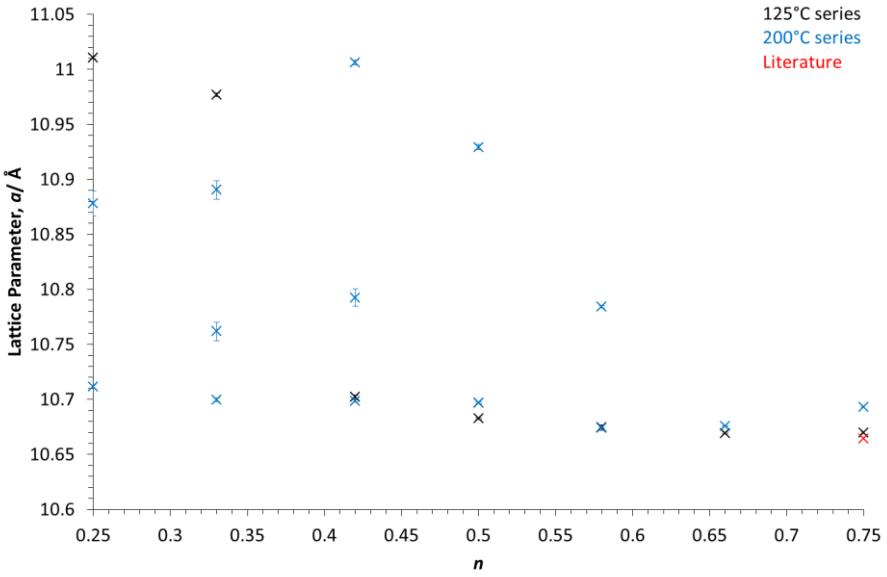

Figure 4.41 – Lattice parameters of cubic $Li_4BH_4(NH_2)_3$ phases from the nLi$_{1.5}$(NH)$_{0.5}$(NH$_2$)$_{0.5}$ + (1 – n)LiBH$_4$ reaction performed at 125 °C (black) and 200 °C (blue). The literature value[96] is shown in red. Error bars are included but in some cases are smaller than the data point symbols

These nLi$_{1.5}$(NH$_2$)$_{0.5}$(NH)$_{0.5}$ + (1 – n)LiBH$_4$ reactions have enabled a new phase to be identified, a hexagonal amide-imide-borohydride phase, Li$_4$BH$_4$NHNH$_2$. The discovery of this phase also helped to characterise the results of the Li$_2$NH + LiBH$_4$ reaction as it regularly formed as an impurity phase in those reactions. It is possible that it was able to form in small amounts due to some amide anions remaining in the lithium imide structure. In terms of the reactions in which a significant proportion of the hexagonal Li$_4$BH$_4$NHNH$_2$ phase was present, the presence of residual amide anions is unlikely to be the sole reason. Hewett previously suggested that LiBH$_4$ may have been acting as a reducing agent when observing similar trends resulting in the formation of more NH$_2$.[81] The formation of Li$_3$BN$_2$ and therefore

release of H_2 in the reactions may enable the hydrogenation of NH^{2-} to NH_2^- and thus allows this new phase to form. It does seem to be the case that the hexagonal $Li_4BH_4NHNH_2$ phase (§5.5) is more thermodynamically stable phase than either the cubic or orthorhombic phase, based on its increased abundance over time (§4.5.1) and through reannealing at 125 °C (§4.4.2.3). The preferential formation of $Li_4BH_4NHNH_2$ in the slow cooled series at 200 °C is perhaps the most clear indication of its stability over the cubic phase (§4.5.2). However, in order to more conclusively determine the thermal properties of $Li_4BH_4NHNH_2$ it would be useful to perform differential scanning calorimetry (DSC) in the future, as well as collecting *in-situ* XRD data as the $n Li_{1.5}(NH_2)_{0.5}(NH)_{0.5}$ + (1 – n)$LiBH_4$ reaction progresses.

4.7 Further High Temperature Synthesis

After determining the hexagonal $Li_4BH_4NHNH_2$ phase (§5.5) was likely to be the most thermodynamically stable phase in the Li_2NH-$LiBH_4$ phase space and subsequently investigating the $LiNH_2$ + $LiBH_4$ reaction to form a purer $Li_4BH_4NHNH_2$ phase, quenching and reannealing of the Li_2NH + $LiBH_4$ reaction products were performed. The aim of these additional experiments was to provide greater clarity on both the kinetic products and any possible thermodynamically stable products through reannealing.

4.7.1 Quenching

As slower cooling of the Li_2NH + $LiBH_4$ reaction resulted predominantly in the formation of the hexagonal $Li_4BH_4NHNH_2$ phase, this was identified as an unsuitable route to forming the cubic phase. In order to try and gain a greater understanding of the number of phases present and potentially isolate more kinetic phases, samples were heated to 200 °C for 12 hours then quenched in ice cold water. This was carried out with a range of

Li$_2$NH:LiBH$_4$ ratios: 3:9, 4:8, 5:7, 6:6, 7:5, 8:4 and 9:3 [n = 0.25, 0.33, 0.42, 0.5, 0.58, 0.66 and 0.75, respectively, using the equation nLi$_2$NH + (1 – n)LiBH$_4$]. The resulting data are shown in Figure 4.42.

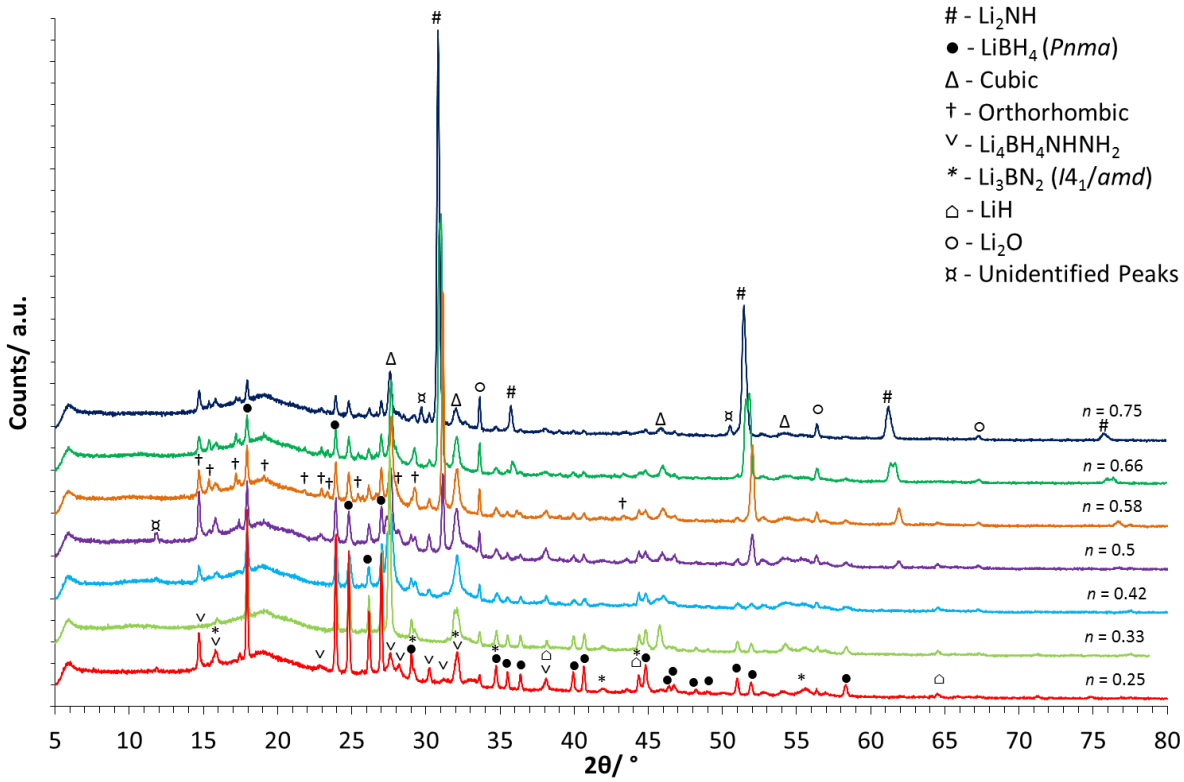

Figure 4.42 – Powder XRD data of the nLi$_2$NH + (1 – n)LiBH$_4$ reaction with various values of n, heated at 200 °C and quenched in cold water after 12 hours, where # = Li$_2$NH, ● = LiBH$_4$ (*Pnma*), Δ = cubic phase, † = orthorhombic phase, ᵛ = Li$_4$BH$_4$NHNH$_2$, * = Li$_3$BN$_2$ (*I*4$_1$/*amd*), ⌂ = LiH, ○ = Li$_2$O and ¤ = unidentified peaks

As is to be expected from a series in which the reactant ratio was changing, there was a clear trend of increasing Li$_2$NH and decreasing LiBH$_4$ with n for nLi$_2$NH + (1 – n)LiBH$_4$. Contrary to what was expected there also appeared to be no orthorhombic phase at the more LiBH$_4$-rich end of the series, although it did form at the more Li$_2$NH-rich end of the series. As these samples were quenched from a melt it may be that some kinetic phases

formed slightly randomly, despite composition, and thus the usual trend was not applicable in this case.

Despite quenching the samples, the hexagonal $Li_4BH_4NHNH_2$ phase (§5.5) was still formed, although not as the dominant phase as was the case in the slow cooled samples. There were also a few unidentified peaks. However, the peak at *ca* 11.8 ° had been seen previously in the XRD data collected after the samples were stored for four months; and the broad peak at *ca* 33 ° has been frequently observed and is possibly due to variation in a disordered cubic phase. As with the other previous reactions, in order to quantify these observations Rietveld refinements were carried out (Table 4.14 and Figure 4.43).

Table 4.14 – Weight percentages determined through Rietveld refinement and fixed intensity Pawley fit for the nLi$_2$NH + (1 – n)LiBH$_4$ reaction with various values of n, heated at 200 °C and quenched in cold water after 12 hours

	Weight Percent							
n	**Li_2NH**	**$LiBH_4$ (*Pnma*)**	**Cubic**	**Ortho**	**Li_3BN_2 ($I4_1/amd$)**	**LiH**	**$Li_4BH_4NHNH_2$**	**Li_2O**
0.25	0	59.7(5)	0	0	8.6(2)	3.5(3)	25.6(5)	2.7(2)
0.33	0	38.2(3)	41.4(3)	0	15.5(2)	3.6(2)	0	1.3(1)
0.42	0	27.5(5)	41.5(5)	0	19.2(4)	3.3(2)	7.2(5)	1.5(1)
0.5	7.2(2)	24.3(5)	24.2(6)	0	17.9(5)	2.1(3)	21.8(6)	2.5(1)
0.58	21.4(2)	19.3(4)	22.2(3)	6.7(3)	12.4(3)	1.6(2)	14.7(5)	1.7(1)
0.66	40.8(4)	13.6(4)	19.5(4)	5.8(3)	9.7(3)	0	8.4(6)	2.2(1)
0.75	53.7(5)	10.7(4)	12.3(4)	4.7(4)	6.0(4)	0	10.1(5)	2.6(1)

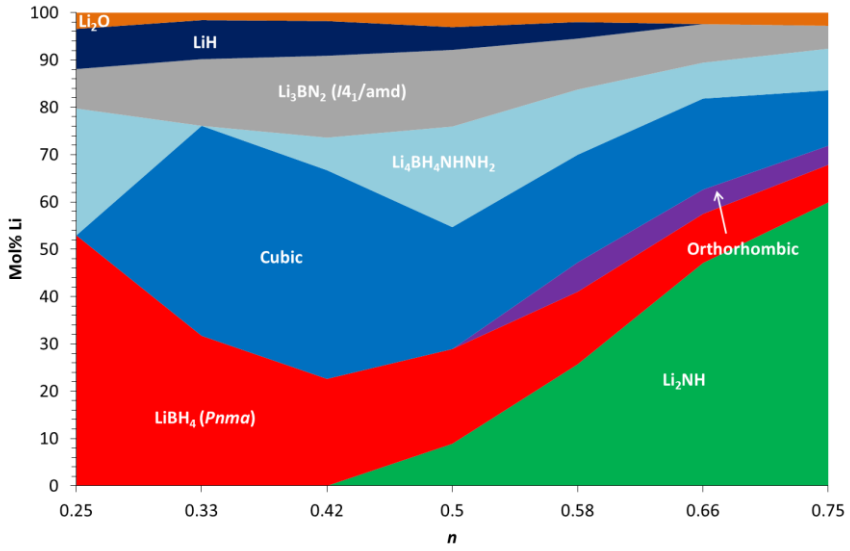

Figure 4.43 – Mole percentage lithium determined through Rietveld refinement for the nLi$_2$NH + (1 – n)LiBH$_4$ reaction with various values of n, heated at 200 °C and quenched in cold water after 12 hours, excluding unknown phases

These data suggest the cubic phase is more abundant between *ca* n = 0.33 and n = 0.42, a similar ratio range to that preferred for the orthorhombic phase at 125 °C. Although this would initially suggest that the cubic phase itself is a more borohydride-rich structure, it was present alongside a significant amount of LiBH$_4$. One possible explanation for this is that in order to form the cubic phase requires an excess of LiBH$_4$, however, the structure itself contains more imide than the reactant ratio used and thus the final product mixture contains a large excess of LiBH$_4$. Although in some cases the cubic phase appeared to be favoured over the orthorhombic phase as a result of reannealing at lower temperatures (§4.4.2.3), slow cooling studies (§4.5.2) and repeated XRD after a prolonged period (§4.5.1) have shown that these conditions favour the hexagonal Li$_4$BH$_4$NHNH$_2$ phase (§5.5). Consequently, it seems to be more likely that the cubic phase is also a kinetic product thus explaining why its formation may be more difficult to predict.

4.7.2 Reannealing

As reannealing at lower temperatures had predominantly resulted in an increase in the hexagonal $Li_4BH_4NHNH_2$ phase, although in some cases alongside an increase in cubic phase (§4.4.2.3), it was important to consider what the results of reannealing at a higher synthesis temperature were. In order to investigate this, a sample which produced a high percentage of the cubic phase after a single heating at 200 °C was reannealed twice more. The weight percentages of products after each stage were then compared. The sample used was initially heated for 12 hours at 200 °C and had the starting composition of $n$$Li_2NH$ + (1 – n)$LiBH_4$ where n = 0.66 (a ratio of 8:4). The results of this experiment were promising, with a notable increase in the cubic phase after repeated heating and removal of $Li_4BH_4NHNH_2$ (Figure 4.44 and Table 4.15). However, there also appeared to be a significant increase in the amount of decomposition products forming with Li_3BN_2 becoming more dominant after the second heating cycle.

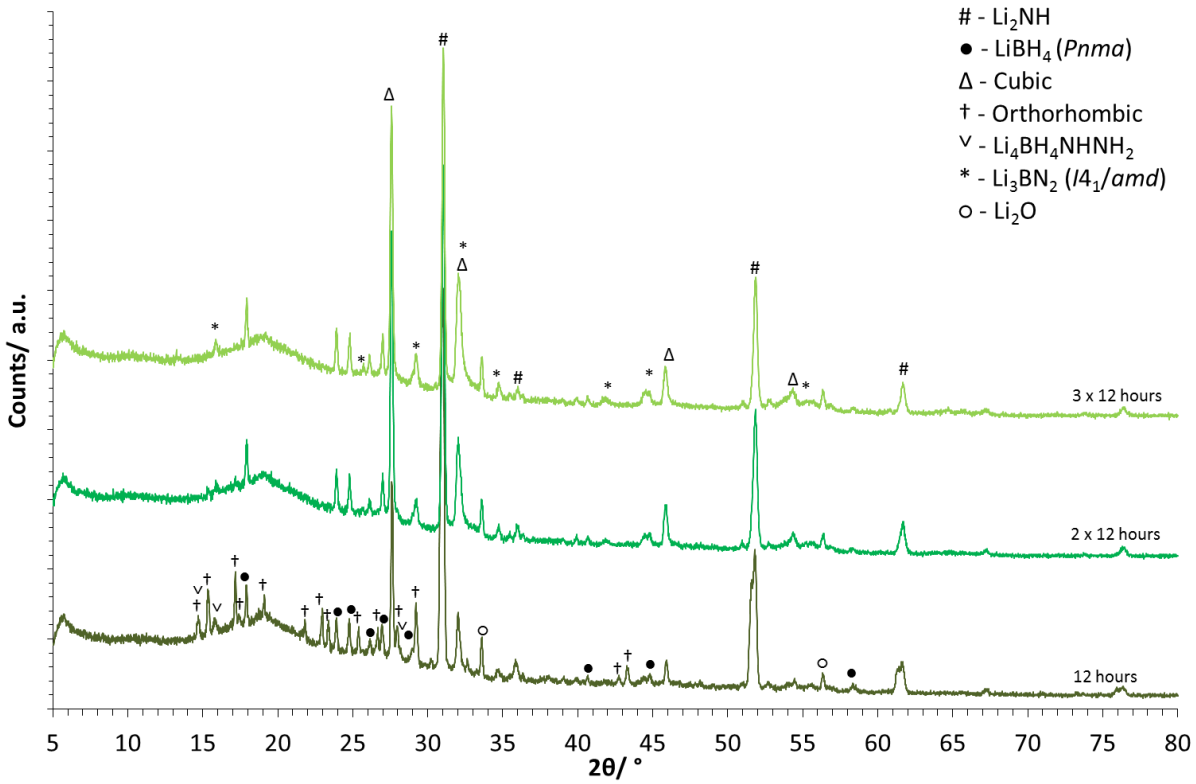

Figure 4.44 – Powder XRD data of the nLi$_2$NH + (1 – n)LiBH$_4$ reaction where n = 0.66, heated at 200 °C for 12 hours and reannealed a further 2 times, where # = Li$_2$NH, ● = LiBH$_4$ (*Pnma*), Δ = cubic phase, † = orthorhombic phase, ᵛ = Li$_4$BH$_4$NHNH$_2$, * = Li$_3$BN$_2$ (*I*4$_1$/*amd*), ⌂ = LiH and ○ = Li$_2$O

Table 4.15 – Weight percentages of the different components of the product mixture of the nLi$_2$NH + (1 – n)LiBH$_4$ reaction where n = 0.66, heated and reannealed at 200 °C

Heating Time/ hrs	Weight Percent						
	Li$_2$NH	LiBH$_4$ (*Pnma*)	Cubic	Ortho	Li$_3$BN$_2$ (*I*4$_1$/*amd*)	Li$_4$BH$_4$NHNH$_2$	Li$_2$O
12	42.3(4)	9.4(3)	16.9(3)	14.3(4)	7.6(3)	7.5(6)	2.0(1)
2 × 12	30.8(3)	11.9(3)	36.3(3)	0	18.8(4)	0	2.2(1)
3 × 12	25.7(3)	11.8(4)	32.8(4)	0	27.1(4)	0	2.6(1)

Figure 4.44 shows a significant increase in the intensity of the cubic phase peaks between one heating and two heating cycles. This occurs alongside the removal of the

orthorhombic phase from the product mixture, suggesting that the orthorhombic phase decomposes to form the cubic phase. However, this also occurred alongside further decomposition products forming, with Li_3BN_2 becoming more abundant after the second heating cycle.

In terms of the starting materials there appeared to be a much more drastic change in the amount of Li_2NH compared with $LiBH_4$, which remained relatively stable. As the amount of cubic phase increased, the amount of Li_2NH decreased suggesting the cubic phase needed more Li_2NH to form. Thus, it is possible that the orthorhombic phase initially formed but was decomposed through repeated heating to form the cubic phase, and in order to correct the anion ratio in the final structure more Li_2NH was required.

Interestingly the $Li_4BH_4NHNH_2$ phase (§5.5), which in previous studies only increased in abundance over time and with slower cooling, was removed by reannealing. One possibility is that regrinding and reannealing at higher temperatures may have resulted in its decomposition; potentially at higher temperatures it decomposes more readily than the cubic phase. As the hexagonal $Li_4BH_4NHNH_2$ phase has been identified as a lithium amide-borohydride-imide, any loss of hydrogen would be likely to result in a lithium borohydride-imide phase being more favourable.

Despite the promise of reannealing as a way of increasing the amount of cubic phase formed, the formation of more decomposition products proved to be a major issue. Potentially through reannealing at lower temperatures it may be possible to increase the amount of cubic phase without decomposition occurring. However, reannealing at 125 °C

did not consistently result in an increase in the amount of the cubic phase and introduced more $Li_4BH_4NHNH_2$.

4.8 Conclusions

This chapter investigates the phases formed from the reaction of lithium imide and lithium borohydride. It is clear from these studies that there are multiple phases, the combination of which has shown huge levels of variation through different changes to the reaction conditions. Based on these investigations the orthorhombic and cubic phases, first indexed by Hewett,[81] do not appear to be thermodynamically stable. Although variations to the reagent ratios have not provided a definitive answer on the true anion ratio of each of these structures, they have highlighted phase space in which each of the phases are favoured. The orthorhombic phase was most dominant in $LiBH_4$-rich conditions, whereas the cubic phase was determined to have a ratio closer to 1:1. The amount of variation between samples, in particular samples heated at 200 °C has allowed the formation of a melt to be confirmed, and helps to provide an explanation for the inconsistent appearance of unidentified peaks, the broad nature of which may suggest high levels of disorder.

The reaction of lithium amide-imide and lithium borohydride resulted in the identification of a previously unknown structure, a hexagonal $Li_4BH_4NHNH_2$ phase (§5.5). This not only allowed for unknown peaks in the lithium borohydride-imide phase space to be identified, but appeared to be a thermodynamically stable material.

Chapter 5 – Structure Determination of New Borohydride-imide Phases

5.1 Introduction

One of the main aims of this project was to determine the structures of the two unknown lithium borohydride-imide phases. Previous work by Hewett had identified these as a cubic and an orthorhombic structure with the proposed space groups *P*23 and *Pnma*, respectively.[81] Using this information, as well as that gained through synthetic studies (Chapter 4), structures of both the orthorhombic and cubic lithium borohydride-imide phases were determined.

5.2 Experimental

Samples of the new lithium borohydride-imide phases (see §4.4 and §4.5) were finely ground in an argon-filled glove box and sealed form the air into 0.5 mm diameter borosilicate capillaries. High resolution powder XRD data were collected on the I11 beamline, using a wavelength of 0.826055 Å at Diamond Light Source. Data were collected using both the position sensitive detector (PSD) and multi-analyser crystal (MAC) detectors. See §2.3 for more detailed information. The sample used for orthorhombic structure determination had been synthesised at 125 °C for 12 hours using a reactant ratio of $2Li_2NH + 3LiBH_4$ (n = 0.4).

Structure solution work on the cubic phase (§4.5) and the hexagonal lithium amide-borohydride-imide phase (§4.6) was performed using data collected on a Siemens D5000 laboratory instrument, which uses a copper source with a wavelength of 1.54056 Å. The

sample used for cubic structure determination was synthesised at 200 °C for 12 hours using a reactant ratio of $1Li_2NH + 1LiBH_4$ (n = 0.5). The lithium amide-borohydride-imide sample had a starting composition of $7Li_{1.5}(NH_2)_{0.5}(NH)_{0.5}{:}5LiBH_4$ [n = 0.58 using the equation $nLi_{1.5}(NH_2)_{0.5}(NH)_{0.5} + (1 - n)LiBH_4$] and was synthesised at 125 °C for 12 hours.

5.3 Orthorhombic Phase Structure Determination

High resolution powder XRD data were collected on a sample containing predominantly the orthorhombic phase, with minimal amounts of additional phases. The PSD allowed high intensity data to be collected at high speed, and therefore, due to the high number of counts, was used for the initial structure solution work. Once a model was produced it was then applied to the higher resolution MAC data to be refined further.

5.3.1 Indexing

Hewett initially reported the new orthorhombic phase as having the space group *Pnma* and lattice parameters a = 10.1459(9) Å, b = 11.483(1) Å, and c = 7.0302(4) Å.[81] Pawley refinements using these starting values were used to fit the data, in order to help determine the presence of the orthorhombic phase during initial synthesis work. However, once the new high resolution data were collected it was important to revisit this unit cell determination and re-index the data in order to confirm the space group and lattice parameters, ensuring there were no other possibilities.

Indexing was carried out using Topas[152] and confirmed the most likely space groups to be $Pna2_1$ and *Pnma*. Both of these space groups have identical systematic absences, in other words identical *hkl*s, and so cannot be differentiated at the indexing stage. Figure 5.1 shows the collected PSD data with the orthorhombic phase tick marks corresponding to

either a *Pnma* or a *Pna*2_1 space group, and Table 5.1 and Table 5.2 show the Wyckoff positions for the two possible space groups.

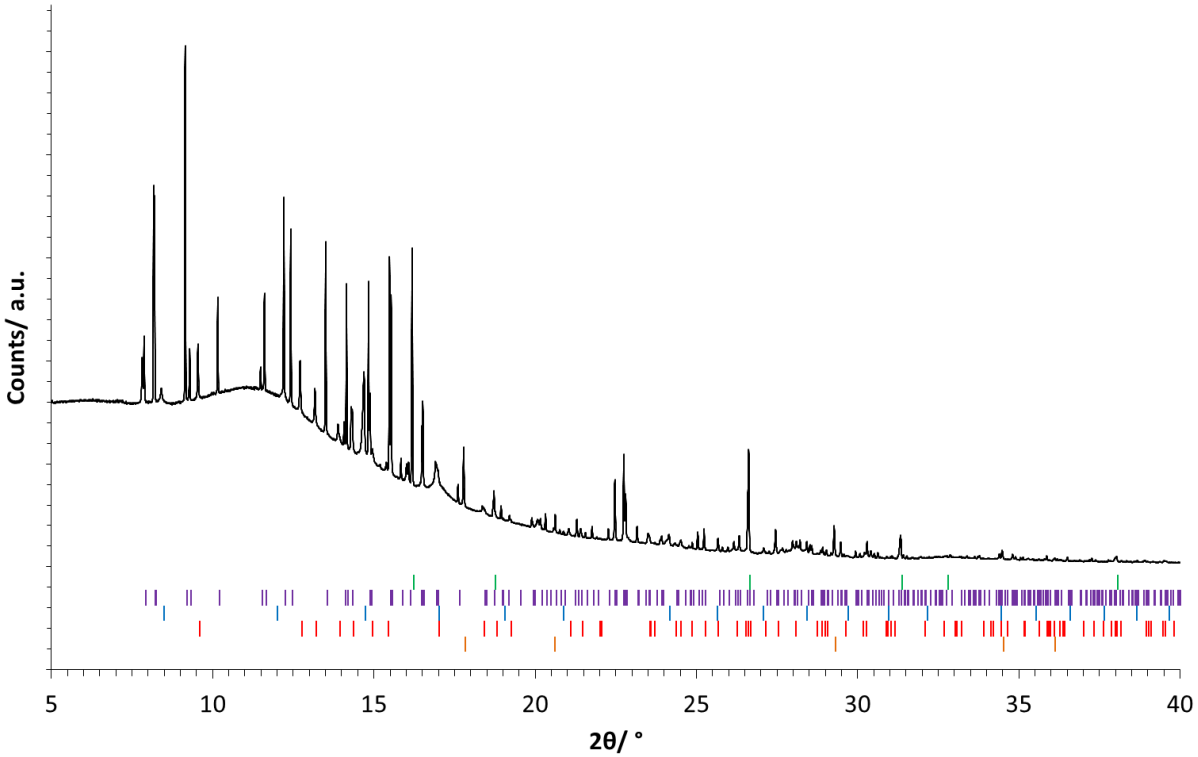

Figure 5.1 – High resolution powder XRD data of $2Li_2NH + 3LiBH_4$, collected using the PSD, where green tick marks = Li_2NH, purple tick marks = orthorhombic phase, blue tick marks = cubic phase, red tick marks = $LiBH_4$ (*Pnma*) and orange tick marks = Li_2O

Table 5.1 – Wyckoff positions for *Pnma* space group[153]

Wyckoff Position	Coordinates
8*d*	(x, y ,z) (–x + 1/2, –y, z + 1/2) (–x, y + 1/2, –z) (x + 1/2, –y + 1/2, –z + 1/2) (–x, –y, –z) (x + 1/2, y, –z + 1/2) (x, –y + 1/2, z) (–x + 1/2, y + 1/2, z + 1/2)
4*c*	(x, 1/4, z) (–x + 1/2, 3/4, z + 1/2) (–x, 3/4, –z) (x + 1/2, 1/4, –z + 1/2)
4*b*	(0, 0, 1/2) (1/2, 0, 0) (0, 1/2, 1/2) (1/2 ,1/2, 0)
4*a*	(0, 0, 0) (1/2, 0, 1/2) (0, 1/2, 0) (1/2, 1/2, 1/2)

Table 5.2– Wyckoff positions for *Pna*2_1 space group[153]

Wyckoff Position	Coordinates
4*a*	(x, y, z) (–x, –y, z + 1/2) (x + 1/2, –y + 1/2, z) (–x + 1/2, y + 1/2, z + 1/2)

5.3.2 Charge Flipping

After indexing, charge flipping was then carried out using Topas[152], starting from the best Pawley fit of the data. Charge flipping[154, 155] works by switching back and forth between real and reciprocal space. In real space it aims to locate where the electron density is most likely to be located. If the density in any area is below that of a given small positive value, it is multiplied by –1, in other words it is charge flipped. The amplitudes determined experimentally are then restored in reciprocal space. This continues until it converges on an energy minimum or the predetermined number of refinement cycles have been reached.

Charge flipping is advantageous as it does not explicitly use composition, form factors or space group symmetry; therefore if for any reason the wrong space group and

composition have been assumed it is still possible to arrive at the correct structure. However, in order to be successful, very high resolution data needs to be used (ideally collecting well-resolved *hkl* intensities for *d*-spacings of less than 0.8 Å) and it can easily become stuck in local energy minima resulting in an incorrect structure.

The charge flipping was initially performed with a view to locating only the most strongly scattering anions; this was to obtain a consistent anion lattice before trying to locate the cations within the structure. The results of this were relatively consistent, although the determined anion lattice was highly disordered and notably denser than both parent phases (1.48 g cm^{-3} and 0.67 g cm^{-3} for lithium imide[156] and lithium borohydride[86], respectively).

Lithium was then introduced into the structure, alongside the anion positions located during the first phase of charge flipping; however, there were issues with charge balancing. The anion lattice was consistently very dense in comparison to the starting materials and introduction of lithium only made the structures more dense, yet there was still a significant overall negative charge. There were also issues with unfeasibly short anion–anion distances, suggesting some of the cations may have been misassigned as anions. It was concluded that charge flipping was not able to provide a sensible structure solution for this phase and so simulated annealing methods were attempted using Topas[152].

5.3.3 Simulated Annealing

Simulated annealing[152] is based on the hill climbing algorithm, aiming to identify the global optimum. In hill climbing, a model would only replace the current one if there was an improvement; however, the introduction of a temperature regime through simulated

annealing means that a less favourable model can replace the current one but only with a reduced probability. This helps to prevent a model being accepted as the solution because it is in a local energy minimum and helps to find the global energy minimum. As the temperature is reduced less energetically favourable models will be less likely to replace the current one and the search is narrowed down. This continues until the most likely global energy minimum is determined or the predetermined maximum number of refinement cycles have been reached. An additional benefit of simulated annealing is that one can apply some chemical restraints into the refinements to guide the optimisation towards chemically sensible configurations. For example, rigid bodies can be used to refine the complex anions in their entirety throughout the process. Also bond length penalties, called 'anti-bump' penalties within Topas, can allow configurations with unfeasibly short bond lengths to be disfavoured. The weighting of any penalties needs to be balanced so as to guide the refinement towards the correct solution, but without constraining the models to local minima.

Simulated annealing refinements were first run including only boron atoms; their occupancies were allowed to vary between 1.0 and 1.4 (where 1.4 represents nitrogen, given that Z = 5 and 7 for boron and nitrogen, respectively) to give an indication as to which sites were favoured by the different anions. This was run with four different anion sites and in all four the starting atomic positions were random so as not to bias the results towards a starting structure. This was run in both $Pna2_1$ and *Pnma* symmetries; however, *Pnma* produced more consistent models, with more sensible anion distances, which fit better to the data and so were carried forward in subsequent work.

In the *Pnma* structure different possible combinations of Wyckoff positions were originally tested and through that the most promising ones were determined. This was based on their fit to the data and observed bond lengths in the structure. The *Pnma* structure in which the four anion sites were split up into two 8*d* sites and two 4*c* sites was found to be the most promising. In the refinements all four sites were initially set with the same occupancy so as not to bias any of them. Consistently the occupancies of the 4*c* sites were refined to 1.4 corresponding to N and the occupancies of the 8d sites refined to 1 corresponding to B. These values suggested the nitrogen to boron ratio to be 1N:2B; however, some of the anion–anion distances were quite short *ca* 1.9 Å and therefore it is possible that, as was the case with charge flipping, some anions were actually misassigned as Li.

After running multiple refinements there were certain configurations which were returned several times, with the boron occupancies consistently favouring either nitrogen or boron. Lithium was subsequently introduced into those anion structures which fit best to the data and the structures were refined. The same issues with charge balancing and short anion–anion distances were still apparent. In order to try and counteract these structural problems, the occupancies of the anions were again allowed to vary, this time between an occupancy representative of Li (0.6) up to an occupancy representative of N (1.4). Unfortunately this threw up issues with the anion lattice. Ions which previously were always sitting at higher occupancies and therefore representative of N were falling below 1 and becoming more representative of Li and this was varying between refinements, therefore a reproducible and reasonable model could not be achieved. It became apparent that tools like simulated annealing would not be able to arrive at the correct solution without a

significantly better constrained model, and so instead it was decided to revisit what was known about the structure to attempt to constrain better the total composition of the unit cell.

5.3.4 Building a Model

As a consequence of the inconsistent results from both charge flipping and simulated annealing, a more manual method was used. A model of the anion structure was built up from the Wyckoff positions (Table 5.1 and Table 5.2) and refined; this method produced much more promising results.

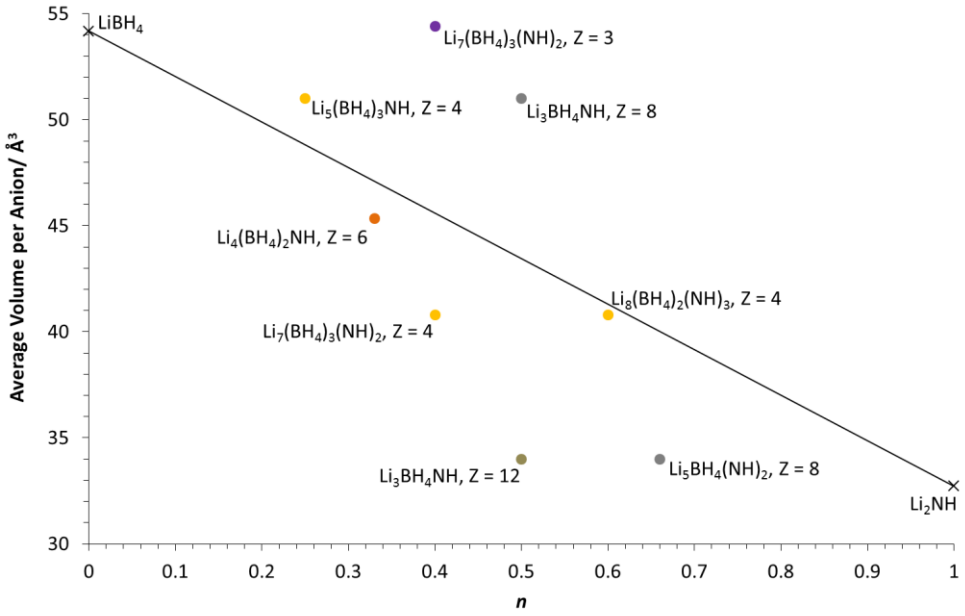

Figure 5.2 – Vegard's plot comparing the ratio of Li_2NH to $LiBH_4$, where $nLi_2NH + (1 - n)LiBH_4$, to the average volume per anion for different Z values

In order to estimate the composition of the unit cell the volumes of the single formula units of the starting materials were considered (32.7 2 $Å^3$ for Li_2NH and 54.2 $Å^3$ for $LiBH_4$).[86,131] Figure 5.2 compares the average volume per anion calculated for different

compositions (imide to borohydride ratios) with various numbers of formula units within the unit cell (Z). This was calculated for values of *n* between 0.25 and 0.75 for Z = 1 up to Z = 12, however, only the key values closest to the line predicted from Vegard's law are included in the plot. The reported values were determined using Equation 5.1. The volume of the unit cell used was 815.99 $Å^3$, determined by a Pawley fit to the data; and the number of anions in a formula unit was based on the simplest anion ratio for a given composition, e.g. a ratio of $7LiBH_4$ to $5Li_2NH$ would result in 12 anions in a single formula unit.

$$Average\ volume\ per\ anion = \frac{Volume\ of\ unit\ cell}{no.of\ anions\ in\ a\ formula\ unit \times Z} \quad (5.1)$$

Initial observation of the Vegard's plot suggested that a $3Li_2NH{:}2LiBH_4$ (*n* = 0.6) stoichiometry where Z = 4 was the most promising match to this empirical observation. However, it was also important to consider the previous synthetic work (discussed in §4.4) and how all the results from that work suggested a more $LiBH_4$-rich composition. Consequently that was ruled out as a possible composition and Z combination, as was a $2Li_2NH{:}1LiBH_4$ stoichiometry (*n* = 0.66) where Z = 8, for the same reason. Based on the plot, the second most likely combination was a stoichiometry of $1Li_2NH{:}2LiBH_4$ (*n* = 0.33) where Z = 6; however, this was again deemed unlikely as Z = 6 was not compatible with the available Wyckoff positions and so could only have resulted in an implausible disordered structure.

Initial experimental work suggested a ratio of $2Li_2NH{:}3LiBH_4$ (*n* = 0.4) was likely to be the most promising ratio. In Figure 5.2 this ratio is shown with both Z = 3 and Z = 4. However, Z = 3 is incompatible with the Wyckoff positions and so was deemed unlikely. Z = 4 is compatible, although it does not lie as close to the empirically predicted line as other

alternatives. Based on the volumes of the single formula units of the starting materials and their densities, a higher stoichiometry of $1Li_2NH:3LiBH_4$ (n = 0.25) looked to be more promising as the true stoichiometry. Combining this ratio with Z = 4 gave an average volume per anion which seemed promising with regards to Vegard's law. Also the fact that this combination sits just above the line, indicating a greater average volume per anion, possibly suggests a less stable phase than either parent structure which could explain why syntheses typically resulted in multiple phases present. As a result of these findings, models were built based on both 1:3 and 2:3 ratios, where Z = 4.

Due to the more consistent results produced from initial simulated annealing work, the main focus was on the space group *Pnma*, although $Pna2_1$ was used for comparison periodically to ensure better results were not possible using the alternative space group.

Looking at the Wyckoff positions for *Pnma* (Table 5.1), for a 2:3 ratio, site multiplicities of either 8 and 4 for B and 8 for N; 3 × 4 for B and 8 for N; or 8 and 4 for B and 2 × 4 for N could be used. There are 3 different sites with a multiplicity of 4; however, there is more flexibility in the movement of anions with 4*c* so this was used as a starting point. For the 1:3 ratio B was on an 8 and 4 site and N on a site of multiplicity 4. Simulated annealing was run using these sites, fixing only the special positions, and the R_{Bragg} values were compared. Anti-bump penalties were used to ensure the bond distances remained sensible with minimum distances set to approximately 10% lower than the bond lengths in the parent compounds to allow for some flexibility. Anion–anion distances were set at a minimum of 3.5 Å, and with the introduction of lithium, distances were set at a minimum of 1.8, 1.6 and

1.8 Å for Li–Li, Li–N and Li–B, respectively. Rigid bodies for the BH_4^- units were also included with a fixed B–H distance of 1.2 Å; however, NH^{2-} was included only as a single N.

Simulated annealing of both the 1:3 and 2:3 models was first carried out with inclusion of only the anions. These simulated annealing refinements showed the 1:3 stoichiometry to be much more stable, regularly producing similar configurations with better R_{wp} values. Despite including a large penalty for short anion–anion distances within the refinement there were still frequently very short distances in the 2:3 structures. Coupled with the notably higher R_{Bragg} values, the 2:3 structure did not appear to give satisfactory models and fits to the data, and thus a 1:3 ratio was found to be more likely to be the true stoichiometry of the structure.

Lithium ions were subsequently introduced into the model: two in 8*d* sites and one in a 4 multiplicity site (4*a*, 4*b* and 4*c* were all tested). Simulated annealing refinements were performed multiple times, with the B and N sites fixed and Li starting in random positions to ensure there was reproducibility in the determined arrangements. The arrangement in which the 4*c* site was occupied gave the most chemically sensible structures with more realistic distances between the ions. In it the lithium ions mostly sat in tetrahedral holes within the anion lattice, although there was some inconsistency between refinements with the lithium ions sometimes clustering together.

After multiple simulated annealing refinements there was one atomic arrangement which was consistently reproduced with an R_{Bragg} value of 3.45. However, due to the symmetry of the structure there were excess hydrogen atoms as one of the BH_4^- anions was located on a 3-fold axis. In order to resolve this issue the rotation of the borohydride

tetrahedra was fixed about the *a* and *c* axes. This allowed rotation about the *b* axis only resulting in the correct number of hydrogen atoms, generated from three hydrogen positions. The fit of this structure to the data is shown in Figure 5.3.

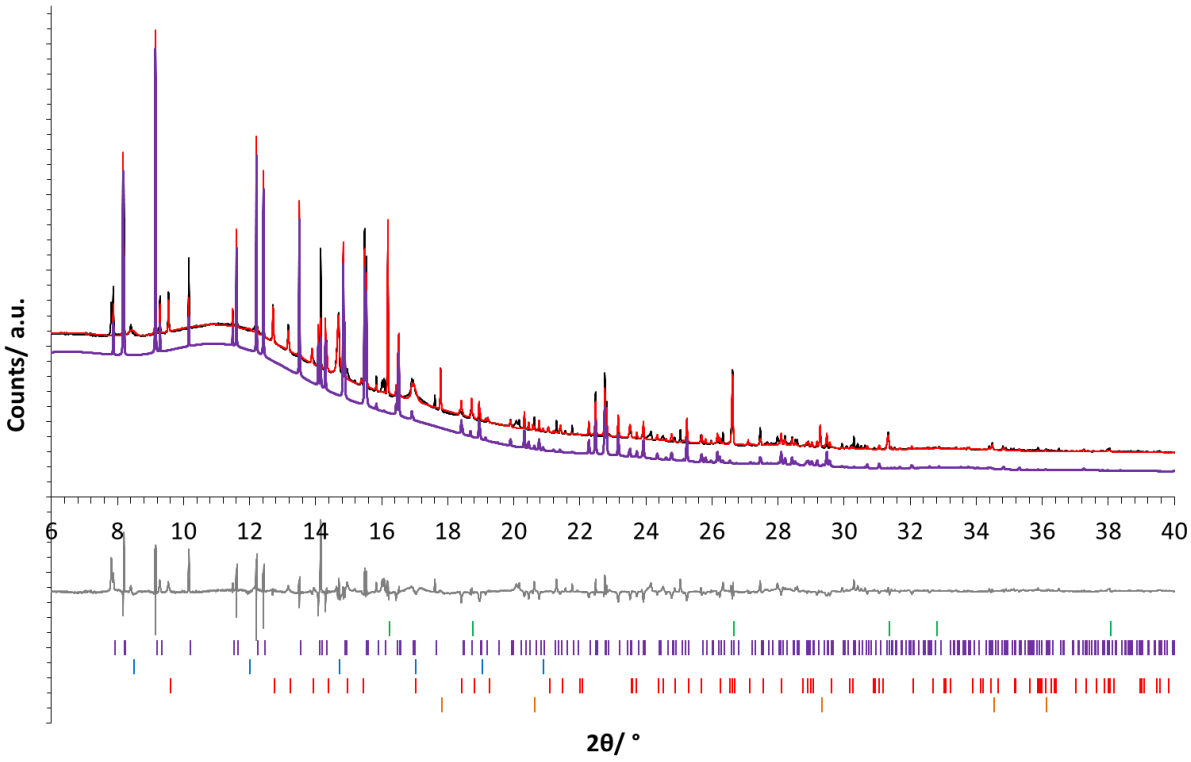

Figure 5.3 – Simulated annealing refinement plot of $1Li_2NH:3LiBH_4$ with hydrogen corrected, R_{Bragg} = 4.48 (PSD data), where black = observed data, red = calculated data and grey = difference, highlighting the orthorhombic fit in purple. Green tick marks = Li_2NH, purple tick marks = orthorhombic phase, blue tick marks = cubic phase, red tick marks = $LiBH_4$ (*Pnma*) and orange tick marks = Li_2O

5.3.4.1 Initial Orthorhombic Structure

This structure, which fitted well to the PSD data, was taken and adapted to fit the higher resolution MAC data. Rietveld refinements were initially carried out up to a 2θ value of 20 °, increasing up to 40 ° once a good fit was achieved. The maximum limits for the

thermal parameters were then reduced (B_{iso} = 10) to try and obtain more reasonable values. For initial refinements they were set to relatively high values (B_{iso} = 15) to allow for more flexibility in the refinement and a better goodness of fit, but values not sensible for the true structure. When refining the thermal parameters, the values corresponding to boron and hydrogen were stable at *ca* 4 and *ca* 3, whilst the lithium and nitrogen values went straight up to the maximum value. These large values are an indication of a large degree of disorder within the structure, which was not represented in the model.

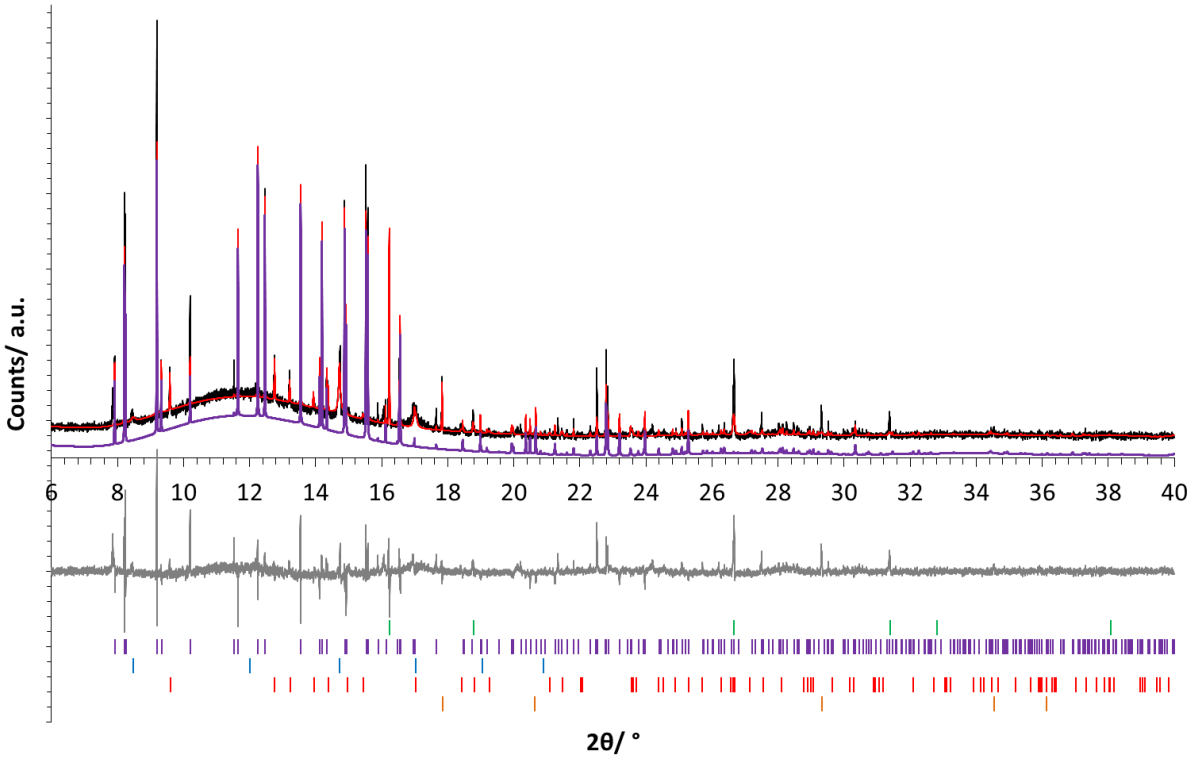

Figure 5.4 – Simulated annealing refinement plot of $1Li_2NH:3LiBH_4$ using MAC data, R_{Bragg} = 9.57, where black = observed data, red = calculated data and grey = difference, highlighting the orthorhombic fit in purple. Green tick marks = Li_2NH, purple tick marks = orthorhombic phase, blue tick marks = cubic phase, red tick marks = $LiBH_4$ (*Pnma*) and orange tick marks = Li_2O

Figure 5.4 shows the fit the of the adapted model to the MAC data. The fit to these data was not as good as the previous fits to the PSD data. However, introduction of more instrument parameters and reducing the thermal parameters, as well as the higher quality of the data would all have contributed. As was the case for many of the refinements, the anion positions within the structure seemed to remain relatively stable, though there were some issues with location of the lithium cations. Figure 5.5 shows the model determined from the refinement to the MAC data.

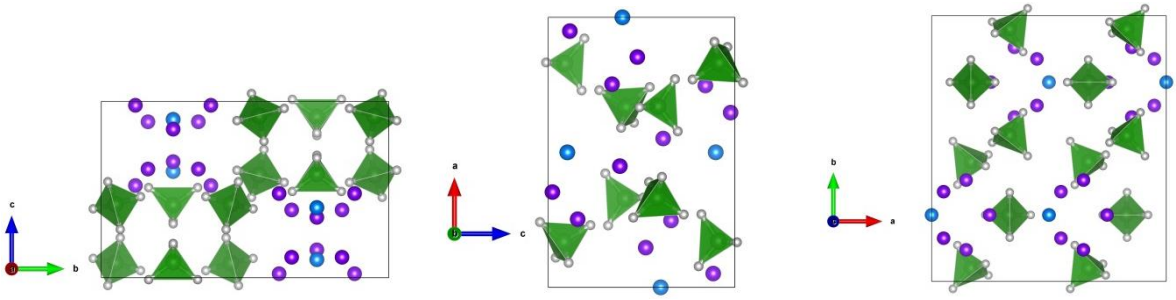

Figure 5.5 –1Li_2NH:3$LiBH_4$ structure viewed down *a*, *b* and *c*. N are represented by blue spheres, BH_4^- are represented by green tetrahedra and Li by purple spheres

Carrying out Rietveld refinements on the data showed notable movement of cations, suggesting they were not stable in their positions. They moved closer together, clustering within the structure. The thermal parameters also needed to be improved, as although there was some stability with some of the ions, they were higher than would be expected in a complete structure. Table 5.3 shows the details of the model as it was after this series of refinements against the MAC data. The shortest interatomic distances in the structure were: 2.19 Å and 2.25 Å for Li–N and Li–B, respectively, 3.60 Å and 3.64 Å for N–B and B–B, and 2.01 Å for Li–Li.

Table 5.3 – Details of the structure of $1Li_2NH:3LiBH_4$ determined through simulated annealing of *Pnma* model, * indicates that a parameter hit its maximum allowed value. One B_{iso} was refined each for N, B, Li and H

Atom	Site	*x*	*y*	*z*	B_{iso}	Symmetry
N(1)	4*c*	0.000(1)	0.25	0.602(2)	10.0(5)*	.*m*.
B(2)	8*d*	0.168(1)	0.049(1)	0.083(2)	4.1(3)	1
H(21)	8*d*	0.242(5)	0.023(5)	0.956(9)	3.1(1.1)	1
H(22)	8*d*	0.091(5)	0.972(5)	0.109(8)	3.1(1.1)	1
H(23)	8*d*	0.230(6)	0.066(6)	0.226(11)	3.1(1.1)	1
H(24)	8*d*	0.110(5)	0.136(4)	0.040(9)	3.1(1.1)	1
B(3)	4*c*	0.829(2)	0.25	0.088(3)	4.1(3)	.*m*.
H(31)	4*c*	0.729(7)	0.25	0.179(11)	3.1(1.1)	.*m*.
H(32)	4*c*	0.922(7)	0.25	0.194(10)	3.1(1.1)	.*m*.
H(33)	8*d*	0.833(7)	0.165(4)	0.989(8)	3.1(1.1)	1
Li(1)	4*c*	0.748(3)	0.25	0.842(4)	10.0(5)*	.*m*.
Li(2)	8*d*	0.647(2)	0.381(2)	0.977(3)	10.0(5)*	1
Li(3)	8*d*	0.949(2)	0.662(2)	0.116(4)	10.0(5)*	1

This initial structure was used as a working model for a large part of the work contained within this thesis. Further work was needed to refine more subtly the anion positions, locate the lithium cations accurately and improve the thermal parameters; however, this model was chemically sensible and fitted well to the collected high resolution data. In the next section the structure is revisited having resolved outstanding questions regarding other phases present within the sample and improving on the fit.

5.3.4.2 Refining the Structure

In the structure solution work up to this point the cubic phase had been fitted to the data as a Pawley fit, using space group *Pm*-3*m*, rather than a full Rietveld structural model. Before progressing any further the Pawley fit of the cubic phase was replaced with a Rietveld fit of the final *Fm*-3*m* structure (detailed in §5.4.2). The NH^{2-} anion was also included as a rigid body to replace the single nitrogen atoms, with the N–H distance fixed at 0.8 Å. Simulated annealing was then run with the inclusion of these additional factors, against the PSD data. Repetition of the refinements with the inclusion of NH^{2-} rigid bodies, for the $1Li_2NH{:}3LiBH_4$ *Pnma* structure, provided a consistent refined structural model.

In order to ensure that the restrictions on minimum atomic distances were not forcing the arrangement of the ions within the structure, the anti-bump penalty was removed and simulated annealing repeated. The structure determined was consistent with those in which the penalty was enforced, thus confirming that the minimum distances were not resulting in the determination of an incorrect structure.

Subsequent Rietveld refinements were performed on the results of the simulated annealing process in order to allow the structure to settle. The rotation of the NH^{2-} rigid body was causing duplication of the H atoms due to its location on a symmetry plane. Consequently the occupancy of the hydrogen was set to 0.5 so the total occupancy across both was one. However, during the refinements the two half occupied hydrogen positions merged on a 4c site, giving a combined occupancy of 1. The fit of this structure to the PSD data is shown in Figure 5.6.

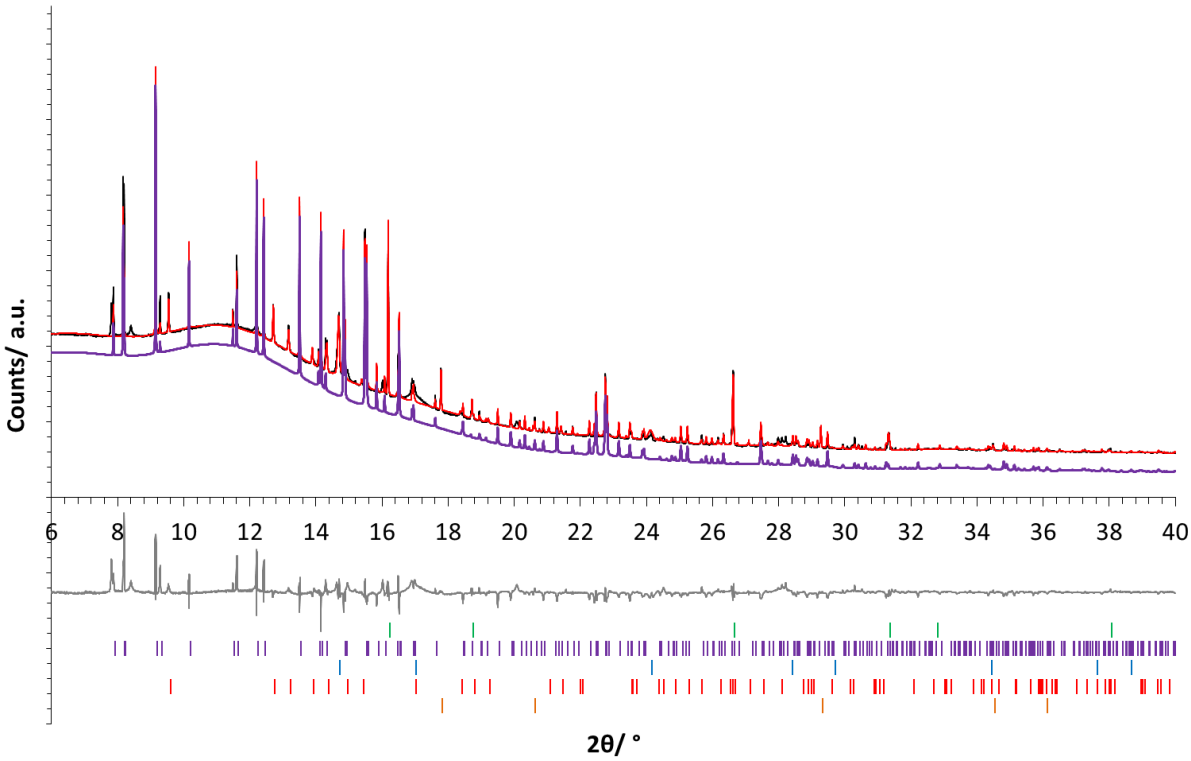

Figure 5.6 – Simulated annealing refinement plot of $1Li_2NH:3LiBH_4$ with NH^{2-} included, R_{Bragg} = 4.99 (PSD data), where black = observed data, red = calculated data and grey = difference, highlighting the orthorhombic fit in purple. Green tick marks = Li_2NH, purple tick marks = orthorhombic phase, blue tick marks = cubic phase, red tick marks = $LiBH_4$ (*Pnma*) and orange tick marks = Li_2O

As with the previous model, once a structure was determined from the PSD data it was then applied to the higher resolution MAC data for further Rietveld refinement. Refinements against the PSD data were resulting in thermal parameters which were consistently hitting the maximum value allowed (B_{iso} = 10), therefore the aim was to determine more realistic values. As before the structure was first fit up to 20 °, only increasing the 2θ range up to 40 ° once there was a good fit and sensible thermal parameters had been obtained. The $Li_5(BH_4)_3NH$ structure determined from these MAC

refinements is shown in Figure 5.7, the details of which are given in Table 5.4. Lattice parameters were refined to *a* = 10.14982(8) Å, *b* = 11.48539(9) Å and *c* = 7.00041(5) Å.

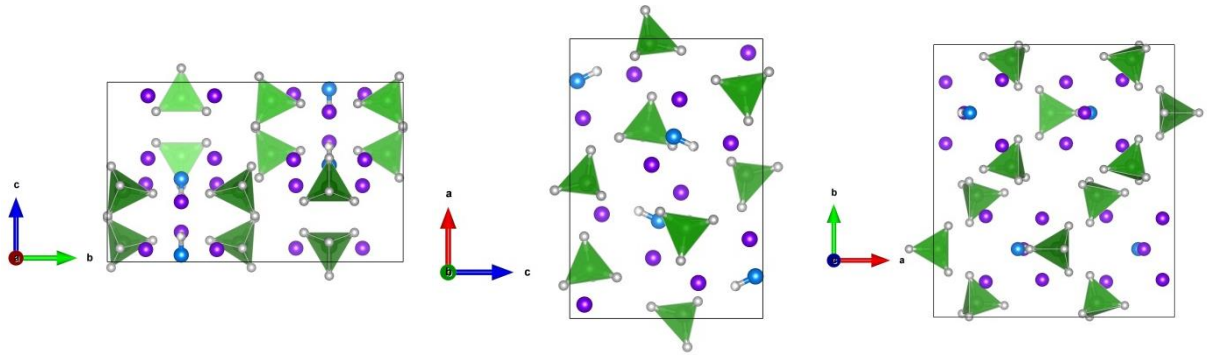

Figure 5.7 –1Li_2NH:3$LiBH_4$ structure viewed down a, b and c with the inclusion of NH^{2-} rigid bodies. N are represented by blue spheres, H by grey spheres, BH_4^- are represented by green tetrahedra and Li by purple spheres

Table 5.4 – Details of the structure of $1Li_2NH:3LiBH_4$ determined through simulated annealing of *Pnma* model, with the inclusion of rigid bodies for both BH_4^- and NH^{2-}

Atom	Site	*x*	*y*	*z*	Occ	B_{iso}	Symmetry
N(1)	4*c*	0.8484(8)	0.25	0.0383(9)	1	1.6(2)	.*m*.
H(11)	4*c*	0.8839(10)	0.25	0.1409(51)	1	4.6(7)	.*m*.
B(2)	8*d*	0.1770(5)	0.0523(4)	0.1012(7)	1	1.5(2)	1
H(21)	8*d*	0.2933(9)	0.0427(48)	0.0748(33)	1	4.6(7)	1
H(22)	8*d*	0.1468(22)	0.0006(24)	0.2436(22)	1	4.6(7)	1
H(23)	8*d*	0.1494(54)	0.1533(12)	0.1190(39)	1	4.6(7)	1
H(24)	8*d*	0.1182(34)	0.0125(29)	-0.0325(22)	1	4.6(7)	1
B(3)	4*c*	0.0156(7)	0.25	0.5894(11)	1	1.5(2)	.*m*.
H(31)	4*c*	0.0421(39)	0.25	0.4224(16)	1	4.6(7)	.*m*.
H(32)	4*c*	-0.1019(8)	0.25	0.6090(57)	1	4.6(7)	.*m*.
H(33)	8*d*	0.0611(18)	0.1647(0)	0.6633(25)	1	4.6(7)	1
Li(1)	4*c*	0.3731(21)	0.25	0.1660(28)	1	8.7(3)	.*m*.
Li(2)	8*d*	0.4504(13)	0.3627(11)	0.5764(21)	1	8.7(3)	1
Li(3)	8*d*	0.2163(13)	0.3702(10)	0.4317(19)	1	8.7(3)	1

Unlike in the initial model in which the lithium ions were constantly moving and clustering together, in this case the lithium appeared to be fairly stable in the given atomic positions. Even with no restrictions on minimum bond distances they remained at chemically sensible distances, with the shortest Li–Li distance sitting at 2.54901 Å. In this model the lithium ions sit in tetrahedral holes in the anion lattice, which is a common arrangement in lithium amide related structures. The fit of this structure to the MAC data is shown in Figure 5.8, which has an R_{Bragg} of 3.01.

The thermal parameters were refined between a minimum B_{iso} of 0 and maximum of 10, with four different displacement parameters, one for each of the different types of ion. The B_{iso} values for boron and nitrogen were refined to low values of 1.5(2) and 1.6(2), respectively. Hydrogen has a slightly higher displacement parameter of 4.6(7); however, in particular with NH^{2-}, any uncertainty/ disorder in its orientation will cause the thermal parameter to be greater than expected. The determination of hydrogen positions using X-rays is also challenging due to its very poor scattering power. The lithium positions in the structure were the most difficult to determine and consequently their higher displacement parameters are likely to be partially due to that. These materials have also shown promise as room temperature lithium ion conductors (Chapter 7) and therefore movement of lithium ions and high displacement parameter values are to be expected.

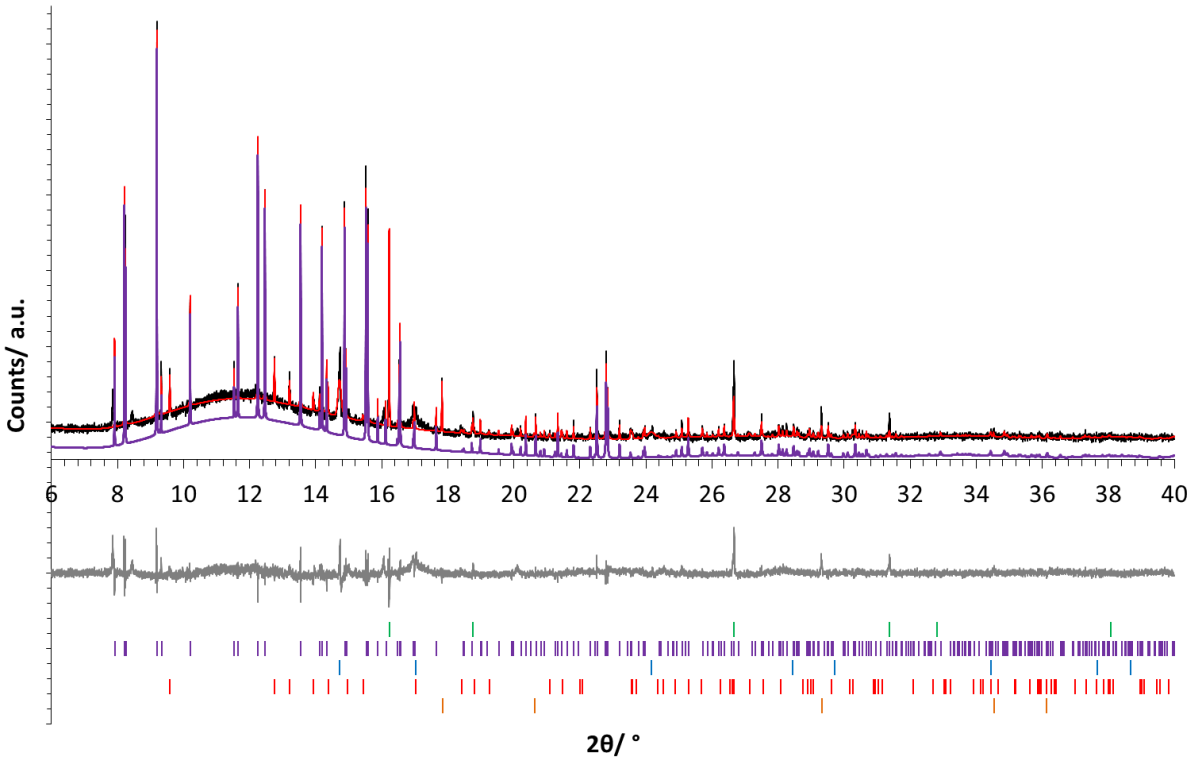

Figure 5.8– Simulated annealing refinement plot of $1Li_2NH:3LiBH_4$ with NH^{2-} included, R_{Bragg} = 3.01 (MAC data), where black = observed data, red = calculated data and grey = difference, highlighting the orthorhombic fit in purple. Green tick marks = Li_2NH, purple tick marks = orthorhombic phase, blue tick marks = cubic phase, red tick marks = $LiBH_4$ (*Pnma*) and orange tick marks = Li_2O

5.3.4.3 Investigating Alternative Structures

During the course of this work Wolczyk *et al.*[148] published their structure of the orthorhombic $Li_5(BH_4)_3NH$ phase, which reported a model that was very similar to the structure presented in this work. The authors reported a structure with *Pnma* symmetry and lattice parameters: a = 10.2031(3), b = 11.5005(2) and c = 7.0474(2) Å. Figure 5.9 shows a comparison between the two structures with the origin of the Wolczyk structure shifted by (x, y + 0.5, –(z + 0.5)) to enable the two structures to be overlaid. The main difference between the two structures was the orientation of the NH^{2-} anion (Figure 5.10). In the

Wolczyk structure the N–H is orientated with the hydrogen facing away from the lithium, whereas in the structure reported here the hydrogen was facing towards the lithium.[148]

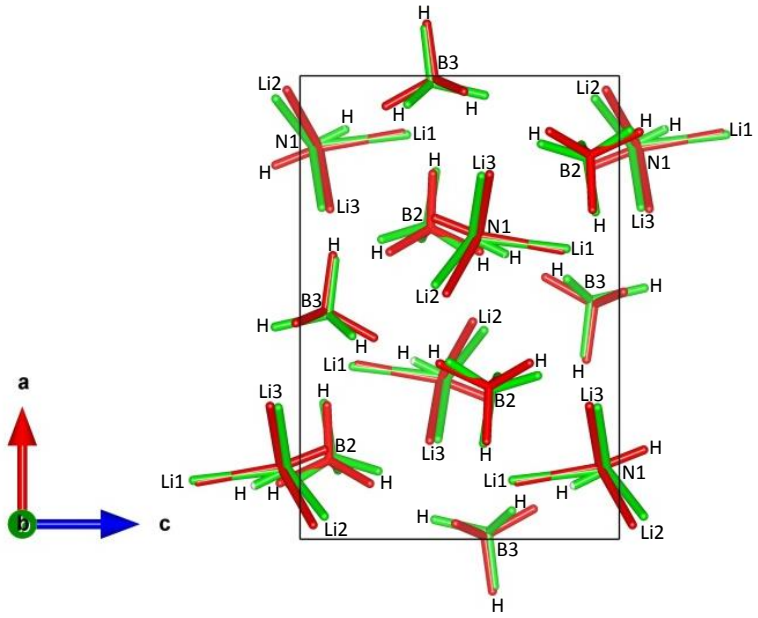

Figure 5.9 – Comparison of $Li_5(BH_4)_3NH$ structure determined in this thesis (green) with Wolczyk structure, origin shifted by (x, y + 0.5, –(z + 0.5)) (red), showing BH_4^- tetrahedra and $[Li_5NH]^{3+}$ unit

Upon the discovery of this work the final orthorhombic structure was revisited, in particular the orientation of the NH^{2-} anion. A comparison was made between the current structure (Table 5.4) and that same structure with the NH^{2-} rotated 180 ° around the *b* axis. Figure 5.10 shows the two different arrangements of the NH^{2-} coordinated with 5 lithium ions. In the original structure the Li–H distance is quite short, determined to be 1.36(5) Å, and as both ions are δ+ this may not be the most favourable arrangement. Alternatively, with the hydrogen facing away from the lithium, the nitrogen adopts a pseudo-octahedral coordination and the distances between the ions are maximised. It means that the δ+ hydrogen is orientated away from the lithium 1+ cation and therefore, on reflection, seemed to be the more likely orientation. In future the positions of the hydrogen atoms could be

more conclusively determined by collecting neutron diffraction data on a deuterated, ^{7}Li and ^{11}B-enriched sample.

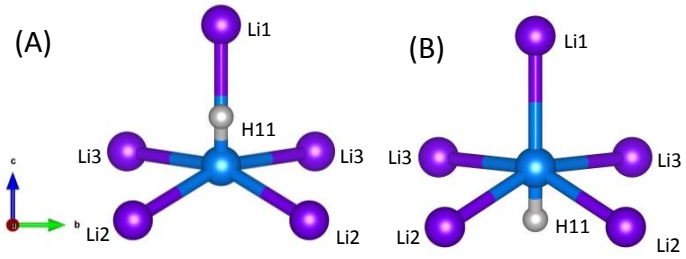

Figure 5.10 – Orientation of N–H in orthorhombic structure (A) original orientation (B) N–H rotated 180 ° about b axis

Rietveld refinements were also performed to compare the fits of the two models to the data. Each orientation of the NH^{2-} was used as a starting point and free rotation of the NH^{2-} rigid body was allowed, as well as unrestricted movement of the different ions within the structure. The refinements showed that both structures were stable, however, the overall fit to the data was improved when the hydrogen was orientated away from the lithium (R_{Bragg} = 2.84 compared with 3.01).

As a result of these comparisons it was determined that the more likely orientation of the N–H was as described in the Wolczyk structure.[148] Thus the structure determined in this work was altered to adopt the new pseudo-octahedral arrangement of the $[Li_5NH]^{3+}$ unit. The final structure is shown in Figure 5.11, the details of which are given Table 5.5.

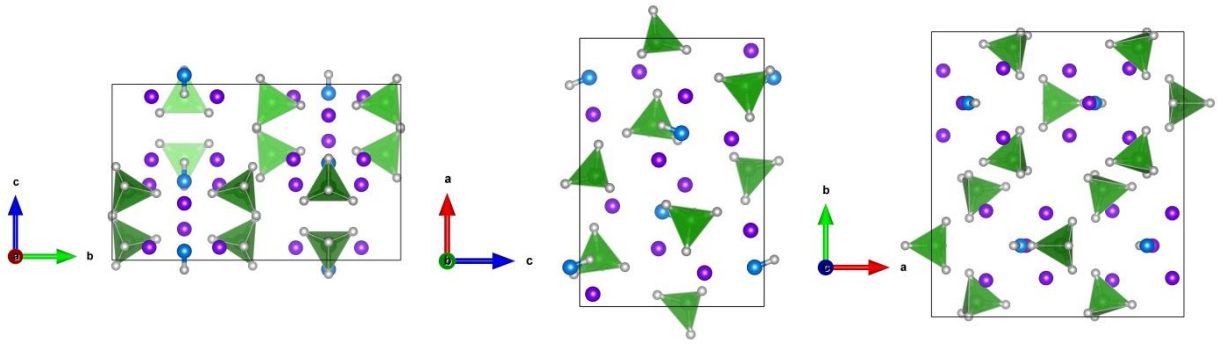

Figure 5.11 – Final $Li_5(BH_4)_3NH$ structure viewed down a, b and c. N are represented by blue spheres, H by grey spheres, BH_4^- are represented by green tetrahedra and Li by purple spheres

Table 5.5 – Details of final structure of $Li_5(BH_4)_3NH$

Atom	Site	x	y	z	Occ	B_{iso}	Symmetry
N(1)	4*c*	0.8537(8)	0.25	0.0517(9)	1	1.6(2)	.*m*.
H(11)	4*c*	0.8248(63)	0.25	0.9454(43)	1	4.6(7)	.*m*.
B(2)	8*d*	0.1776(5)	0.0525(4)	0.1027(7)	1	1.5(2)	1
H(21)	8*d*	0.2941(9)	0.0430(46)	0.0777(32)	1	4.6(7)	1
H(22)	8*d*	0.1466(21)	0.0009(23)	0.2447(21)	1	4.6(7)	1
H(23)	8*d*	0.1499(52)	0.1536(12)	0.1201(38)	1	4.6(7)	1
H(24)	8*d*	0.1197(33)	0.0128(28)	0.9683 (22)	1	4.6(7)	1
B(3)	4*c*	0.0139(7)	0.25	0.5870(11)	1	1.5(2)	.*m*.
H(31)	4*c*	0.0434(4)	0.25	0.4210(18)	1	4.6(7)	.*m*.
H(32)	4*c*	0.8962(8)	0.25	0.6020(60)	1	4.6(7)	.*m*.
H(33)	8*d*	0.0580(19)	0.1647(0)	0.6625(25)	1	4.6(7)	1
Li(1)	4*c*	0.3747(19)	0.25	0.1767(27)	1	8.7(3)	.*m*.
Li(2)	8*d*	0.4537(12)	0.3637(11)	0.5713(20)	1	8.7(3)	1
Li(3)	8*d*	0.2161(13)	0.3717(10)	0.4270(21)	1	8.7(3)	1

Table 5.6 – Bond lengths and angles for final orthorhombic $Li_5(BH_4)_3NH$ structure. * indicates parameter was fixed during refinement

Bond	Interatomic distances/ Å
N(1)-Li(1)	1.91(3)
N(1)-Li(2)	1.86(2)
N(1)-Li(3)	1.98(1)
N(1)-B(2)	3.65(6)
	3.77(8)
N(1)-B(3)	3.58(11)
	3.64(11)
B(2)-Li(1)	3.07(1)
B(2)-Li(2)	2.56(1)
	2.75(1)
B(2)-Li(3)	2.46(2)
	2.64(1)
B(2)-B(2)	3.983(7)
B(2)-B(3)	4.308(8)
B(3)-Li(1)	2.33(3)
B(3)-Li(2)	2.80(2)
B(3)-Li(3)	2.72(2)
Li(1)-Li(2)	3.16(3)
Li(1)-Li(3)	2.76(3)
	3.81(3)
Li(2)-Li(2)	2.61(2)
	3.42(2)
Li(2)-Li(3)	2.62(2)
	3.76(2)
Li(3)-Li(3)	2.80(2)
N-H*	0.80(4)
B-H*	1.2(1)

Bond	Angle/ °
Li(1)-N(1)-Li(2)	113.4(4)
Li(1)-N(1)-Li(3)	90.2(4)
Li(2)-N(1)-Li(2)	89.0(4)
Li(2)-N(1)-Li(3)	85.7(3)
Li(3)-N(1)-Li(3)	89.7(4)
Li(1)-B(2)-Li(3)	58.6(3)
Li(1)-B(2)-Li(2)	110.8(3)
	169.1(3)
Li(1)-B(2)-Li(3)	113.1(3)
Li(2)-B(2)-Li(2)	80.1(3)
Li(2)-B(2)-Li(3)	60.4(3)
	114.5(3)
	117.6(3)
Li(3)-B(2)-Li(3)	129.9(3)
Li(1)-B(3)-Li(2)	123.2(3)
Li(1)-B(3)-Li(3)	97.5(3)
Li(2)-B(3)-Li(2)	55.7(3)
Li(2)-B(3)-Li(3)	106.1(2)
	139.2(3)
Li(3)-B(3)-Li(3)	61.8(2)
H-B-H*	109.5(6)

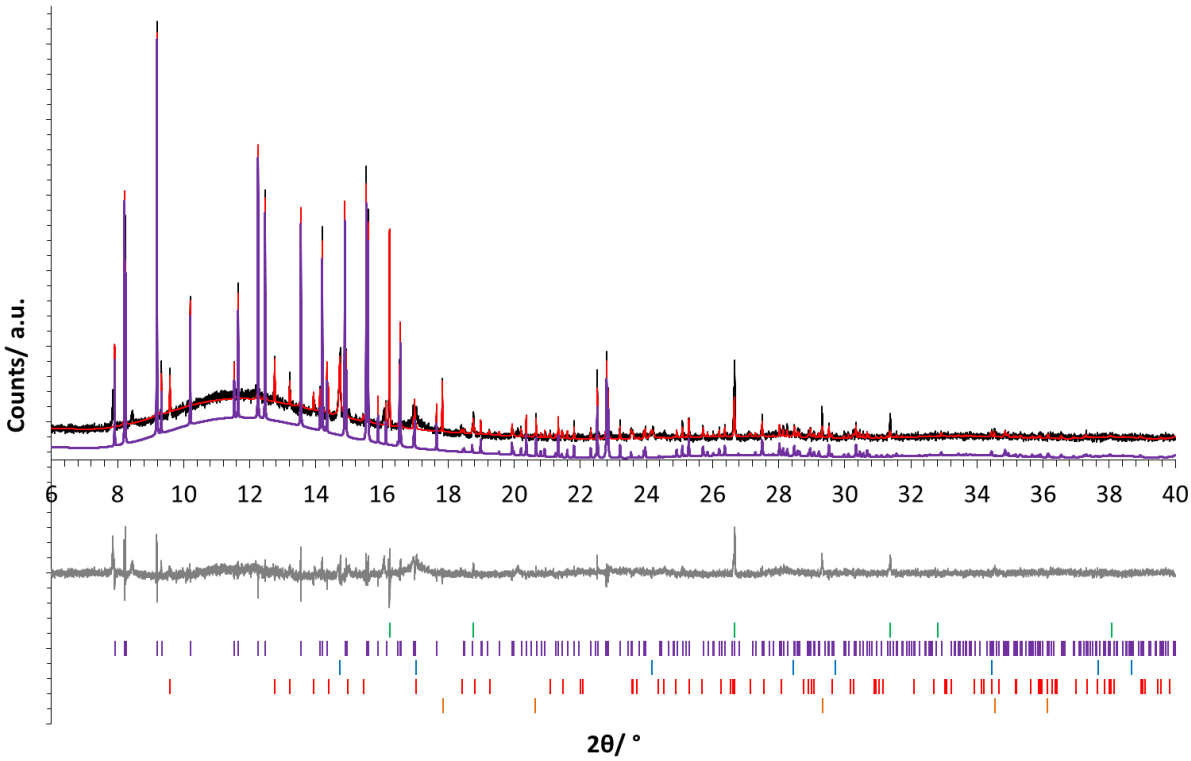

Figure 5.12– Final refinement plot of $Li_5(BH_4)_3NH$, R_{Bragg} = 2.84 (MAC data), where black = observed data, red = calculated data and grey = difference, highlighting the orthorhombic fit in purple. Green tick marks = Li_2NH, purple tick marks = orthorhombic phase, blue tick marks = cubic phase, red tick marks = $LiBH_4$ (*Pnma*) and orange tick marks = Li_2O

Table 5.7 – Final refinement parameters for orthorhombic $Li_5(BH_4)_3NH$ structure

Final Refinement Parameters	
Lattice Parameters	
a/ Å	10.14982(8)
b/ Å	11.48539(9)
c/ Å	7.00041(5)
α/ °	90
β/ °	90
γ/ °	90
Cell Volume/ $Å^3$	816.07(1)
Cell Formula Units (Z)	4
Space Group	*Pmna*
Fit Indices	
χ^2	1.25
R_{Bragg}	2.84
R_{wp}	8.71
R_{exp}	7.79
R_p	6.54

The structure of $Li_5(BH_4)_3NH$ reported by Wolczyk *et al*. was determined using a combination of synchrotron XRD data, density functional theory (DFT) calculations and solid state NMR.[148] Rietveld refinement of the synchrotron data provided a model which was determined to be rich in borohydride, with a comparison between the data sets collected on different Li_2NH:$LiBH_4$ reactant ratios all supporting a 1:3 structure. DFT calculations were then performed and produced a model which was in agreement with that determined from the Rietveld method, the difference between the two being the rotation of the BH_4^- tetrahedra.[148]

One of the key features highlighted in the DFT calculations was the $[Li_5NH]^{3+}$ unit, which was described as a square pyramidal Li_5N arrangement with hydrogen orientated perpendicular to the base, away from the lithium ions. This was investigated on a molecular level in the gas phase and was determined to have C_{2v} symmetry and be entirely ionic in nature (apart from the N–H bond). It was subsequently determined that the $[Li_5NH]^{3+}$ unit behaved as a complex cation in the structure, with the surrounding BH_4^- anions playing an important role in its stabilisation. DFT also confirmed the BH_4^- coordination to be 5-fold, although much more irregular than the coordination of lithium around the NH^{2-}anions. All three lithium positions are in a deformed tetrahedral coordination with three BH_4^- and one NH^{2-}.[148]

NMR was then used to support the structure determined from both synchrotron XRD data and DFT calculations. ^{1}H NMR confirmed the existence of eight different hydrogen environments, three with a multiplicity of four and five with a multiplicity of eight. ^{7}Li NMR showed a single large resonance with a low spinning sideband, determining all lithium environments were high in symmetry. ^{11}B NMR gave a single signal with a large spinning sideband pattern indicating an asymmetrical arrangement of lithium ions around the BH_4^-. Finally ^{15}N NMR showed that both NH^{2-} were in very similar environments, demonstrated by the presence of only one resonance.[148]

The final structure reported in this thesis and the Wolczyk structure are very similar; the two are compared in Table 5.8.

Table 5.8 – Comparison of final $Li_5(BH_4)_3NH$ structure with Wolczyk structure, origin shifted (*x*, *y* + 0.5, –(*z* + 0.5))

	Parameter	Final Structure	Wolczyk Structure[148]
	a (Å)	10.14982(8)	10.2031(3)
	b (Å)	11.48539(9)	11.5005(2)
	c (Å)	7.00041(5)	7.0474(2)
Atom			
N(1)	*x*	0.8537(8)	0.84453
	y	0.25	0.25
	z	0.0517(9)	0.06054
H(11)	*x*	0.8248(63)	0.80733
	y	0.25	0.25
	z	0.9454(43)	0.92368
B(2)	*x*	0.1776(5)	0.17100
	y	0.0525(4)	0.04171
	z	0.1027(7)	0.09149
H(21)	*x*	0.2941(9)	0.28847
	y	0.0430(46)	0.02165
	z	0.0777(32)	0.08404
H(22)	*x*	0.1466(21)	0.12002
	y	0.0009(23)	–0.01556
	z	0.2447(21)	0.21860
H(23)	*x*	0.1499(52)	0.15436
	y	0.1536(12)	0.14560
	z	0.1201(38)	0.12347
H(24)	*x*	0.1197(33)	0.12115
	y	0.0128(28)	0.01891
	z	0.9683(22)	0.93770
B(3)	*x*	0.0139(7)	0.00686
	Y	0.25	0.25

	z	0.5870(11)	0.57857
H(31)	*x*	0.0434(4)	0.06502
	y	0.25	0.25
	z	0.4210(18)	0.73059
H(32)	*x*	0.8962(8)	0.88782
	y	0.25	0.25
	z	0.6020(60)	0.60278
H(33)	*x*	0.0580(19)	0.03356
	y	0.1647(0)	0.16195
	z	0.6625(25)	0.48674
Li(1)	*x*	0.3747(19)	0.37639
	y	0.25	0.25
	z	0.1767(27)	0.18062
Li(2)	*x*	0.4537(12)	0.46908
	y	0.3637(11)	0.36846
	z	0.5713(20)	0.54097
Li(3)	*x*	0.2161(13)	0.21298
	y	0.3717(10)	0.38013
	z	0.4270(21)	0.40632

The unit cell reported by Wolczyk *et al*.[148] is slightly larger than the one determined in this thesis. However, the lattice parameters determined in the Wolczyk study were determined at 77 °C and consequently would be expected to be slightly larger due to thermal expansion. The boron and nitrogen atoms in both the structures are located in the same positions and there is only a slight displacement of lithium ions between the two models.

The main discrepancy between the two structures, although only subtle, is in the hydrogen positions. Although the Wolczyk structure did inform a change of the orientation of the NH^{2-} anion, the two are not perfectly matched. The NH^{2-} is rotated *ca* 56 ° about the *b* axis between the two structures. The BH_4^- tetrahedra in the 4*c* site are also rotated *ca* 60 ° about the *a* axis. Interestingly Wolczyk *et al*. reported that the difference between the structure determined by the Rietveld method and the one determined by DFT was in the rotation of the BH_4^- units.[148] It is not clear from the report which method the final orientation came from; however, this discrepancy highlights the need for further investigation into the hydrogen positions. Rietveld refinements were carried out with the BH_4 units in both rotations and the fit to the data did not differ. One possibility is that the BH_4 are disordered and therefore there is not a single correct rotation.

Overall the two structures agree with one another and their independent determination suggests that this is likely to be the true $Li_5(BH_4)_3NH$ structure. In future work it may be useful to collect neutron data on a deuterated, ^{7}Li and ^{11}B-enriched sample in order to look more closely at the subtleties in the different hydrogen positions.

Wang *et al*. have also published work on the orthorhombic phase and have proposed an alternative structure, although details of the atomic positions were not included.[147] They proposed a $1Li_2NH{:}1LiBH_4$ structure, with the space group $Pna2_1$ and lattice parameters: a = 10.121 Å, b = 6.997 Å and c = 11.457 Å. Figure 5.13 shows a comparison of the model determined in this work to the proposed structure by Wang *et al.*

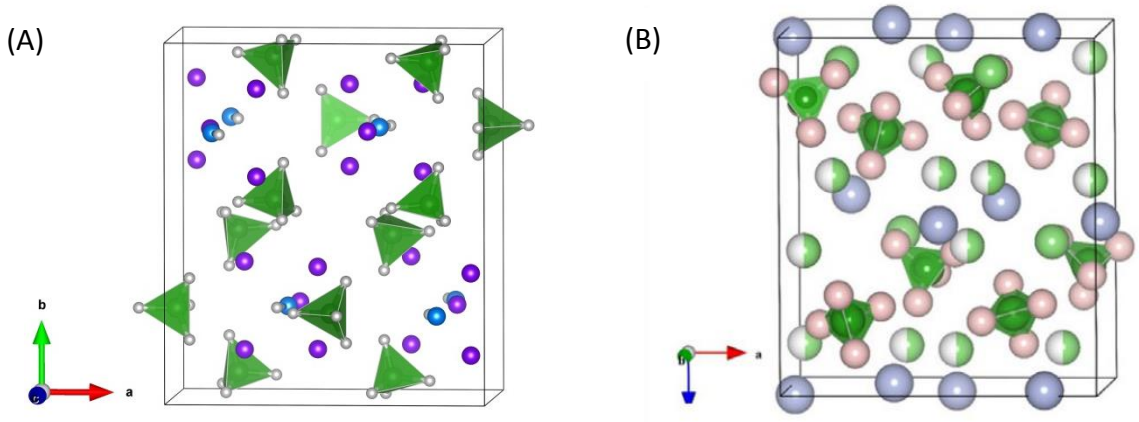

Figure 5.13 – Comparison of (A) the orthorhombic structure determined in this thesis (N = blue, H = grey, BH_4^- = green and Li = purple) and (B) the orthorhombic model depicted by Wang *et al.* (N = blue, H = pink, BH_4^- = green, Li = light green, Li/vacancies = green/white)[147]

The structure suggested by Wang *et al*. was not fully resolved and the author stated that the atomic positons were only partially determined.[147] However, the publication of an alternative structure meant it was important to investigate alternative structures with the same ratio and space group. Thus the ratio suggested in Wang *et al*.'s work was investigated in both *Pna*2_1 and *Pnma* space groups.

The model suggested by Wang *et al*. contained 8 formula units per unit cell. When comparing it to other combinations of anion ratios and formula units, it does result in significantly larger average volume per anion than if Vegard's law was obeyed (Figure 5.2). However, the other alternative, compatible with the Wyckoff positions in both *Pnma* and *Pna*2_1, would have been a unit cell containing 12 formula units. Z = 12 sits significantly below the line in the Vegard's plot and consequently would result in a much denser structure than either of the parent materials. A structure where Z = 8 combined with a ratio of $1Li_2NH{:}1LiBH_4$ is therefore the most logical assumption.

In the *Pnma* model all the ions were located in 8*d* sites, 1 × 8*d*, 1 × 8*d* and 3 × 8*d* for N, B and Li, respectively, allowing maximum flexibility in their positions. The $Pna2_1$ structure has only one possible Wyckoff position and therefore the multiplicities in this instance were 2 × 4*a*, 2 × 4*a* and 6 × 4*a* for N, B and Li, respectively. Simulated annealing refinements in both *Pnma* and $Pna2_1$ gave models which fitted more poorly to the data than the 1:3 structure. There was also less agreement between structures determined using the same constraints, and a significant amount of clustering of the lithium ions.

In earlier synthetic studies (§4.4) the orthorhombic structure was found to be favoured at a ratio of $2Li_2NH{:}3LiBH_4$ over both a 1:3 and 1:1 ratio. However, structure solution work suggested this was not the composition of the model and therefore it was ruled out. Interestingly, both Wang[147] and Wolczyk[148] also reported 2:3 as the best ratio for synthesis, and as a result the possibility of one of the sites being mixed, with both NH^{2-} and BH_4^- present, was considered.

In order to investigate this, an additional nitrogen site was added to the final $Li_5(BH_4)_3NH$ structure (presented in Figure 5.7). An extra 4*c* nitrogen site was added just slightly displaced from the 4*c* boron site and the combined occupancy of both sites was fixed at a total of one. When Rietveld refinements were carried out the new nitrogen site shifted significantly from the boron position and therefore was no longer representative of a mixed site. The occupancy of the new nitrogen position was also refined to a value close to zero. This process was then repeated with the addition of a new nitrogen 8*d* site, but again this resulted in the nitrogen shifting significantly from the boron site, with a very low occupancy. As a result of these findings it seemed unlikely that there was a mixed boron/nitrogen site, in

particular not a level of doping that would equate to a NH^{2-} to BH_4^- ratio close to 2:3. As a result of this investigation, it was deemed that the $Li_5(BH_4)_3NH$ structure, with the space group *Pnma* and lattice parameters *a* = 10.14982(8) Å, *b* = 11.48539(9) Å and *c* = 7.00041(5) Å, was likely to be the true structure of the orthorhombic phase.

5.4 Cubic Phase Structure Determination

Structure solution work on the orthorhombic phase found it to have a $1Li_2NH$ to $3LiBH_4$ ratio. Therefore, in order to optimise the cubic phase the reverse anion ratio was considered as a potential solution. This ratio was consequently used in initial structural studies of the cubic phase.

Assuming a $3Li_2NH$ to $1LiBH_4$ ratio, and thus a high imide content, suggested that the structure was similar to the parent lithium imide structure. As discussed in Chapter 3 disordered lithium imide has the space group *Fm*-3*m*, a high symmetry, face-centred, cubic structure. Previous work by Hewett[81] determined the space group of the cubic phase to be *P*23 where *a* = 5.609(2) Å. *P*23, a primitive cubic structure, has identical *hkl* values to *Pm*-3, *P*432, *P*-43*m* and *Pm*-3*m*. *Pm*-3*m* is the most commonly observed primitive cubic space group for inorganic structures,[157] so this was the first space group to be tested. *Fm*-3*m* was also looked at as an alternative. The main difference between the two space groups was the presence of a low angle ordering peak at 16 ° corresponding to the (001) reflection of *Pm*-3*m,* which appeared to be present in the XRD data (Figure 5.15).

The lithium imide structure was transformed into space group *Pm*-3*m* using Vesta.[158] The imide anions sitting on the corners of the unit cell (0,0,0) were replaced with borohydride anions (Figure 5.14) and the starting thermal parameters were literature values

reported for lithium imide.[131] This proposed cubic structure gave a $3Li_2NH$ to $1LiBH_4$ ratio, details of which are given in Table 5.9.

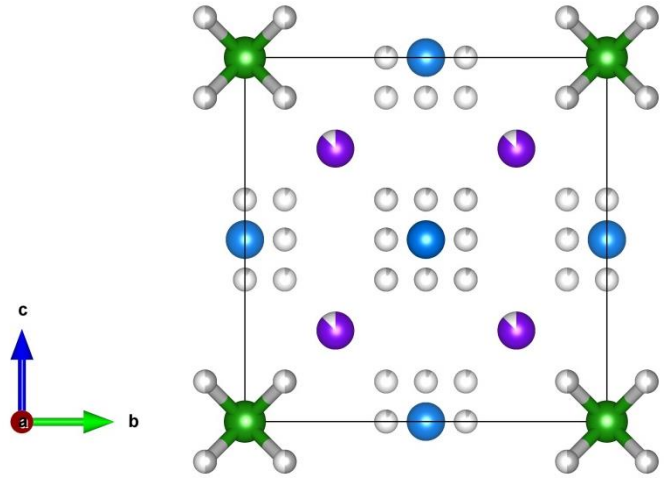

Figure 5.14 – Proposed cubic structure based on a $3Li_2NH + 1LiBH_4$ ratio. Boron is represented by green spheres, nitrogen by blue spheres, lithium by purple spheres and hydrogen by grey spheres

Table 5.9 – Details of proposed *Pm*-3*m* structure of cubic structure based on a $3Li_2NH$ to $1LiBH_4$ ratio

Atom	Site	*x*	*y*	*z*	Occupancy	B_{iso}	Symmetry
Li(1)	8*g*	0.25	0.25	0.25	0.875	3.0	.3*m*
B(1)	1*a*	0	0	0	1.0	1.0	*m*–3*m*
N(1)	3*c*	0	0.5	0.5	1.0	1.0	4/*mm*. *m*
H(1)	8*g*	0.11	0.11	0.11	0.5	1.0	.3*m*
H(2)	24*l*	0.11	0.61	0.5	0.083	1.0	*m*. .
H(3)	12*i*	0	0.61	0.61	0.083	1.0	*m*.*m* 2

For the possible *Pm*-3*m* structure, the (111) peak at 28 ° and (022) peak at 46 ° fitted well to the XRD data, but still there were some issues with the fit of other peaks. One of the highest intensity peaks at 32 °, the (002) peak, fitted very poorly and there was another peak

at 44 ° which remained unassigned to any of the known phases. This fit is shown in Figure 5.15.

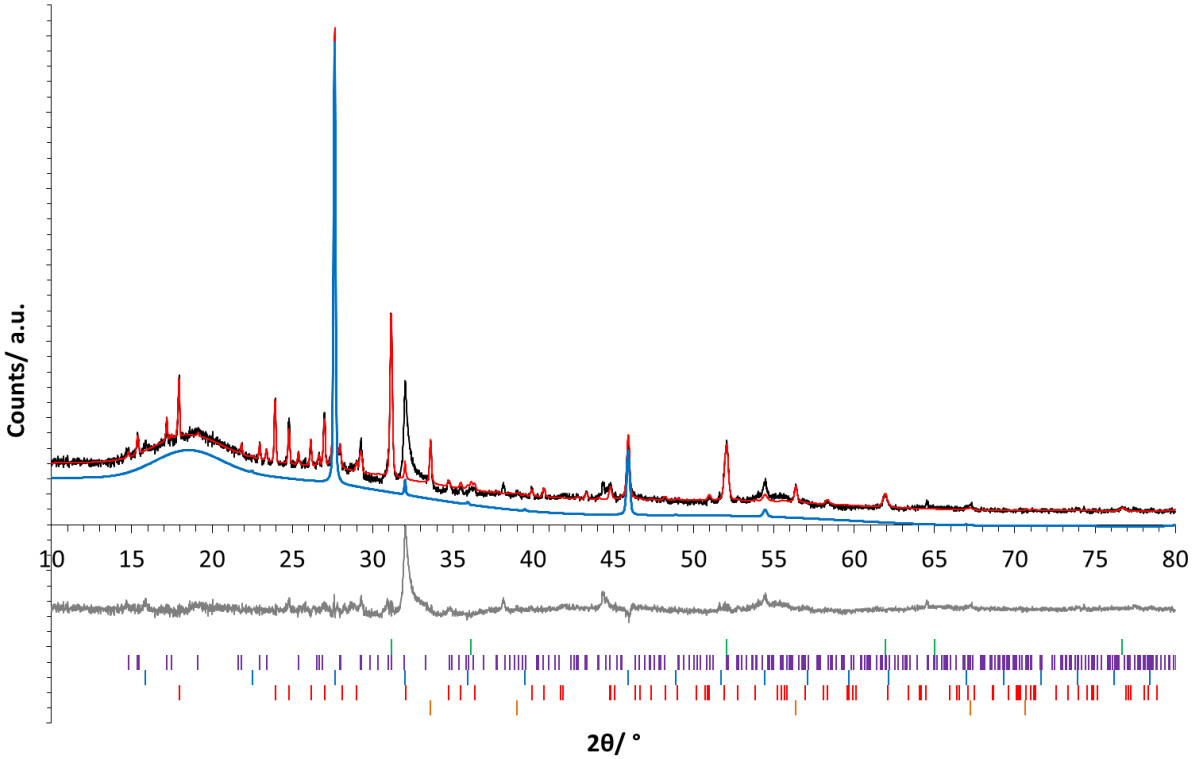

Figure 5.15 – Powder XRD showing *Pm*-3*m* fit to unknown cubic phase, where black = observed data, red = calculated data and grey = difference, highlighting the cubic fit in blue. Green tick marks = Li_2NH, purple tick marks = orthorhombic phase, blue tick marks = cubic phase, red tick marks = $LiBH_4$ (*Pnma*) and orange tick marks = Li_2O

While *Pm*-3*m* was a reasonable starting model for this structure, the intensity issues of the (002) peak at 32 ° and exclusion of the observed peak at 44 ° (Figure 5.15) suggested that either additional phases were present or the cubic structure was in fact lower symmetry than initially thought. There was also the added issue that the (002) peak overlapped with a peak from the orthorhombic phase, resulting in some uncertainty in the contribution of the cubic phase to the overall intensity. These issues with the fit suggested there may be more

disorder in the final structure than was accounted for in the *Pm*-3*m* model. There may also be some distortion from the ideal cubic structure.

5.4.1 Varying the Lithium Positions

In order to resolve these issues with the fit, variations in the positions of each of the ions and occupancies of the sites were considered. Interestingly it was found that completely removing the lithium from the cubic structure, creating an anion only model, significantly improved the fit to the data. Although the fit to the (022) peak at *ca* 46 ° worsened, the fit to the (002) peak at 32 ° was dramatically improved (Figure 5.16).

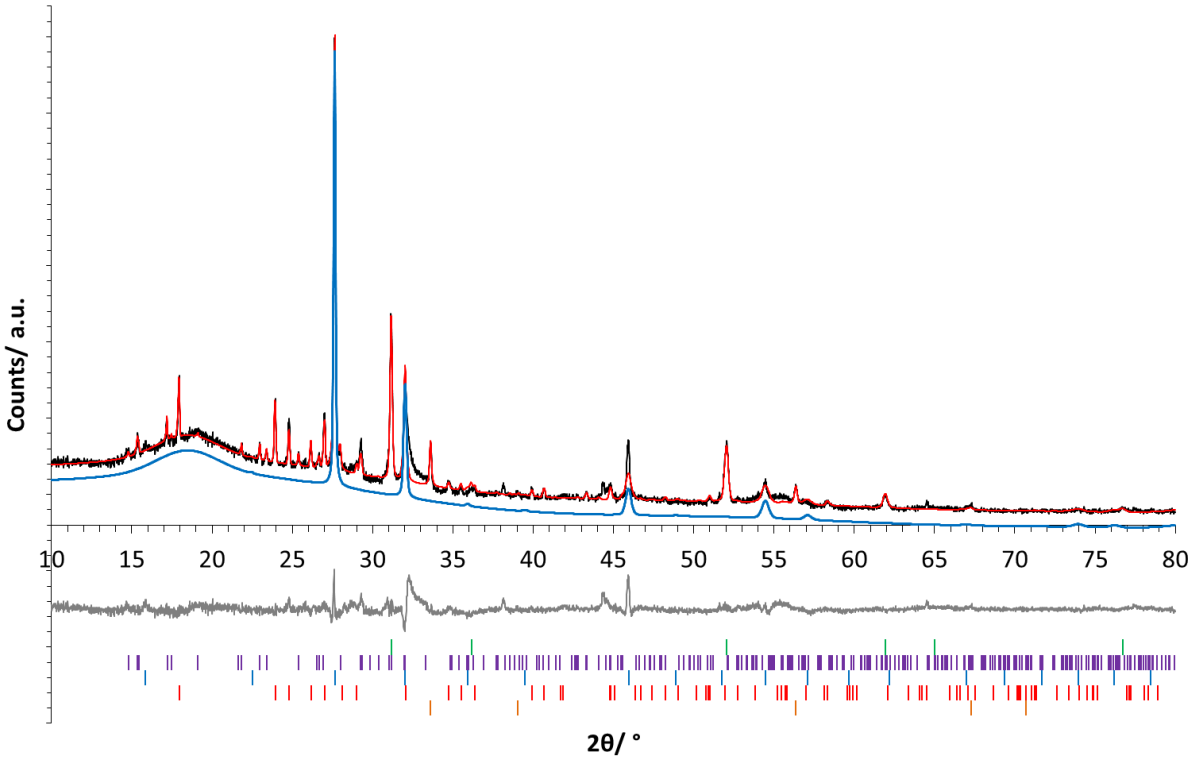

Figure 5.16 – Powder XRD showing *Pm*-3*m* fit without lithium ions to unknown cubic phase, where black = observed data, red = calculated data and grey = difference, highlighting the cubic fit in blue. Green tick marks = Li_2NH, purple tick marks = orthorhombic phase, blue tick marks = cubic phase, red tick marks = $LiBH_4$ (*Pnma*) and orange tick marks = Li_2O

This significant improvement of the fit to the data suggested that the structure might have multiple lithium sites with lower occupancies, rather than the single 8*g* site proposed in the first model. Consequently additional lithium sites were added into the structure, with lithium in 8*g* (x,x,x), 3*d* (1/2,0,0) and 1*b* (1/2,1/2,1/2) sites. The occupancies across all three sites were allowed to refine, although the combined total was fixed at seven lithium ions to ensure the structure remained charge-balanced. This alternative structure is shown in Figure 5.17 and detailed in Table 5.10.

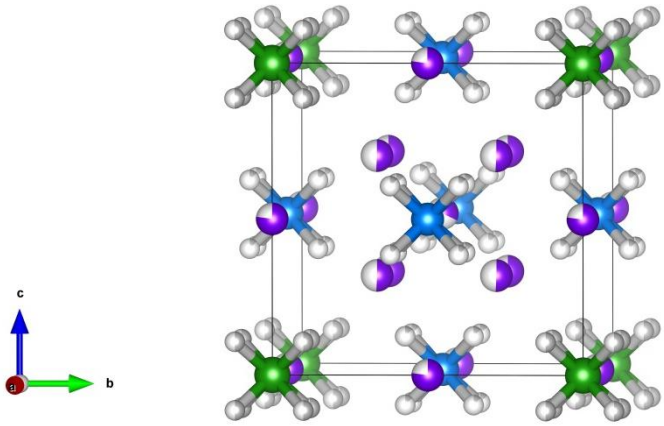

Figure 5.17 – Cubic structure based on a $3Li_2NH + 1LiBH_4$ ratio with disordered lithium. Boron are represented by green spheres, nitrogen by blue spheres, lithium by purple spheres and hydrogen by grey spheres

Table 5.10 – Details of proposed *Pm*-3*m* structure with disordered lithium of the cubic phase based on a $3Li_2NH$ to $1LiBH_4$ ratio

Atom	Site	*x*	*y*	*z*	Occupancy	B_{iso}	Symmetry
Li(1)	8*g*	0.308	0.308	0.308	0.52	20.0	.3*m*
Li(2)	3*d*	0.5	0	0	0.8	20.0	4/*mm*. *m*
Li(3)	1*b*	0.5	0.5	0.5	0.31	20.0	*m*–3*m*
B(1)	1*a*	0	0	0	1.0	9.3	*m*–3*m*
N(1)	3*c*	0	0.5	0.5	1.0	9.3	4/*mm*. *m*
H(1)	8*g*	0.11	0.11	0.11	0.5	14.0	.3*m*
H(2)	24*m*	0.61	0.61	0.11	0.125	14.0	*m*. .

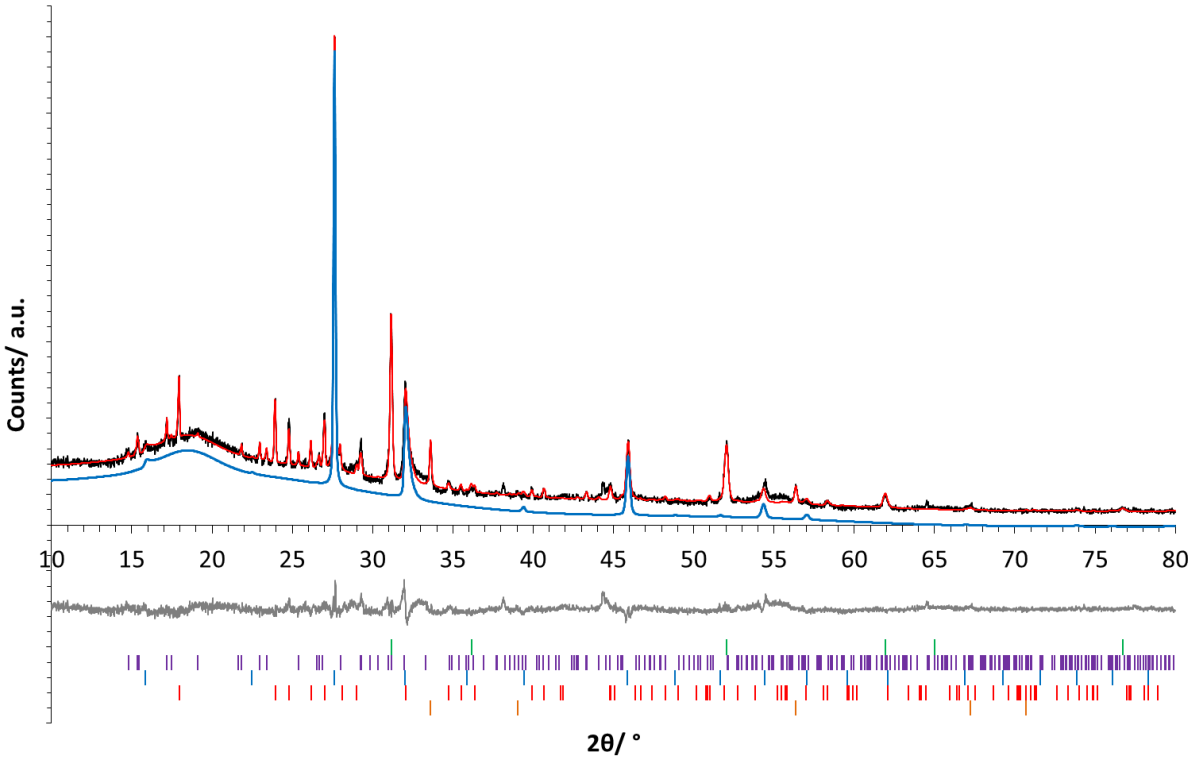

Figure 5.18 – Powder XRD showing *Pm*-3*m* fit with disordered lithium to unknown cubic phase, where black = observed data, red = calculated data and grey = difference, highlighting the cubic fit in blue. Green tick marks = Li_2NH, purple tick marks = orthorhombic phase, blue tick marks = cubic phase, red tick marks = $LiBH_4$ (*Pnma*) and orange tick marks = Li_2O

Figure 5.18 shows the fit of the disordered lithium structure. The intensities in both the (001) peak at 16 ° and the (002) peak at 32 ° were drastically improved and suggested that a disordered lithium lattice was more likely than the initial, highly ordered, *Pm*-3*m* structure. However, it is important to note that at this stage the peak at *ca* 44 ° remained unidentified and therefore it appeared likely that there was another phase present.

5.4.2 Investigating Decomposition Products

In order to try and identify the phase responsible for the presence of a peak at 44 ° possible decomposition products were investigated. As a result of this lithium hydride was found to fit to the unidentified peak as well as to a couple of very small peaks at 38 ° and 65 °. The presence of LiH then posed the question of whether or not other decomposition products, such as known polymorphs of lithium boron nitride, were present. Until this point all the hydrogen in the system was assumed to be contained within imide and borohydride anions; however, the presence of LiH meant that there would have been insufficient hydrogen to form these complex hydrides.

In initial work the presence of Li_3BN_2 was ruled out due to previously reported dehydrogenation data which demonstrated that hydrogen loss from a mixture of Li_2NH and $LiBH_4$ began at 250 °C, peaking at 300 °C (320 °C for more Li_2NH-rich samples).[81] Nevertheless, the discovery of LiH within the sample meant that hydrogen would have had to have been lost from another component of the mixture, suggesting dehydrogenation was in fact occurring. As there is significant overlap between Li_3BN_2, the cubic phase and other phases in the XRD data, to confirm whether or not Li_3BN_2 was present Raman data were collected.

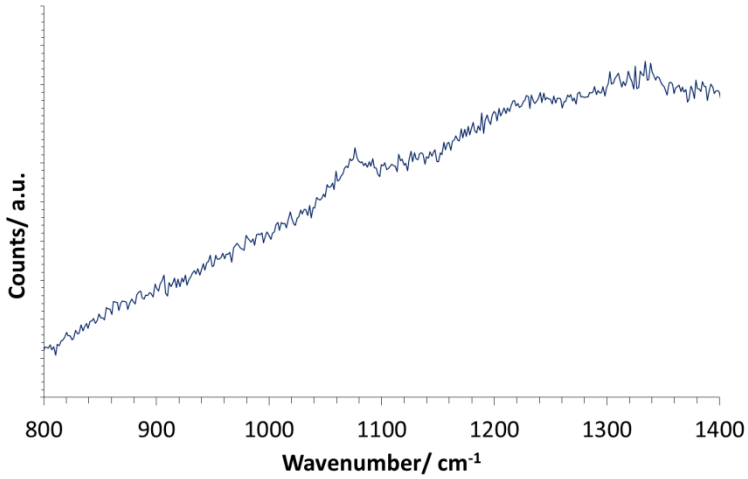

Figure 5.19 – Raman data of nLi$_2$NH + (1 – n)LiBH$_4$ where, n = 0.5, heated at 200 °C for 12 hours

Figure 5.19 shows a small but significant peak at *ca* 1050 cm^{-1} characteristic of a symmetric B=N stretching vibration in Li_3BN_2 from the $[N=B=N]^{3-}$ ion.[81] Unfortunately, the identification of Li_3BN_2 in the cubic sample cast doubt on the disordered *Pm*-3*m* structure. Fitting the different Li_3BN_2 polymorphs to the XRD data confirmed that in this case it was the *I*4$_1$/*amd* polymorph which was present.

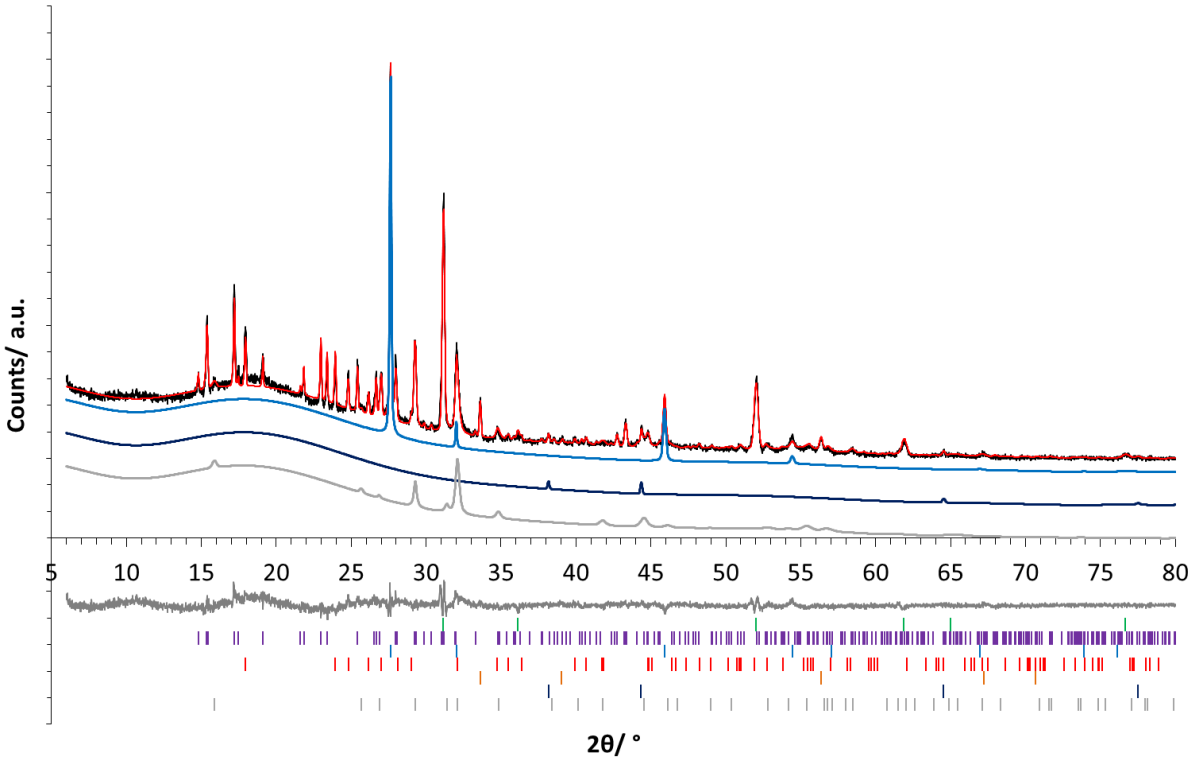

Figure 5.20– Powder XRD showing fit of *Fm*-3*m* Li_3BH_4NH cubic phase (blue), LiH (dark blue) and Li_3BN_2 *I*4_1/*amd* polymorph (grey) to data. Green tick marks = Li_2NH, purple tick marks = orthorhombic phase, blue tick marks = cubic phase, red tick marks = $LiBH_4$ (*Pnma*), orange tick marks = Li_2O, dark blue tick marks = LiH and grey tick marks = Li_3BN_2 (*I*4_1/*amd*)

The highest intensity peak for the *I*4_1/*amd* polymorph was observed at 32 °, overlapping with the (002) peak of the cubic structure (Figure 5.20). This therefore meant that the intensity of this peak could no longer be unambiguously attributed to disorder of the lithium lattice, but was instead consistent with the presence of a decomposition product. Additionally, the cubic ordering peak at 16 ° which resulted in the determination of a *Pm*-3*m* structure could no longer be used as confirmation of a primitive structure; the (101) reflection of Li_3BN_2 was located at the same 2θ value (Figure 5.20) and therefore, although it

is possible there is still some ordering of the cubic lattice there was no longer any unambiguous experimental evidence to support that hypothesis.

The presence of only two unique reflections belonging to the cubic phase meant that only a limited amount of information about the structure could be determined. After confirming the presence of Li_3BN_2 only the (111) peak at 28 ° and (022) peak at 46 ° could be identified as belonging solely to the cubic phase. In addition the lack of structural information and the presence of the cubic phase at all Li_2NH:$LiBH_4$ reactant ratios (discussed in detail in Chapter 4) meant that a 1:1 ratio was the most sensible assumption. Thus the cubic model proposed in this work is an *Fm*-3*m* structure with a $1Li_2NH$:$1LiBH_4$ ratio (Li_3BH_4NH) and a lattice parameter of 5.5850(4) Å (Figure 5.22). It is possible that the cubic phase is a highly disordered structure, potentially with a variable anion ratio and lithium content. The range of different lattice parameters refined for the cubic phase (Figure 5.21) supports this hypothesis, the changing size of the unit cell was perhaps as a result of accommodating different compositions within the structure. Despite this, the model detailed in Table 5.11 is chemically sensible and was used during analysis throughout this thesis.

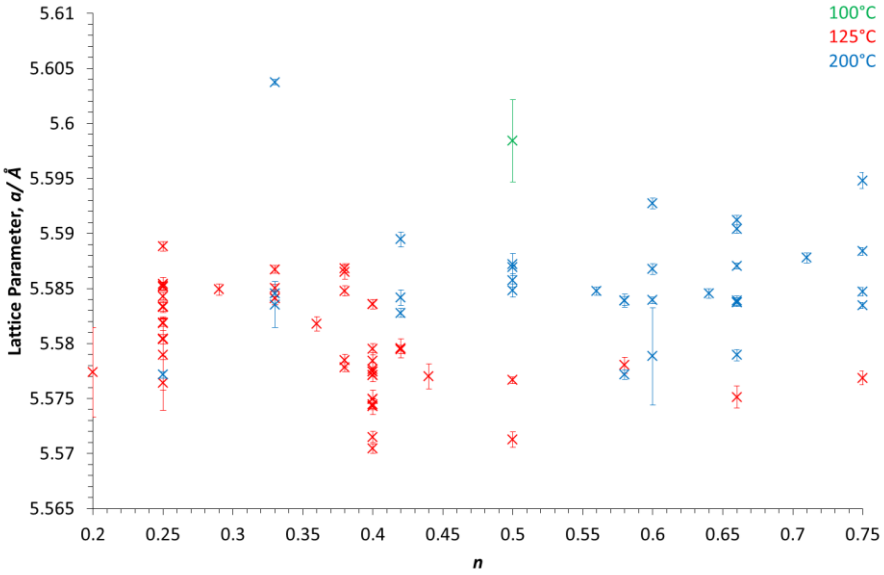

Figure 5.21 – Lattice parameters of the Li_2NH-$LiBH_4$ cubic phase synthesised across a range of different compositions and temperatures for $nLi_2NH + (1 - n)LiBH_4$

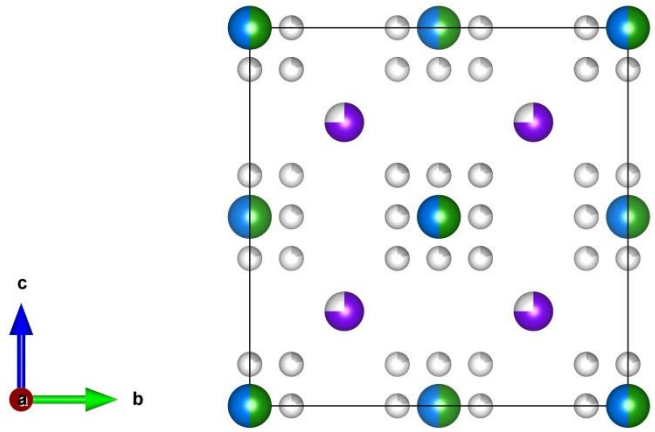

Figure 5.22 – *Fm*-3*m* cubic structure with a 1 imide to 1 borohydride anion ratio (Li_3BH_4NH). Boron are represented by green spheres, nitrogen by blue spheres, lithium by purple spheres and hydrogen by grey spheres

Table 5.11 – Details of proposed *Fm*-3*m* structure of the cubic phase based on a 1Li_2NH to 1$LiBH_4$ ratio (Li_3BH_4NH) , * indicates that a parameter hit its maximum allowed value

Atom	Site	*x*	*y*	*z*	Occupancy	B_{iso}	Symmetry
Li(1)	8*c*	0.25	0.25	0.25	0.75	10.8*	–43*m*
B(1)	4*a*	0	0	0	0.5	10.8*	*m*–3*m*
N(1)	4*a*	0	0	0	0.5	10.8*	*m*–3*m*
H(1)	48*h*	0.11	0.11	0	0.208	10.8*	*m*.*m*2

Table 5.12 – Bond lengths and angles for proposed cubic Li_3BH_4NH structure

Bond	Interatomic distances/ Å
Li-B/N	2.41916(0)
	4.63234(0)
B/N-B/N	3.95047(0)
	5.58681(0)
Li-Li	2.79341(0)
	3.95047(0)
	4.83832(0)
B-H	1.06443(0)
N-H	0.86910(0)

Bond	Angle/ °
B/N-B/N-B/N	30.0(0)
	60.0(0)
	90.0(0)
Li-B/N-Li	70.5288(0)
B/N-Li-B/N	40.4576(0)
	100.0250(0)
B-H	109.5(0)

Table 5.13 – Final refinement parameters for cubic Li_3BH_4NH

Final Refinement Parameters	
Lattice Parameters	
a/ Å	5.5850(4)
b/ Å	5.5850(4)
c/ Å	5.5850(4)
α/ °	90
β/ °	90
γ/ °	90
Cell Volume/ $Å^3$	174.21(4)
Cell Formula Units (Z)	4
Space Group	*Fm*-3*m*
Fit Indices	
χ^2	2.69
R_{Bragg}	3.32
R_{wp}	7.06
R_{exp}	4.30
R_p	5.22

5.5 Lithium Amide-Borohydride-Imide Structure

Studies involving the reaction of lithium amide-imide and lithium borohydride [$n$$Li_{1.5}(NH_2)_{0.5}(NH)_{0.5}$ + (1 – n)$LiBH_4$] resulted in the formation of a new, previously unreported structure (§4.6). Comparison of each of the samples across the reaction series ensured that the all of the peaks corresponded to a single phase as the relative intensities of the observed reflections were consistent. The peaks were indexed and were determined to belong to a hexagonal structure with the space group $P6_2$ and lattice parameters a = 6.9489(2) Å and c =

15.1988(6) Å (Figure 5.23). However, $P6_2$ has identical systematic absences to multiple other space groups ($P3_1$, $P3_2$, $P3_112$, $P3_121$, $P3_212$, $P3_221$, $P6_4$, $P6_222$ and $P6_422$), therefore it was also important to consider all of these as potential solutions. This structure solution work was carried out using laboratory data only as synchrotron data was not available. The data used was from a sample with the starting composition $7Li_{1.5}(NH_2)_{0.5}(NH)_{0.5}$:$5LiBH_4$ [n = 0.58 using the equation $nLi_{1.5}(NH_2)_{0.5}(NH)_{0.5} + (1 - n)LiBH_4$].

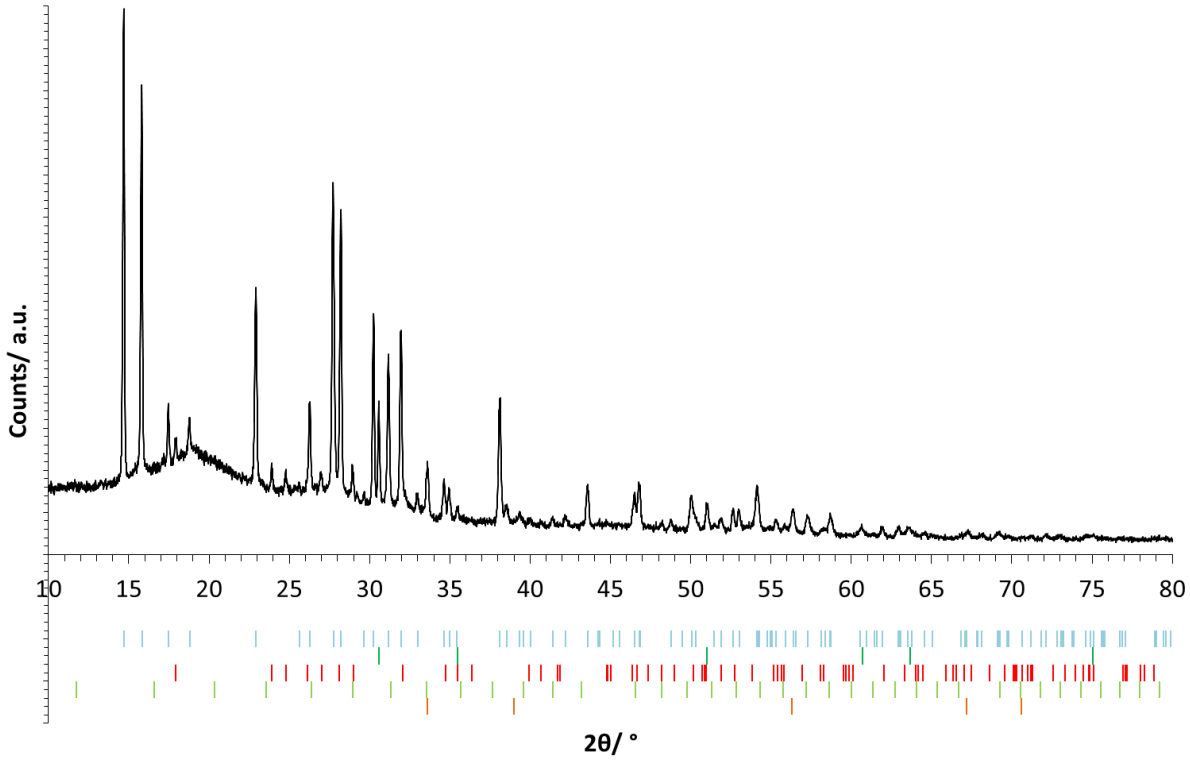

Figure 5.23 – Powder XRD data of $nLi_{1.5}(NH_2)_{0.5}(NH)_{0.5} + (1 - n)LiBH_4$ where n = 0.58. Light blue tick marks = hexagonal lithium amide-borohydride-imide, green tick marks = Li_2NH, red tick marks = $LiBH_4$ (*Pnma*), light green tick marks = $Li_4BH_4(NH_2)_3$ and orange tick marks = Li_2O

In order to build a model of the lithium amide-borohydride-imide phase, first the anion ratio needed to be considered. The phase was most abundant when a reactant ratio of $7Li_{1.5}(NH_2)_{0.5}(NH)_{0.5}$:$5LiBH_4$ was used, closely followed by a ratio of 8:4, equating to roughly a

1:1:1 anion ratio. Consequently, a ratio of $1NH_2^-$ to $1BH_4^-$ to $1NH^{2-}$ was determined to be a sensible starting point.

When considering this ratio and applying it to all of the possible space groups, some of them were eliminated based on their available Wyckoff positions. A structure containing six NH, six NH_2 and six BH_4 seemed the most logical as that gave a density of *ca* 1.15 g cm^{-3}, between the reported values for $LiNH_2$, Li_2NH and $LiBH_4$ (1.17 g cm^{-3}, 1.43 g cm^{-3} and 0.67 g cm^{-3}, respectively).[76,86,131] It also enabled a structure to be built with no mixed sites as the multiplicities of the sites across all the space groups were either 3, 6 or 12.

The general position in both $P6_222$ and $P6_422$ is a 12*k* site and therefore they were considered to be unlikely candidates as no atoms could be located in the general position without significant site disorder, and so were consequently ruled out. $P3_1$ and $P3_2$ were also ruled out after only limited investigations as they both only contain a single Wyckoff position, a general position with multiplicity of three. Although adopting one of these space groups would be possible, it was assumed that a structure with as many different sites as this hexagonal phase was more likely to adopt a higher symmetry space group. Elimination of these less likely space groups left $P3_112$, $P3_121$, $P3_212$, $P3_221$, $P6_2$ and $P6_4$ to be considered as possible space groups.

In each of the remaining space groups there is a general position with a multiplicity of six (6*c*) and two special positions, both with a multiplicity of three (3*a* and 3*b*); these are summarised in Table 5.14. Simulated annealing was therefore performed for each space group in four different arrangements: all anions in 6*c* sites; BH_4 in 3*a* and 3*b* sites and NH/NH_2 in 6*c* sites; NH in 3*a* and 3*b* sites and BH_4/NH_2 in 6*c* sites; and finally NH_2 in 3*a* and

3*b* sites and BH_4/NH in 6*c* sites. In each case there were also 4 × 6*c* sites occupied by lithium to ensure the structure was charge balanced.

Table 5.14 – Wyckoff positions for the possible space groups for the hexagonal lithium amide-borohydride-imide phase

Wyckoff Position	$P3_112$	$P3_121$	$P3_212$	$P3_221$	$P6_2$	$P6_4$
6*c*	(*x*, *y*, *z*)	(*x*, *y*, *z*)	(*x*, *y*, *z*)	(*x*, *y*, *z*)	(*x*, *y*, *z*)	(*x*, *y*, *z*)
3*b*	(*x*, –x, 5/6)	(*x*, 0, 5/6)	(*x*, –x, 1/6)	(*x*, 0, 1/6)	(1/2, 1/2, *z*)	(1/2, 1/2, *z*)
3*a*	(*x*, –x, 1/3)	(*x*, 0, 1/3)	(*x*, –x, 2/3)	(*x*, 0, 2/3)	(0, 0, *z*)	(0, 0, *z*)

The refinements were carried out with the inclusion of rigid bodies for each of the complex anions: NH_2^-, NH^{2-} and BH_4^-; and each were able to rotate and be translated as a single unit. Restrictions on minimum atomic distances were also included to ensure chemically sensible structures: 3.2 Å, 1.6 Å and 1.8 Å for anion–anion, anion–lithium and lithium–lithium distances, respectively. These values were based on the distances in similar structures and reduced slightly to allow for less restricted movement when running the refinements.

The results of simulated annealing consistently showed a better fit to the data for the $P3_212$ and $P3_221$ space groups, in particular where BH_4 was located in the 3*a* and 3*b* sites. In each of the other space groups there were recurring issues with short atomic distances, fit of the structure to the data or both. Many of those in which the bond distance penalties were obeyed sat exactly on the penalty boundary, and thus when the restriction was removed reverted to a structure with short bonds which were not chemically sensible.

From the results of simulated annealing, the $P3_212$ and $P3_221$ space groups were investigated more closely. In each space group the best fits were obtained for the case of an arrangement in which the borohydride resided in the 3*a* and 3*b* special positions. Although the initial results showed promise, with repeated simulated annealing runs resulting in the same anion arrangement, the lithium positions did not seem sensible in either structure. Consequently, the anion positions were fixed and simulated annealing was run again, this time with only the lithium positions refining. This process highlighted issues with the $P3_212$ space group as the lithium ions tended to be arranged solely within one half of the unit cell. As a result of this observation the focus of this work shifted to the $P3_221$ space group.

Although refining the lithium positions in the $P3_221$ space group did not have the same issues as the $P3_212$ structure, there was no consistency between the simulated annealing results and the lithium positions varied significantly between structures. This led to a consideration of the orthorhombic structure (§5.3) in which a pseudo-octahedral $[Li_5NH]^{3+}$ unit is present. An attempt was made to incorporate this arrangement into the $P3_221$ structure in order to reduce the degrees of freedom available for the simulated annealing. A refinement was subsequently set up in which the NH and lithium were included as single Li_5NH units, located in a 6*c* site, alongside the BH_4 and NH_2 rigid bodies in 3*a*/3*b* and 6*c* sites, respectively. This set up resulted in an additional lithium 6*c* site and therefore in order to adjust for this the lithium–lithium anti-bump penalty was removed and the lithium occupancies were allowed to merge.

Although the resulting structures were slightly lithium-rich they identified where the most suitable lithium positions were. The use of ‘occ_merge’ within the refinement meant

that where Li ions were in close proximity the occupancies of the respective sites would be reduced, indicating that the true lithium position may have been situated somewhere between the two sites. The Li_5NH rigid body constraints were subsequently removed to allow the Li positions to move more freely from their determined positions during final Rietveld refinements. During subsequent refinements it became apparent that two of the lithium sites were merging, and so one of them was removed, finally resulting in a charge-balanced structure. The proposed structure is detailed in Figure 5.24 and Table 5.15. Bond lengths and angles are reported in Table 5.16 and the refinement parameters are reported in Table 5.17.

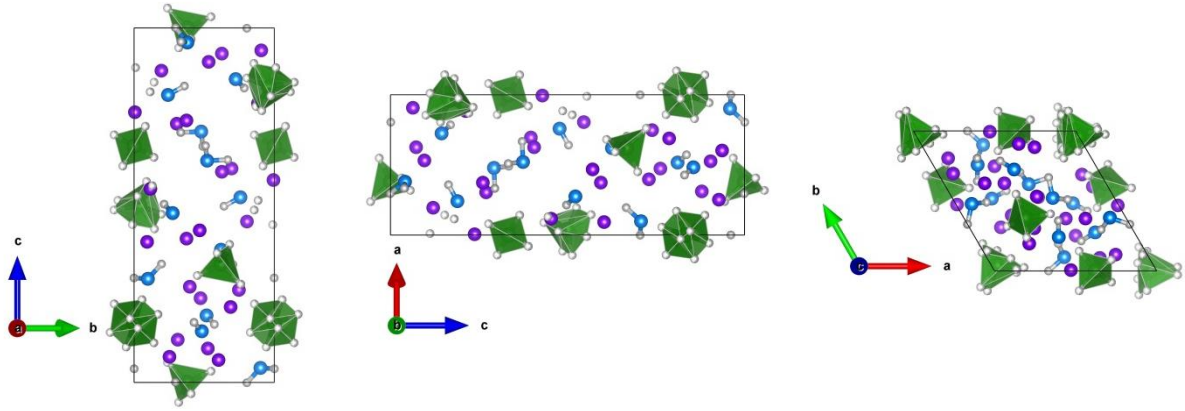

Figure 5.24 – Proposed $P3_221$ $Li_4BH_4NHNH_2$ structure, where N = blue, H = grey, BH_4^- = green and Li = purple

Table 5.15 – Details of proposed *P*$3_2$21 $Li_4BH_4NHNH_2$ structure

Atom	Site	x	y	z	Occ	B_{iso}	Symmetry
N(1)	6*c*	–0.098(3)	0.380(3)	–0.041(1)	1	4.5(2)	1
N(2)	6*c*	–0.758(3)	0.517(4)	0.189(1)	1	4.5(2)	1
B(3)	3*b*	0.961(3)	0	1/6	1	4.5(2)	.2.
B(4)	3*a*	1.622(4)	0	2/3	1	4.5(2)	.2.
Li(1)	6*c*	–0.696(6)	0.397(6)	0.270(3)	1	4.5(2)	1
Li(2)	6*c*	–0.626(5)	0.748(6)	0.261(2)	1	4.5(2)	1
Li(3)	6*c*	–0.468(7)	0.526(5)	0.096(2)	1	4.5(2)	1
Li(4)	6*c*	–0.805(4)	0.311(5)	0.121(2)	1	4.5(2)	1
H(11)	6*c*	–0.196(13)	0.296(25)	0.001(6)	1	4.5(2)	1
H(12)	6*c*	0.001(17)	0.333(21)	–0.038(9)	1	4.5(2)	1
H(21)	6*c*	–0.642(12)	0.573(80)	0.164(9)	1	4.5(2)	1
H(31)	6*c*	1.011(101)	0.141(39)	0.112(12)	0.5	4.5(2)	1
H(32)	6*c*	0.911(59)	0.057(32)	0.233(12)	0.5	4.5(2)	1
H(33)	6*c*	0.805(39)	–0.170(47)	0.141(25)	0.5	4.5(2)	1
H(34)	6*c*	1.115(61)	–0.028(90)	0.180(29)	0.5	4.5(2)	1
H(41)	6*c*	1.682(10.991)	–0.080(8.232)	0.611(2.791)	0.5	4.5(2)	1
H(42)	6*c*	1.593(11.265)	0.142(7.106)	0.635(3.105)	0.5	4.5(2)	1
H(43)	6*c*	1.451(5.069)	–0.142(7.604)	0.698(2.281)	0.5	4.5(2)	1
H(44)	6*c*	1.762(6.550)	0.080(7.020)	0.723(2.364)	0.5	4.5(2)	1

Table 5.16 – Bond lengths and angles for $P3_221$ $Li_4BH_4NHNH_2$ structure. * indicates parameter was fixed during refinement

Bond	Interatomic distances/ Å	Bond	Angle/ °
N(1)-N(1)	3.70(3)	Li(1)-N(1)-Li(2)	58.1(4)
N(1)-N(2)	3.29(3)		71.1(4)
	3.25(2)		80.4(4)
	3.85(3)		89.2(5)
N(1)-B(3)	3.82(3)		126.3(4)
N(1)-B(4)	3.69(1)	Li(1)-N(1)-Li(3)	36.6(4)
	3.37(1)		72.6(4)
N(1)-Li(1)	2.90(4)		95.6(4)
	2.21(5)		99.7(4)
N(1)-Li(2)	2.39(5)	Li(1)-N(1)-Li(4)	62.8(3)
	2.21(4)		77.1(4)
	3.50(4)		79.3(3)
N(1)-Li(3)	3.38(5)		95.8(4)
	3.82(3)		134.9(5)
N(1)-Li(4)	3.38(3)	Li(2)-N(1)-Li(3)	35.5(3)
	3.85(3)		59.2(3)
N(2)-N(2)	3.55(4)		72.1(4)
N(2)-B(3)	3.13(2)		106.3(3)
N(2)-B(4)	3.07(3)		115.3(4)
	3.32(2)		122.5(4)
N(2)-Li(1)	1.66(4)	Li(2)-N(1)-Li(4)	54.8(3)
	3.29(5)		58.8(3)
N(2)-Li(2)	1.77(5)		65.1(4)
N(2)-Li(3)	1.68(5)		76.1(4)
	2.44(5)		81.4(4)
N(2)-Li(4)	1.66(4)		88.1(3)
	3.27(3)		133.7(3)

B(3)-B(4)	3.76(3)		140.2(4)
B(3)-Li(1)	3.03(5)		153.6(4)
B(3)-Li(2)	3.82(5)	Li(3)-N(1)-Li(4)	32.9(3)
B(3)-Li(3)	3.33(6)		60.8(3)
B(3)-Li(4)	2.07(2)		100.0(3)
B(4)-Li(1)	3.34(5)		147.2(4)
B(4)-Li(2)	2.54(4)		165.3(3)
B(4)-Li(3)	1.80(5)	Li(1)-N(2)-Li(3)	59.1(5)
B(4)-Li(4)	2.15(4)		103.5(4)
Li(1)-Li(2)	2.24(6)	Li(2)-N(2)-Li(3)	61.1(5)
	3.10(5)	Li(3)-N(2)-Li(3)	40.7(4)
Li(1)-Li(3)	2.43(5)	Li(3)-N(2)-Li(4)	63.7(3)
	2.98(6)		127.4(5)
	3.44(6)	Li(1)-B(3)-Li(3)	44.7(3)
Li(1)-Li(4)	2.37(6)		167.4(4)
	3.60(4)	Li(2)-B(3)-Li(3)	56.3(3)
Li(2)-Li(3)	2.33(3)		83.3(3)
	3.40(4)	Li(3)-B(3)-Li(3)	67.7(3)
	3.49(5)		132.7(3)
Li(2)-Li(4)	3.30(5)		144.3(3)
	3.39(5)	Li(3)-B(3)-Li(4)	55.8(4)
	3.57(5)		140.6(4)
	3.84(4)	Li(1)-B(4)-Li(1)	76.6(3)
Li(3)-Li(3)	2.92(5)	Li(1)-B(4)-Li(2)	42.1(4)
Li(3)-Li(4)	2.09(3)		118.7(4)
	2.76(4)	Li(1)-B(4)-Li(3)	45.3(5)
	3.87(5)		77.7(6)
Li(4)-Li(4)	3.93(5)	Li(1)-B(4)-Li(4)	104.4(4)
N-H (NH)*	0.8		112.7(5)
N-H (NH_2)*	0.9	H-B-H*	109.5
B-H*	1.2	H-N-H (NH_2)*	100.9

Table 5.17 – Final refinement parameters of hexagonal $Li_4BH_4NHNH_2$ structure

Final Refinement Parameters	
Lattice Parameters	
a/ Å	6.9483(1)
b/ Å	6.9483(1)
c/ Å	15.1981(7)
α/ °	90
β/ °	90
γ/ °	120
Cell Volume/ $Å^3$	635.47(4)
Cell Formula Units (Z)	6
Space Group	$P3_221$
Fit Indices	
χ^2	5.05
R_{Bragg}	6.49
R_{wp}	9.32
R_{exp}	4.15
R_p	6.31

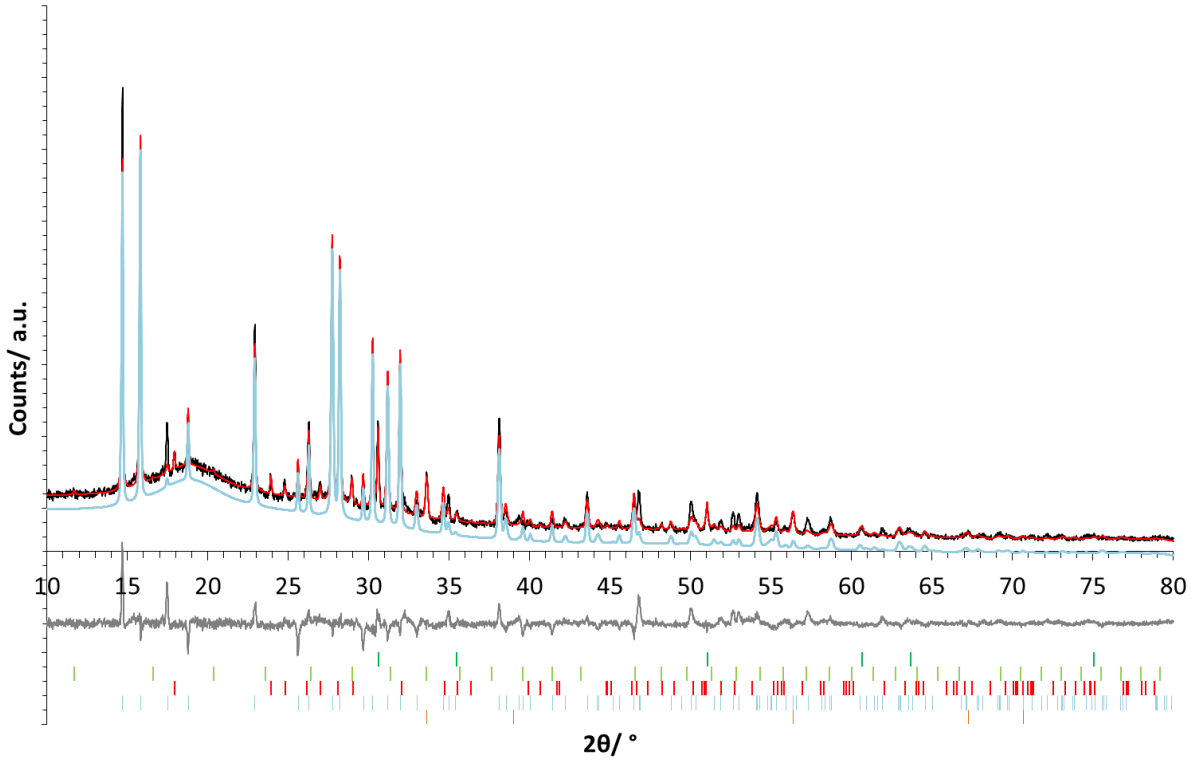

Figure 5.25 – Fit of proposed $P3_221$ $Li_4BH_4NHNH_2$ structure to XRD data, where black = observed data, red = calculated data and grey = difference, highlighting the $Li_4BH_4NHNH_2$ fit in blue. Light blue tick marks = hexagonal lithium amide-borohydride-imide, green tick marks = Li_2NH, red tick marks = $LiBH_4$ (*Pnma*), light green tick marks = $Li_4BH_4(NH_2)_3$ and orange tick marks = Li_2O

The final structure presented for the hexagonal lithium amide-borohydride-imide has the formula $Li_4BH_4NHNH_2$, space group $P3_221$ and lattice parameters, a = 6.9483(1) Å and c = 15.1981(7) Å. The structure presented here was determined solely from laboratory diffraction data and therefore due to the quality of the data there were some limitations to what could be achieved, particularly with regards to lithium and hydrogen positions. Every attempt has been made to determine sensible hydrogen positions; however, the weak scattering combined with the use of lower quality data has meant that positions could not be unambiguously determined. The positions presented in the structure here resulted in the

best fit to the data, although, with the collection of high resolution data, improvements could be made. In addition a single thermal parameter had to be refined for all atoms in the model as the quality of the data meant that applying individual values gave chemically unrealistic results. Again, these values could be improved with high resolution data, as there is too much uncertainty with lab diffraction data. In particular, the inclusion of neutron diffraction data on an isotopically enriched sample would be hugely beneficial in determining the hydrogen (deuterium) and lithium positions.

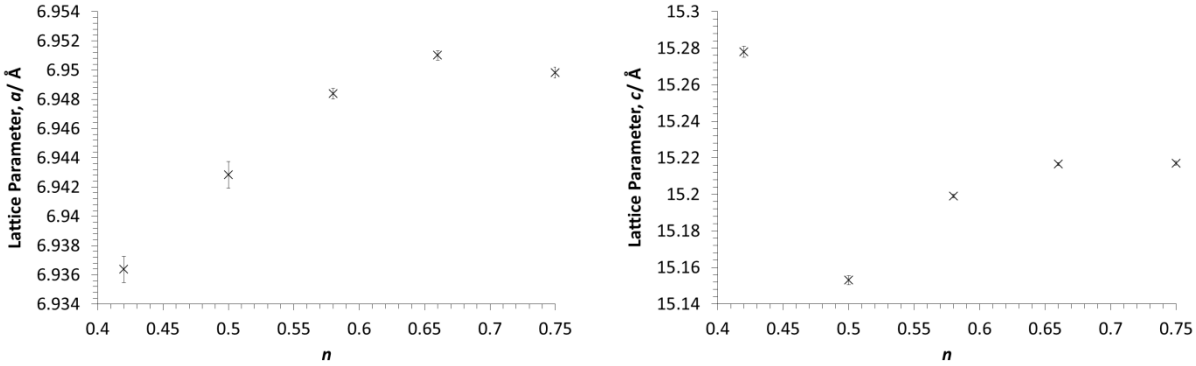

Figure 5.26 – Lattice parameters of $Li_4BH_4NHNH_2$ unit cell across a range of compositions where *n* corresponds to the equation $nLi_{1.5}(NH_2)_{0.5}(NH)_{0.5} + (1 - n)LiBH_4$

Another consideration with regards to this new lithium amide-borohydride-imide phase is the possibility of some compositional variation. The prosed $Li_4BH_4NHNH_2$ structure was refined against the data from the $nLi_{1.5}(NH_2)_{0.5}(NH)_{0.5} + (1 - n)LiBH_4$ reaction series (§4.6.1) in order to determine lattice parameters. The data presented in Figure 5.26 indicate that there may in fact be some variation as there was an overall increase in lattice parameters with increasing lithium amide-imide content. It is however, important to note that the low weight percentages and therefore broader peaks, particularly at the more $LiBH_4$-rich end of the scale, are likely to have resulted in a significant error in the determined

values. The data presented here act more as an indication that compositional variation may have occurred and that through further studies and the collection of high resolution data, it may be possible to observe a solid solution range.

5.6 Conclusions

Through refinements of powder XRD data the structures of three new materials have been determined: $Li_5(BH_4)_3NH$, an orthorhombic lithium borohydride-imide; Li_3BH_4NH, a cubic lithium borohydride-imide; and $Li_4BH_4NHNH_2$, a hexagonal lithium amide-borohydride-imide. The orthorhombic structure presented in this thesis has also been shown to agree with a structure of the same material presented by Wolczyk *et al*.[148] further supporting it as the true structure. However, additional work may help to confirm the hydrogen positions, in particular the rotation of the BH_4 tetrahedra, which could be achieved through analysis of neutron diffraction data. The cubic structure has been determined based on very limited information, due to the existence of very few unique reflections in the diffraction data. However, the structure is likely to be a highly disordered cubic phase and therefore the assumption of a Li_3BH_4NH composition is a sensible model. Finally a hexagonal model of the $Li_4BH_4NHNH_2$ phase has been proposed through laboratory powder XRD data alone. Further work and analysis of high resolution synchrotron data will enable more detail to be determined in the final structure and provide a greater level of certainty to the model.

Chapter 6 – *In-Situ* Studies of the Lithium Borohydride-Imide Phase Space

6.1 Introduction

Synthetic studies into the reaction of lithium imide and lithium borohydride illustrated that there was a large amount of complexity within the Li_2NH-$LiBH_4$ phase space, described in detail in Chapter 4. They have shown that a lower synthesis temperature of 125 °C favours the new orthorhombic phase, $Li_5(BH_4)_3NH$, and that a higher synthesis temperature of 200 °C favours the cubic phase with the nominal composition Li_3BH_4NH. However, alongside these new lithium borohydride-imides there were other phases present, including starting materials and some resulting from decomposition reactions.

In order to gain a greater understanding of the processes occurring and the behaviour of the different materials within the reaction mixture, a series of *in-situ* experiments were performed. Reactions were followed during both heating and cooling and data were collected using high resolution powder XRD and X-ray PDF.

6.2 Experimental

Various ratios of lithium borohydride (Sigma Aldrich, 90% purity) and lithium imide (synthesised using the optimum reaction conditions determined previously, §3.3.3) were ground together and sealed in glass capillaries, in an argon-filled glovebox. High resolution powder XRD data were collected on the I11 beamline at Diamond Light Source, using a wavelength of 0.826042 Å. X-ray PDF data were collected on the X-ray Pair Distribution Function beamline, I15-1 at Diamond Light Source, using a wavelength of 0.161669 Å. For

both beamlines, the temperature of the samples was controlled using a hot gas blower (Cyberstar S. A., France). See §2.3, §2.4 and §2.5 for more detailed information.

6.3 *In-Situ* Borohydride-imide High Resolution XRD Study

In order to gain a better understanding of the different reactions occurring, the formation of products and behaviour of the different phases within the lithium borohydride-imide phase space, an *in-situ* high resolution XRD study was carried out. Lithium imide and lithium borohydride were ground together in various ratios: 3:9, 4:8, 5:7, 6:6, 7:5, 8:4 and 9:3 (n = 0.25, 0.33, 0.42, 0.5, 0.58, 0.66 and 0.75, respectively, for the composition $n\mathrm{Li_2NH}$ + $(1 - n)\mathrm{LiBH_4}$), loaded into capillaries and then sealed. The loaded capillaries were then heated *in-situ* while XRD data were collected continuously, with a new data set being recorded approximately every 30 seconds.

A fixed heating/cooling ramp rate of 5 °C $\mathrm{min^{-1}}$ was used throughout the experiment. The samples were first heated up to 125 °C where they were held for 10 minutes. The temperature was then ramped up to 200 °C and held for an additional 30 minutes. Finally the sample was cooled back down to 40 °C. Due to amount of experimental time allocated, and the cooling rate of the hot air blower, only the 3:9 (n = 0.25) sample was heated from room temperature (23 °C); the other samples were all heated from an initial temperature of 40 °C.

A waterfall plot of the diffraction data collected on the 3:9 (n = 0.25) sample is shown in Figure 6.1. The data show that the starting materials were all present as expected and there were no unknown peaks at the start of the heating cycle, confirming there were no issues with the seal of the capillary. The lithium borohydride structural transition from the

low temperature *Pnma* structure to the high temperature $P6_3mc$ structure was also seen as expected at 108 °C.[86]

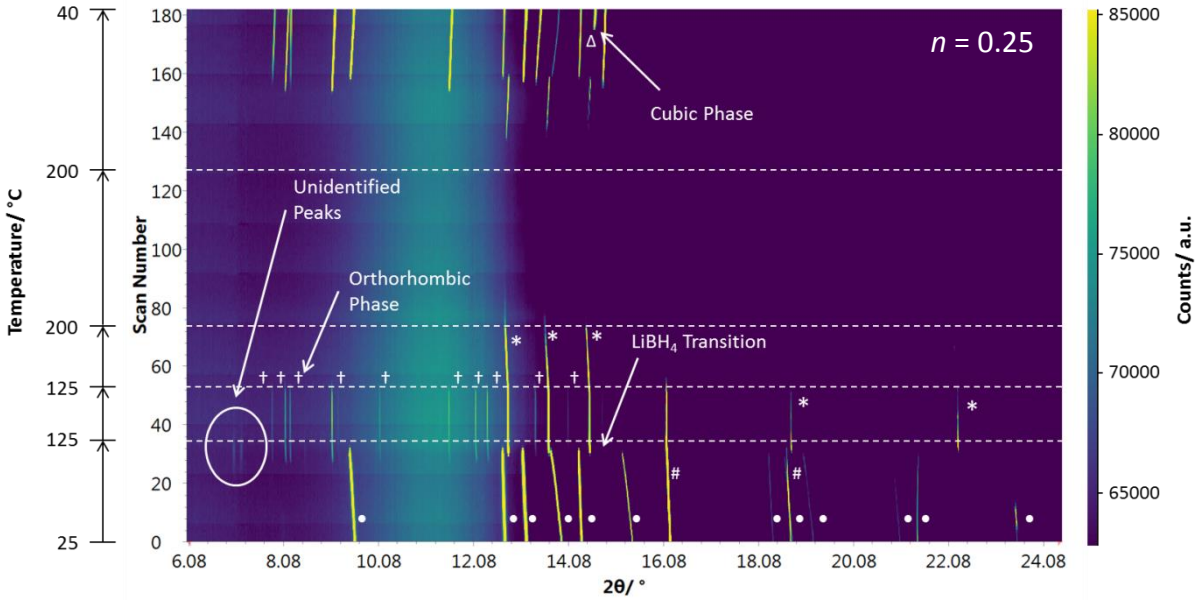

Figure 6.1 – Waterfall plot showing *in-situ* XRD data collected during heating and subsequent cooling of nLi$_2$NH + (1 – n)LiBH$_4$ sample, where n = 0.25. # = Li$_2$NH, ● = LiBH$_4$ (*Pnma*), * = LiBH$_4$ ($P6_3mc$), † = orthorhombic phase and Δ = cubic phase

The formation of the orthorhombic phase was observed upon heating, first appearing at *ca* 100 °C and continuing to grow in intensity as the temperature was increased up to, and subsequently held at 125 °C. As the temperature was ramped up once again the orthorhombic phase quickly disappeared. These observations support the suggested synthesis temperature of 125 °C as close to the optimum temperature, determined in earlier work (§4.4.2).

At a similar temperature to the orthorhombic phase formation there were also two additional peaks which appeared at low 2θ, circled in Figure 6.1. However, they quickly disappeared as the temperature was increased up to and held at 125 °C. These peaks

corresponding to *d*-spacings of 6.59 and 6.74 Å, the same *d*-spacings as the unidentified pair of peaks seen in the reannealing experiment carried out at 100 °C (§4.4.1). Careful searching through the diffraction data failed to identify further peaks due to this phase, and it was not possible to identify them as being related to other known phases. Due to the scarcity of information, these peaks have not been attributed to a particular phase, yet their appearance in this *in-situ* data suggests that the phase they belong to is favoured at lower temperatures, *ca* 100 °C. Their disappearance as the temperature was increased also suggests that the phase they belong to quickly transforms when the temperature is increased much above 100 °C.

As the temperature continued to increase, the lithium borohydride and lithium imide reflections were also no longer visible in the data. The absence of any peaks in the diffraction patterns suggested the formation of either a melt or an amorphous phase at *ca* 130 °C. This supported the theory suggested in earlier synthetic work that the samples were melting (§4.5) – a theory based on the inconsistency of the product mixture compositions and their shiny appearance which was later confirmed by a melting point experiment (§4.5). Although the formation of a low-temperature melt in the lithium borohydride-imide system was a new finding, the closely related lithium amide-borohydride system has been reported to form a melt at low temperatures, with a melting temperature at the eutectic point of only 90 °C.[97] Upon reflection, knowing the structural and chemical similarities between these two systems, the formation of a low-temperature melt was not entirely unexpected.

No additional peaks appeared after the formation of the melt and thus, after being held at 200 °C for 30 minutes the sample was cooled back down. Peaks began to appear at

ca 130 °C, the first of which belonged to the high temperature lithium borohydride phase that subsequently transitioned into its low temperature polymorph below 108 °C. Multiple unidentified peaks then began to appear in the pattern as temperature continued to fall. Identification of these phases using Rietveld refinement determined that the relative peak intensities from known phases were inconsistent and unreliable. This was attributed to either large amounts of preferred orientation caused by preferred crystal growth along the capillary axis, or the presence of relatively few large crystallites in the illuminated volume of the diffraction experiment, which when collected with the one-dimensional detector of I11 resulted in poor powder averaging. Attempts to refine the amount of preferred orientation using models with a few refinable parameters failed. As the relative intensities could not be relied upon, the observed reflections may equally have been due to the orthorhombic phase or alternatively the hexagonal lithium amide-borohydride-imide phase; the unreliable relative ratios meant that this could not be unambiguously confirmed. Finally, at *ca* 66 °C another phase began to appear, with a slightly broader peak shape, at 2θ = 14.6 °. This is where the main cubic peak lies and therefore was thought to be due to the formation of the cubic phase (nominally Li_3BH_4NH).

Equivalent variable temperature diffraction experiments were repeated for samples of all the other lithium imide to lithium borohydride ratios: 4:8, 5:7, 6:6, 7:5, 8:4 and 9:3 (n = 0.33, 0.42, 0.5, 0.58, 0.66 and 0.75, respectively); although for the 9:3 sample data were only recorded up to the end of heating at 200 °C due to loss of beam during cooling. Each sample followed a similar trend, although the relative peak intensities between the various phases differed. An additional point to note is the presence of Li_2NH in the more Li_2NH-rich samples. Looking at only the 3:9 (n = 0.25) sample it appeared that the Li_2NH was completely

contained within the molten phase. However, it was clear from the other imide-rich samples that Li_2NH remained as a crystalline solid. The lithium imide peaks were always present in the diffraction data (2θ = 16.2 °, 18.7 °), even during the prolonged heating at 200 °C. The data for each of these samples are shown in Figure 6.2 and Figure 6.3.

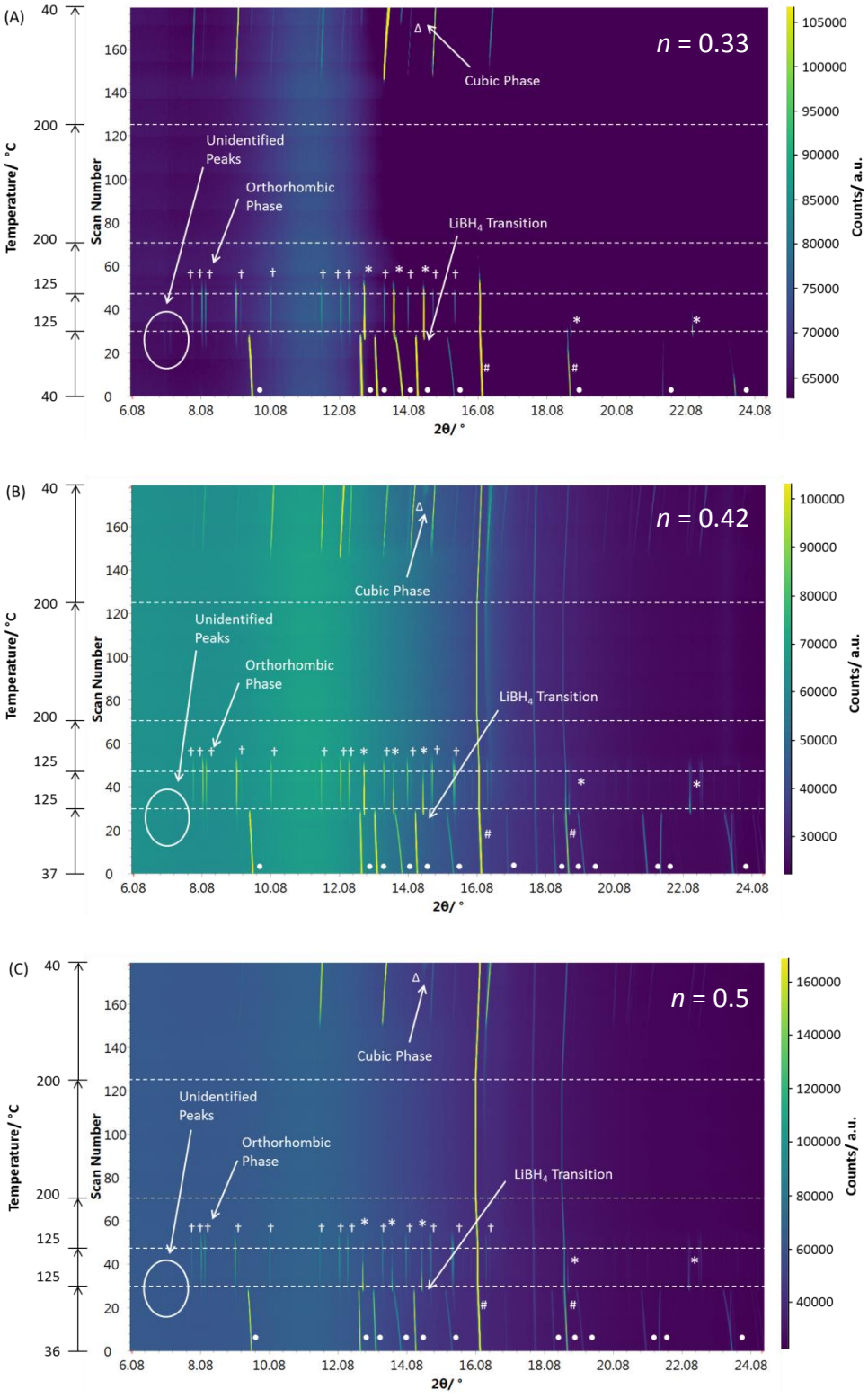

Figure 6.2 – Waterfall plots showing *in-situ* XRD data collected during heating and subsequent cooling of nLi$_2$NH + (1 – n)LiBH$_4$ sample. (A) n = 0.33 (B) n = 0.42 and (C) n = 0.5. # = Li$_2$NH, ● = LiBH$_4$ (*Pnma*), * = LiBH$_4$ (*P*6$_3$*mc*), † = orthorhombic phase and Δ = cubic phase

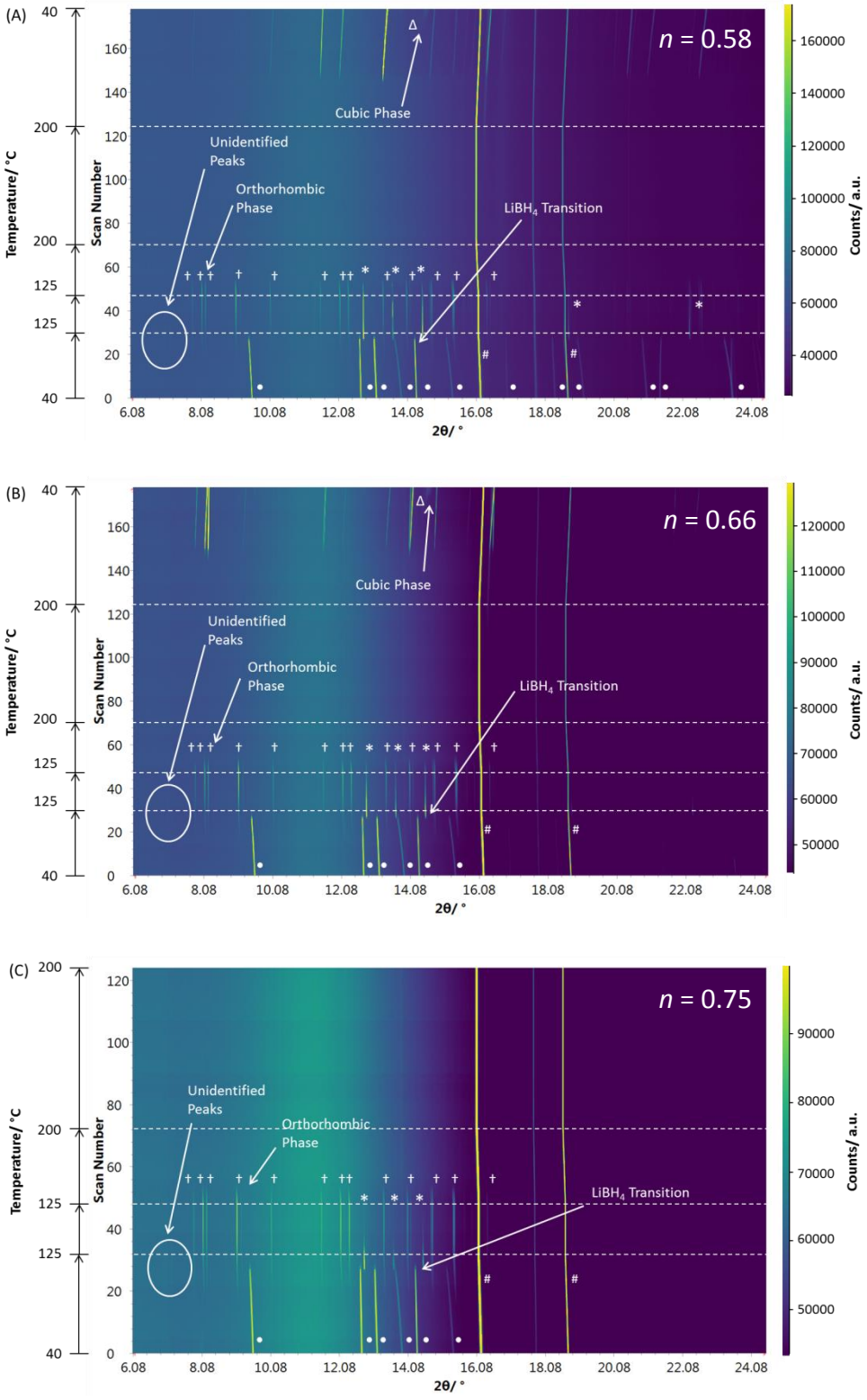

Figure 6.3 – Waterfall plots showing *in-situ* XRD data collected during heating and subsequent cooling of nLi$_2$NH + (1 – n)LiBH$_4$ sample. (A) n = 0.58 (B) n = 0.66 and (C) n = 0.75. # = Li$_2$NH, ● = LiBH$_4$ (*Pnma*), * = LiBH$_4$ (*P*6$_3$*mc*), † = orthorhombic phase and Δ = cubic phase

6.3.1 QPA of the *In-Situ* Heating data

With the aim of following the different reactions and phase transitions occurring during the *in-situ* XRD experiment in a more quantitative way, Rietveld refinements with quantitative phase analysis (QPA) were carried out on the data collected during heating.

The formation of a melt meant that QPA had to be carried out using an internal standard to ensure that the molten phase was still accounted for. Lithium oxide was present in all the samples as a small impurity phase, and as the capillaries were sealed the amount present in each system was stable. Consequently Li_2O was used as the internal standard.

Initial Rietveld refinements were carried out on the first room temperature scan of each sample. As these samples contained only starting material and Li_2O, accurate weight percentages of all three phases, including Li_2O, could be determined. Once the weight percentage of Li_2O was determined, it was then fixed at the value refined from the first scan, and that value was used for all subsequent scans. This meant that as the samples were heated, and new unknown phases began to form, the weight percentages were determined relative to the stable Li_2O. The remaining weight percentage unaccounted for by the known crystalline phases was then attributed to the 'amorphous' phase.

It is important to note that the orthorhombic structure used for this analysis (§5.3.4.1) was not the final structure. However, QPA was used in this instance to study the trends in the data and was not concerned with absolute values. The errors associated with the differences in the orthorhombic model will not invalidate the identified trends and any associated error from its use would have been encompassed by the expected error from performing these large scale batch refinements.

The results of these refinements with QPA for each of the imide to borohydride ratios are displayed in Figure 6.4 (3:9, n = 0.25), Figure 6.5 (4:8, n = 0.33), Figure 6.6 (5:7, n = 0.42), Figure 6.7 (6:6, n = 0.5), Figure 6.8 (7:5, n = 0.58), Figure 6.9 (8:4, n = 0.66) and Figure 6.10 for (9:3, n = 0.75). Although some of the weight percentages for the amorphous phase drop below 0%, this is within the error of these refinements (§2.4). The peak shape of both the high temperature $P6_3mc$ $LiBH_4$ phase and the orthorhombic phase were also constrained to prevent the peaks from fitting to the background as the sample became molten.

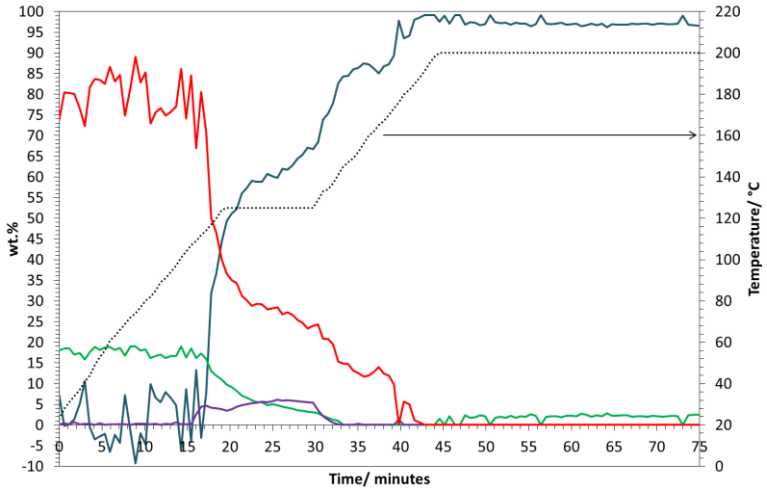

Figure 6.4 – Changing weight percentages of the different phases during heating of $n$$Li_2NH$ + (1 – n)$LiBH_4$, where n = 0.25, determined from Rietveld refinement of *in-situ* high resolution powder XRD data. Weight percentage values are shown as solid lines where blue = amorphous, green = Li_2NH, red = $LiBH_4$, purple = orthorhombic phase, Li_2O is not shown. The temperature is plotted as a dashed black line and corresponds to the secondary *y*-axis

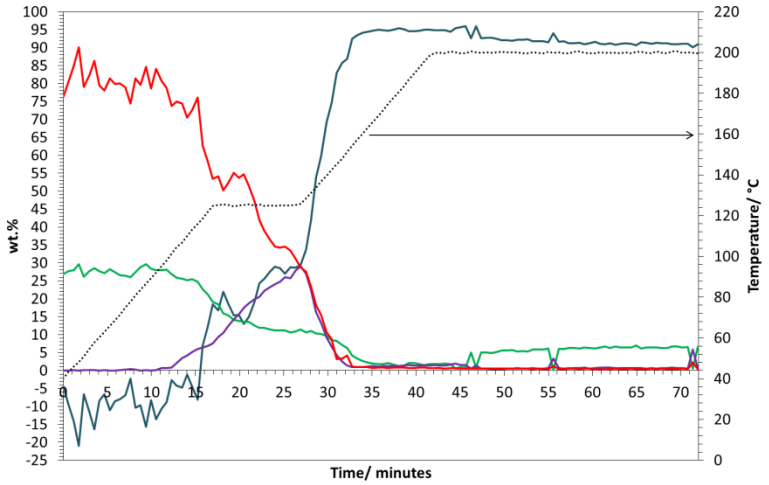

Figure 6.5 – Changing weight percentages of the different phases during heating of $n$$Li_2NH$ + (1 – n)$LiBH_4$, where n = 0.33, determined from Rietveld refinement of *in-situ* high resolution powder XRD data. Weight percentage values are shown as solid lines where blue = amorphous, green = Li_2NH, red = $LiBH_4$, purple = orthorhombic phase, Li_2O is not shown. The temperature is plotted as a dashed black line and corresponds to the secondary *y*-axis

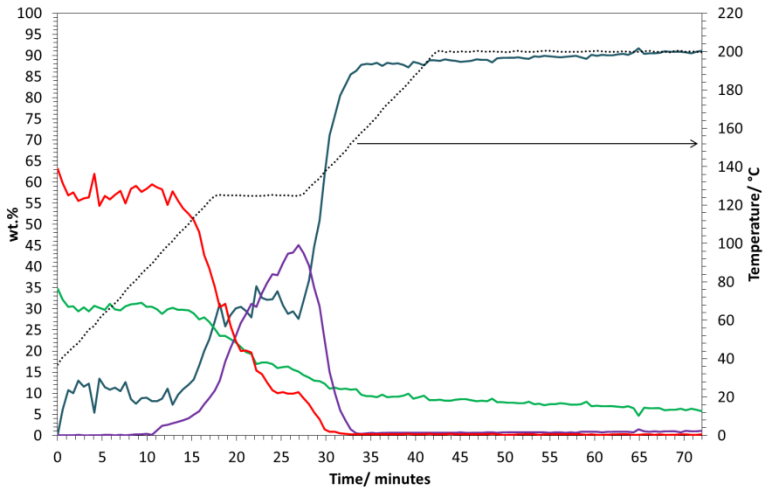

Figure 6.6 – Changing weight percentages of the different phases during heating of $n$$Li_2NH$ + (1 – n)$LiBH_4$, where n = 0.42, determined from Rietveld refinement of *in-situ* high resolution powder XRD data. Weight percentage values are shown as solid lines where blue = amorphous, green = Li_2NH, red = $LiBH_4$, purple = orthorhombic phase, Li_2O is not shown. The temperature is plotted as a dashed black line and corresponds to the secondary *y*-axis

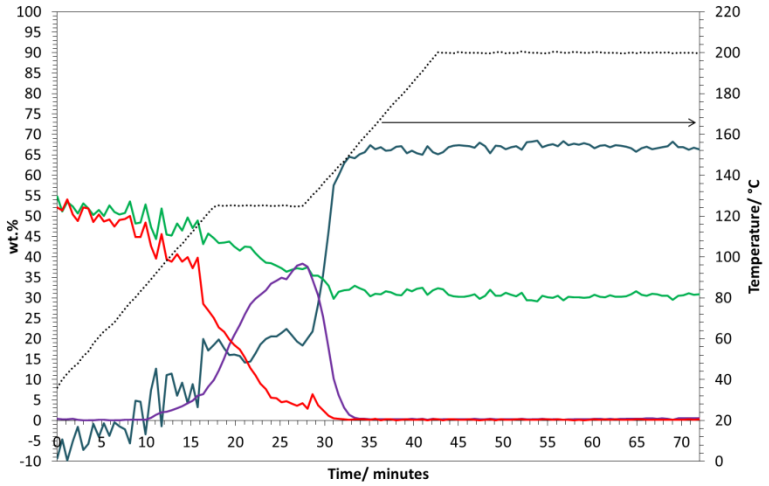

Figure 6.7 – Changing weight percentages of the different phases during heating of $n$$Li_2NH$ + (1 – n)$LiBH_4$, where n = 0.5, determined from Rietveld refinement of *in-situ* high resolution powder XRD data. Weight percentage values are shown as solid lines where blue = amorphous, green = Li_2NH, red = $LiBH_4$, purple = orthorhombic phase, Li_2O is not shown. The temperature is plotted as a dashed black line and corresponds to the secondary *y*-axis

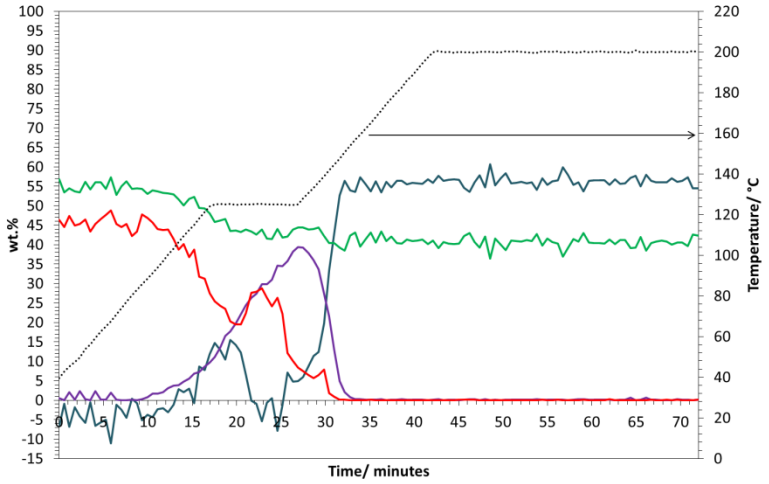

Figure 6.8 – Changing weight percentages of the different phases during heating of $n$$Li_2NH$ + (1 – n)$LiBH_4$, where n = 0.58, determined from Rietveld refinement of *in-situ* high resolution powder XRD data. Weight percentage values are shown as solid lines where blue = amorphous, green = Li_2NH, red = $LiBH_4$, purple = orthorhombic phase, Li_2O is not shown. The temperature is plotted as a dashed black line and corresponds to the secondary *y*-axis

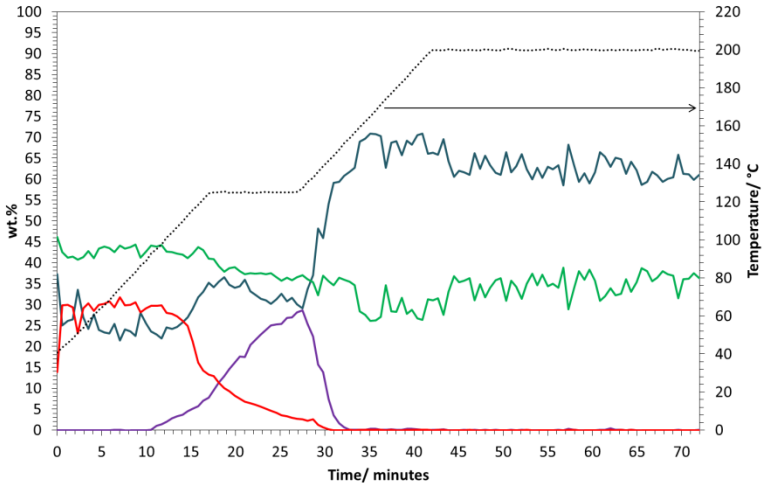

Figure 6.9 – Changing weight percentages of the different phases during heating of $n$$Li_2NH$ + (1 – n)$LiBH_4$, where n = 0.66, determined from Rietveld refinement of *in-situ* high resolution powder XRD data. Weight percentage values are shown as solid lines where blue = amorphous, green = Li_2NH, red = $LiBH_4$, purple = orthorhombic phase, Li_2O is not shown. The temperature is plotted as a dashed black line and corresponds to the secondary *y*-axis

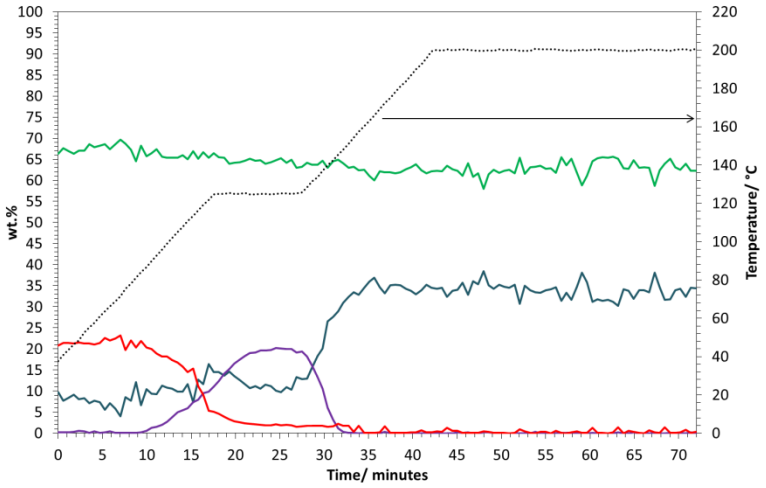

Figure 6.10 – Changing weight percentages of the different phases during heating of $n$$Li_2NH$ + (1 – n)$LiBH_4$, where n = 0.75, determined from Rietveld refinement of *in-situ* high resolution powder XRD data. Weight percentage values are shown as solid lines where blue = amorphous, green = Li_2NH, red = $LiBH_4$, purple = orthorhombic phase, Li_2O is not shown. The temperature is plotted as a dashed black line and corresponds to the secondary *y*-axis

The data collected from all of these samples provides a detailed picture of the formation of the different phases during heating. Figure 6.11 gives the weight percentage of the orthorhombic phase determined at the end of the prolonged heating at 125 °C. In each case this was the maximum weight percentage of the orthorhombic phase at any stage in the reaction, supporting 125 °C as the most suitable temperature for synthesis of the orthorhombic phase.

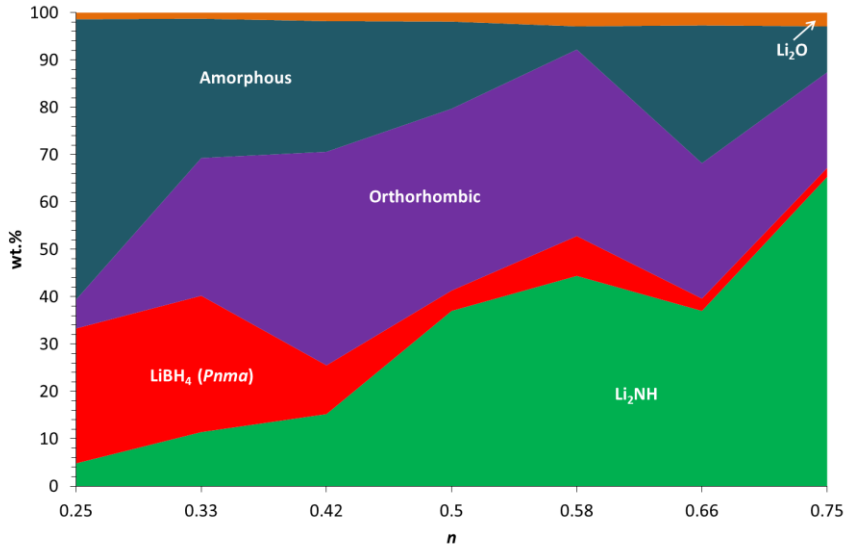

Figure 6.11 – Weight percentages of the different phases at the end of heating at 125 °C determined from Rietveld refinement of high resolution powder XRD data

The refinement data showed that by the end of the prolonged heating at 125 °C, the most orthorhombic phase was formed using a 5:7 (n = 0.42) ratio. The orthorhombic phase was present alongside a close to 1:1 ratio of Li_2NH to $LiBH_4$. However, as the initial reagents were more $LiBH_4$-rich, it was apparent that significantly more $LiBH_4$ had reacted. The amount of orthorhombic phase remained fairly high at more imide-rich compositions and was likely the same within error for both the 6:6 (n = 0.5) and 7:5 (n = 0.58) ratios, although this was alongside a larger excess of Li_2NH.

Rather than looking solely at the final weight percentages, tracking how they changed over time helped to provide a picture of the relative rates of the different processes which were occurring. Figure 6.12 shows the changes in the weight percentages of the different phases while the temperature was held at 125 °C as a function of composition.

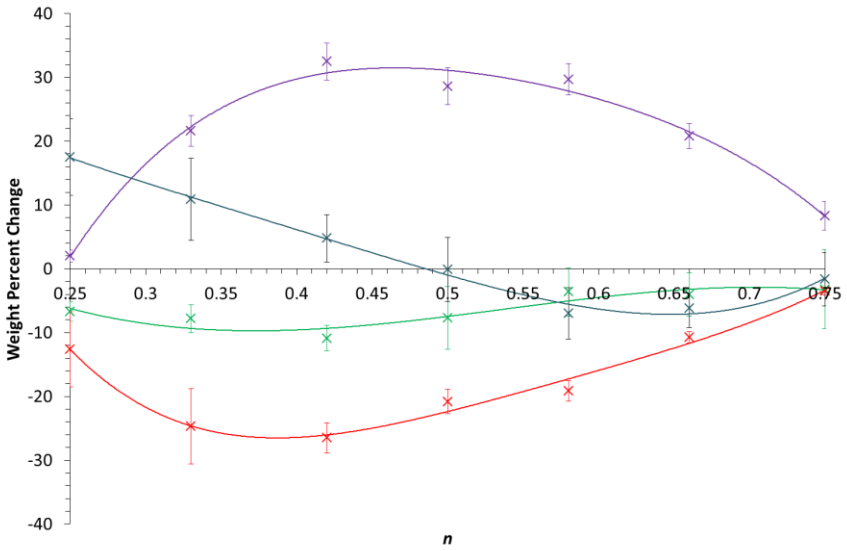

Figure 6.12 – Weight percentage changes of the different phases during the 10 minute heat treatment at 125 °C. A positive change means that the amount of that phase increased after the 10 minute dwell. Data points are shown as crosses, where blue = amorphous, green = Li_2NH, red = $LiBH_4$ and purple = orthorhombic phase. Solid lines are added to guide the eye

Although completely accurate values cannot be expected from this QPA, it is interesting to note the trend in both the Li_2NH and $LiBH_4$ percentage changes. Across the entire composition range the amount of $LiBH_4$ reacting was much greater than Li_2NH; the change in weight percentages roughly estimated to be around three times greater for all except the two most extreme compositions (n = 0.25 and n = 0.75) in which there was only a small amount of the orthorhombic phase present. Considering the 5:7 (n = 0.42) sample as an example, the changes in weight percent can roughly be equated to molar ratios of 1:3 for

Li_2NH:$LiBH_4$, with only a small amount of change in the amorphous phase. This potentially indicates that the determined $1Li_2NH$:$3LiBH_4$ ratio of the orthorhombic structure is correct. Unfortunately, the simultaneous increase in the amount of amorphous phase and its unknown composition mean that the decrease in both starting materials cannot be solely attributed to the formation of the orthorhombic phase. As a result, although the ratio extracted from this analysis may help to support the proposed composition, it cannot be used to confirm the composition of the orthorhombic phase.

As well as the changing weight percentages, the temperatures at which different processes occurred are also important. The temperature at which the orthorhombic phase was first identified varied slightly between the different samples from 107 °C for the most $LiBH_4$-rich ratio (3:9, n = 0.25) down to 86 °C for the most Li_2NH-rich ratio (9:3, n = 0.75) averaging out at *ca* 94 °C. Interestingly, other than a small fluctuation for the 8:4 (n = 0.66) sample, the formation of the orthorhombic phase began at an increasingly lower temperature with increasing Li_2NH content. However, it is important to note that in those samples containing significantly less orthorhombic phase (particularly the 3:9, n = 0.25 sample) the point at which it first began to form was more difficult to detect. Despite the range of temperatures determined between the different samples, it is clear that the orthorhombic phase began to form at fairly low temperatures. Other than the two unidentified peaks (d-spacings of 6.59 Å and 6.74 Å, respectively), which appeared before the orthorhombic phase and then disappeared during heating at 125 °C, the orthorhombic phase was the first product phase to form.

As the samples were heated up towards a target temperature of 200 °C peaks belonging to the crystalline phases began to disappear. Although both the orthorhombic phase and $LiBH_4$ appeared to melt, this did not occur concurrently. For samples with reactant ratios 5:7, 6:6, 7:5 and 8:4 (n = 0.42, 0.5, 0.58 and 0.66, respectively) the lithium borohydride melted first at *ca* 143 °C followed by the orthorhombic phase at *ca* 154 °C. The sample with a reactant ratio of 4:8 (n = 0.33) was the only sample in which these two processes occurred at the same time; and in the most Li_2NH-rich sample (9:3, n = 0.75) the orthorhombic phase melted first at 148 °C followed by lithium borohydride at 154 °C.

The 3:9 (n = 0.25) sample had a large temperature difference between the two occurrences, with the orthorhombic phase melting at *ca* 139 °C and the $LiBH_4$ not entirely melting until *ca* 190 °C. This significant deviation from the other samples could have been due to the large amount of $LiBH_4$ present. The amount of $LiBH_4$ was continuously decreasing in intensity; therefore it is likely that the composition of the melt contained the maximum amount of $LiBH_4$ at a given temperature and only by increasing the temperature could more $LiBH_4$ be accommodated, until the liquidus temperature was reached at which point the sample was completely molten. Lithium borohydride itself has a melting point of 275 °C[159] and therefore its melting must have been due to its interaction with other materials contained within the melt.

6.3.2 *In-Situ* Cooling Data

Quantitative phase analysis provided a great deal of insight into the processes occurring upon heating. Unfortunately, the same level of detail could not be achieved with analysis of the data collected on cooling. Analysis of the final product mixture for each

sample showed large discrepancies in the relative ratios of the peaks, which was determined to be due to preferred orientation upon recrystallisation.

Only the cubic phase and Li_2NH were fitted to the cooling data. Li_2NH was easily fitted as it did not melt and therefore was not affected by preferred orientation, whilst the cubic phase was fitted based predominantly on the main (111) cubic peak (14.6 °). As Li_2O was present as an internal standard all the other phases, crystalline or not, were accounted for in the 'amorphous' phase. Figure 6.13 shows the results of QPA for cooling of the 5:7 (*n* = 0.42) sample.

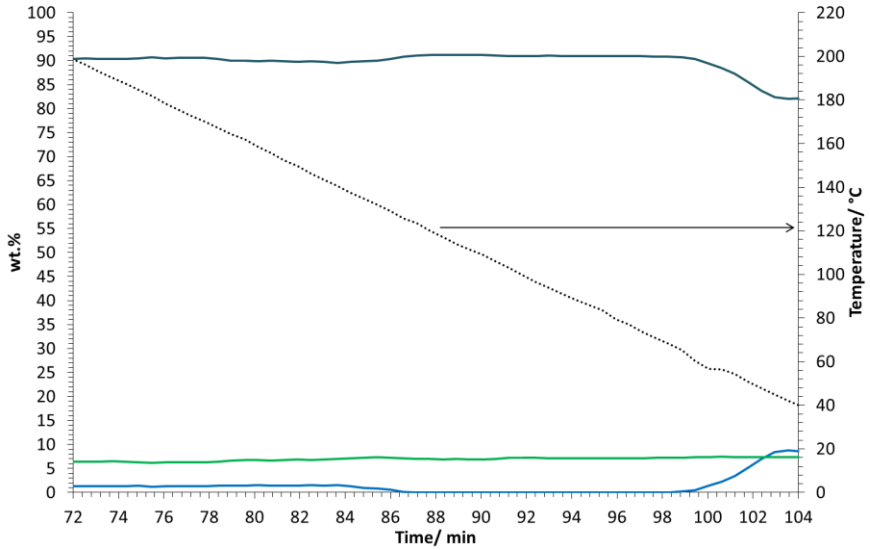

Figure 6.13 – Changing weight percentages of the different phases during cooling, at a rate of 5 °C min^{-1}, of $nLi_2NH + (1 - n)LiBH_4$, where *n* = 0.42, determined from Rietveld refinement of *in-situ* high resolution powder XRD data. Weight percentage values are shown as solid lines where dark blue = amorphous, green = Li_2NH and royal blue = cubic phase, Li_2O is not shown. The temperature is plotted as a dashed black line and corresponds to the secondary *y*-axis

Due to the limitations with regards to preferred orientation, quantitative data could not be obtained, however, it was still useful in determining the point at which the cubic

phase formed upon cooling. As shown in Figure 6.13 this was *ca* 65 °C for the 5:7 (*n* = 0.42) sample. This process was repeated for each of the samples and the cubic phase formation temperature was found to be between 65 and 70 °C for each of them. The evidence of the cubic phase forming very late in the cooling process provided by this investigation helped to explain why the cooling rates played such an important role in its formation (detailed in §4.5.2), and thus emphasised the importance of controlling the cooling rates in any future work on this phase. It also indicated that the cubic phase may form more readily from a melt whereas the orthorhombic phase may be favoured through the solid reaction. This is in line with the synthesis temperatures of 125 °C and 200 °C used for the orthorhombic and cubic phases, respectively in Chapter 4.

6.4 *In-Situ* Borohydride-imide X-ray PDF Study

The *in-situ* high resolution powder XRD data showed the formation of the orthorhombic phase upon heating, formation of a melt at higher temperatures, and subsequent crystallisation of both starting materials alongside new lithium borohydride-imide phases on cooling. After analysing these findings, X-ray PDF data were collected in an attempt to increase understanding of the processes occurring, in particular during the melt, and the formation of the different phases. The weak scattering from these phases poses a particular problem for PDF data collection, where good statistics are required at high *Q* (see §2.5). Great care was taken during the data processing and initial benchmarking was performed with known phases.

Due to the complex nature of the system, data were first collected on the starting materials in order to observe the changes in the single phase systems with increasing

temperature. Samples of lithium imide and lithium borohydride were both loaded into capillaries and sealed. The samples were then heated *in-situ* and data were collected in 25 °C increments up to 200 °C and for the $LiBH_4$ sample then again at 250 °C and 300 °C. At each target temperature the sample was held for 5 minutes before completing a 10 minute data collection. Figure 6.14 shows the fit of an average Li_2NH structure to the room temperature PDF data, shown as $D(r)$. Upon heating the data showed there was thermal expansion of the Li_2NH structure, but there were no other notable changes to the PDF.

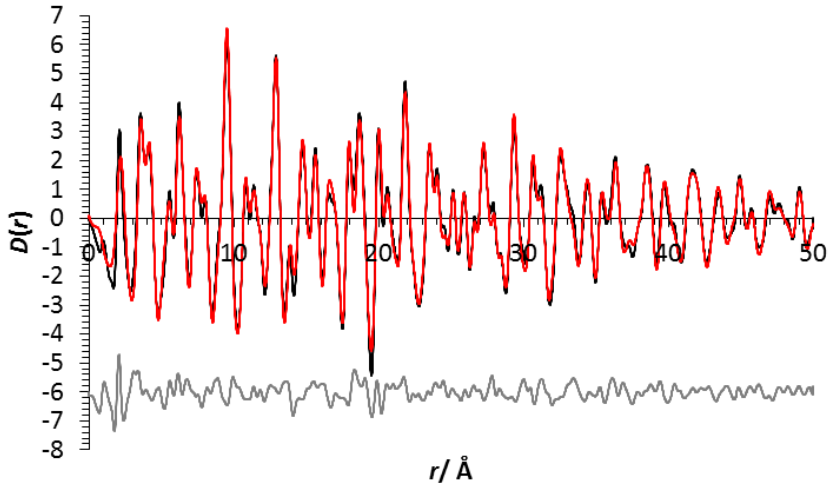

Figure 6.14 – Fits of refined Li_2NH structure against PDF data collected at 25 °C, where black = observed data, red = calculated data and grey = difference

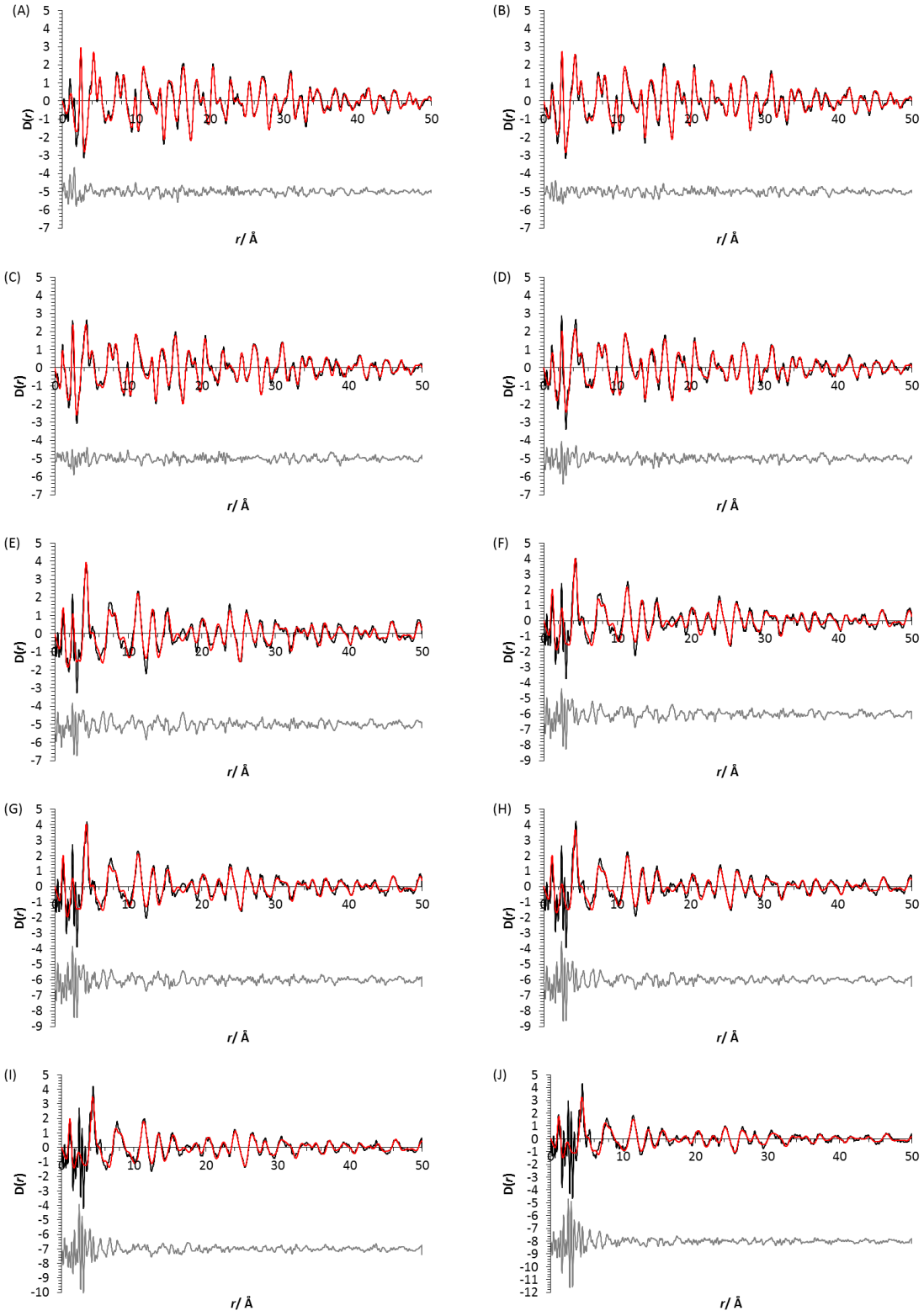

Figure 6.15 – Fits of refined $LiBH_4$ structure against i*n-situ* PDF data, where black = observed data, red = calculated data and grey = difference (A) 25 °C (B) 50 °C (C) 75 °C (D) 100 °C (E) 125 °C (F) 150 °C (G) 175 °C (H) 200 °C (I) 250 °C (J) 300 °C

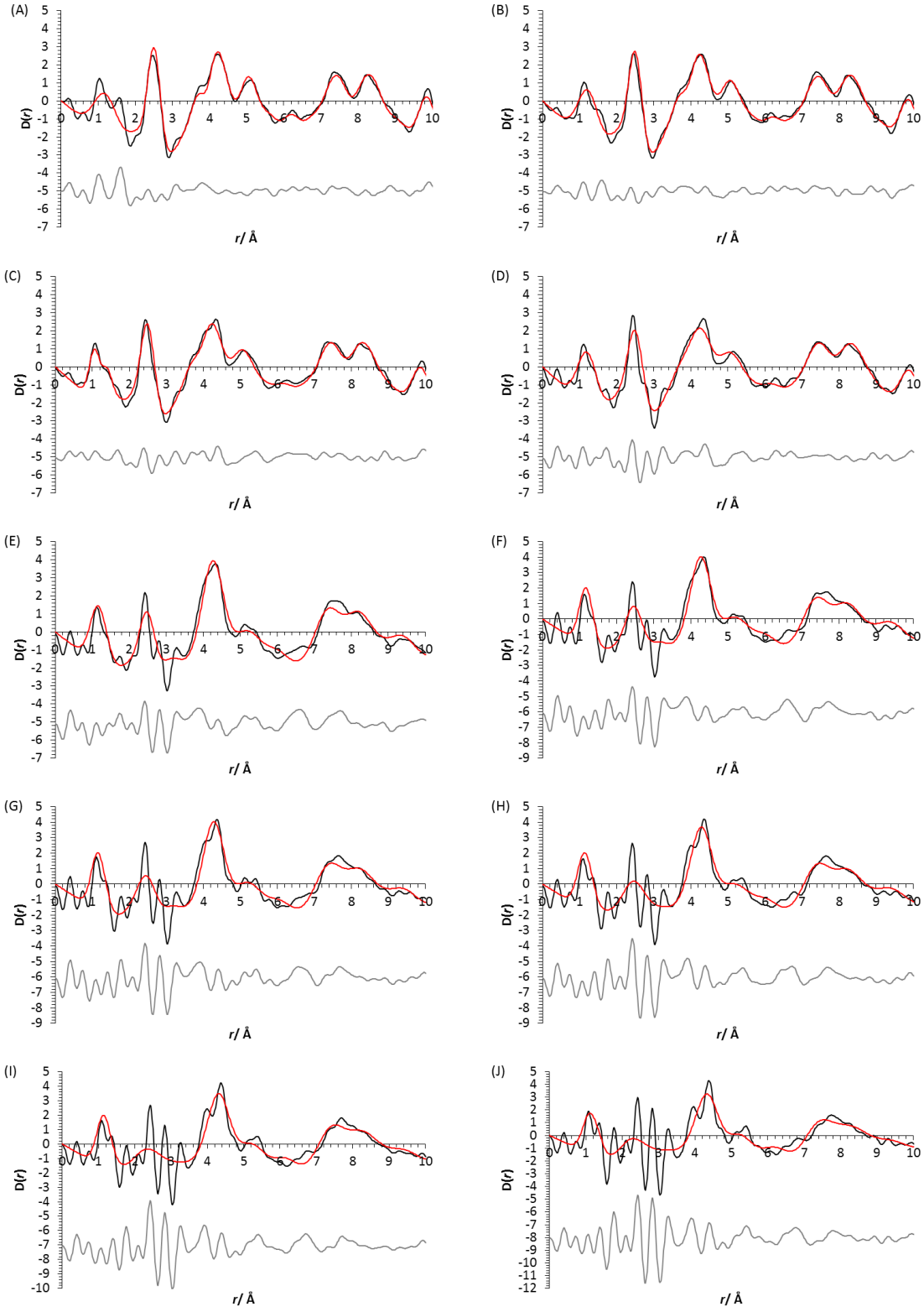

Figure 6.16 – Zoomed in plots showing low-*r* region of fits of refined $LiBH_4$ structure against i*n-situ* PDF data, where black = observed data, red = calculated data and grey = difference (A) 25 °C (B) 50 °C (C) 75 °C (D) 100 °C (E) 125 °C (F) 150 °C (G) 175 °C (H) 200 °C (I) 250 °C (J) 300 °C

Figure 6.15 shows the PDF data collected on $LiBH_4$, shown as $D(r)$. The loss of long range order as the sample was heated was the first thing which was apparent from the data. This is evident in the loss of intensity at higher r values and was to be expected as $LiBH_4$ approached the melting point at 275 °C and subsequently exceeded it. [159] There was also a notable change in the data between 100 and 125 °C which again was to be expected as $LiBH_4$ transitioned from the low temperature orthorhombic structure to the high temperature hexagonal structure at *ca* 108 °C.[87] It is important to note that despite the sample being heated to 300 °C, it was determined that due to the fairly large sample size it did not all reach the final target temperature. Although the data show a reduction in intensity, the presence of peaks at high r indicates that there was still some crystalline material present, confirmed by the Bragg data recorded simultaneously.

Attempts were made to model both $LiBH_4$ structures to the *in-situ* data. Lattice parameters and atomic positions were refined within the unit cell symmetry of the room temperature and high temperature structures of $LiBH_4$, depending on the temperature. An r-dependent peak-width function with three parameters was refined for each element type. The known room temperature structure of $LiBH_4$[86] gave a reasonable fit to the PDF data below 125 °C. However, after the transition to the high temperature phase in the 125 °C dataset, there were significant discrepancies in the low-r part of the data, as evidenced by the larger features in the difference line below 6 Å (Figure 6.16). As long range order was lost the number of peaks corresponding to short range order, up to *ca* 6 Å, increased significantly. Attempts to improve the fit to this part of the data using different local structure models failed to significantly improve the fit with a moderate number of refinable parameters. The position of each of the peaks gives a particular atomic distance and

therefore this suggested that there were strongly preferred local environments which were not encapsulated in the average structure.

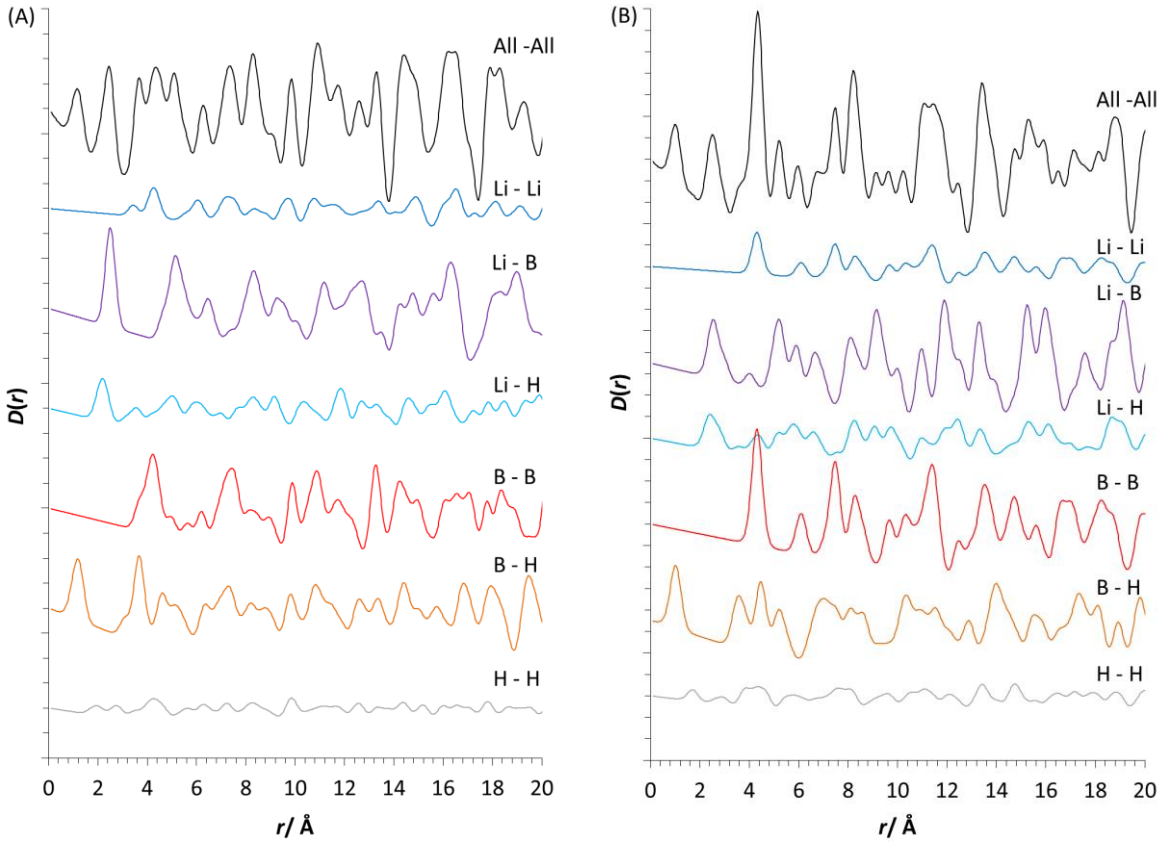

Figure 6.17 – Simulated partial PDF plots for lithium borohydride (A) low temperature polymorph *Pnma* and (B) high temperature polymorph *P*6$_3$*mc*. Total PDF is in black, Li–Li is in blue, Li–B is in purple, B–B is in red, Li–H is in light blue, B–H is in orange and H–H is in grey

Attempts were made to identify which bonds may be involved in these preferred local environments by looking at the individual pairs of potentials for the room and high temperature phases. Figure 6.17 shows simulated plots for both the orthorhombic and hexagonal $LiBH_4$ structures, simulated using PDFgui,[160] and the partial plots highlight the atomic distances giving rise to the individual peaks in the PDF. Focusing on the high temperature structure the simulated plots indicate that: the peak at *ca* 1 Å was due to B–H;

the peak at *ca* 2.5 Å was due to Li–B and Li–H predominantly; and the peak at *ca* 4.5 Å was due to a combination of B–B, B–H, Li–Li and H–H interactions. Consequently, although the splitting of the peak at *ca* 1 Å could likely be attributed to changing B–H distances giving rise to two different bond lengths, the changes in the other peaks could not be unambiguously allocated to one particular interaction. These significant changes to the PDF at low-*r* highlighted the complexity of the structure and the challenges associated with refining local distortions and disorder. It was made apparent that dynamics play an important role in these highly mobile complex hydrides as the melting point is approached. *Ab initio* molecular dynamics studies have previously shown how the local structure of $LiBH_4$ is highly dominated by the rotational diffusivity of the BH_4^- anion,[161] thus a simple small-box description fails to encapsulate the range of correlated motions occurring in the material.

Following from this, data were collected on mixtures of lithium imide and lithium borohydride. Lithium imide and lithium borohydride were ground together in various ratios: 2:10, 3:9, 4:8, 5:7, 6:6, 7:5, 8:4 and 9:3 [n = 0.16, 0.25, 0.33, 0.42, 0.5, 0.58, 0.66 and 0.75, respectively, for the compositions $n Li_2NH + (1 - n)LiBH_4$], loaded into capillaries and then sealed. The loaded capillaries were then heated *in-situ* up to 200 °C and data were recorded in 25 °C increments on heating and 50 °C increments on cooling. At each target temperature the sample was first allowed to equilibrate for 5 minutes before commencing a 10 minute data collection. Given the complexity of the multi-phase behaviour identified by high resolution powder XRD, and the apparently complex dynamics giving rise to multifaceted peak shapes as a function of *r*, in even an ostensibly simple starting material, $LiBH_4$, it was decided that structural modelling of the PDF for the mixed phases would not be feasible.

Instead, general trends in the data were drawn out to infer information about the eutectic behaviour in these materials.

Figure 6.18 shows the data collected on heating and Figure 6.19 the data collected on cooling for the 3:9 sample. Based on the Bragg data, which were collected simultaneously, the 3:9 (*n* = 0.25) sample was confirmed to be the composition at which the eutectic point is located, in agreement with the I11 data; both more $LiBH_4$-rich and more Li_2NH-rich samples still contained crystalline starting material after the formation of a melt.

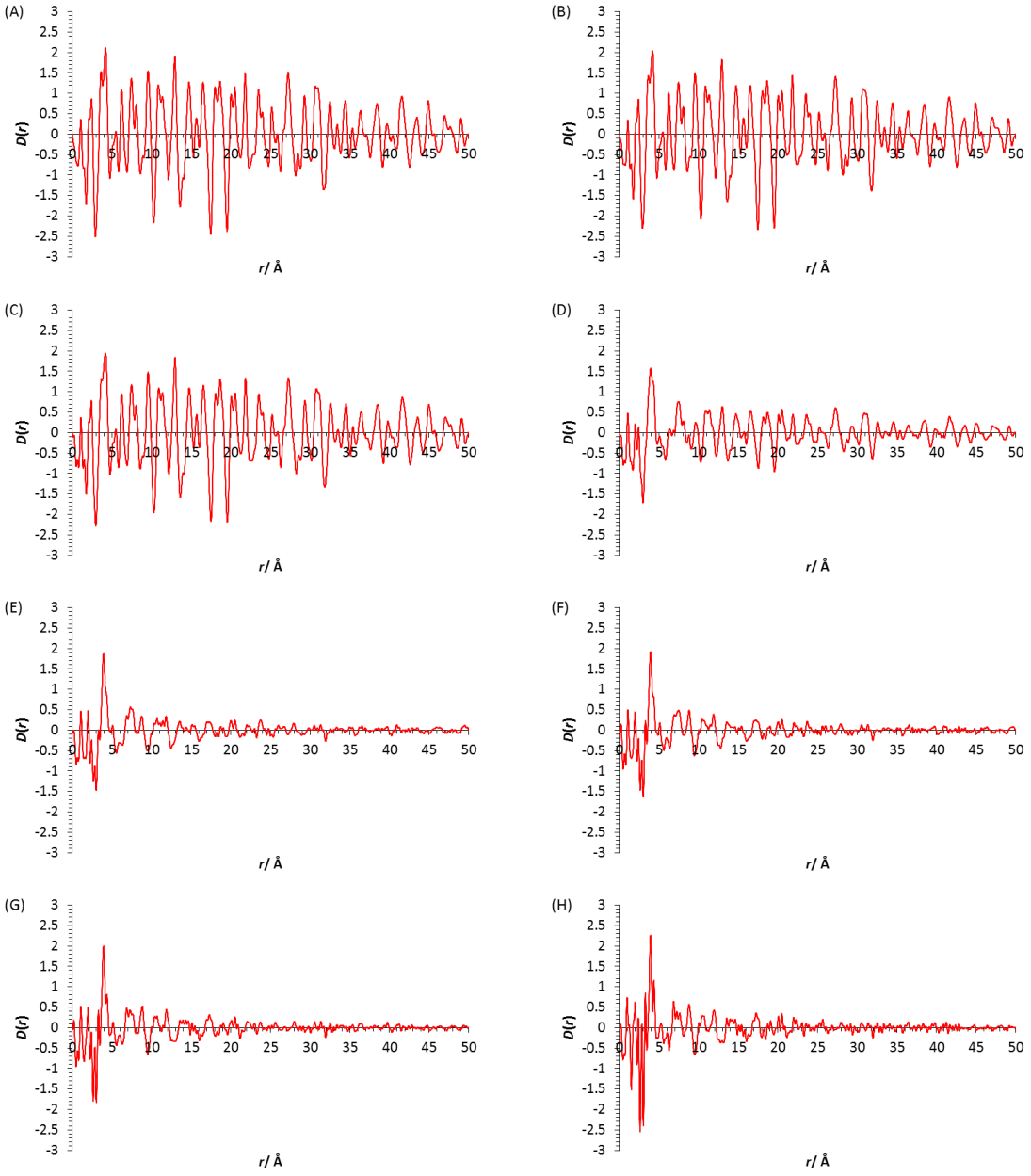

Figure 6.18 – *In-situ* PDF data collected during heating of nLi$_2$NH + (1 – n)LiBH$_4$, where n = 0.25 (A) 25 °C (B) 50 °C (C) 75 °C (D) 100 °C (E) 125 °C (F) 150 °C (G) 175 °C (H) 200 °C

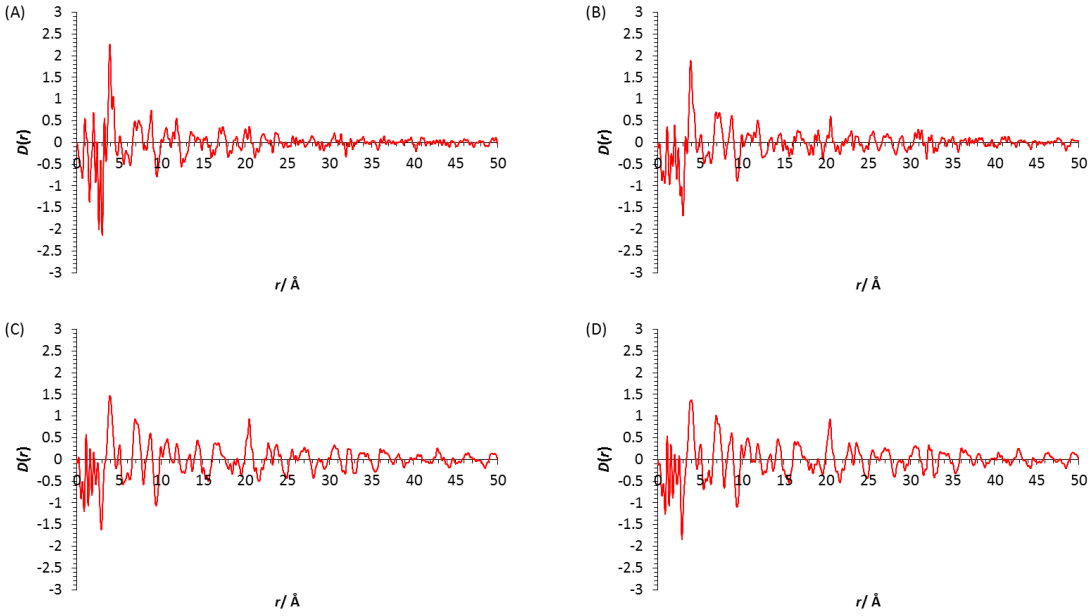

Figure 6.19 – *In-situ* PDF data collected during cooling of nLi$_2$NH + (1 – n)LiBH$_4$, where n = 0.25 (A) 150 °C (B) 100 °C (C) 50 °C (D) cooled to room temperature

The loss of long range ordering with heating was very apparent, with a significant reduction between 75 °C and 100 °C and again between 100 °C and 125 °C. Interestingly, the high resolution powder XRD data, collected on I11, determined the melting point of the mixture to be *ca* 140 to 150 °C (§6.3), whereas, these PDF data appear to show that the loss of long range order starts to occur significantly before that, as evidenced by a reduction in intensity of peaks at high-*r*. In fact the PDF data recorded at 125 °C and at 150 °C were very similar. One possible explanation for this is that the long range order is not lost, but that the co-existence of more phases upon formation of the orthorhombic phase (from *ca* 100 °C) means there are more pair contributions at similar distances, resulting in the PDF becoming flatter as a function of r.

In order to visualise these changes in the PDF data, all the data sets were plotted together in a three-dimensional waterfall plot (Figure 6.20). It shows the transition from a

highly crystalline sample, through to the formation of a melt and subsequent crystallisation of the final products, seen through the return of long range order upon cooling.

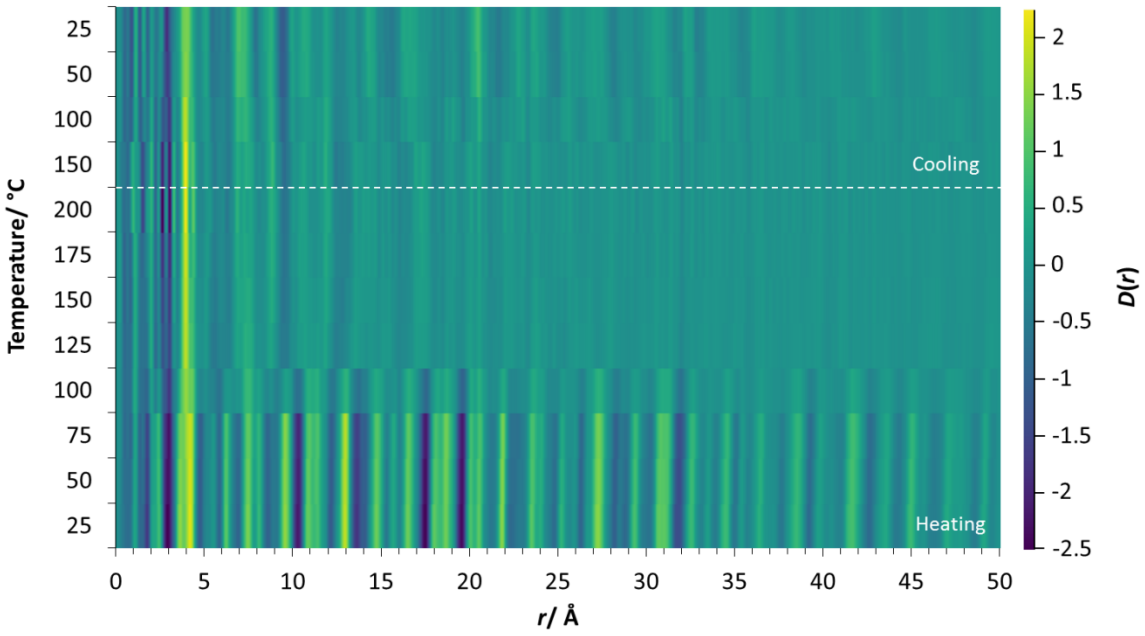

Figure 6.20 – *In-situ* PDF data collected during heating and then subsequent cooling of nLi$_2$NH + (1 – n)LiBH$_4$, where n = 0.25

The complexity of this multiphase system and the challenges associated with it meant that refining the various structures against the collected PDF data was not possible with the knowledge of the system to date. Nevertheless, the data collected still enabled changes in the long range order to be observed and through principal component analysis (PCA) the significance of each of the changes could be tracked.

Principal component analysis[162] aims to determine the directions in the data in which there is the greatest variance and subsequently simplify it into fewer dimensions, known as 'principal components'. The principal components are vectors in the data which are linear combinations of the variables in the original data set. There are only as many as there are

dimensions in the original data, with principal component 1 having the maximum variance along the line but minimum variation perpendicular to it. The second (and so on) are selected in the same way although they cannot be correlated with the previous ones. However, as the majority of the variance is captured in the first principal components, the later ones can often be disregarded as they contribute little to the overall understanding, reducing the number of dimensions and thus complexity of the data.

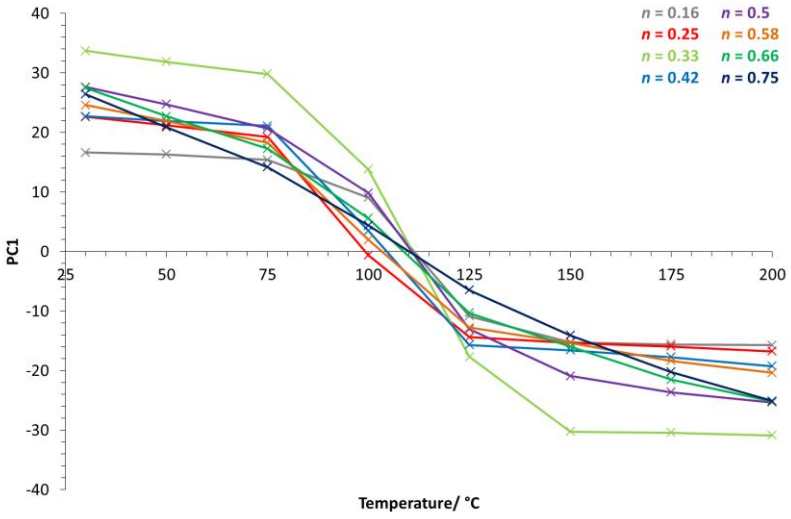

Figure 6.21 – Relative intensity of principal component as a function of temperature during heating, where *n* = 0.16 is grey, *n* = 0.25 is red, *n* = 0.33 is light green, *n* = 0.42 is blue, *n* = 0.5 is purple, *n* = 0.58 is orange, *n* = 0.66 is green and *n* = 0.75 is dark blue

The results of the PCA show that from 75 °C to 150 °C was where the samples underwent the most change, with the most dramatic changes (where principle component 1 was changing most rapidly) occurring between 75 °C and 125 °C. It is clear from these results that where there was a significant amount of Li_2NH present, there was the smallest amount of change in the PDF data. The 8:4 and 9:3 samples (n = 0.66 and 0.75, respectively) both exhibited the steadiest gradient which was to be expected due to the fact that excess Li_2NH

remains crystalline above the melting temperature for the mixture and so there samples changed the least over the temperature range studied.

A 'model-free' coherence length scale was then determined using Topas to estimate the coherent (i.e. repeating or crystalline) domain in each of the samples. A spherical function of the form $S[\pi r^2(¼(r/R)^3) - ((3r/R)+4)]/(4\pi r^2)$ was used, where r is the PDF distance in Å, R is the radius of a sphere of coherent domain in Å and S is a refined scale factor. This function was fit to the absolute magnitude of the PDF, i.e. only the positive peaks, to determine an approximate spherical radius at which the PDF becomes uncorrelated. The extracted radius is based on the curve of the red line in Figure 6.22, for a large value of R the line would have very little curvature and for a very small R it would quickly drop off to zero. The shape of the line is the shape of the $D(r)$ of a uniformly dense sphere.[163]

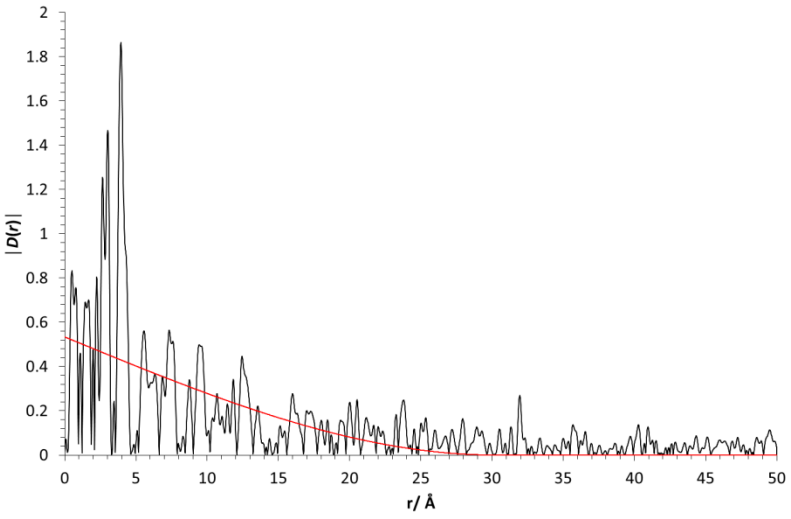

Figure 6.22 – Plot depicting fit to determine model-free coherence radius, where the black line is the absolute magnitude of the PDF and the red line corresponds to the shape of *D*(*r*) for a uniformly dense sphere of radius 15 Å

Figure 6.23 shows the extracted coherence radius as the samples were heated and subsequently cooled back down. The data clearly showed the eutectic point at n = 0.25. As expected for each sample the coherent radius decreased upon heating, happening most rapidly at the lowest temperatures at the eutectic point. However, upon cooling the samples did not have the same coherent radius as the starting materials. This may have been due to the presence of some amorphous phase in the final product mixture, or alternatively the presence of multiple phases with similar pair-distances at high-r giving the impression that the final sample was more disordered than the starting phases. Interestingly, even in the melt there was still a degree of local ordering, giving rise to a coherence radius of *ca* 15 Å. It is therefore most probable that there remained significant local ordering between the cations and anions within the molten phase, as has previously been calculated for $Li_4BH_4(NH_2)_3$.[164]

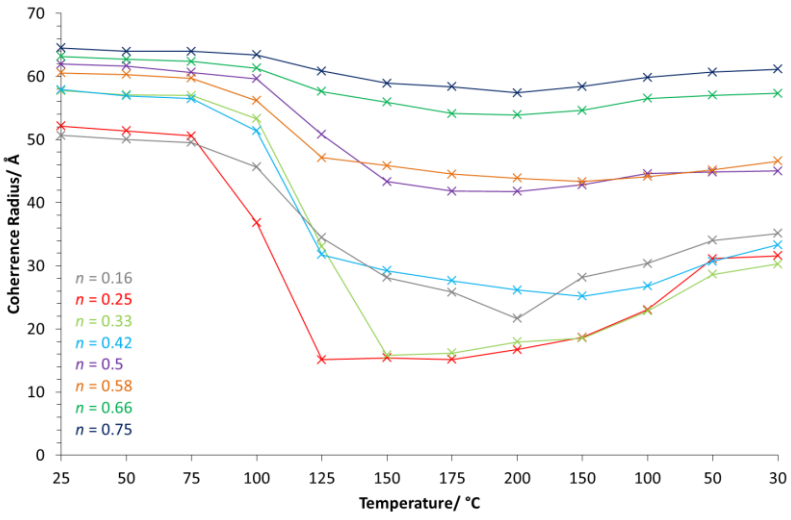

Figure 6.23 – Estimated coherence length scale in each of the samples as a function of temperature, where n = 0.16 is grey, n = 0.25 is red, n = 0.33 is light green, n = 0.42 is blue, n = 0.5 is purple, n = 0.58 is orange, n = 0.66 is green and n = 0.75 is dark blue

The PDF data presented in this thesis highlight the complexity of the lithium imide–lithium borohydride system, and due to these complexities and associated challenges, complete structures of the different phases upon heating have not been able to be determined. Despite this the data have provided a picture of the point in the heating process at which the most change occurs with regards to ordering and has supported the findings from the high resolution powder XRD data (§6.3).

6.5 Conclusions

The *in-situ* studies performed on the reaction of lithium imide and lithium borohydride provided an increased understanding of the processes occurring as the samples were heated and the stages at which the different structures formed. High resolution XRD data showed: the formation of the orthorhombic phase occurring upon heating, beginning at *ca* 100 °C; the structural transition of $LiBH_4$; the formation of a melt which occurred at *ca* 140 °C to 150 °C upon heating; and the crystallisation of the cubic phase between 65 °C and 70 °C upon cooling.

In-situ X-ray PDF studies were then collected and agreed with what was observed in the high resolution XRD data. The data showed that a large amount of order was lost at 100 °C, the temperature at which the orthorhombic phase was first observed. Then once the temperature reached 125 °C, there was very little long range order remaining in the mixture. However, this apparent lower temperature for loss of order may at least in part be due to the larger number of phases present with similar atom-atom distances and the relatively broad peaks due to the high mobility of ions within these phases. Unfortunately the complexity of the lithium borohydride-imide system and the weak scattering of the atoms

meant that although trends could be observed in the data, more structural details could not be determined. In future work, it may be useful to collect neutron data and by performing combined analysis of both the X-ray and neutron data perhaps more structural details could be obtained.

Chapter 7 – Conductivity Testing

7.1 Introduction

The purpose of this research has been to gain a greater understanding of the lithium borohydride-imide phase space, with one of the possible uses for these materials being solid state lithium ion conductors. As was discussed in §1.5 there are several advantages to using complex hydrides as lithium ion conductors such as their stability, light weight and softness.[64,67]

Lithium imide and the high temperature structure of lithium borohydride have both shown promise as lithium ion conductors; particularly lithium imide with a reported conductivity of 3×10^{-4} S cm^{-1} at room temperature.[72] There have also been high conductivities reported for materials in the lithium amide-borohydride phase space, *ca* 10^{-4} S cm^{-1} for both $Li_2BH_4NH_2$ and $Li_4BH_4(NH_2)_3$,[165] a system very similar to the one discussed in this research. Thus, it seemed plausible that the lithium borohydride-imides would also be promising solid state lithium ion conductors.

7.2 Experimental

Samples were pressed into pellets with a diameter of 7 mm and a thickness of *ca* 1 mm (Li_2NH pellets were subsequently sintered at 400 °C). These pellets were then sandwiched between two lithium electrodes, pressed together and sealed in a coin cell (detailed in §2.7). The samples were heated up to 80 °C, heating in 10 °C increments and allowing the temperature to stabilise at each stage before carrying out an A.C. impedance

measurement. Temperatures were held below 80 °C as the samples were housed in coin cells and it was important to ensure the integrity of the plastic O-ring seal.

7.3 Conductivity Studies

In order to investigate the conductivity of these materials, A.C. impedance spectroscopy was carried out. Conductivity values were determined from the resistance values (Z') at the end of the semicircle corresponding to the bulk conductivity. In an ideal Nyquist plot there are two semicircles, one corresponding to the bulk and the other to the grain boundary.[125] In these data there was only a single semicircle (an example plot is shown in Figure 7.1a), passing through the origin (additional Nyquist plots in Appendix 9.2). The plot of capacitance versus frequency (Figure 7.1b) shows a high frequency plateau with a capacitance of 8×10^{-12} F cm^{-1}. This value is typical for bulk capacitance with a typical permittivity of *ca* 10; capacitance values for grain boundaries are typically between 10^{-11} and 10^{-8} F cm^{-1}.[125]

It is not uncommon for only a single semicircle to be observed, meaning that the bulk and grain boundary contributions cannot be resolved (§2.7). This is often the case when the resistance of one is significantly greater than the other. The contribution of the grain boundary is directly affected by the density of the pellet. A higher capacitance can be achieved through higher density pellets which are well sintered and have small distances between the grains. Similarly, a lower capacitance can result if a sample is poorly sintered i.e. less dense.[125] The interface between the sample and the electrode is also an important consideration when looking at the different regions of the Nyquist plot. Where there is no impedance barrier to charge transfer between the electrode and the ceramic electrolyte,

only a single semicircle corresponding to the bulk is observed.[125] Alternatively in a semiconducting ceramic a single semicircle may be observed due to the grain boundary resistance dominating the plot.[125] Where a single semicircle is observed in a Nyquist plot it is often important to also plot M' vs M". The data is weighted differently in this case and therefore it may show features not visible in the original Nyquist plot. However, in this instance the M' vs M" plot also shows a single feature (Figure 7.1).

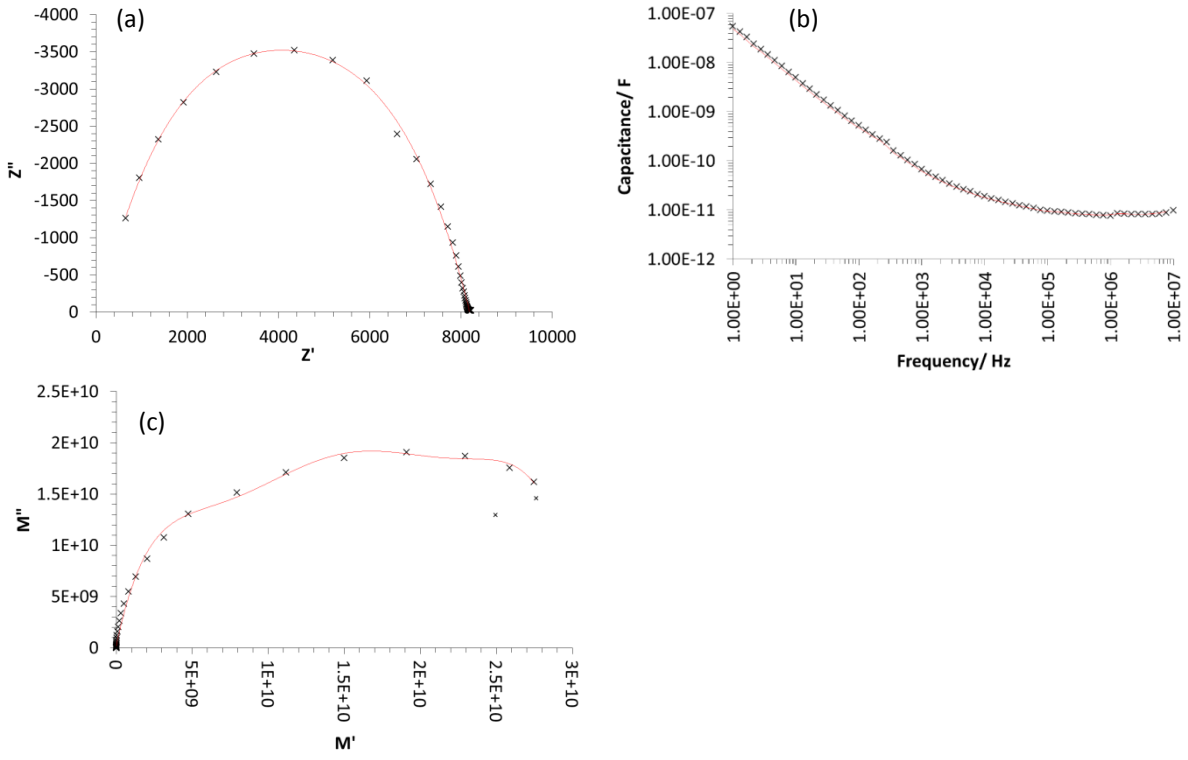

Figure 7.1 – (a) Nyquist plot (b) plot of capacitance against frequency and (c) plot of M' vs M" for a sample containing predominantly the orthorhombic phase, *n* = 0.42 for nLi$_2$NH + (1 – n)LiBH$_4$ synthesised at 125 °C for 12 hours; data collected at 80 °C

Conductivity data were collected on a range of different samples: multiple samples formed at 125 °C with a focus on the orthorhombic structure (*n* = 0.25, 0.33, 0.42 and 0.5 for nLi$_2$NH + (1 – n)LiBH$_4$); a majority cubic phase sample (*n* = 0.5 for nLi$_2$NH + (1 – n)LiBH$_4$

synthesised at 200 °C); a sample with a majority lithium amide-borohydride-imide hexagonal phase (n = 0.58 for nLi$_{1.5}$(NH$_2$)$_{0.5}$(NH)$_{0.5}$ + (1 – n)LiBH$_4$ synthesised at 125 °C); as well as both starting materials. The results of these measurements are shown in Figure 7.2.

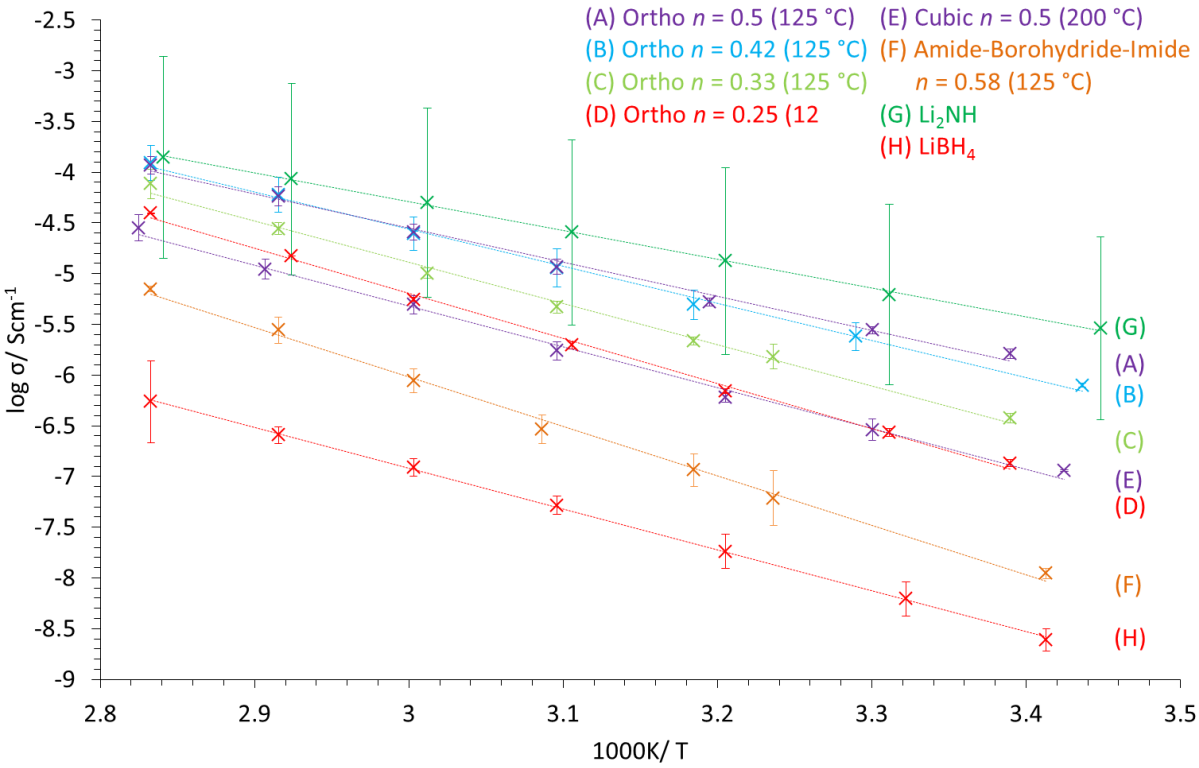

Figure 7.2 – Arrhenius plot showing ionic conductivity as a function of temperature for selected samples: (A) n = 0.5 for nLi$_2$NH + (1 – n)LiBH$_4$ at 125 °C; (B) n = 0.42 for nLi$_2$NH + (1 – n)LiBH$_4$ at 125 °C; (C) n = 0.33 for nLi$_2$NH + (1 – n)LiBH$_4$ at 125 °C; (D) n = 0.25 for nLi$_2$NH + (1 – n)LiBH$_4$ at 125 °C; (E) n = 0.5 for nLi$_2$NH + (1 – n)LiBH$_4$ at 200 °C; (F) n = 0.42 for nLi$_{1.5}$(NH$_2$)$_{0.5}$(NH)$_{0.5}$ + (1 – n)LiBH$_4$ at 125 °C; (G) Li$_2$NH, pellet sintered at 400 °C; (H) LiBH$_4$ (Sigma Aldrich, 90% purity)

The data presented in Figure 7.3 shows that the two starting materials are at either end of the conductivity scale. Li$_2$NH demonstrated a conductivity of 6.2 × 10^{-6} S cm^{-1} at 302 K and LiBH$_4$ a conductivity of 6.2 × 10^{-9} S cm^{-1} at 301 K. These values were used for comparison to the data collected on the new lithium borohydride-imide materials. However,

it is important to note that although the data collected for $LiBH_4$ is close to that reported in the literature, there is a significant deviation for Li_2NH (Figure 7.3). The relative density of the $LiBH_4$ pellet was close to 100% when comparing the real and theoretical density; however, for Li_2NH the real density was only 68% of the theoretical density which may be in part responsible for this deviation. A significant deviation from the theoretical density is due to microstructural defects, meaning there are likely to be a large number of pores in the pellet and possibly larger grains, resulting in poorer packing.[166] The lithium imide pellets were also very fragile and more difficult to form compared to the other pellets; this may have contributed to the decrease in conductivity too, as the contacts within the coin cell may not have been as good as for the other pellets.

The conductivity of $LiBH_4$ reported in the literature was determined through collecting A.C. impedance data on a 10 mm diameter pellet, between 0.8 and 1.2 mm in thickness. The pellet was sandwiched between two lithium foils and a stainless steel collector, forming a two electrode system.[167] On the other hand, the literature value reported for Li_2NH was determined by collecting A.C. impedance data on a pellet 9.3 mm in diameter with a thickness of 2 to 5 mm, which had been sintered for 30 minutes at 600 °C under nitrogen. The authors estimated that this method of forming pellets resulted in a density of between 85 and 87% of the theoretical density of Li_2NH, notably higher than the 68% determined in this work. The sides of sample were then polished flat and ionically blocking electrodes were applied to the pellet (potassium and graphite), with measurements being performed in a vacuum.[72]

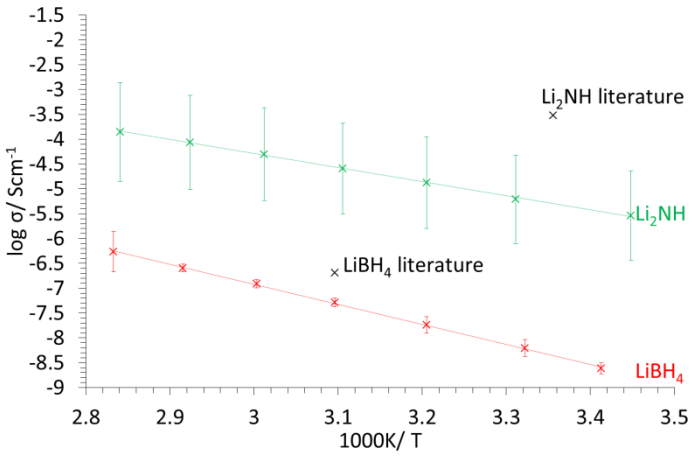

Figure 7.3 – Comparison of conductivity data collected in this study and conductivities of Li_2NH and $LiBH_4$ reported in the literature[72,167]

Considering first the lithium borohydride-imide samples synthesised at 125 °C, there was a clear trend of increasing conductivity with increasing lithium imide content. This agrees with what would be expected as lithium imide has a much higher conductivity than lithium borohydride, therefore increasing its content should increase overall conductivity. However, the samples were formed of multiple different phases and thus it was difficult to directly attribute the conductivity to a specific phase. Pellets A and B had similar conductivities despite a large increase in the amount of Li_2NH, indicating that the changing weight percentages of the other phases must have played a significant role too. The composition of the lithium borohydride-imide samples are given in Table 7.1.

Table 7.1 – Weight percentages of the different phases in the various lithium borohydride-imide samples synthesised for 12 hours, where *n* corresponds to $n$$Li_2NH$ + (1 – n)$LiBH_4$, determined by Rietveld refinement with QPA

Pellet	*n*	Weight Percent							σ/ S cm^{-1} (323 K)
		Li_2NH	$LiBH_4$	Cubic	Orthorhombic	Li_3BN_2	LiH	Li_2O	
Synthesised at 125 °C									
A	0.5	24.6(3)	1.8(5)	17.6(3)	52.4(4)	0	0	3.5(2)	1.2 X 10^{-5}
B	0.42	9.7(2)	2.7(7)	24.0(5)	62.1(6)	0	0	1.5(2)	1.1 X 10^{-5}
C	0.33	0	15.7(7)	21.6(5)	60.6(7)	0	0	2.1(2)	4.7 X 10^{-6}
D	0.25	0	72.6(9)	8.8(5)	15.8(1.0)	0	0	2.7(2)	2.0 X 10^{-6}
Synthesised at 200 °C									
E	0.5	12.0(2)	13.4(4)	37.1(4)	14.5(4)	17.4(4)	2.9(3)	2.7(1)	1.7 X 10^{-6}

Comparison of these samples against a sample with a large proportion of cubic lithium borohydride-imide phase, synthesised at 200 °C for 12 hours (pellet (E) in Figure 7.2), suggests that the orthorhombic phase may have a greater conductivity than the cubic phase. It is clear from the data that the same composition ($1Li_2NH$:$1LiBH_4$) heated to 125 °C compared with 200 °C had better conductivity (2.8×10^{-6} S cm^{-1} at 303 K and 2.9×10^{-7} S cm^{-1} at 303 K, respectively). However, as none of the samples were pure, and there were multiple other phases which would have contributed to the overall conductivity, it could not be confirmed that this was solely down to the orthorhombic and cubic phases. Synthesis at 200 °C resulted in decomposition of some of the products resulting in two additional phases, Li_3BN_2 and LiH, only adding to the complexity of the mixture.

The newly identified lithium amide-borohydride-imide hexagonal phase was also tested to determine its conductivity. Although there was a small amount of starting material, and small lithium oxide impurity in the sample, it was mostly formed of the *hexagonal* phase (86.4(6) wt.%). The lithium amide-borohydride-imide phase demonstrated poorer conductivity than any of the lithium borohydride-imide samples. This decline in conductivity was not unexpected as lithium amide is reported as a poor lithium ion conductor, with its conductivity reportedly less than 10^{-8} S cm^{-1} at room temperature.

Activation energies for each of the different samples were also determined from the Arrhenius plot and are given in Table 7.2. The greatest activation energy was calculated for the hexagonal amide-imide-borohydride phase; whereas the lowest, excluding starting materials, was calculated for sample A [n = 0.5 for $n$$Li_2NH$ + (1 – n)$LiBH_4$] synthesised at 125 °C. The data collected on the samples synthesised at a lower temperature (samples A to D) clearly show an increase in activation energy with increasing borohydride content. The activation energies calculated from the recorded conductivity data agree with what is reported in the literature for both $LiBH_4$ and Li_2NH, *i.e*. 0.79 eV and 0.58 eV, respectively.[72,167]

Table 7.2 – Activation energies of the different samples determined from the Arrhenius plot

Pellet	Composition	E_a/ eV
A	n = 0.5 for $n$$Li_2NH$ + (1 – n)$LiBH_4$	0.67(1)
B	n = 0.42 for $n$$Li_2NH$ + (1 – n)$LiBH_4$	0.73(1)
C	n = 0.33 for $n$$Li_2NH$ + (1 – n)$LiBH_4$	0.81(1)
D	n = 0.25 for $n$$Li_2NH$ + (1 – n)$LiBH_4$	0.88(1)
E	n = 0.5 for $n$$Li_2NH$ + (1 – n)$LiBH_4$	0.80(1)
F	n = 0.5 for $n$$Li_{1.5}(NH_2)_{0.5}(NH)_{0.5}$ + (1 – n)$LiBH_4$	0.97(1)
G	Li_2NH	0.56(1)
H	$LiBH_4$	0.78(1)

During the course of this project, research on the Li_2NH–$LiBH_4$ phase space was published by Wang *et al.*[147] and Wolczyk *et al.*[148] and in both cases A.C. impedance spectroscopy data were collected.

Wolczyk recorded the conductivity of the orthorhombic phase, $Li_5(BH_4)_3NH$, between room temperature and 100 °C, reporting a room temperature conductivity of *ca* 10^{-6} S cm^{-1}.[148] This sits within the range of values determined for the different orthorhombic samples reported in this thesis, although it is closest in value to the least conductive of the four samples. On the other hand, the activation energy reported agrees with the most orthorhombic-rich sample measured in this study, with a value of 0.73 eV.

Wang *et al.* reported conductivities of 3 × 10^{-6} S cm^{-1} for $2Li_2NH$:$3LiBH_4$ (n = 0.4) and 1 × 10^{-5} S cm^{-1} for $1Li_2NH$:$1LiBH_4$ (n = 0.5) at room temperature. In the reported study

samples were heated up to 120 °C from room temperature and displayed significant increases in conductivity from *ca* 80 °C, the more borohydride-rich 2:3 sample surpassing the 1:1 ratio at the higher temperatures (1.4×10^{-2} S cm^{-1} compared with 7.6×10^{-3} S cm^{-1} at 393 K, respectively).[147] This dramatic increase in conductivity at *ca* 80 °C was not reported by Wolczyk, and the maximum temperature in this study was below the reported jump. As synthesis of the orthorhombic phase does not produce a pure product, it may be that any discrepancies in the conductivities are due to differences in the number and amount of different phases present. It may be that in the study by Wang *et al*. there was a larger amount of starting materials and therefore one explanation could be that more orthorhombic phase began to form thus changing the conductivity.

7.4 Conclusions

Despite the limited temperature range for this study a clear and reproducible trend in conductivities was determined and the data collected were similar to those reported by both Wang and Wolczyk. These data show that lower temperature synthesis, which resulted in a greater abundance of the orthorhombic phase, gave rise to higher conductivities. In addition, all the lithium borohydride-imides had greater conductivities than the hexagonal lithium amide-borohydride-imide.

Further studies to investigate the higher temperature conductivities and compare them to the values determined by Wang *et al.* would be useful. However, in order for these materials to be used as solid state lithium ion conductors it is important to demonstrate high conductivities at temperatures as close to room temperature as possible. It would also be interesting to look at the more Li_2NH-rich end of the scale, synthesised at 125 °C, to see

whether an excess of Li_2NH has a significant effect on the conductivity. As was demonstrated in this work lithium imide itself, although a good lithium ion conductor, is very difficult to handle and forms very brittle and fragile pellets, therefore forming a lithium borohydride-imide or alternatively a Li_2NH-$LiBH_4$ composite is possibly a good way of harnessing the high conductivities whilst creating a more practical material.

Chapter 8 – Final Conclusions

The aim of this project was to study the Li-BH_4-NH-NH_2 phase space and subsequently determine the structures of new phases which were identified within it. The reason for investigating this phase space was to find potential new materials to be used as electrolytes in all solid state lithium ion batteries. Therefore the lithium ion conductivity was measured for different materials in the system to assess their viability.

Initial work focussed on the synthesis of lithium imide, as a precursor to any new lithium borohydride-imide materials it was important to optimise its synthesis. Both the reaction of Li_3N with $LiNH_2$ and the reaction of $LiNH_2$ with LiH were investigated and enabled a reliable synthesis method to be determined for use in subsequent work. Through the use of Raman spectroscopy a more accurate determination of amide and imide ion content was able to be performed and ensured the synthesis method could be optimised. Following on from the synthesis of Li_2NH, work was then able to progress into investigating the formation of mixed anion $Li_{(1+x)}(NH_2)_{(1-x)}(NH)_x$ phases, which successfully demonstrated an ability to tune the amide to imide ratio in the cubic Li_2NH structure.

Research then moved on to look at the reaction of lithium imide and lithium borohydride. The synthesis resulted in the formation of two lithium borohydride-imide phases, one cubic and one orthorhombic and investigations into how variations to the reactant ratios and reaction conditions could result in a different product mixture were performed. Studies highlighted that the orthorhombic phase formed more abundantly in a more $LiBH_4$-rich reactant mixture at *ca* 125 °C; with the best conditions determined to be a $19Li_2NH{:}31LiBH_4$ ratio [n = 0.38 using the equation $nLi_2NH + (1 - n)LiBH_4$] heated at 125 °C

for 2 x 0.5 hours, which produced a product mixture containing 74.4(4) wt.% orthorhombic phase. However, studies into the cubic phase proved more challenging and through more detailed synthetic studies at 200 °C it became evident that the cubic phase could not be consistently formed. The appearance of the products of the higher temperature reactions led to questions over the behaviour of the materials at the synthesis temperature and through melting point experiments it was determined that the samples were melting, helping to explain the inconsistencies in the results.

Slow cooling of the higher temperature Li_2NH + $LiBH_4$ reactions resulted in the formation of another phase, a structure later identified as a hexagonal lithium amide-borohydride-imide. Its preferential formation upon slow cooling of the Li_2NH-$LiBH_4$ reactant mixture suggested it was a thermodynamically stable phase, and through more detailed studies into the $n Li_{1.5}(NH_2)_{0.5}NH_{0.5}$ + (1 – n)$LiBH_4$ reaction it was determined to be amide-imide-rich compared to borohydride. Structure solution work, using laboratory XRD data enabled a working model of this phase to be produced, a hexagonal $P3_221$ structure with the composition $Li_4BH_4NHNH_2$. In future work, through collection of high resolution synchrotron data a more definitive structure will be able to be produced. The limitations of using laboratory data meant that it was difficult to determine the lithium and hydrogen positions precisely.

In order to gain a greater understanding of the phase space, *in-situ* high resolution XRD data and *in-situ* X-ray PDF data were collected to follow the $n Li_2NH$ + (1 – n)$LiBH_4$ reaction. The subsequent analysis demonstrated the formation of a melt upon heating as well as highlighting the temperatures at which the different phases form. The orthorhombic

phase forming rapidly upon heating from *ca* 100 °C and the cubic phase forming very late in the cooling process between 65 and 70 °C. Unfortunately due to the complexity of the system and the weak X-ray scattering power of the materials, limited information could be drawn from the X-ray PDF data. However, as more knowledge is gained about the system and with the determination of structural models, it may be possible to understand more about the mechanisms involved. An important starting point would be to study the behaviour of each of the starting materials during heating as their behaviour only added to the complexity of this recently studied system and perhaps a combined study of X-ray and neutron data would result in an increased gain of structural information.

Collection of high resolution powder XRD data allowed a structure of the orthorhombic phase to be determined. It was confirmed to have the composition $Li_5(BH_4)_3NH$, space group *Pnma* and lattice parameters a = 10.14982(8) Å, b = 11.48539(9) Å and c = 7.00041(5) Å. The model determined in this work also agreed with the structure published by Wolczyk *at al*.,[148] the main discrepancy being in the rotation of the BH_4 tetrahedra. Collection of neutron diffraction data of a deuterated sample will help to confirm the correct orientation and location of the hydrogen in the structure.

The structure of the cubic phase could not be definitively determined. Confirmation of the formation of decomposition products meant that the working model had to be revisited and consequently the final model presented in this thesis has the nominal formula Li_3BH_4NH and space group *Fm*-3*m*. It may be possible through the collection of synchrotron data to learn more about the structure of this material. However, the lack of unique

reflections means this will be challenging. The broad, asymmetric peaks suggest that there may be a range of compositions of the cubic structure.

Finally conductivity data were collected on several samples resulting from these studies. The data demonstrated the potential of the materials for use as solid state electrolytes and highlighted the importance of ease of processing. Li_2NH alone, although a promising lithium ion conductor was difficult to press into pellets consistently; however, incorporation of lithium borohydride-imides and $LiBH_4$ resulted in much more robust and reproducible pellets.

This work has produced a detailed study of the Li-BH_4-NH-NH_2 system providing an insight into the processes and structures resulting from the various reactions. It has enabled the structures of two lithium borohydride-imides, Li_3BH_4NH and $Li_5(BH_4)_3NH$, and a new lithium amide-borohydride-imide, $Li_4BH_4NHNH_2$, to be determined.

References

1 BP, *BP Statistical Review of World Energy 2019*, 2019.

2 J. D. Holladay, J. Hu, D. L. King and Y. Wang, *Catal. Today*, 2009, **139**, 244–260.

3 N. Nitta, F. Wu, J. T. Lee and G. Yushin, *Mater. Today*, 2015, **18**, 252–264.

4 C. Liu, Z. G. Neale and G. Cao, *Mater. Today*, 2016, **19**, 109–123.

5 J. B. Goodenough and K. S. Park, *J. Am. Chem. Soc.*, 2013, **135**, 1167–1176.

6 W. Xu, J. Wang, F. Ding, X. Chen, E. Nasybulin, Y. Zhang and J.-G. Zhang, *Energy Environ. Sci.*, 2014, **7**, 513–537.

7 D. Aurbach, E. Zinigrad, Y. Cohen and H. Teller, *Solid State Ionics*, 2002, **148**, 405–416.

8 X. Yao, B. Huang, J. Yin, G. Peng, Z. Huang, C. Gao, D. Liu and X. Xu, *Chinese Phys. B*, 2015, **25**, 018802.

9 J. D. Craddock, T. D. Rantell, J. C. Hower, D. T. Whitlow, J. Wiseman and M. C. Weisenberger, *Fuel*, 2017, **187**, 229–241.

10 M. S. Whittingham, *Science (80-.).*, 1976, **192**, 1126–1127.

11 D. W. Murphy and F. A. Trumbore, *J. Cryst. Growth*, 1977, **39**, 185–199.

12 K. Mizushima, P. C. Jones, P. J. Wiseman and J. B. Goodenough, *Solid State Ionics*, 1981, **3–4**, 171–174.

13 A. Du Pasquier, I. Plitz, S. Menocal and G. Amatucci, *J. Power Sources*, 2003, **115**, 171–178.

14 J. Dahn, E. Fuller, M. Obrovac and U. Vonsacken, *Solid State Ionics*, 1994, **69**, 265–270.

15 A. Rougier, P. Gravereau and C. Delmas, *J. Electrochem. Soc.*, 1996, **143**, 1168–1175.

16 F. Jiao and P. G. Bruce, *Adv. Mater.*, 2007, **19**, 657–660.

17 C. Masquelier and L. Croguennec, *Chem. Rev.*, 2013, **113**, 6552–6591.

18 K. Nanjundaswamya, A. Padhi, J. Goodenough, S. Okada, H. Ohtsukab, H. Arai and J. Yamakib, *Solid State Ionics*, 1996, **92**, 1–10.

19 A. Yamada, S. C. Chung and K. Hinokuma, *J. Electrochem. Soc.*, 2001, **148**, A224–A229.

20 F. Wang, H. C. Yu, M. H. Chen, L. Wu, N. Pereira, K. Thornton, A. Van Der Ven, Y. Zhu, G. G. Amatucci and J. Graetz, *Nat. Commun.*, 2012, **3**, 1–8.

21 P. Poizot, S. Laruelle, S. Grugeon, L. Dupont and J. Tarascon, *Nature*, 2000, **407**, 496–

499.

22 X. He, J. Ren, L. Wang, W. Pu, C. Jiang and C. Wan, *J. Power Sources*, 2009, **190**, 154–156.

23 C. Nan, Z. Lin, H. Liao, M. K. Song, Y. Li and E. J. Cairns, *J. Am. Chem. Soc.*, 2014, **136**, 4659–4663.

24 D. Aurbach, E. Pollak, R. Elazari, G. Salitra, C. S. Kelley and J. Affinito, *J. Electrochem. Soc.*, 2009, **156**, A694.

25 D. Aurbach, Y. Talyosef, B. Markovsky, E. Markevich, E. Zinigrad, L. Asraf, J. S. Gnanaraj and H. J. Kim, *Electrochim. Acta*, 2004, **50**, 247–254.

26 P. E. de Jongh, D. Blanchard, M. Matsuo, T. J. Udovic and S. Orimo, *Appl. Phys. A*, 2016, **122**, 251.

27 P. Knauth, *Solid State Ionics*, 2009, **180**, 911–916.

28 J. C. Bachman, S. Muy, A. Grimaud, H.-H. Chang, N. Pour, S. F. Lux, O. Paschos, F. Maglia, S. Lupart, P. Lamp, L. Giordano and Y. Shao-Horn, *Chem. Rev.*, 2016, **116**, 140–162.

29 P. P. Kumar and S. Yashonath, *J. Chem. Sci.*, 2006, **118**, 135–154.

30 B. Y. J. Brous, E. Ba and A. S. Corps, *Acta Crystallogr.*, 1953, **6**, 67–70.

31 Y. Inaguma, C. Liquan, M. Itoh, T. Nakamura, T. Uchida, H. Ikuta and M. Wakihara, *Solid State Commun.*, 1993, **86**, 689–693.

32 H. Kawai and J. Kunwano, *J. Electrochem. Soc.*, 1994, **141**, L78–L79.

33 O. Bohnke, C. Bohnke and J. L. Fourquet, *Solid State Ionics*, 1996, **91**, 21–31.

34 L. O. Hagman and P. Kierkegaad, *Acta Chem. Scand.*, 1968, **22**, 1822–1832.

35 J. B. Goodenough, H. Y.-P. Hong and J. A. Kafalas, *Mater. Res. Bull.*, 1976, **11**, 203–220.

36 M. I. Kimpa, M. Z. H. Mayzan, J. A. Yabagi, M. M. Nmaya, K. U. Isah and M. A. Agam, in *IOP Conference Series: Earth and Environmental Science*, 2018, vol. 140.

37 W. Thangadurai and V. Weppner, *Ionics (Kiel).*, 2006, **12**, 81–92.

38 M. Casciola, U. Costantino, L. Merlini, I. G. K. Andersen and E. K. Andersen, *Solid State Ionics*, 1988, **26**, 229–235.

39 M. Subramanian, R. Subramanian and A. Clearfield, *Solid State Ionics*, 1986, **18–19**, 562–569.

40 A. Martinez-Juarez, J. M. Rojo, J. E. Iglesias and J. Sanz, *Chem. Mater.*, 1995, **7**, 1857–1862.

41 H. Aono, E. Sugimoto, Y. Sadaoka, N. Imanaka and G. ya Adachi, *Solid State Ionics*, 1990, **40**–**41**, 38–42.

42 V. Thangadurai, S. Narayanan and D. Pinzaru, *Chem. Soc. Rev.*, 2014, **43**, 4714.

43 H. M. Kasper, *Inorg. Chem.*, 1969, **8**, 1000–1002.

44 E. J. Cussen, *Chem. Commun.*, 2006, 412–413.

45 D. Mazza, *Mater. Lett.*, 1988, **7**, 205–207.

46 V. Thangadurai, H. Kaack and W. J. F. Weppner, *J. Am. Ceram. Soc.*, 2003, **86**, 437–440.

47 V. Thangadurai and W. Weppner, *J. Am. Ceram. Soc.*, 2005, **88**, 411–418.

48 V. Thangadurai and W. Weppner, *Adv. Funct. Mater.*, 2005, **15**, 107–112.

49 R. Murugan, V. Thangadurai and W. Weppner, *Angew. Chemie - Int. Ed.*, 2007, **46**, 7778–7781.

50 J. Awaka, N. Kijima, H. Hayakawa and J. Akimoto, *J. Solid State Chem.*, 2009, **182**, 2046–2052.

51 Q. Liu, Z. Geng, C. Han, Y. Fu, S. Li, Y. bing He, F. Kang and B. Li, *J. Power Sources*, 2018, **389**, 120–134.

52 C. A. Geiger, E. Alekseev, B. Lazic, M. Fisch, T. Armbruster, R. Langner, M. Fechtelkord, N. Kim, T. Pettke and W. Weppner, *Inorg. Chem.*, 2011, **50**, 1089–1097.

53 M. A. Howard, O. Clemens, K. S. Knight, P. A. Anderson, S. Hafiz, P. M. Panchmatia and P. R. Slater, *J. Mater. Chem. A*, 2013, **1**, 14013.

54 M. A. Howard, O. Clemens, E. Kendrick, K. S. Knight, D. C. Apperley, P. A. Anderson and P. R. Slater, *Dalt. Trans.*, 2012, **41**, 12048–12053.

55 C. Deviannapoorani, L. Dhivya, S. Ramakumar and R. Murugan, *J. Power Sources*, 2013, **240**, 18–25.

56 J. H. Kennedy, S. Sahami, S. W. Shea and Z. Zhang, *Solid State Ionics*, 1986, **18** & **19**, 368–371.

57 J. H. Kennedy and Y. Yang, *J. Electrochem. Soc.*, 1986, 2437–2438.

58 B. T. Ahn and R. A. Huggins, *Solid State Ionics*, 1991, **46**, 237–242.

59 S. Kondo and K. Takada, *Solid State Ionics*, 1992, **53**–**56**, 1183–1186.

60 R. Kanoo and M. Murayama, *J. Electrochem. Soc.*, 2001, **148**, A742–A746.

61 M. Murayama, N. Sonoyama, A. Yamada and R. Kanno, *Solid State Ionics*, 2004, **170**, 173–180.

62 N. Kamaya, K. Homma, Y. Yamakawa, M. Hirayama, R. Kanno, M. Yonemura, T. Kamiyama, Y. Kato, S. Hama, K. Kawamoto and A. Mitsui, *Nat. Mater.*, 2011, **10**, 682–686.

63 P. Bron, S. Johansson, K. Zick, J. S. A. Der Günne, S. Dehnen and B. Roling, *J. Am. Chem. Soc.*, 2013, **135**, 15694–15697.

64 A. Unemoto, M. Matsuo and S.-I. Orimo, *Adv. Funct. Mater.*, 2014, **24**, 2267–2279.

65 M. Matsuo, Y. Nakamori, S.-I. Orimo, H. Maekawa and H. Takamura, *Appl. Phys. Lett.*, 2007, **91**, 224103.

66 H. Oguchi, M. Matsuo, T. Sato, H. Takamura, H. Maekawa, H. Kuwano and S. Orimo, *J. Appl. Phys.*, 2010, **107**, 096104.

67 H. Maekawa, M. Matsuo, H. Takamura, M. Ando, Y. Noda, T. Karahashi and S.-I. Orimo, *J. Am. Chem. Soc.*, 2009, **131**, 894–895.

68 A. Züttel, P. Wenger, S. Rentsch, P. Sudan, P. Mauron and C. Emmenegger, *J. Power Sources*, 2003, **118**, 1–7.

69 S. Isobe, T. Ichikawa, S. Hino and H. Fujii, *J. Phys. Chem. B*, 2005, **109**, 14855–14858.

70 U. V. Alpen, A. Rabenau and G. H. Talat, *Appl. Phys. Lett.*, 1977, **30**, 621–623.

71 B. A. Boukamp and R. A. Huggins, *Mater. Res. Bull.*, 1978, **13**, 23–32.

72 B. A. Boukamp and R. A. Huggins, *Phys. Lett.*, 1979, **72A**, 464–466.

73 P. A. Anderson, P. A. Chater, D. R. Hewett and P. R. Slater, *Faraday Discuss.*, 2011, **151**, 271–284.

74 R. A. Davies, D. R. Hewett, E. Korkiakoski, S. P. Thompson and P. A. Anderson, *J. Alloys Compd.*, 2015, **645**, S343–S346.

75 R. A. Davies and P. A. Anderson, *Int. J. Hydrogen Energy*, 2015, **40**, 3001–3005.

76 W. I. F. David, M. O. Jones, D. H. Gregory, C. M. Jewell, S. R. Johnson, A. Walton and P. P. Edwards, *J. Am. Chem. Soc.*, 2007, **129**, 1594–1601.

77 J. W. Makepeace, M. O. Jones, S. K. Callear, P. P. Edwards and W. I. F. David, *Phys. Chem. Chem. Phys.*, 2014, **16**, 4061–70.

78 P. Chen, Z. Xiong, J. Luo, J. Lin and K. L. Tan, *J. Phys. Chem. B*, 2003, **107**, 10967–10970.

79 T. Ichikawa, N. Hanada, S. Isobe, H. Leng and H. Fujii, *J. Phys. Chem. B*, 2004, **108**, 7887–7892.

80 Y. H. Hu and E. Ruckenstein, *J. Phys. Chem. A*, 2003, **107**, 9737–9739.

81 D. R. Hewett, PhD Thesis, University of Birmingham, 2012.

82 Y. H. Hu and E. Ruckenstein, *Ind. Eng. Chem. Res.*, 2006, **45**, 4993–4998.

83 J. W. Makepeace and W. I. F. David, *J. Phys. Chem. C*, 2017, **121**, 12010–12017.

84 C. Li, P. Peng, D. W. Zhou and L. Wan, *Int. J. Hydrogen Energy*, 2011, **36**, 14512–14526.

85 K. Takahashi, K. Hattori, T. Yamazaki, K. Takada, M. Matsuo, S.-I. Orimo, H. Maekawa and H. Takamura, *J. Power Sources*, 2013, **226**, 61–64.

86 J. P. Soulié, G. Renaudin, R. Černý and K. Yvon, *J. Alloys Compd.*, 2002, **346**, 200–205.

87 H. Hagemann, Y. E. Filinchuk, D. Chernyshov and W. van Beek, *Phase Transitions*, 2009, **82**, 344–355.

88 A. Borgschulte, A. Jain, A. J. Ramirez-Cuesta, P. Martelli, A. Remhof, O. Friedrichs, R. Gremaud and A. Züttel, *Faraday Discuss.*, 2011, **151**, 213–230.

89 T. Ikeshoji, E. Tsuchida, K. Ikeda, M. Matsuo, H. W. Li, Y. Kawazoe and S. I. Orimo, *Appl. Phys. Lett.*, 2009, **95**, 221901.

90 V. Epp and M. Wilkening, *Phys. Rev. B*, 2010, **82**, 020301.

91 J. S. G. Myrdal, D. Blanchard, D. Sveinbjörnsson and T. Vegge, *J. Phys. Chem. C*, 2013, **117**, 9084–9091.

92 D. Sveinbjörnsson, J. S. G. Myrdal, D. Blanchard, J. J. Bentzen, T. Hirata, M. B. Mogensen, P. Norby, S.-I. Orimo and T. Vegge, *J. Phys. Chem. C*, 2013, **117**, 3249–3257.

93 M. Aoki, K. Miwa, T. Noritake, G. Kitahara, Y. Nakamori, S. Orimo and S. Towata, *Appl. Phys. A*, 2005, **80**, 1409–1412.

94 F. E. Pinkerton, G. P. Meisner, M. S. Meyer, M. P. Balogh and M. D. Kundrat, *J. Phys. Chem. B*, 2005, **109**, 6–8.

95 F. E. Pinkerton, *J. Alloys Compd.*, 2005, **400**, 76–82.

96 P. A. Chater, W. I. F. David, S. R. Johnson, P. P. Edwards and P. A. Anderson, *Chem. Commun.*, 2006, 2439–2441.

97 P. A. Chater, PhD Thesis, University of Birmingham, 2009.

98 P. A. Chater, W. I. F. David and P. A. Anderson, *Chem. Commun.*, 2007, 4770–4772.

99 Y. E. Filinchuk, K. Yvon, G. P. Meisner, F. E. Pinkerton and M. P. Balogh, *Inorg. Chem.*, 2006, **45**, 1433–1435.

100 P. A. Anderson, P. A. Chater, W. I. F. David, I. C. Evans and A. L. Kersting, in *2009 MRS Fall Meeting*, 2010.

101 G. P. Meisner, M. L. Scullin, M. P. Balogh, F. E. Pinkerton and M. S. Meyer, *J. Phys.*

Chem. B, 2006, **110**, 4186–4192.

102 T. Noritake, M. Aoki, S. Towata, A. Ninomiya, Y. Nakamori and S. Orimo, *Appl. Phys. A Mater. Sci. Process.*, 2006, **83**, 277–279.

103 M. Matsuo, A. Remhof, P. Martelli, R. Caputo, M. Ernst, Y. Miura, T. Sato, H. Oguchi, H. Maekawa, H. Takamura, A. Borgschulte, A. Züttel and S.-I. Orimo, *J. Am. Chem. Soc.*, 2009, **131**, 16389–16391.

104 W. Li, G. Wu, Z. Xiong, Y. P. Feng and P. Chen, *Phys. Chem. Chem. Phys.*, 2012, **14**, 1596–1606.

105 C. F. Burmeister and A. Kwade, *Chem. Soc. Rev.*, 2013, **42**, 7660–7667.

106 Z. Dauter and M. Jaskolski, *J. Appl. Crystallogr.*, 2010, **43**, 1150–1171.

107 R. E. Dinnebier and S. J. L. Bilinge, *Powder Diffraction: Theory and Practice*, The Royal Society of Chemistry, Cambridge, 2008.

108 C. J. Rhodes, *Sci. Prog.*, 2015, **98**, 192–200.

109 Bird's Eye View of a Synchotron, https://www.diamond.ac.uk/Science/Machine/Components.html, (accessed 22 January 2020).

110 Introduction to Synchrotron Powder Diffraction, http://pd.chem.ucl.ac.uk/pdnn/inst2/intro.htm, (accessed 23 January 2020).

111 S. P. Thompson, J. E. Parker, J. Potter, T. P. Hill, A. Birt, T. M. Cobb, F. Yuan and C. C. Tang, *Rev. Sci. Instrum.*, 2009, **80**, 075107.

112 Welcome to I11, https://www.diamond.ac.uk/Instruments/Crystallography/I11.html, (accessed 23 January 2020).

113 H. M. Rietveld, *J. Appl. Crystallogr.*, 1969, **2**, 65–71.

114 R. A. Young, *The Rietveld Method*, Oxford University Press, 1993.

115 L. B. McCusker, R. B. Von Dreele, D. E. Cox, D. Louër and P. Scardi, *J. Appl. Crystallogr.*, 1999, **32**, 36–50.

116 G. S. Pawley, *J. Appl. Crystallogr.*, 1981, **14**, 357–361.

117 A. A. Coelho, *TOPAS-Academic V6*, Coelho Software, Brisbane, Australia, 2016.

118 T. Egami and S. J. L. Billinge, *Underneath the Bragg Peaks: Structural Analysis of Complex Materials*, Elsevier Ltd., Oxford, Second Edi., 2012.

119 C. A. Young and A. L. Goodwin, *J. Mater. Chem.*, 2011, **21**, 6464.

120 D. A. Keen, *J. Appl. Crystallogr.*, 2001, **34**, 172–177.

121 Science and Technology Facilities Council, *GudrunX*, 2017.

122 Beamline Layout and Optics, https://www.diamond.ac.uk/Instruments/Crystallography/I15-1/layout.html, (accessed 23 January 2020).

123 P. A. Chater, D. S. Keeble, M. G. Tucker, J. P. Sutter, M. Hillman and H. Wilhelm, The XPDF beamline at Diamond Light Source: An integrated hardware-software approach to X-ray PDF, https://www.diamond.ac.uk/Instruments/Crystallography/I15-1/BL-presentations/base/0/text_files/file1/document/XPDF DSE2015 Poster.pdf, (accessed 23 January 2020).

124 P. Larkin, *Infrared and Raman Spectroscopy, Principles and Spectral Interpretation*, Elsevier, 2011.

125 J. T. S. Irvine, D. C. Sinclair and A. R. West, *Adv. Mater.*, 1990, **2**, 132–138.

126 E. Barsoukov and J. R. Macdonald, *Impedance Spectroscopy: Theory, Experiment, and Applications*, John Wiley & Sons Incorporated, Second Edi., 2005.

127 D. Johnson, *ZView: a Software Program for IES Analysis*, Scribner Associates Inc., Southern Pines, NC, 2002.

128 P. Patel, *MSci Project Dissertation*, School of Chemistry, University of Birmingham, 2016.

129 D. H. Gregory, *J. Mater. Chem.*, 2008, **18**, 2321–2330.

130 K. Ohoyama, Y. Nakamori, S. I. Orimo and K. Yamada, *J. Phys. Soc. Japan*, 2005, **74**, 483–487.

131 T. Noritake, H. Nozaki, M. Aoki, S. Towata, G. Kitahara, Y. Nakamori and S. Orimo, *J. Alloys Compd.*, 2005, **393**, 264–268.

132 M. P. Balogh, C. Y. Jones, J. F. Herbst, L. G. Hector and M. Kundrat, *J. Alloys Compd.*, 2006, **420**, 326–336.

133 L. Nh and R. A. Forman, *Nature*, 1936, **138**, 936–937.

134 Y. Kojima and Y. Kawai, *J. Alloys Compd.*, 2005, **395**, 236–239.

135 B. Paik and A. Wolczyk, *J. Phys. Chem. C*, 2019, **123**, 1619–1625.

136 J. Yang, J. Lamsal, Q. Cai, W. B. Yelon and W. J. James, in *MRS Proceedings*, 2008, vol. 1098.

137 A. A. Coelho, J. Evans, I. Evans, A. Kern and S. Parsons, *Powder Diffr. Suppl.*, 2011, **26**, S22–S25.

138 J. P. O. Bohger, R. R. Eβmann and H. Jacobs, *J. Mol. Struct.*, 1995, **348**, 325–328.

139 R. S. Chellappa, D. Chandra, M. Somayazulu, S. A. Gramsch and R. J. Hemley, *J. Phys. Chem. B*, 2007, **111**, 10785–10789.

140 J. Zhang and Y. H. Hu, *Int. J. Hydrogen Energy*, 2012, **37**, 10467–10472.

141 R. Niewa and D. A. Zherebtsov, *Zeitschrift fur Krist. - New Cryst. Struct.*, 2002, **217**, 317–318.

142 D. J. Bull, N. Sorbie, D. Moser, M. T. F. Telling, R. I. Smith, D. H. Gregory and D. K. Ross, *Faraday Discuss.*, 2011, **151**, 1–8.

143 A. Santoru, C. Pistidda, M. H. Sørby, M. R. Chierotti, S. Garroni, E. Pinatel, F. Karimi, H. Cao, N. Bergemann, T. T. Le, J. Puszkiel, R. Gobetto, M. Baricco, B. C. Hauback, T. Klassen and M. Dornheim, *Chem. Commun.*, 2016, **52**, 11760–11763.

144 Walker, *Solid-State Hydrogen Storage: Materials and Chemistry*, Elsevier, 2008.

145 H. J. Beister, S. Haag, R. Kneip, K. Strossner and K. Syassen, *Angew. Chemie - Int. Ed. English*, 1988, **27**, 1101–1103.

146 A. Huq, J. W. Richardson, E. R. Maxey, D. Chandra and W. M. Chien, *J. Alloys Compd.*, 2007, **436**, 256–260.

147 H. Wang, H. Cao, W. Zhang, J. Chen, H. Wu, C. Pistidda, X. Ju, W. Zhou, G. Wu, M. Etter, T. Klassen, M. Dornheim and P. Chen, *Chem. - A Eur. J.*, 2018, **24**, 1342–1347.

148 A. Wolczyk, B. Paik, T. Sato, C. Nervi, M. Brighi, S. P. Gharibdoust, M. Chierotti, M. Matsuo, G. Li, R. Gobetto, T. R. Jensen, R. Černý, S. I. Orimo and M. Baricco, *J. Phys. Chem. C*, 2017, **121**, 11069–11075.

149 F. E. Pinkerton and J. F. Herbst, *J. Appl. Phys.*, 2006, **99**, 113523.

150 K. B. Harvey and N. R. McQuaker, *J. Chem. Phys.*, 1971, **55**, 4390–4396.

151 Gomes S., Hagemann H. and Yvon K., *J. Alloys Compd.*, 2002, **346**, 5.

152 A. A. Coelho, *J. Appl. Crystallogr.*, 2000, **33**, 899–908.

153 M. I. Aroyo, J. Perez-Mato, C. Capillas, E. Kroumova, S. Ivantchev, G. Madariaga, A. Kirov and H. Wondrarschek, *Zeischrift fur Krist.*, 2006, **221**, 15–27.

154 G. Oszlányi and A. Sütó, *Acta Crystallogr. Sect. A Found. Crystallogr.*, 2008, **64**, 123–134.

155 A. van der Lee, *J. Appl. Crystallogr.*, 2013, **46**, 1306–1315.

156 V. R. Juza and K. Opp, *Zeitschrift für Anorg. und Allg. Chemie*, 1951, **266**, 325–330.

157 W.-K. Li, G.-D. Zhou and T. C. W. Mak, *Advanced Structural Inorganic Chemistry*, Oxford University Press, Oxford, 2008.

158 K. Momma and F. Izumi, *J. Appl. Crystallogr.*, 2011, **44**, 1272–1276.

159 H. I. Schlesinger and H. C. Brown, *J. Am. Chem. Soc.*, 1940, **62**, 3429–3435.

160 C. L. Farrow, P. Juhas, J. W. Liu, D. Bryndin, E. S. Boin, J. Bloch, T. Proffen and S. J. L. Billinge, *J. Phys. Condens. Matter*, 2007, **19**, 335219.

161 P. C. Aeberhard, K. Refson and W. I. F. David, *Phys. Chem. Chem. Phys.*, 2013, **15**, 8081–8087.

162 J. Lever, M. Krzywinski and N. Altman, *Nat. Methods*, 2017, **14**, 641–642.

163 K. Kodama, S. Iikubo, T. Taguchi and S. I. Shamoto, *Acta Crystallogr. Sect. A Found. Crystallogr.*, 2006, **62**, 444–453.

164 D. E. Farrell, D. Shin and C. Wolverton, *Phys. Rev. B - Condens. Matter Mater. Phys.*, 2009, **80**, 1–8.

165 Y. Zhou, M. Matsuo, Y. Miura, H. Takamura, H. Maekawa, A. Remhof, A. Borgschulte, A. Zuttel, T. Otomo and S. Orimo, *Mater. Trans.*, 2011, **52**, 654–657.

166 H. Naceur, A. Megriche and M. El Maaoui, *J. Adv. Ceram.*, 2014, **3**, 17–30.

167 L. Zhan, Y. Zhang, X. Zhuang, H. Fang, Y. Zhu, X. Guo, J. Chen, Z. Wang and L. Li, *Solid State Ionics*, 2017, **304**, 150–155.

Chapter 9 Appendix

9.1 Rietveld Plots for Initial Lithium Imide Series

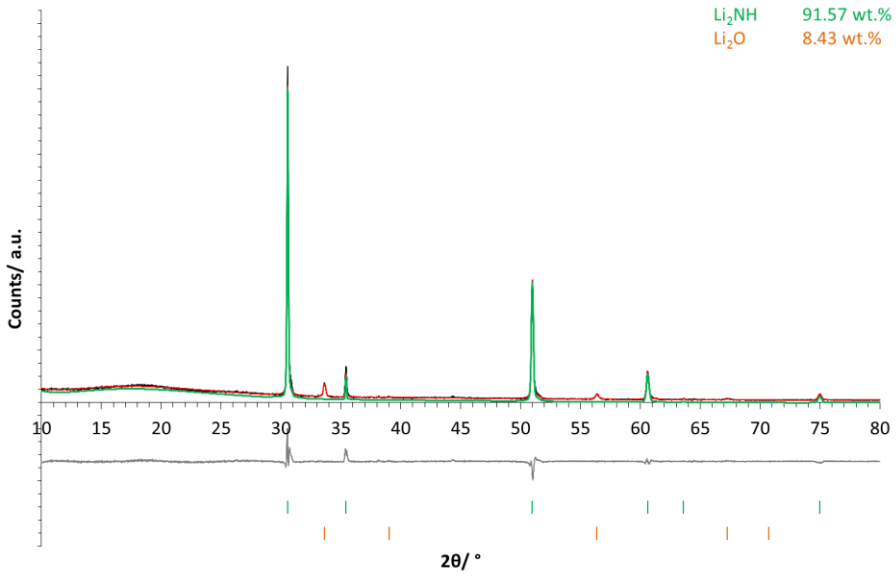

Figure 9.1 – Refinement plot showing the products of heating $LiNH_2$ + LiH at 400 °C for 12 hours. Green tick marks = Li_2NH, orange tick marks = Li_2O, with the cubic Li_2NH phase fit plotted in green

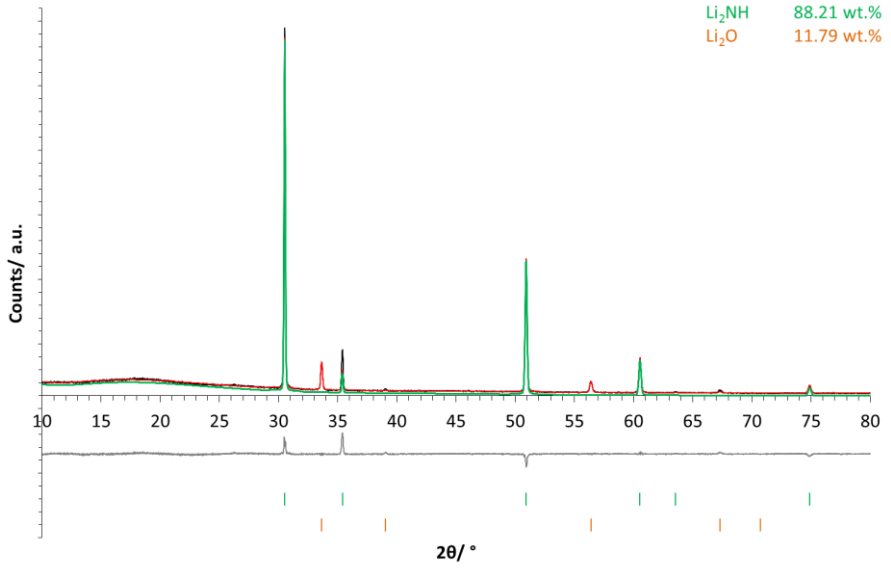

Figure 9.2 – Refinement plot showing the products of heating $LiNH_2$ + LiH at 450 °C for 12 hours. Green tick marks = Li_2NH, orange tick marks = Li_2O, with the cubic Li_2NH phase fit plotted in green

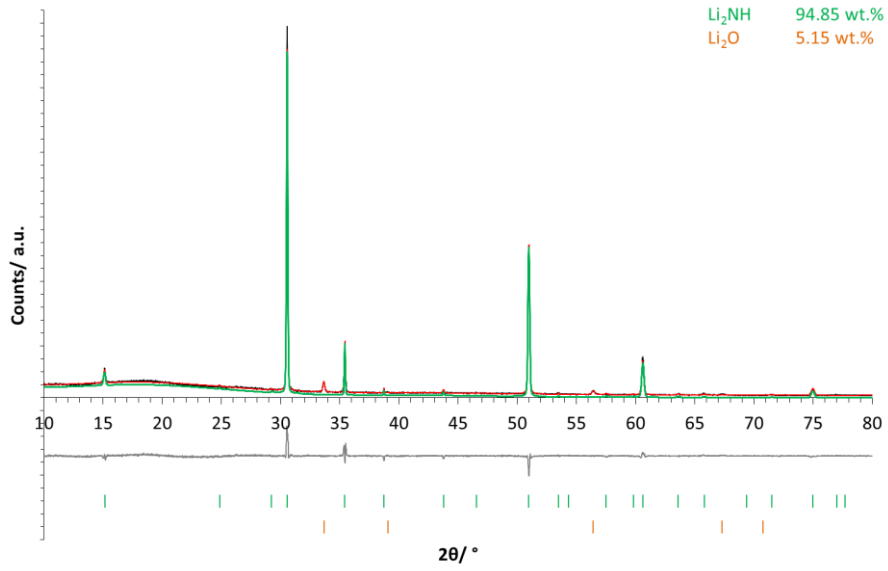

Figure 9.3 – Refinement plot showing the products of heating $LiNH_2$ + LiH at 500 °C for 12 hours. Green tick marks = Li_2NH, orange tick marks = Li_2O, with the cubic Li_2NH phase fit plotted in green

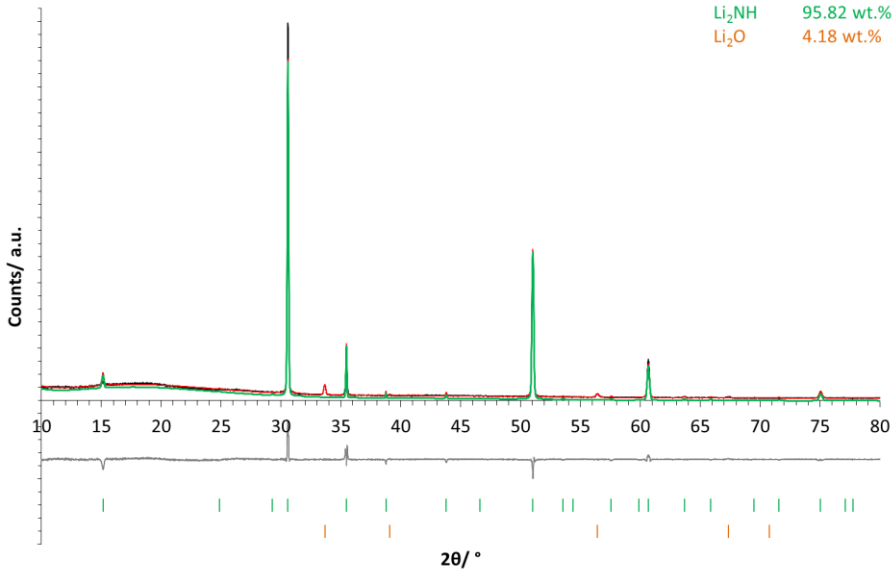

Figure 9.4 – Refinement plot showing the products of heating $LiNH_2$ + LiH at 525 °C for 12 hours. Green tick marks = Li_2NH, orange tick marks = Li_2O, with the cubic Li_2NH phase fit plotted in green

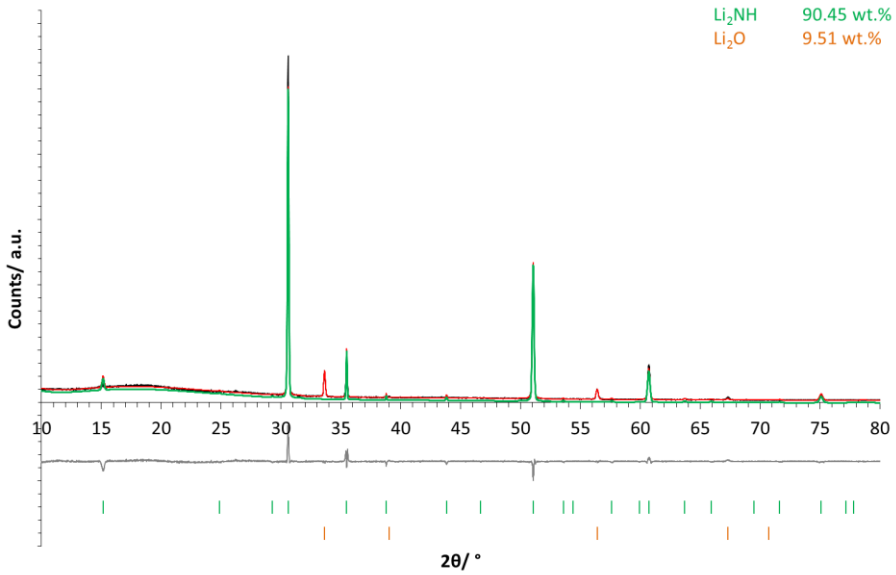

Figure 9.5 – Refinement plot showing the products of heating $LiNH_2$ + LiH at 550 °C for 12 hours. Green tick marks = Li_2NH, orange tick marks = Li_2O, with the cubic Li_2NH phase fit plotted in green

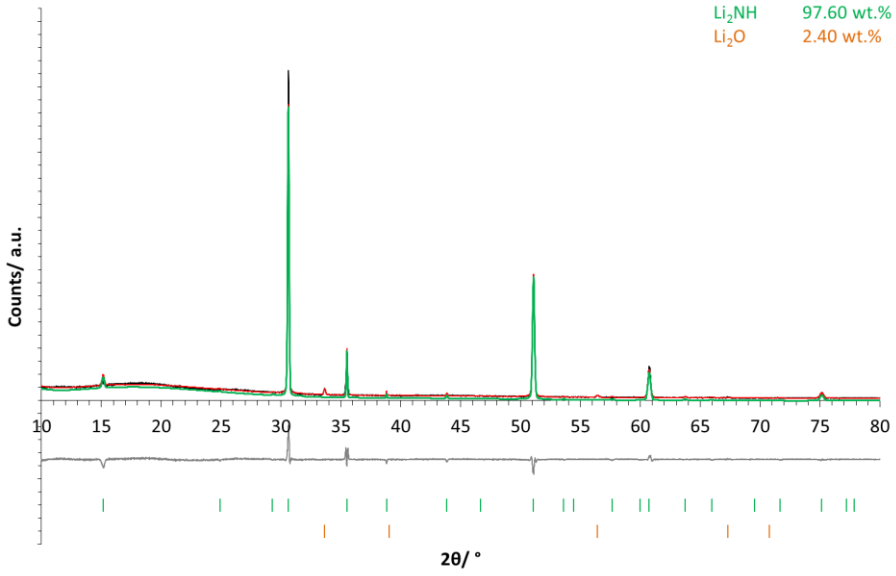

Figure 9.6 – Refinement plot showing the products of heating $LiNH_2$ + LiH at 575 °C for 12 hours. Green tick marks = Li_2NH, orange tick marks = Li_2O, with the cubic Li_2NH phase fit plotted in green

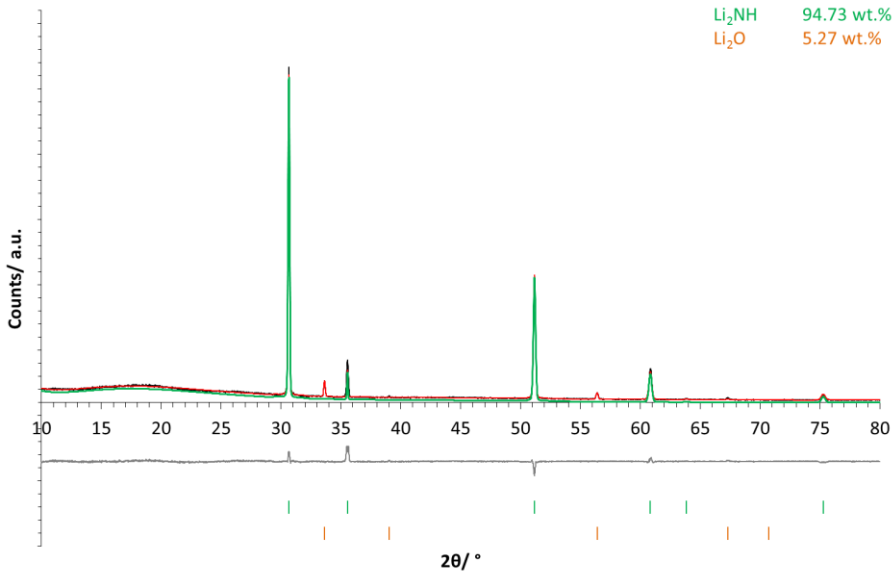

Figure 9.7 – Refinement plot showing the products of heating $LiNH_2$ + LiH at 600 °C for 12 hours. Green tick marks = Li_2NH, orange tick marks = Li_2O, with the cubic Li_2NH phase fit plotted in green

9.2 Nyquist Plots

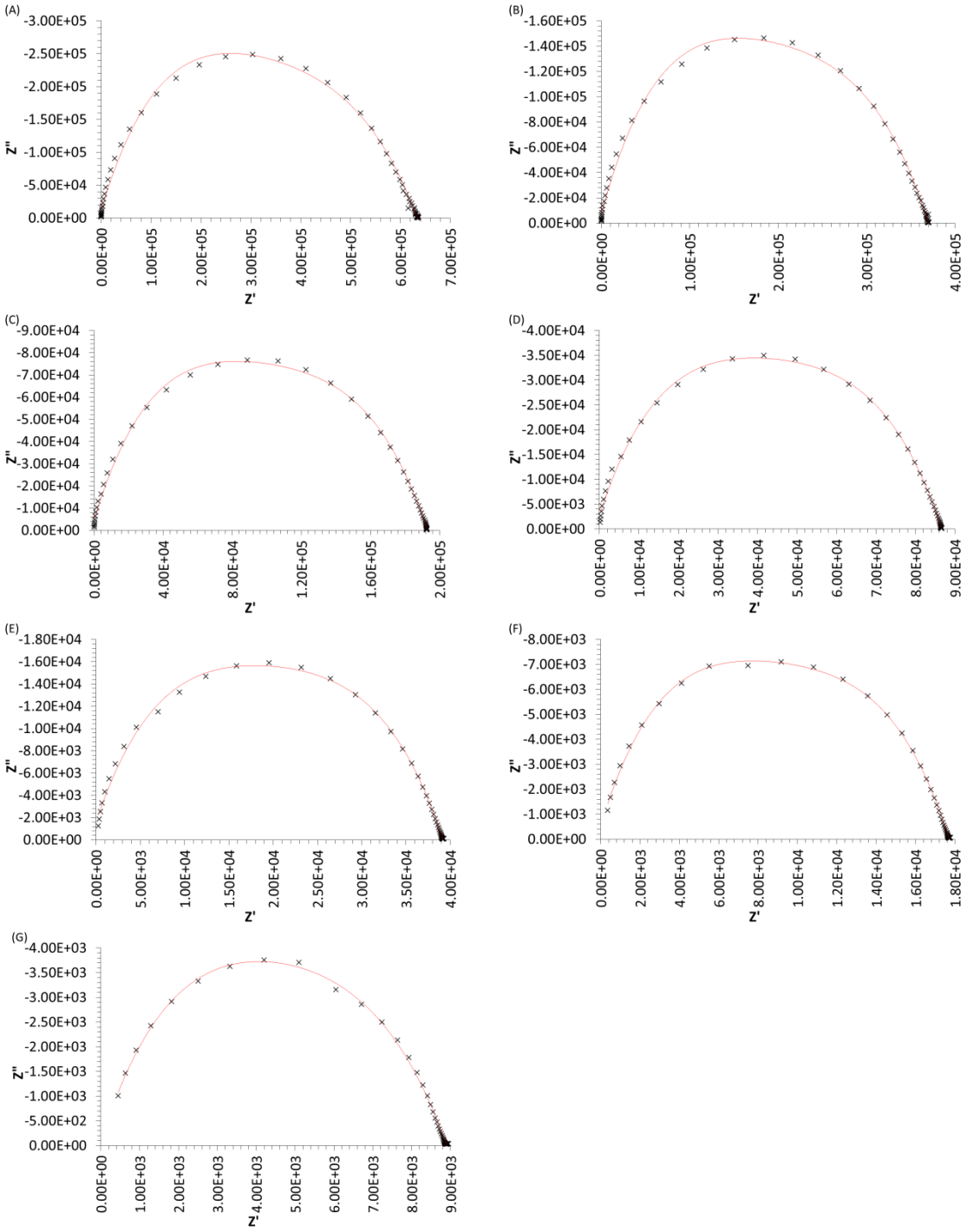

Figure 9.8 – Nyquist plots for orthorhombic sample synthesised at 125 °C for 12 hours where *n* = 0.5 for nLi$_2$NH + (1 – n)LiBH$_4$ (A) 22 °C (B) 30 °C (C) 40 °C (D) 50 °C (E) 60 °C (F) 70 °C (G) 80 °C

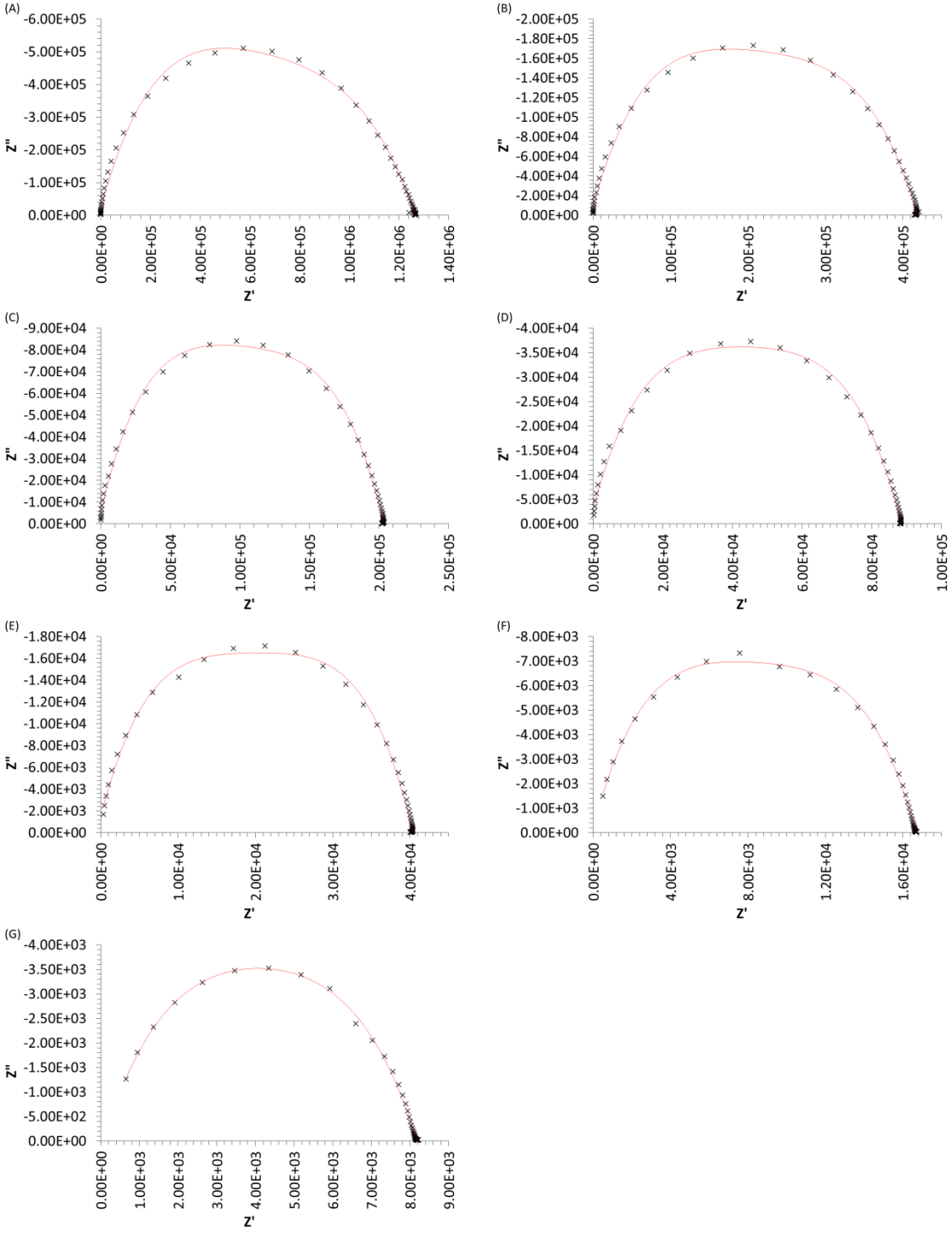

Figure 9.9 – Nyquist plots for orthorhombic sample synthesised at 125 °C for 12 hours where *n* = 0.42 for nLi$_2$NH + (1 – n)LiBH$_4$ (A) 18 °C (B) 31 °C (C) 41 °C (D) 50 °C (E) 60 °C (F) 70 °C (G) 80 °C

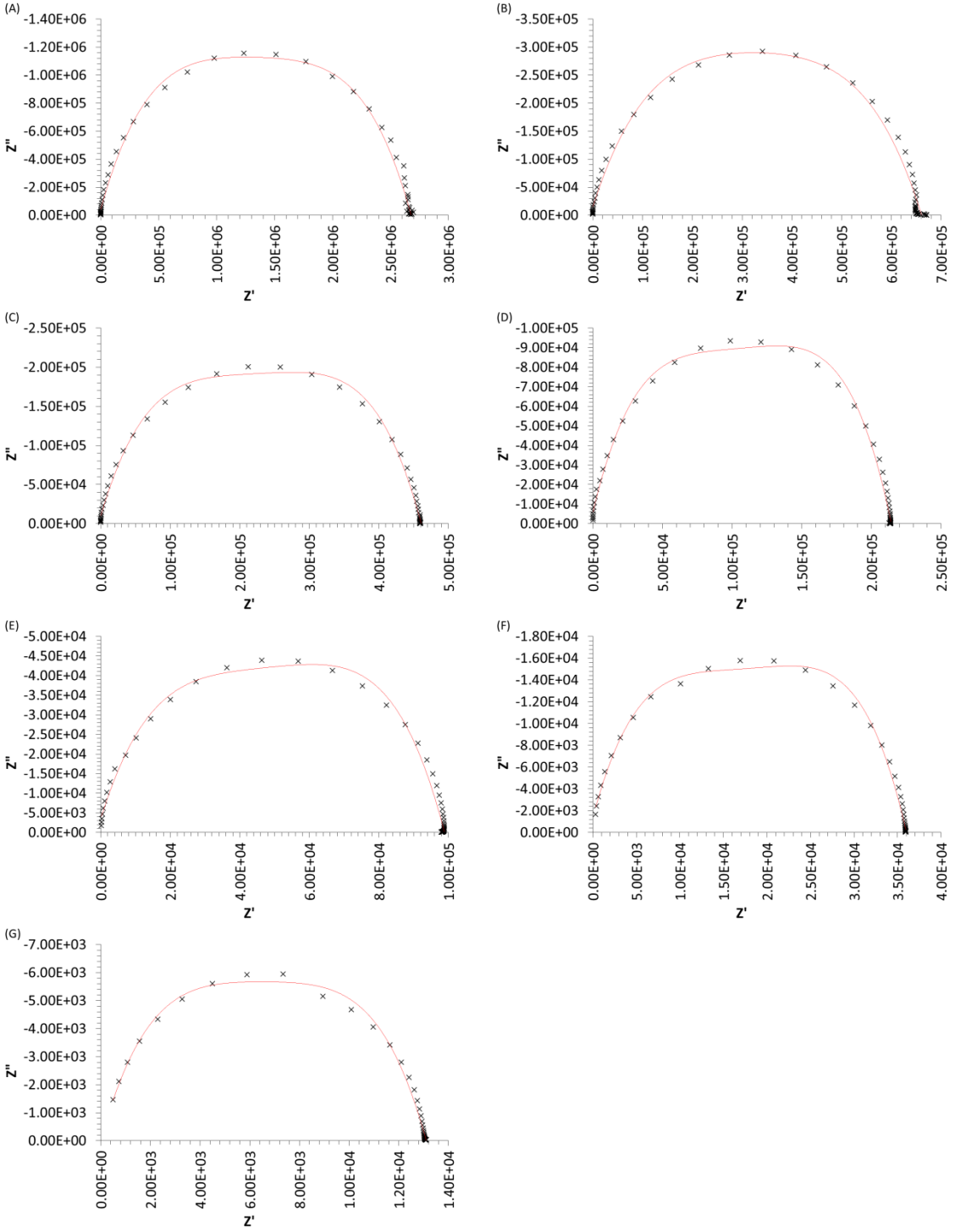

Figure 9.10 – Nyquist plots for orthorhombic sample synthesised at 125 °C for 12 hours where *n* = 0.33 for nLi$_2$NH + (1 – n)LiBH$_4$ (A) 22 °C (B) 36 °C (C) 41 °C (D) 50 °C (E) 59 °C (F) 70 °C (G) 80 °C

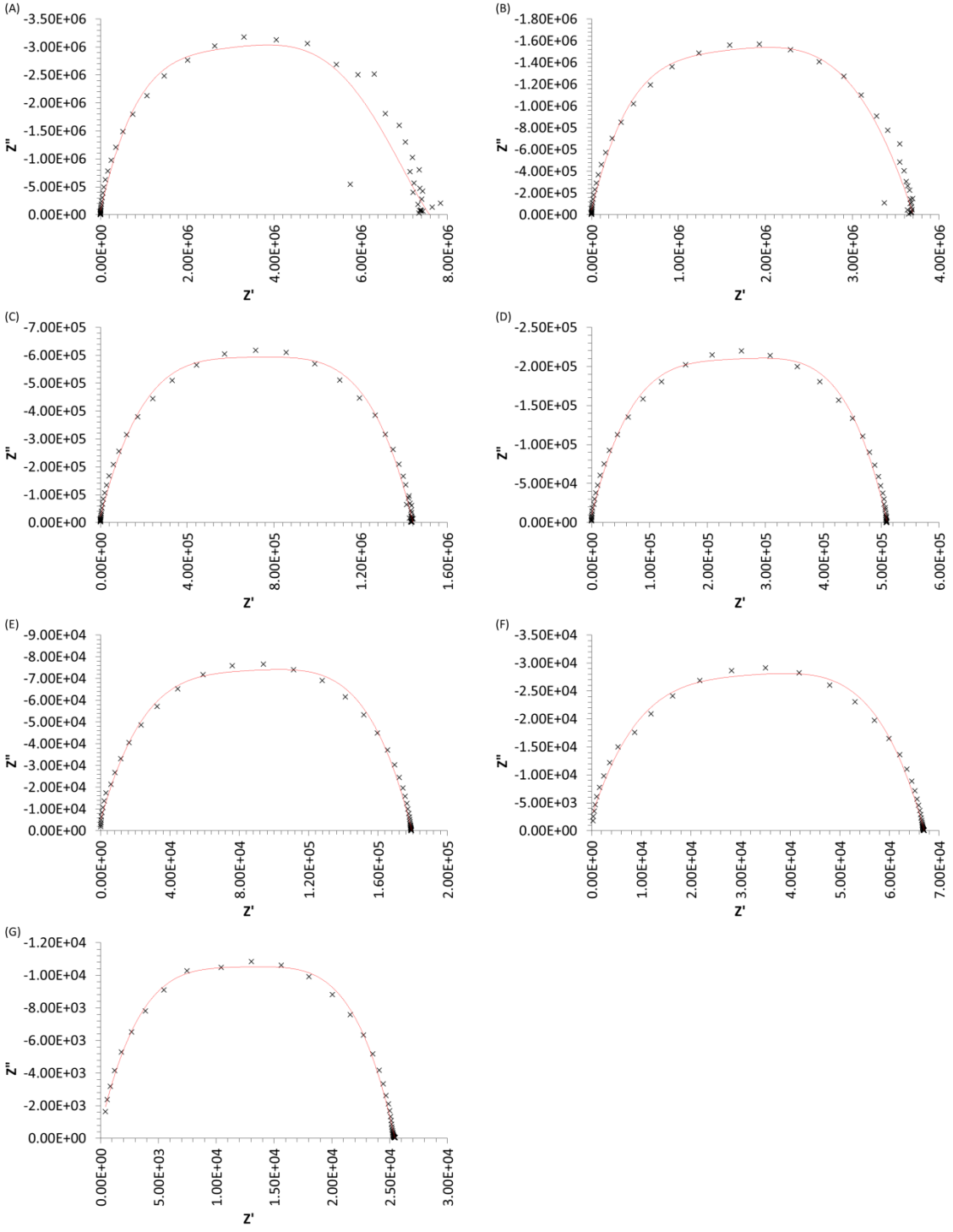

Figure 9.11 – Nyquist plots for orthorhombic sample synthesised at 125 °C for 12 hours where *n* = 0.25 for nLi$_2$NH + (1 – n)LiBH$_4$ (A) 22 °C (B) 29 °C (C) 39 °C (D) 49 °C (E) 60 °C (F) 69 °C (G) 80 °C

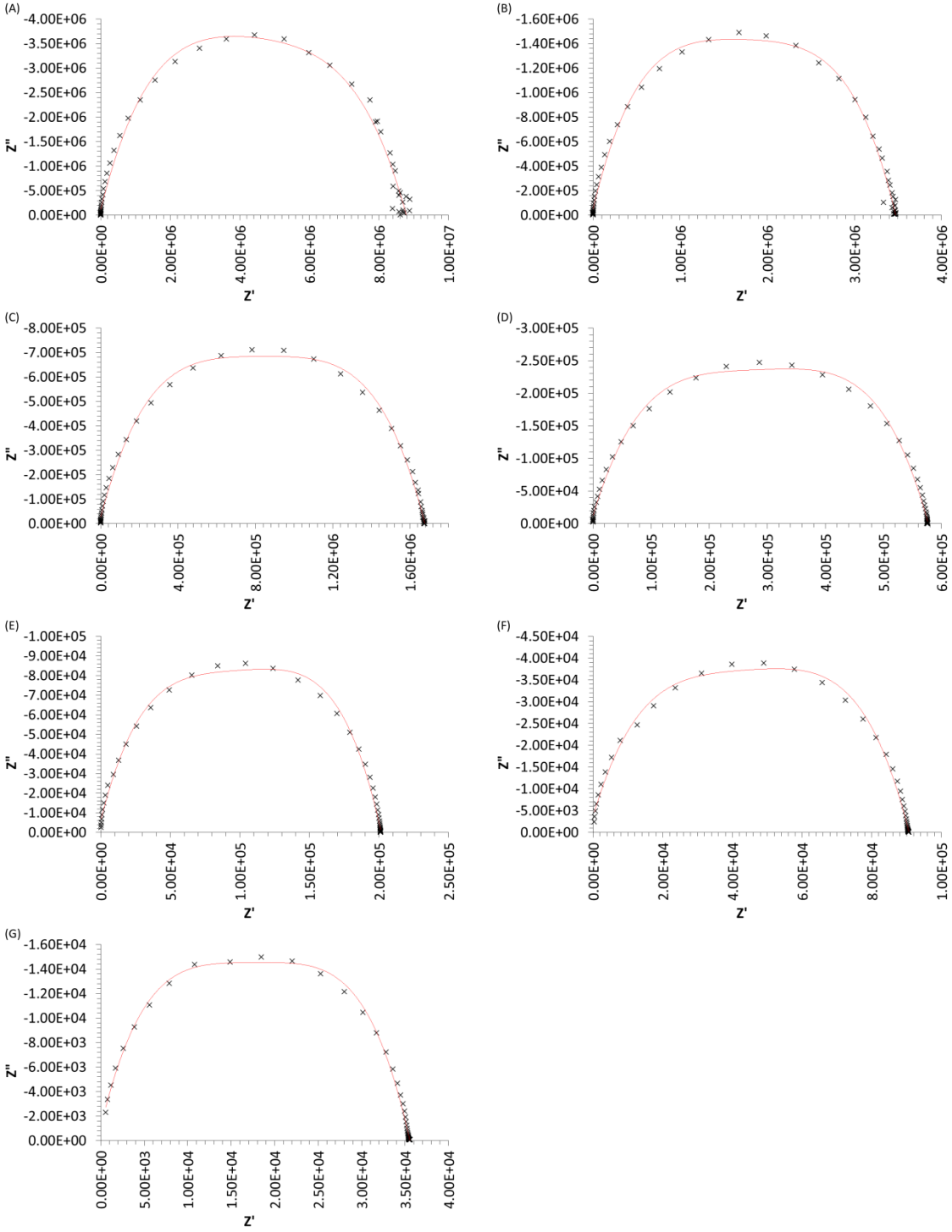

Figure 9.12 – Nyquist plots for cubic sample synthesised at 200 °C for 12 hours where *n* = 0.5 for nLi$_2$NH + (1 – n)LiBH$_4$ (A) 19 °C (B) 30 °C (C) 39 °C (D) 50 °C (E) 60 °C (F) 71 °C (G) 81 °C

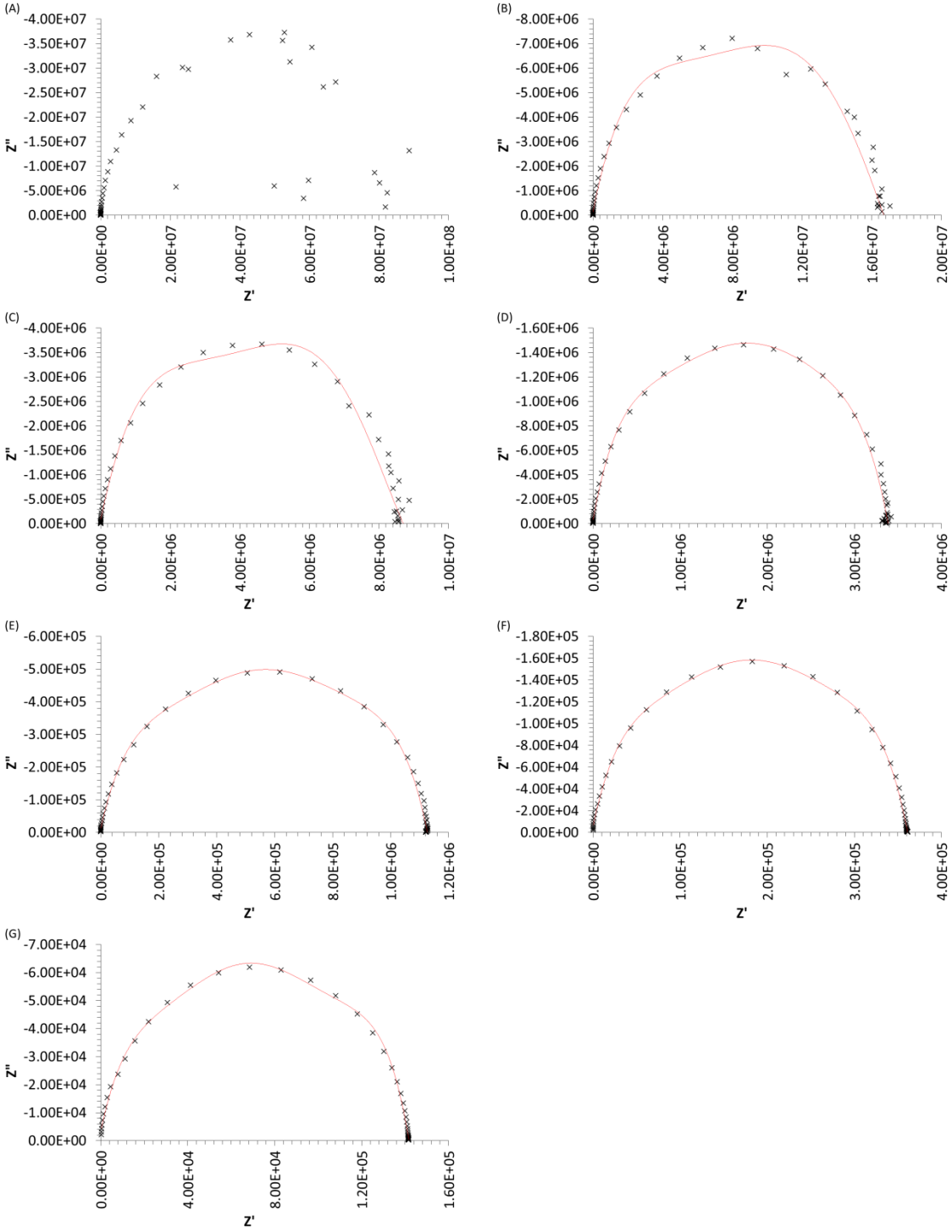

Figure 9.13 – Nyquist plots for lithium amide-borohydride-imide sample synthesised at 125 °C for 12 hours where n = 0.58 for $n Li_{1.5}(NH_2)_{0.5}(NH)_{0.5}$ + (1 – n)$LiBH_4$ (A) 20 °C (B) 36 °C (C) 41 °C (D) 51 °C (E) 60 °C (F) 70 °C (G) 80 °C

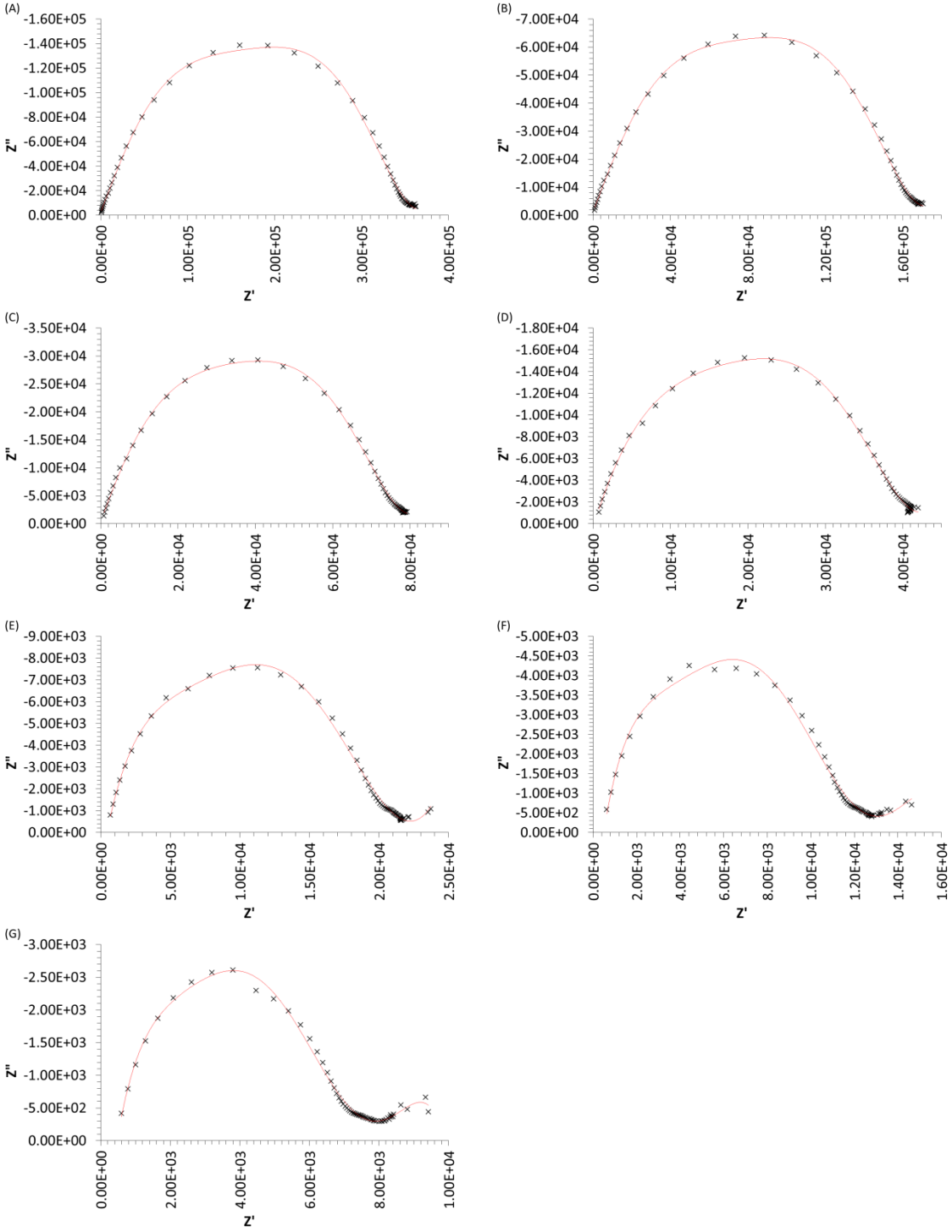

Figure 9.14 – Nyquist plots for Li_2NH (A) 17 °C (B) 29 °C (C) 39 °C (D) 49 °C (E) 59 °C (F) 69 °C (G) 79 °C

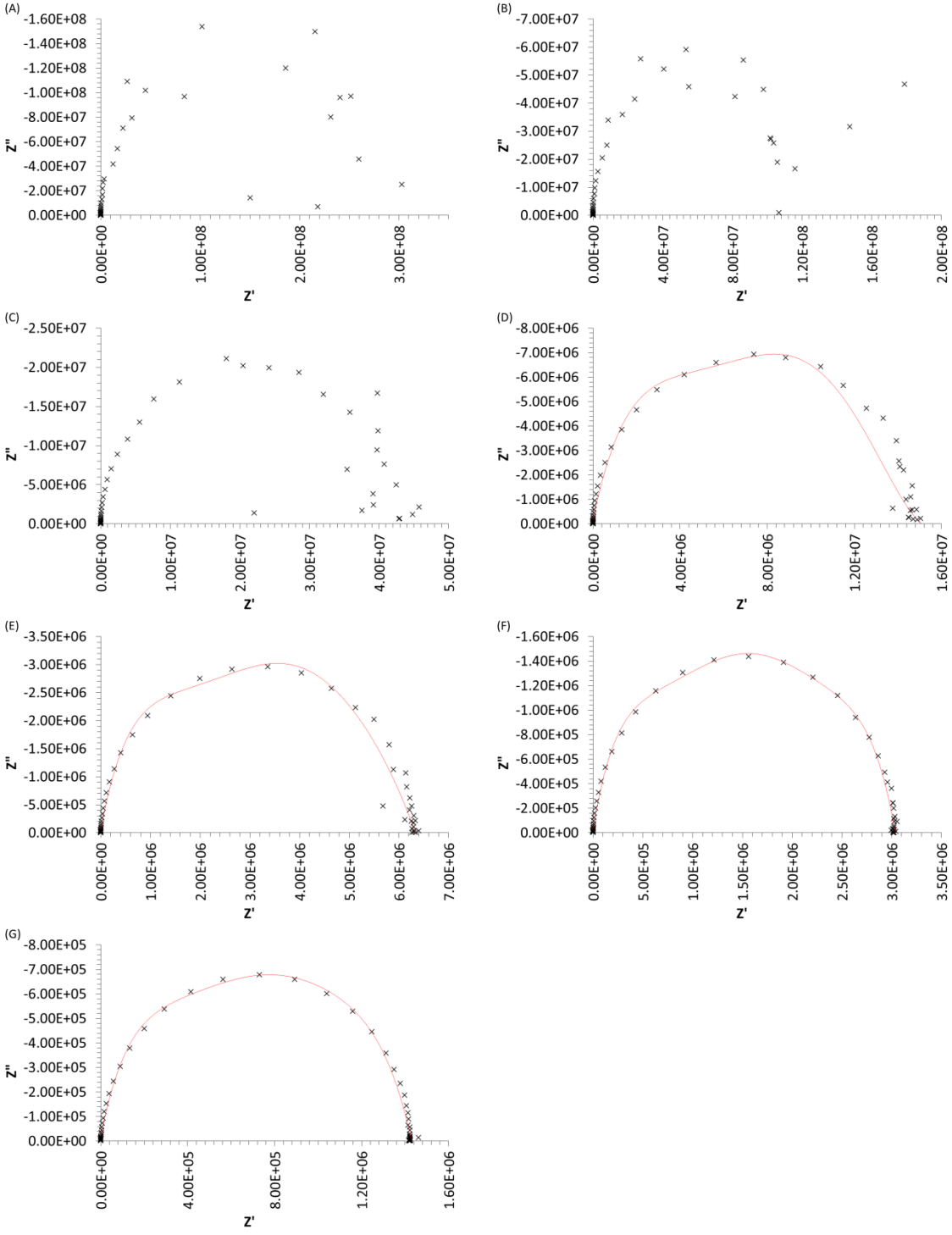

Figure 9.15 – Nyquist plots for $LiBH_4$ (A) 20 °C (B) 28 °C (C) 39 °C (D) 50 °C (E) 60 °C (F) 70 °C (G) 80 °C